Cranfield University

Gregory J. Smallwood

A Critique of Laser-Induced Incandescence for the Measurement of Soot

School of Engineering

Ph.D. Thesis

Cranfield University
School of Engineering
Department of Automotive Engineering

Ph.D. Thesis

Academic Year 2008-2009

Gregory J. Smallwood

A Critique of Laser-Induced Incandescence for the Measurement of Soot

Supervisor: N. Vaughan

October 2008

This thesis is submitted in fulfilment of the requirements
for the degree of Doctor of Philosophy

ABSTRACT

The health and environmental risks due to airborne nanoparticles are important issues facing the citizens and governments of the industrialized countries. To assess and mitigate these risks, increasingly stringent regulations are being enacted to reduce the particulate emissions from the combustion of hydrocarbon fuels, which primarily consist of soot. Improvements to the understanding of the formation of soot nanoparticles and their impact on the health and the environment are required. This necessitates advances in the state of quantitative measurement of soot.

Laser-induced incandescence (LII) is an optical diagnostic technique for the measurement of concentration and primary particle diameter of soot with high selectivity. Limitations with conventional LII were identified and a significantly enhanced technique, autocompensating LII (AC-LII), was developed employing time-resolved two-colour pyrometry, low fluence, and an absolute intensity calibration to address these limitations. AC-LII was shown to measure the soot particle temperature and automatically compensate for variations in the measurement environment that affected the peak soot particle temperature. With low fluence, AC-LII was shown to avoid soot sublimation, which impacted the measurements of concentration and size with high fluences.

AC-LII was applied to flames and to combustion-generated emissions. At low ambient temperatures it was discovered that the measured concentration varied with fluence. To mitigate this issue, it was recommended that AC-LII be performed at a moderate fluence near the sublimation threshold. In order to assess the impact of distributions of the soot primary particle diameter and of aggregate size, analysis coupling experiments with a state-of-the-art numerical model of the heat transfer was performed. The results showed that AC-LII signal evaluation should begin immediately after an initial anomalous cooling period but before distribution effects become dominant.

The sensitivity of AC-LII was optimized and applied to measure atmospheric black carbon concentrations. Comparison to other instruments demonstrated that AC-LII has significant advantages for the measurement of soot, and represents a major advancement

in techniques for nanoparticle characterization.

ACKNOWLEDGEMENTS

To Doug Greenhalgh, my thesis supervisor, I am grateful and appreciative of his incredible patience and staunch support throughout the course of this research. His perceptive insights aided me in extracting the key nuggets of truly useful science from a massive set of results. Every time I saw him, Doug had words of inspiration that thoroughly motivated me. Best of all, Doug has treated me as a colleague, and I look forward to years of camaraderie whenever we get together.

To Dave Snelling, who has been my research partner and mentor, I wish to express gratitude and thanks for his support, stimulating discussions, enthusiasm and, most of all, friendship since I joined the research community so many years ago.

To Will Bachalo, who had the courage to licence AC-LII and invest a small fortune in the development of a commercial instrument, thanks most of all for believing in me. I am truly grateful for your friendship and encouragement.

Good efforts in scientific research result from discussion of good ideas and subsequent accurate implementation of the experiments (physical and numerical). For this I must thank Fengshan Liu and Kevin Thomson, and all the members past and present of the LII Project. I would especially like to thank the gifted team of skilled technical staff that I have had the privilege to work with, Bob Sawchuk, Dan Clavel, and Daniel Gareau. Dave Snelling and Kevin Thomson proofread this manuscript, for which I am indebted.

I express my gratitude to Nick Vaughan, who stepped in as my thesis supervisor and skilfully guided me through its completion over the last year. For their work on laser-induced incandescence and support while I was onsite at Cranfield, thank you to Glenn Sherwood and Vivien Beyer. I am grateful to Binnie Hunt for keeping a watchful eye on me over the years.

There is a tremendous community that has evolved in the field of laser-induced incandescence. Christof Schulz of the University of Duisburg-Essen, who co-founded the LII Workshops with me, is singled out for praise due to his unwavering

encouragement. I also give thanks to the dozens of researchers at numerous organizations I have worked with in so many collaborative efforts.

I am grateful to the National Research Council Canada for providing financial support and all the staff with the Institute for Chemical Process and Environmental Technology for their moral support for the duration of this project.

The greatest thanks of all belong to Susan, my wife and best friend, who has been outstanding throughout, and our children Chelsea, Megan, and Bryden, all of whom have brought me great happiness.

Greg Smallwood

Ottawa, October 2008

TABLE OF CONTENTS

LIST OF FIGURES

LIST OF TABLES

NOMENCLATURE

A	constant
A_p	cross-sectional area of the probe volume as viewed by the detection system
c	speed of light in vacuum, 2.9979×10^{8} m/s
c_s	specific heat of soot
c_p	heat capacity at constant pressure of the surrounding gas
c_V	heat capacity at constant volume of the surrounding gas
c_{Vvol}	volumetric heat capacity of the surrounding gas
C	Cunningham correction factor for non-continuum effects
C_a	absorption cross-section
C_{vol}	volumetric scattering coefficient
d_{32}	Sauter mean particle diameter
d_f	particle fractal dimension
d_g	geometric mean for the log-normal distribution of d_p
d_p	primary particle diameter
$d_{p,LII}$	effective primary particle diameter for carbon black determined by LII
$D_{eff,fm}$	diameter of a heat conduction equivalent sphere in the free-molecular regime
D_g	geometric mean for the log-normal distribution of D_m
D_m	particle mobility diameter
e	elementary charge
$E(m)$	soot absorption function
f	Eucken factor
$F(m)$	soot scattering function
f_V	soot volume fraction, SVF
F_0	laser fluence
G	geometry dependent heat transfer coefficient
h	Planck constant, 6.6262×10^{-34} J s
ΔH_v	heat of vaporization
I_b	blackbody radiation intensity
I_p	radiation intensity emitted by a spherical soot particle
k	Boltzmann constant, 1.3806×10^{-23} J/K
k_g	thermal conduction coefficient of the ambient gas
k_0,k_L	aggregate fractal prefactors
Kn	Knudsen number
L	Lagrangian Invariant
L_{ag}	maximum dimension of an aggregate (Feret's diameter)
m	refractive index
m_g	mass of the ambient gas molecule
M	mass of primary particle
M_v	molecular weight of carbon vapour
n	number of elementary charges per particle
n_p	concentration of primary particles in the probe volume
NA	numeric aperture
N_{ag}	number concentration of aggregates
N_g	geometric mean for the log-normal distribution of N_p

N_p	number of primary particles in an aggregate
N_A	Avogadro's number, 6.022×10^{23}
N_{PV}	number of particles in the probe volume
N_v	molecular flux of carbon vapour
$p(d_p)$	probability distribution of d_p
$p(N_p)$	probability distribution of N_p
p_g	ambient gas pressure
P_p	power radiated by a single particle
$q(t)$	temporal laser power density per unit fluence
$\dot{q}_a$	rate of laser energy absorption by the particle
$\dot{q}_c$	rate of conduction heat loss from the particle to the surrounding gas
$\dot{q}_i$	rate of soot particle internal energy change
$\dot{q}_r$	rate of heat loss due to thermal radiation
$\dot{q}_s$	rate of heat loss due to soot sublimation
$q(\theta)$	scattering vector
r	aperture radius
R	universal gas constant, 8.313 J/mole K
R_g	radius of gyration
R_p	equivalent spectral radiance for the particles in the probe volume
R_S	spectral radiance of the calibration source
S	structure factor
S_{CB}	carbon black specific surface area
$S_{CB,LII}$	carbon black specific surface area determined by LII
t	time
t_{max}	time of peak soot temperature
T	temperature of a single soot particle
T_e	effective temperature of soot particle ensemble
T_g	gas temperature
T_i	initial soot particle temperature after heating
T_{max}	peak soot temperature
T_δ	limiting sphere temperature
V_a	volume of the aggregate
V_{CAL}	signal from the calibration source
V_{EXP}	signal from the particles
w_b	equivalent width of the laser light beam
Z_p	particle electrical mobility

Greek symbols

α	thermal accommodation coefficient
γ	specific heat coefficient ratio
γ^*	average specific heat coefficient ratio
Δ_f	equivalent bandwidth of the optical detection channel
ε_p	emissivity of soot particle
η	calibration factor

θ	scattering angle
λ	wavelength
λ_C	centre wavelength of the optical detection channel
λ_g	mean free path in the ambient gas
λ_{high}	upper detection wavelength
λ_{low}	lower detection wavelength
μ	gas viscosity
ν_s	space-filling volume fraction
ρ_s	density of soot
ρ_p	density of carbon black particles
σ_{ag}	aggregate differential scattering cross-section
$\sigma_{d,g}$	geometric standard deviation for the log-normal distribution of d_p
$\sigma_{D,g}$	geometric standard deviation for the log-normal distribution of D_m
$\sigma_{N,g}$	geometric standard deviation for the log-normal distribution of N_p
σ_{SB}	Stefan-Boltzman constant
$\tau(\lambda)$	spectral responsivity of optical detection system
τ_{max}	peak spectral responsivity of optical detection system

$\overline{\quad}$	arithmetic mean

ACRONYMS

2D-LOSA	two-dimensional line-of-sight attenuation
AC-LII	autocompensating laser-induced incandescence
AMS	aerosol mass spectrometer
APM	aerosol particle mass analyzer
ARB	Air Resources Board
ARP	Aerospace Recommended Practices
ATOFMS	atomic time-of-flight mass spectroscopy
BC	black carbon
CARS	coherent anti-Stokes Raman spectroscopy
CE-CERT	College of Engineering Center for Environmental Research & Technology
CNC	condensation nuclei counter
CPC	condensation particle counter
COV	coefficient of variation
CRUISER	Canadian Regional and Urban Investigation System for Environmental Research
DC	direct current
DISI	direct-injection spark-ignition
DLCA	diffusion-limited cluster aggregate
DMA	differential mobility analyzer
DPF	diesel particulate filter
DSMC	direct simulation Monte Carlo
EC	elemental carbon
EGR	exhaust gas recirculation
ELPI	electrical low pressure cascade impactor
ELS	elastic light scattering
EPA	Environmental Protection Agency
FSN	filter smoke number
FWHM	full-width at half of maximum
HCCI	homogeneous charge compression ignition
HELD	high energy laser diagnostics
HEPA	high efficiency particulate air
HS-LII	high sensitivity laser-induced incandescence
Nd:YAG	neodymium-doped yttrium aluminium garnet
LDF	laminar diffusion flame
LIBS	laser-induced breakdown spectroscopy
LIDELS	laser-induced desorption + elastic light scattering
LIF	laser-induced fluorescence
LII	laser-induced incandescence
LTC	low temperature combustion
NIR	near-infrared
NRC	National Research Council Canada
NSSA	normalized specific surface area
NTE	not-to-exceed
OBD	on-board diagnostics
PAH	polycyclic aromatic hydrocarbons

PC	personal computer
PEMS	portable emissions measurement systems
PM	particulate matter
PMT	photomultiplier tube
ppm	parts-per-million
ppb	parts-per-billion
ppt	parts-per-trillion
PTFE	polytetrafluoroethylene
RDG	Rayleigh-Debye-Gans
RDG-PFA	Rayleigh-Debye-Gans polydisperse fractal aggregate
ROD	relative optical density
RPM	revolutions per minute
SAE	Society of Automotive Engineers
SEM	scanning electron microscope
SLPM	standard litres per minute
SMD	Sauter mean diameter
SMPS	scanning mobility particle sizer
SSE	spectral soot extinction
STSA	statistical thickness surface area
SVF	soot volume fraction, f_V
SWNT	single-walled carbon nanotubes
TDI	turbocharged direct injection
TEM	transmission electron microscope
TEOM®	tapered element oscillating microbalance
TPM	total particulate matter
UV	ultraviolet
VIS	visible

1. INTRODUCTION

The nature of soot and its incandescence has fascinated humankind, and scientists in particular, for centuries. Michael Faraday spoke at length about both the soot particles and the incandescence they produce during his Christmas Lectures to a juvenile audience, presented eloquently in a series of six lectures on *The Chemical History of a Candle*.[1] In these lectures Faraday indicated an interest in the formation of soot, and the fate of these carbon particles, Figure 1-1.

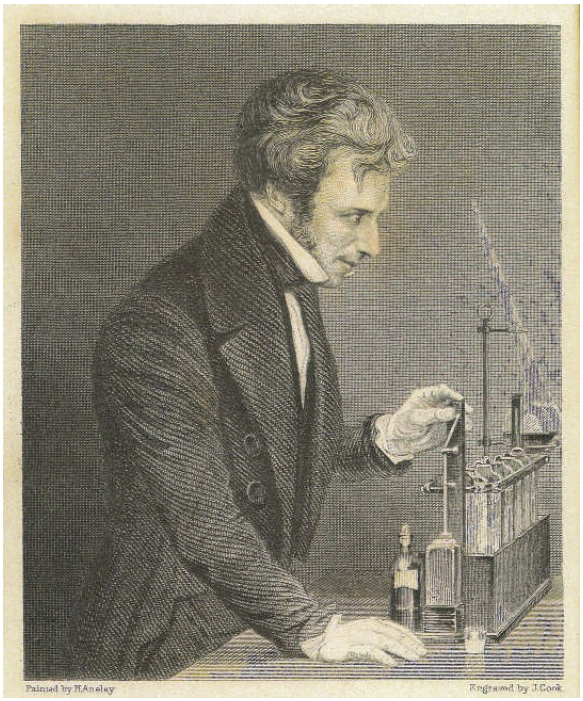

"*Suppose I take a candle and examine that part of it which appears brightest to our eyes. Why, there I get these black particles, which already you have seen many times evolved from the flame… what is that black substance? Why, it is the same carbon which exists in the candle… You would hardly think that all those substances which fly about London, in the form of soots and blacks, are the very beauty and life of the flame… it is to this presence of solid particles in the candle flame that it owes its brilliancy.*"

"*The heat that is in the flame of a candle decomposes the vapor of the wax, and sets free the carbon particles; they rise up heated and glowing as this now glows, and then enter into the air… as a perfectly invisible substance… Is it not beautiful to think that such a process is going on, and that such a dirty things as charcoal can become so incandescent?*"

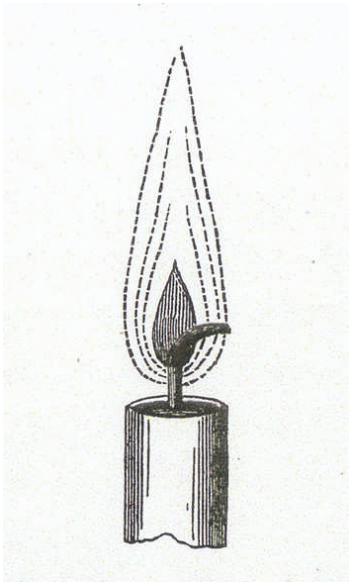

Figure 1-1. Lectures on the Chemical History of a Candle by Michael Faraday[1]

Understanding soot properties is no less important today. To improve this understanding of the formation of soot nanoparticles, and their impact on the health of humans and on the environment, advances must be made in the state of quantitative measurement of these nanoparticles. Laser-induced incandescence (LII) is an optical diagnostic that has been applied for over three decades to perform measurements on the characteristics of soot.[2] The development of LII to enhance its capability for the quantitative measurement of soot concentration, active surface area, and primary particle diameter is the primary subject of this work.

Soot is defined in the Oxford English Dictionary[3] as:

"*A black carbonaceous substance or deposit consisting of fine particles formed by the combustion of coal, wood, oil, or other fuel.*"

This definition is consistent with the understanding by combustion scientists, who use the term soot to refer to the dry solid particles produced through the incomplete combustion of hydrocarbon fuels. However, scientists in other fields use different terminology to describe similar or identical particles. Chemists characterizing the particles emitted from combustion sources use the term elemental carbon (EC), which is an operationally defined quantity determined through chemical analysis. Atmospheric scientists refer to black carbon (BC) as "the main light-absorbing component of aerosols."[4] In industry, these particles are intentionally produced as carbon black (CB). Throughout this document the terms soot, black carbon, elemental carbon, and carbon black will be used interchangeably, depending on the context, to refer to the solid, predominantly carbon, particles produced by combustion.

This introduction documents the need for the measurement of soot, discusses briefly some of the available instruments for making measurements, reviews the laser-induced incandescence method, and briefly covers some applications of LII up to the early 2000's. As such it details the rationale for laser-induced incandescence and demonstrates that it is the key technique for the quantitative measurement of soot. A synopsis covering the objectives and an overview of this work concludes this section.

1.1. BACKGROUND

The development of diagnostics and instruments for the characterization of soot nanoparticles has been driven by the desire of combustion scientists to better understand the processes of soot formation and oxidation in flames.[5] The presence of soot is essential in some processes: it is the product in carbon black; it provides the source of light radiation in pyrotechnic and pyrophoric flares; and is the dominant source of radiant heat transfer in boilers and furnaces. Nevertheless, there is a much larger community encompassing industry, academia, and government who are interested in the fate of the nanoparticles that escape from the combustion zone and are emitted into the surroundings. As such, soot is an undesirable product in many combustion processes where it is expelled with the exhaust, contributing to air pollution. The diagnostics that are available are insufficient to meet the characterization needs of this larger community.[6] As this work seeks to address the needs of those who are interested in the fate of soot particle emissions, the focus of this section is on measurement of the unwanted particulates, primarily from diesel, gasoline, and gas turbine engines, although the techniques described in most cases are equally effective in measuring soot in flames and from non-engine sources.

The most significant anthropogenic sources of particulate matter (PM) are emissions from the combustion of hydrocarbon fuels. Combustion-generated nanoparticles primarily consist of soot, a solid nonvolatile fractal aggregate predominantly composed of carbon, and a variety of volatile and semi-volatile liquid species which may condense on the surface of the soot particles or nucleate as the exhaust is cooled and diluted during the emission process. The solid fraction may also contain ash (metal sulphates and oxides). The volatile species are mainly organics, but may include nitrates, sulphates, and many other species. To assess the environmental and health risks posed by nanoparticles emitted by hydrocarbon combustion, and to propose potential mitigation strategies, additional information about their morphology and chemistry is required.

Soot formation is a multifaceted process involving the conversion of hydrocarbon fuels with molecules containing relatively few carbon atoms into a solid nanoparticle containing millions of carbon atoms in a period of a few milliseconds. It involves phase

changes, a large number of different chemical species and complex chemistry, pyrolysis, isomerization, nucleation, surface growth, and agglomeration, along with many other processes, which must all occur in an environment with temperature and species conditions conducive for soot formation and growth. A complete description of soot formation can be found in Bockhorn.[7] The resulting soot appears, Figure 1-2, as near-spherical primary particles that cluster to form aggregates.[8, 9] Despite decades of study in which numerous kinetic models have been proposed, the mechanisms governing soot formation remain elusive.[10] Soot particle microstructures can vary from graphitic to amorphous, depending on the original fuel and combustion conditions. The ash in PM emissions from engines is mostly from additives in the lubricating oil, but there are also metal oxides from engine wear and corrosion of exhaust system components. The volatile matter is mostly hydrocarbon from the fuel and lubricant, and hydrated sulphuric acid, and is found either adsorbed on the surface of solid particles, or in the form of small droplets no larger than the primary soot particles, where the latter are typically on the order of 20-50 nm in diameter.

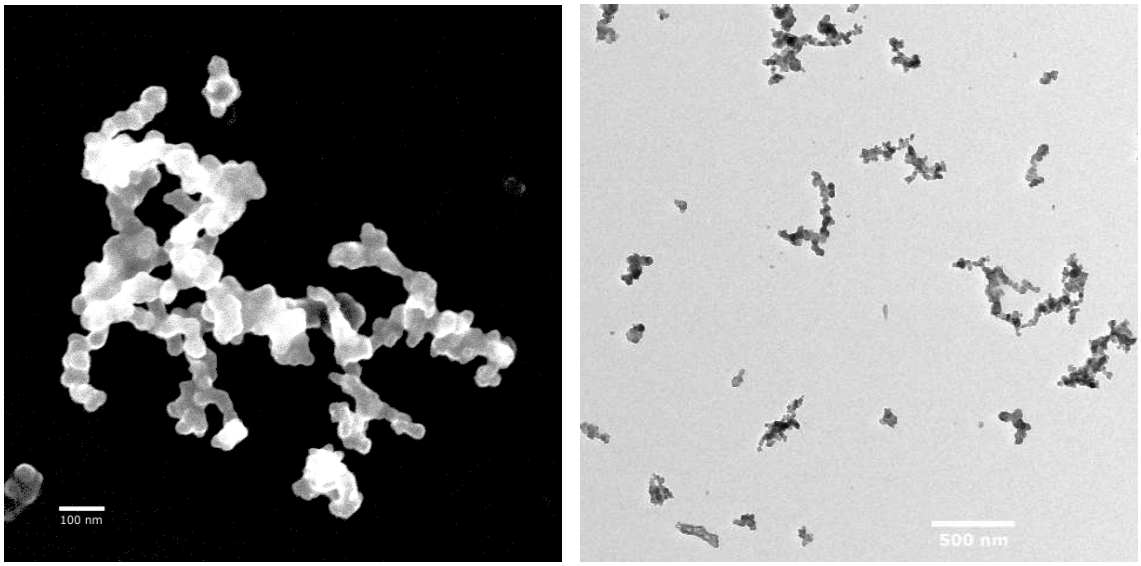

Figure 1-2. SEM (scanning electron microscope) image (left) and TEM (transmission electron microscope) image (right) of soot particles collected from a flame by thermophoretic sampling. The near-spherical primary particles and the aggregates they form are discernible.

Emission characterization, atmospheric characterization, atmospheric modelling, and studies on the health and environmental effects of combustion-generated nanoparticle emissions depend heavily on accurate and precise measurements of the nanoparticle characteristics. Reducing the environmental impact and improving operating efficiency of combustion are high priorities for industrialized countries and can only be achieved with the aid of improved instruments for characterizing soot.

1.1.1. Air quality and health effects

Regulators, health researchers, and environmental scientists have started focusing on nanoparticles because of increased concerns on the health impacts of ultrafine particulate matter.[6, 9-11] Health and environmental research indicates that characteristics including the size, size distribution, surface area, number, and chemical composition of the particles are important. Interaction between these characteristics is unknown, but it is recognized that they must be investigated once the instruments are available to assess these characteristics independently.

The health risk due to inhalation of airborne nanoparticles is seen as an important issue facing the citizens of the industrialized countries. These nanoparticles contribute significantly to poor atmospheric air quality and related adverse health and environmental effects, including cardiovascular, respiratory, and allergic distress, and smog, poor visibility, and climate change.[11]

Commercial-scale production of engineered nanomaterials, such as single-walled carbon nanotubes (SWNT) may pose a similar health risk to production personnel. The Royal Society has highlighted the need for urgent research into developing nanometrology tools to address the risk associated with "the health, safety and environmental hazards of nanotechnologies as being restricted to discrete manufactured nanoparticles and nanotubes in a free rather than embedded form."[12] Interestingly, they further conclude that "We recommend that researchers and regulators looking to develop methods to measure and monitor airborne manufactured nanoparticulates liaise with those who are working on the measurement of pollutant nanoparticles from sources such as vehicle emissions."[12]

Recent studies of the health effects of air pollution show that increased levels of soot

and other tiny particles found in large and midsize cities increase the risk of premature death from cancer and heart disease.[13] Breathing high concentrations of lung-penetrating particulates has been shown by Arden et al.[14] to be an important environmental risk factor for cardiopulmonary and lung cancer mortality. Studies by the American Cancer Society concluded that as the concentration of soot particulates increases, the risk of early death rises by 4 to 8 percent and the number of aggravated asthma cases increases depending on the concentration and long-term exposure.[15] Fortunately, soot particulates emitted by cars, trucks, power plants, factories, aircraft, and other combustion processes have been reduced substantially over the past decade and will drop further under pending regulations. However certain regions undergoing rapid industrial development are producing higher levels of particulate emissions. These emissions travel on the jet stream to produce a global rather than simply a national or urban problem. Not only the mass of the particulates but also the size and number density play a significant role in the health effects on humans and other living organisms as well as upon the climate.

Past efforts have focused on reducing the mass of the combustion-generated particulates in the PM_{10} size range (particulates below 10 μm aerodynamic diameter) which were visible and hence, readily associated with emissions at the source. Reductions in the mass of PM_{10} do not necessarily mean reductions of the smaller particles in the size range, as the larger particles in the size range contribute most of the mass. However, especially deleterious are the smaller sized respirable aerosols and particulate matter that are known to produce adverse health effects and are suspected of producing high altitude clouds which adversely affect the earth's climate.[16, 17] $PM_{2.5}$ range (particulates below 2.5 μm aerodynamic diameter) particulates have been advanced as the regulatory standard for ambient particulates in the USA while future regulations may be established for $PM_{1.0}$. It is known that particles in the 0.3 μm size range deposit in the lungs and particles smaller than 0.3 μm find their way into the alveoli. Irrespective of their chemical composition, evidence indicates that these fine particles have harmful effects. Vehicle emissions data show that the majority of the particles emitted with the exhaust fall in the range of 0.1 μm. However, it is the larger particles, centred around 0.3 μm, that dominate the mass-weighted size distribution.[18]

1.1.2. Regulations

Demand for improved environmental performance has led to increasingly restrictive emission regulations for vehicles throughout Europe, North America, and Japan. Proposed regulations indicate that this trend to lower emissions levels will continue for the foreseeable future. Although the mass of PM was previously regulated only for diesel vehicles, recent regulations have been introduced in North America that limit PM mass for all light duty vehicles. While PM mass is regulated for environmental and health concerns, there is also a strong need to control soot and other particulates in the exhaust plume because of their adverse influence on the performance of the power generation systems.

The emissions performance requirements for diesel powered vehicles and aircraft gas turbine engines have been raised throughout Europe in an effort to reduce the level of particulate emissions. Exploiting these engine technologies will necessitate the development of emission control systems and further regulation is likely. Certain non-road sources are unregulated, but restrictions that will be implemented in the near future are being extended to off-road vehicles such as farm tractors and construction equipment.

Diesel-powered vehicles are desirable for the transportation of goods and people, but they present a dilemma to governments. The need to reduce CO_2 emissions favours lean-burn technologies (diesel, direct injection spark ignition) over less fuel efficient engines, but these lean burn engines tend to produce more particulate mass, exacerbating the PM issue. The solution is that emissions control systems must be implemented on these vehicles in order to reduce pollutant formation and the emissions must be monitored to ensure adequate performance of the systems and compliance with regulations. There are many developments occurring worldwide in the regulation of particulate matter. These have led to the introduction of diesel particulate filters in some jurisdictions.

The aforementioned regulations and trends to reduced emission rates are based on the mass emission rates of PM. Currently, particle size and total particle number emissions from diesel engines are not regulated. At least two factors have led to this oversight: a

general lack of instrumentation to adequately characterize the size and number of fine amorphous particulates; and the general lack of medical research evidence to define acceptable levels of PM as a function of aggregate size. However, the research cited above indicates that particulate levels existing in urban areas are producing significant hazards to our health. Instrumentation developments are progressing that will allow more reliable and convenient means for characterizing the particulates that will lead to improved correlations between particulate loading and expression of deleterious health effects. Recent worldwide trends in regulation of combustion-generated nanoparticles have begun to emphasize the need for separate determination of volatile and nonvolatile nanoparticles, as the measurement of nonvolatile particle emissions has been determined to be far more reproducible and precise than that of volatile particles.[19, 20] These trends are leading to a move away from mass-only regulation to regulations that also include number, size, and separate measurement of nonvolatile and volatile particles. This transformation is affecting on-road and aviation vehicles first, but is anticipated to spread to other transportation modes and other sectors of the economy.

To develop processes and techniques for limiting the emission of soot to meet increasingly stringent and specific regulations, we must first possess suitable means for reliably measuring various soot-related parameters. These methods must have adequate measurement range to monitor and characterize the pollutant emissions over a very wide range of concentrations, and must operate under a range of environmental conditions from *in situ* exhaust to atmospheric monitoring. In the case of particulate matter, information on the particle mass, size, and volume fraction is needed. The lack of availability of suitable diagnostics has resulted in a degree of uncertainty in the correlation of the particulate loading with health effects. Improvements in the instrumentation are needed to help in developing the test protocols, standards and regulations that will preserve the environment and limit risks to health. Laser-induced incandescence (LII) has emerged as a technique for measuring soot concentration and size without apparent interference from non-soot matter because it is evaporated and/or does not contribute to the signal.

1.1.3. Characteristics of particulate emissions

Particulates present challenging measurement problems, both in determining the

appropriate quantity to be measured and the technique to perform the measurement. Due to the aggregate morphology and often complex composition of PM, these nonspherical particles are difficult to characterize as there are many parameters to specify. As an example, the size of the aggregate can be characterized by the number of primary particles in the aggregate, the diameter of a sphere with equivalent bulk material volume, the Feret diameter, the aerodynamic diameter, and the mobility diameter.

One common characteristic is that there is typically a high number density of particulates (10^5–10^{10} particles/cm^3)[18] even when the total volume concentration is relatively low so that particle counting techniques often require the flow to be diluted until the number density is within the range of the instrument. Conversely, the range of loading from soot sources is very wide, ranging from volume concentrations of <0.1 ppt for smog-free ambient atmospheric measurements to >10 ppm for in-flame or carbon black reactor measurements – greater than 8 orders of magnitude.[21]

Soot formation occurs in flames via nucleation of primary particles, growth of the individual primary particles, and collisions leading to rapid aggregation. The aggregation process leads to a significant reduction in the number density of particles. The particle size changes rapidly, increasing due to aggregation and decreasing due to oxidation of the particles. Once the soot exits regions with temperatures and conditions sufficient to maintain the formation and oxidation reactions, the soot volume concentration is fixed. The aggregates are fractals in that, within specified size limits, they appear identical when viewed over a range of sizes. The fractal concept allows the soot aggregates to be simply described by a fractal dimension.[22, 23]

In engine exhaust there can be significant levels of unburned hydrocarbons and other combustion byproducts which can condense on the soot particles. In North America, hydrated sulphuric acid is one of these adsorbed byproducts; however, its contribution is likely to be significantly reduced as low sulphur fuel regulations have recently come into effect. The net effect is that soot may become an increasingly large fraction of the total particulate matter that is emitted. Stimulated by UV radiation, further changes occur after emission as the particles react with other species in the atmosphere. The relation between particle size and mass is not known *a priori*, due to the variations in

morphology and composition of the particulates. Also, freshly emitted soot particles are initially hydrophobic, but over time the surface oxidizes slowly and combined with the deposition of water soluble inorganic material, the particles become hydrophilic.24 The change in structure of the particles during this process is unknown, and so is the exposure to humans, as they may inhale a mix of fresh and aged particles with a wide range of coatings.

1.1.4. Current measurement standard

From the perspective of monitoring, particulate matter emissions from diesel engines are currently defined as the mass of the matter that can be collected from a dilute exhaust stream on a filter kept below 52°C. The method, referred to as gravimetric sampling, excludes condensed water but includes organic compounds that condense at or above this temperature. These measurements provide time-average PM emissions data over the time period required to collect a measurable mass of soot. Thus, transient PM measurements using this technique are impractical and agglomeration of the collected PM and other condensed material likely occurs on the filter making measurement of particulate size and size distribution on the filter difficult or impossible. Furthermore, as diesel engines improve, the quantity of PM generated is reduced, which pushes this gravimetric technique closer to its reproducibility and sensitivity limits, and thus limit its utility for the future.

1.2. MEASUREMENT METHODS

The parameters of most interest in characterizing particulates are the mass concentration; volume concentration; number density; aggregate size; aggregate size distribution; active surface area; and composition. Some of the available instruments that claim to measure one or more of these properties are discussed below, including those that measure mass, count particles, use optical transmission/reflectance/scattering to determine concentration, measure size distributions, measure surface area, and determine chemical composition.

An average mass concentration of particulates can be determined by the gravimetric filter method, and an average volume concentration can be determined by light extinction techniques. The number concentration can be determined by particle

counting techniques up to about 10^5–10^7 particles/cm^3. There are instruments available to determine the aerodynamic and mobility diameters, and it is possible to measure a representative distribution of the mobility diameter. However, measured particle size distributions which consider all particulates are very sensitive to condensed particles since the amount and way that condensed particles formed is highly dependent on the sampling condition. Concerns regarding the influence of dilution ratio, residence time, temperature, preconditioning, and sampling line materials, as well as the limitations of the instruments available to measure particulates are being voiced with increasing frequency. Differences in measured particulate size distributions and/or mass due to the sampling issues are attributed to marked variations in the quantity of condensed aerosols while it is generally accepted that the measurement of soot is insensitive to the sampling conditions. Many of the issues have been summarized by Witze.[25]

Conversely, soot aggregates, being solid particles, are generally unaffected by sampling, thus measurements of particulate matter which isolate the soot show consistent measurements (total mass and size distribution) independent of the sampling method. Evidence has indicated that soot emissions have characteristic size distributions which could be used to distinguish them from other aerosols.[26]

There currently are no satisfactory *in situ* or online sampling methods for determining active surface area, which has significant health impacts as it provides the delivery mechanism for toxics, and is also important in determining performance of carbon black. Similarly, methods for determining composition are *ex situ* and offer poor reproducibility.

For mass concentration measurements, the standard gravimetric filter technique is nearing its reproducibility and sensitivity limits with modern low emission engines, and it does not offer transient measurement capability. The tapered element oscillating microbalance (TEOM®) is another gravimetric method that does have a transient capability, but has similar sensitivity limits, as it is limited by the change in mass necessary to create a measurable change in the frequency of oscillation.

Volume concentration can be determined by line-of-sight light extinction methods, provided the refractive index of the particles is known, the distribution of particles along

the measurement path is uniform, and the length of the path is known. The particle volume concentration is proportional to light absorption so the measured extinction must be corrected for scattering. The aethelometer is an instrument that employs light extinction to infer concentration. Number density can be determined by particle counting instruments such as the condensation nuclei counter (CNC) as long as the criterion of a single particle in the probe volume can be met, thus limiting the upper concentration.

Light scattering methods are often employed to determine the particle size but the interpretation applied to the signals (Mie or Rayleigh) greatly simplifies the true situation as these interpretations assume spherical particles. Unfortunately, the aggregates have a much more complex interaction with light than Mie theory provides.[27] The high number density of particles further complicates scattering, as a distribution of particle sizes is likely to be present in the probe volume at any given moment, and it is the large aggregates that preferentially contribute to the scattering. These light scattering approaches can lead to erroneous results when applied to aggregated nanoparticles, and do not distinguish between volatile and nonvolatile nanoparticles. One example of a scattering instrument is the nephelometer. Dilution can be used to achieve single particle scattering, but then issues arise with detecting small particles due to weak signals.

There are several types of instruments available to measure size distributions. The aerodynamic diameter distribution can be determined with the electrical low pressure cascade impactor (ELPI). Although it suffers anomalies due to particle bounce, the need to correct the largest sizes, and a lack of sensitivity at low concentrations, it does provide a relatively coarse distribution rapidly, allowing transient distribution measurements. The mobility diameter can be measured with the scanning mobility particle sizer (SMPS) which provides a high resolution size distribution. Issues with the SMPS for PM measurements include that it is too slow for transient measurements, the effective density of the particle is a function of the mobility diameter[28], multiple charge effects causing larger particles to appear in smaller size bins, and there are limits on the maximum measurable number density of particles. The morphology of highly nonspherical soot aggregates cannot be adequately described with nanoparticle metrics

such as mobility diameter or aerodynamic diameter, nor can the instruments for these metrics distinguish between volatile and nonvolatile nanoparticles.

Active surface area can be measured by a variety of instruments, including the epiphaniometer, the diffusion charger, and the photoelectric aerosol sensor. These use radioactive isotopes, corona discharge, and ultraviolet light, respectively, to charge the particles. For all these techniques, the charge is proportional to the surface area, although for ultraviolet light it is also dependent upon the particle composition. Atomic time-of-flight mass spectroscopy (ATOFMS) can provide great detail on the elemental composition of the particles, but only for a single particle at a time, and thus it is difficult to obtain representative sampling.[29]

Further details on these methods and others are provided in several reviews, such as that by Witze[25] and references therein. For a review of common optical methods, such as line-of-sight light extinction and light scattering techniques, refer to Zhao and Ladommatos[30] and references therein.

This overview of available instruments is not comprehensive. However, none are able to differentiate between volatile and nonvolatile species in real-time while measuring concentration and morphology. Further, many of these instruments only provide "order of magnitude" accuracy. In summary, no existing instrument can characterize the structure and chemistry of soot particles quickly in the environment and as emitted from an engine.[31]

Laser-induced incandescence (LII) is a technique that has emerged for quantitative measurements of nonvolatile particulate concentration and morphology, addressing some of the key characteristics described above, and is discussed in detail in the remainder of this section.

1.3. CONVENTIONAL LASER-INDUCED INCANDESCENCE (LII) METHOD

Laser-induced incandescence is an optical diagnostic technique which uses a pulsed laser to heat soot nanoparticles to temperatures significantly above the ambient temperature, and uses one or more photodetectors to measure the characteristics of the

incandescent emission radiating from the heated soot. The incandescence measurements are analyzed to determine information about the concentration and/or characteristics related to the size of the soot particles. LII can be applied as a point, line, area or even volume measurement, but unless otherwise stated, references to LII are for point measurements.

1.3.1. Background

Eckbreth first identified LII as an interference in CARS measurements made in sooting flames.[32] Since this time, laser-induced incandescence has emerged as a useful diagnostic for acquiring spatially and temporally resolved quantitative measurements of soot particle volume fraction over a very wide range of soot concentrations.[33] It is a powerful species selective diagnostic, as it responds only to the presence of refractory materials with a high optical absorption cross-section, such as soot.[34]

LII experiments as recently as the late 1990's and early 2000's employed relatively simple systems, along with basic and often incorrect physical models of the heat and mass transfer processes. Advances in LII are being developed by a international community of laser diagnostics researchers[35] to maximize the potential of the technique to make quantitative measurements of the soot concentration and primary particle diameter, and extend it to include the morphology of the particles (primary particle size distribution and aggregate size distribution).[34]

Since the identification of the phenomenon[2, 32] laser-induced incandescence (LII) has undergone significant research and development. Comparisons of the method have been made with the gravimetric sampling technique,[36] and there have been some successful measurements of the soot primary particle diameter.[37, 38] LII has been applied to a range of soot sources and different applications. This method for measuring soot volume fraction and primary particle size produced by combustion systems has the advantages of offering a very wide dynamic range (no adjustments to the instrument) and measurement range (adjustments to the instrument to increase the range) with a sensitivity estimated to be better than one part per trillion (~2 $\mu g/m^3$).[39] The measurements are made with high spatial and temporal resolution allowing in situ measurements of the time-resolved soot emissions.

Although the theory and analysis associated with the method, which involves nanosecond time response to nanoscale particles, is complex, the application of the method is relatively straightforward. With this technique, a pulsed laser with light pulse duration below 20 nanoseconds is used to rapidly heat the soot particles within the measurement volume from the local ambient temperature to close to the soot sublimation temperature (> 4000 K). Incandescence from the soot particles is sensed by a photodetector and the signal is recorded for subsequent analysis. Complex analysis of the nanoscale heat and mass transfer space and time are required in describing the laser light energy absorption by the soot particles and the subsequent soot incandescence as the soot cools.

LII has a well-defined but complex response to volatile particulate matter. It is insensitive to liquid particles, because they absorb a negligible amount of laser energy compared to carbon. For carbon particles coated with volatile material, the latter are believed to vaporize early in the laser heating period. In general, it is reasonable to state that LII measures the volume fraction of carbonaceous material in the exhaust. Although metallic ash may also be present at low concentrations, it has a low absorptivity and emissivity relative to carbon and is unlikely to survive the high temperatures, resulting in a negligible contribution to the incandescence.

The LII technique is capable of real-time measurements during transient vehicle operation, making it a valuable tool for optimizing gasoline and diesel engine soot emissions performance. The measurement frequency is limited by the repetition rate of high-power pulsed lasers (typically 10-30 Hz, which corresponds to one measurement per engine cycle at 1200-3600 rpm). Therefore, while it is not possible to obtain crank-angle resolution in real-time, ensemble-averaging for many engine cycles can be used to reconstruct cycle-resolved transient behaviour. However, the real-time measurement frequency is more than adequate to observe engine and vehicle transients, such as those that occur in driving cycles.

LII measurements generally provide a relative measure of the soot volume fraction and thus, a means for calibration is required to relate the signal to the soot concentration. Conventionally, a comparison of the LII results to a system with a soot volume fraction measured by traditional methods is used to calibrate the instrument. Thus,

"conventional LII" is the term applied to LII systems that rely on correlation to a soot source of known concentration for their calibration, such that all subsequent measurements are relative to the soot source used for calibration. One method frequently reported is scaling of the LII signals to match the soot volume fraction (SVF) profile in a laminar diffusion flame as determined by line-of-sight extinction measurements, as shown in Figure 1-3.[40] Others have used techniques such as comparison to cavity ringdown measurements to calibrate conventional LII.[41] Conventional LII instruments rely on high-fluence LII and may require recalibration by correlation to another nanoparticle measurement technique for each different application. LII instruments operating at high fluence also cause substantial sublimation of the soot, the very species they are attempting to measure.

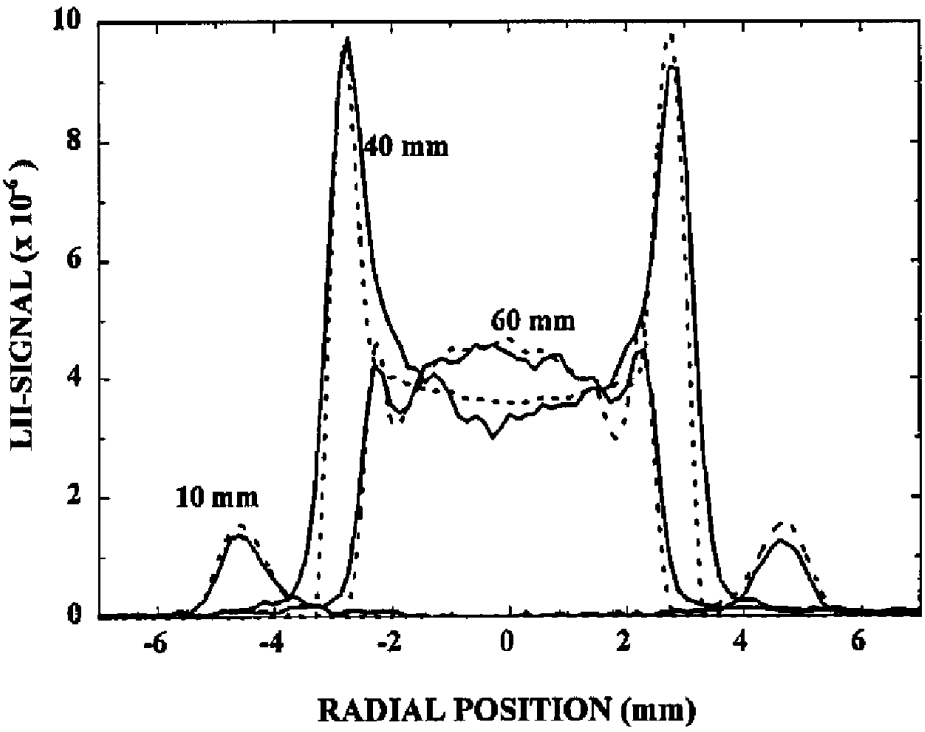

Figure 1-3. Calibration by comparison of the LII signal to the SVF profiles obtained by laser extinction (Ni et al.[42]). [—— LII data; - - - - laser extinction/scattering data]

In addition to measuring soot concentration, the LII signal can also be interpreted to determine the active surface area of the particle, which in turn can be used to resolve the

primary particle diameter. LII has also been used in a semi-quantitative sense to visualize two-dimensional soot distributions for applications in flames, in-cylinder engine measurements, microgravity experiments, etc. An extension of the two-dimensional measurements has been demonstrated, as shown in Figure 1-4, by recording multiple parallel equidistant planes simultaneously, and performing tomographic analysis to reconstruct a three-dimensional image of soot distribution.

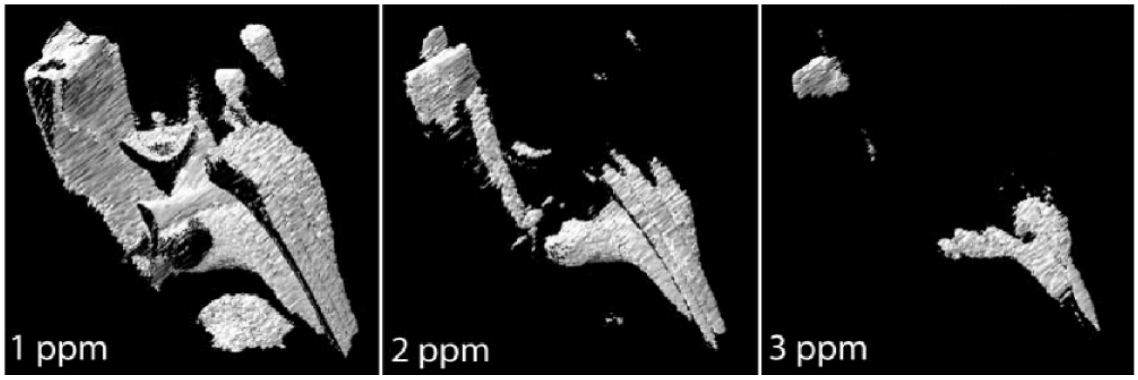

Figure 1-4. 3-D iso-concentration surfaces acquired in a turbulent non-premixed flame representing soot volume fractions of 1, 2, and 3 ppm, respectively.[43]

In the following sections, the model describing nanoscale (time and space) heat transfer to and from the soot particles will be presented, the approach used for measuring soot volume fraction and primary particle size will be discussed, and representative experimental results showing the recently developed capabilities will be presented and discussed. For further examination of prior LII theory, experimental approaches and practical applications, Kohse-Höinghaus and Jeffries[5] offers an extensive review.

1.3.2. Theory

1.3.2.1. Heat transfer model

The first effort to model the nanoscale heat and mass transfer processes of soot in LII was made by Eckbreth.[32] Subsequent improvement and application of this model have been presented by Melton,[44] Dasch,[45] Tait and Greenhalgh,[46] Hofeldt,[47] Mewes and Seitzman,[48] McManus et al.,[49] and more recently by Snelling et al.,[50] Will et al.,[51]

Snelling et al.,[52] and Schraml et al.[53] An adequate treatment of the sublimation term is the key to the success of a conventional LII model to predict the time-resolved soot particle size, soot temperature, and the excitation curve. Soot sublimation reduces the soot particle size and provides an effective cooling mechanism that limits the further rise of soot particle temperature. Unfortunately, the basic heat and mass transfer physical models applied in the late 1990's were often incorrect in their formulation. This was first recognized by Smallwood et al.[54] in attempting to rationalize the various soot sublimation models reported in the literature.

Soot absorbs and emits light predominantly on the scale of the primary particles. The laser light heating process in LII is independent of particle size, and the emitted incandescent light is nominally volumetric, when the following assumptions apply:

(a) soot primary particles are small compared to the laser wavelength (Rayleigh regime);

(b) laser heating increases the temperature of all particles at the same rate, regardless of size;

(c) when the particles reach the sublimation temperature, additional absorbed energy goes into sublimation rather than sensible energy, so that the particles remain at the same temperature for the duration of the laser heating period; and

(d) sublimation causes negligible particle-size reduction, so that the incandescent radiation from the particles is independent of laser fluence above the sublimation threshold.

The analysis outlined here follows the work of Snelling *et al.*[50, 52] who improved upon the analyses of Hofeldt.[47] and is formulated based on the heat transfer to and from isolated primary particles. This represented the state of modelling of the nanoscale energy transfer processes involved in LII when this work was initiated. Substantial development in the numerical models has occurred recently,[34, 55] and relevant elements are discussed in Section 3.1.

The heat transfer processes occurring in LII are represented as an energy balance equation for a single primary particle, which is written as[52]

$$\dot{q}_i = \dot{q}_a + \dot{q}_s - \dot{q}_c - \dot{q}_r \tag{1}$$

where the terms represent the rates of soot particle internal energy change, $\dot{q}_i$, of laser energy absorption by the particle, $\dot{q}_a$, of heat loss due to soot sublimation, $\dot{q}_s$, of conduction heat loss from the particle to the surrounding gas, $\dot{q}_c$, and of heat loss due to thermal radiation, $\dot{q}_r$, respectively. The formulation of these terms based on Snelling *et al*.[50, 52] is presented below. The validity of this model is supported in a recent review of the nanoparticle energy balance equation theory.[56]

1.3.2.1.1. Internal Energy

The soot particle internal energy change is represented by

$$\dot{q}_i = \frac{1}{6}\pi {d_p}^3 \rho_s c_s \frac{\mathrm{d}T}{\mathrm{d}t} \tag{2}$$

where ρ_s is the density of soot, and is taken to be 1.9 g/cm^3, an average of reliable literature data.[57-59]

1.3.2.1.2. Absorption

The laser energy absorption by the soot particle is represented as

$$\dot{q}_a = C_a F_0 q(t) \tag{3}$$

where C_a is the absorption cross-section of a primary soot particle, F_0 is the laser fluence, and $q(t)$ represents the pulsed laser temporal power density per unit laser fluence. In this analysis, the soot aggregates are taken as an agglomerate of just touching primary spheres of nearly monodisperse diameter d_p that are well within the Rayleigh limit.[9] For a soot primary particle of diameter d_p, whose size parameter $x_p = \pi d_p/\lambda$ is sufficiently small for the particle to be considered in the Rayleigh regime (*i.e.*, $x_p < 0.3$) in the visible spectral range, its emissivity, ε_p, at wavelength λ is written as

$$\varepsilon_p = \frac{4\pi d_p E(m)}{\lambda} \tag{4}$$

where $E(m)$ is the absorption function of the refractive index, m, defined as

$$E(m) = \mathrm{Im}\left(\frac{m^2 - 1}{m^2 + 2}\right) \tag{5}$$

For a wavelength of 1064 nm and a refractive index obtained from the dispersion relationship from Dalzell and Sarofim,[60] m =1.63 + 0.7i and $E(m)$ = 0.30, while at 532 nm, m =1.59 + 0.58i and $E(m)$ = 0.26.

The absorption coefficient C_a for these soot particles is expressed as[61]

$$C_a = \frac{\pi^2 d_p^3 E(m)}{\lambda} \tag{6}$$

where C_a is proportional to the wavelength dependent soot absorption function, $E(m)$, and inversely proportional to the laser wavelength, λ.

1.3.2.1.3. Sublimation

The heat loss due to soot sublimation is represented by

$$\dot{q}_s = \frac{\Delta H_v}{M_v}\frac{\mathrm{d}M}{\mathrm{d}t} \tag{7}$$

where ΔH_v is the heat of sublimation (the energy required to sublimate a unit mole of solid carbon into multiple gaseous carbon species), M_v is the average molecular weight of the sublimated gaseous carbon species, M is the mass of the soot primary particle, and t is time. The rate of the soot particle mass reduction dM/dt is related to the mass balance of the soot particle written as

$$\frac{\mathrm{d}M}{\mathrm{d}t} = \frac{1}{2}\rho_s \pi d_p{}^2 \frac{\mathrm{d}d_p}{\mathrm{d}t} = -\pi d_p{}^2 N_v \frac{M_v}{N_A} \tag{8}$$

where N_v is the molecular flux associated with soot sublimation and N_A is Avogadro's number.

1.3.2.1.4. Conduction

The conduction heat loss from the particle to the surrounding gas is represented by

$$\dot{q}_c = \frac{2k_g(T - T_g)\pi d_p^3}{(d_p + G\lambda_g)} \tag{9}$$

where k_g is the thermal conduction coefficient of the ambient gas, T_g is the ambient gas temperature, T is the instantaneous particle temperature, λ_g is the mean free path in the ambient gas, and G is a geometry dependent heat transfer coefficient specified as

$$G = \frac{8f}{\alpha(\gamma + 1)} \tag{10}$$

where f is the Eucken factor equal to 5/2 for monatomic species, α is the accommodation coefficient, and $\gamma = c_p/c_V$ is the ratio of specific heat coefficients. c_p is heat capacity at constant pressure of the surrounding gas, and c_V is the heat capacity at constant volume of the surrounding gas. Snelling *et al.*[50] reported the work of Leroy et al.[62] in which measurements were made indicating that the accommodation coefficient of nitrogen on solid graphite in the temperature range of 300 to 1,000 K gave a value of 0.26, and this value is frequently used for α.

1.3.2.1.5. Radiation

The heat loss due to thermal radiation from the soot particle is represented as

$$\dot{q}_r = 4\pi^2 \, \sigma_{SB} \, T^4 \left(\frac{E(m)}{\lambda} \right) \tag{11}$$

where σ_{SB} is the Stefan-Boltzman constant and the parenthetical expression is evaluated at the wavelength of interest. Compared to the other terms, the magnitude of the heat loss due to radiation is insignificant.

1.3.2.1.6. Model Results

The relative importance of the heat transfer terms on the time-resolved temperature of the soot particle for a simulation of a high fluence LII experiment is shown in Figure 1-5. It can be observed that the absorption and sublimation are dominant on the time

scale of the laser pulse, and that conduction to the surrounding gas dominates once sublimation ends. Radiation is almost two orders of magnitude lower than conduction, and is insignificant in terms of heat transfer, but is important as it produces the LII signal that is measured.

Identification of errors propagated through the literature has led to an improved understanding with this numerical model of nanoscale (temporal and spatial) heat transfer to and from the particles, in order to support understanding of the physical processes occurring during the LII event.[54] This model performs well in predicting the time-resolved behaviour of the LII signals from soot measured in a flame for a range of laser fluence.

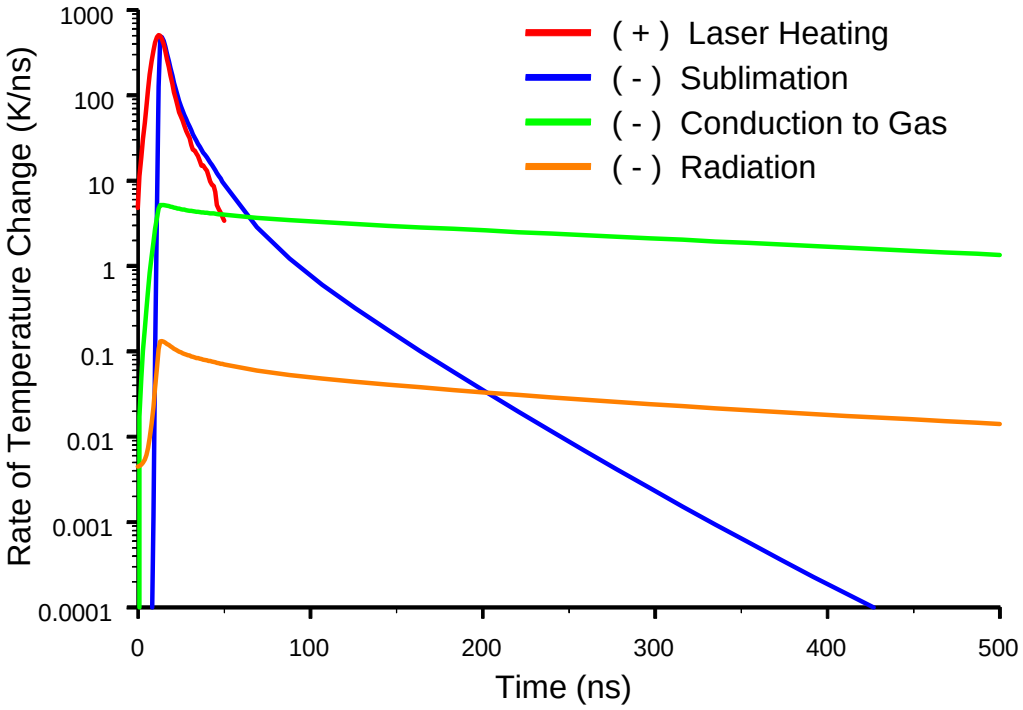

Figure 1-5. Model results illustrating the time dependent effect of the various heat transfer terms on the rate of temperature change of the particle.

1.3.2.2. Excitation curve

The relationship between the LII signal and the excitation fluence is referred to as the excitation curve. The spatial distribution of laser light fluence can have a significant

effect upon the measured LII signal level, as shown in the excitation curves presented in Figure 1-6. Regardless of the spatial fluence profile, as the energy of the laser light is increased there is an initial sharp increase in LII signal. A peak laser fluence can be reached such that a further increase in energy produces very little increase in LII signal.

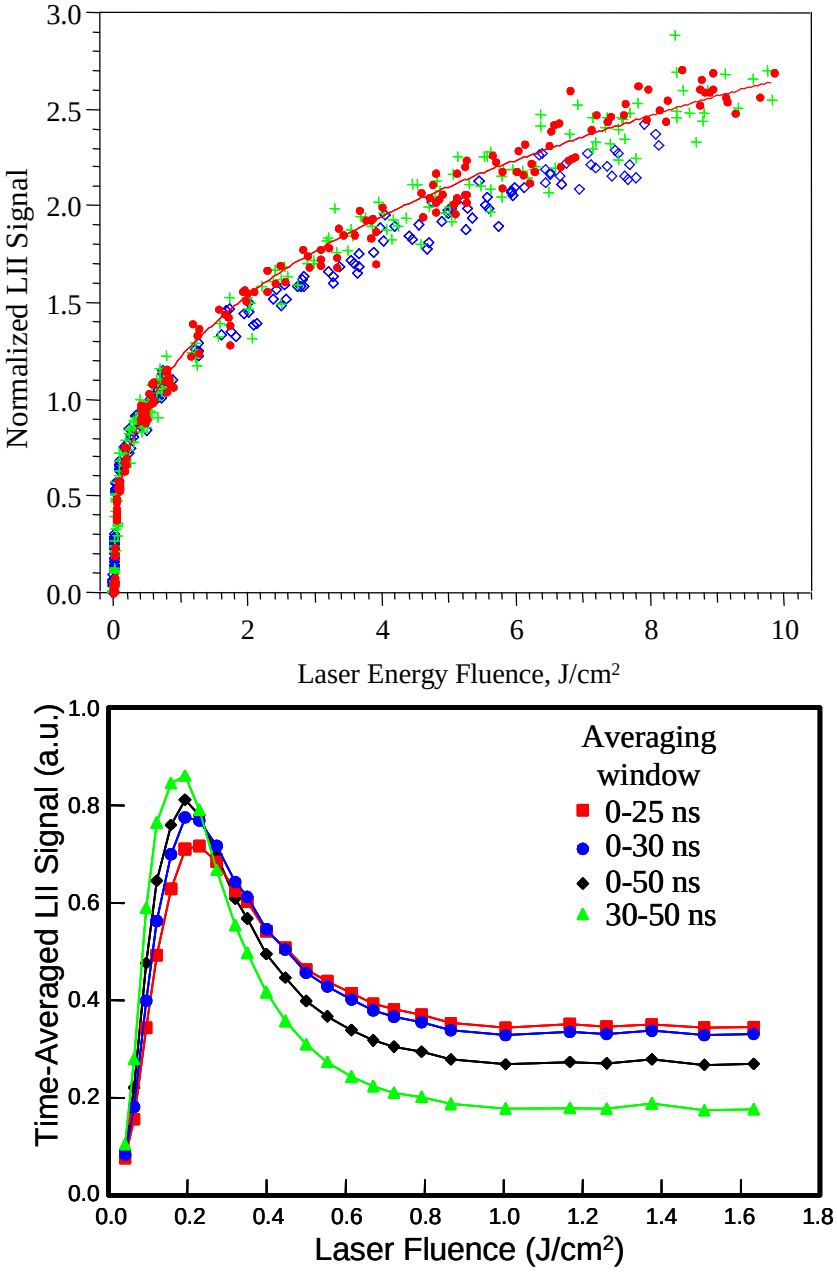

Figure 1-6. Fluence dependence of LII signal as a function of laser beam spatial profile: above, Gaussian profile (Shaddix and Smyth[63]) and below, top-hat profile (Witze et al.[64]).

Conventional LII is typically operated in this plateau region, where the LII signal is somewhat independent of the laser fluence.[42, 45, 46, 50, 63, 65] The behaviour at fluence beyond the plateau region is dramatically different for the homogeneous (top-hat) profile in comparison to the Gaussian profile. This is due to sublimation of the carbon causing a mass (and volume) loss. For the top-hat profile, this results in a decrease in the LII signal. For the Gaussian profile, the decrease in the LII signal due to mass loss at the centre of the laser light beam where the peak fluence is located is offset by the increasing contribution from the wings of the spatial profile, resulting in a slight increase in the overall LII signal.

The variation in the spatial profile for a Gaussian light beam means that the particles in the probe volume will be heated to different temperatures, making theoretical interpretation of the LII signals much more difficult.

1.3.2.3. Soot volume fraction (SVF)

To determine the soot volume fraction, the LII signal must be scaled to data obtained in a source of known volume concentration. Frequently, the source has been a laminar flame which has been characterized by line-of sight extinction.

To obtain radially-resolved spatial information, the three-point Abel algorithm of Dasch[66] can be applied to invert the line-of-sight transmission measurements. Details of an enhanced two-dimensional technique are given by Snelling et al.[67] For visible wavelengths, errors of 30% and greater in soot concentration are expected depending on the size and morphology of the soot aggregates. There are significant uncertainties in the refractive index of soot and its wavelength dependence which can mask such effects.[50]

LII measurements can be performed at the same locations in the laminar flame and then scaled by a single factor to the Abel-inverted data as shown in Figure 1-3, so that the integrated soot volume fraction over the total flame width is as close as possible for the extinction and LII data at all heights. In general it has been observed that there is linear agreement between the soot profiles from LII and Abel inverted transmission measurements over the range from 0.5 – 5 ppm.[40, 42, 50, 65] Vander Wal, using gravimetric sampling for calibration, has observed good linearity in the 0.035-1.5 ppm

soot concentration range.[68]

1.3.2.4. Primary particle diameter

After particle sublimation ends, the dominant cooling mechanism for the particles is conduction to the surrounding gas. Assuming monodisperse primary particles, the temperature difference between the particles, T, and the ambient gas, T_g, would decay steadily with a single exponential behaviour during this period. An equation of the form

$$T - T_g = A \cdot e^{-t/\tau} \tag{12}$$

is fit to the temperature data to determine τ, the time constant of the exponential decay, and where A is a constant.[69] This method requires *a priori* knowledge of the ambient gas temperature, which may be determined by thermocouple or other means. The primary particle diameter can be determined directly from the decay of the LII signal, as shown in Figure 1-7.

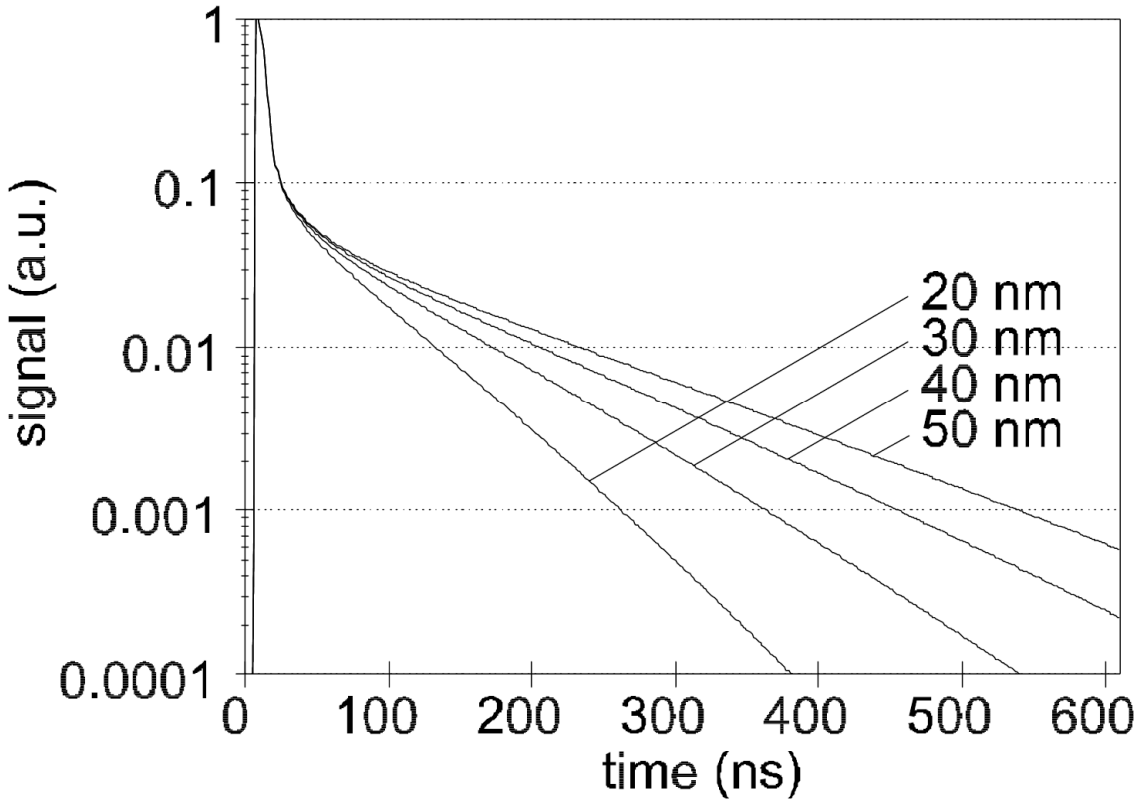

Figure 1-7. Numerically modelled LII signal decay of soot at STP ambient conditions for a range of primary particle diameters, normalized to the maximum (Schraml et al.[39]).

The particle diameter d_p is then determined from the relation derived from McCoy and Cha[70]

$$d_p = \frac{12 k_g \alpha \tau}{G \lambda_g c_s \rho_s} \tag{13}$$

where α is the thermal accommodation coefficient.

1.3.3. Measurement of soot with conventional LII

Experimental methods for the measurement of soot concentration and primary particle diameter with conventional LII have been recently reviewed by Schulz et al.[34] As such, typical methods are only briefly mentioned here, with more detail to be found in Schulz et al.[34] and its references. Considerations for conventional LII include excitation and detection wavelengths, the laser spatial and temporal profiles, and detection strategies. Conventional LII is performed with high fluence so that the peak signal is nominally saturated, with the intention that the signal is therefore not sensitive to small variations in the laser fluence.

Lasers are typically pulsed Nd:YAG lasers operating at 532 nm (second harmonic) or 1064 nm (fundamental), with pulse durations of 5-15 ns. UV wavelengths have been used, but are known to promote photodissociation as well as particle heating.[71] Use of 1064 nm is less likely to stimulate emission from the C_2 Swan bands at high fluence[72] and due to the smaller scattering cross-section at longer wavelengths, will mitigate possible interferences from elastically scattered light. Due to the broad spectral range of particle incandescence, almost any detection wavelength in the visible to near-infrared range is suitable. For flame measurements, lower wavelengths have been preferred, to discriminate against flame luminosity. As discussed above, spatial profiles have ranged from full Gaussian to near top-hat. Although the temporal profile is known to affect the signals generated with LII,[73, 74] very little attention has been focused on this issue, as it is difficult to vary the laser temporal profile in a controlled manner.

Gated detection and time-resolved detection are the two strategies that have dominated. With gated detection, the signal is measured for a very short period (tens of nanoseconds) typically shortly after the end of the laser pulse,[42] but as this does not

follow the decay of the signal, it is typically used for concentration measurements only. Time-resolved LII uses a fast response photodetector and a transient recorder to follow the time history of the LII signal over a longer period of time (microseconds) until the incandescence is no longer detectable.[75] This permits the measurement of primary particle diameter in addition to the concentration of soot particles.

1.4. VARIANTS OF LII

Many unique adaptations of LII have been developed, a few of which are mentioned here. LII has been used for qualitative planar imaging to determine soot temporal and spatial distributions, and this has found application for in-cylinder imaging.[76] Laser induced incandescence (LII) has the potential to yield two-dimensional spatially- and temporally-resolved distributions of soot volume fraction.[77, 78] To extend incandescence lifetimes and avoid conduction cooling, LII experiments have been performed under high vacuum conditions by Beyer et al.[79] and in low pressure flames.[80] In attempts to improve the sensitivity of the technique, intra-cavity LII has been performed with a *cw* laser.[81, 82]

LII has also been applied to refractory and metallic particles other than soot.[83-86] Qualitative LII signals have been achieved from carbon nanotubes,[87] but significant investigation is required to understand the differences in the nanoscale behaviour between conventional soot and engineered nanoparticles such as SWNT, particularly for quantitative measurements. For instance, challenges remain to differentiate the SWNT from other carbon nanoparticles such as amorphous carbon or carbon black that are present and are interfering species during the production of SWNT.[88] Identification of SWNT could be explored by investigating differences in a range of signals and properties, some of which have been identified in a recent review.[89] It is anticipated that the optical absorption properties of SWNT may differ from those of soot particles.[90]

1.5. APPLICATIONS

In addition to the applications described in detail below, namely diesel, gasoline, and gas turbine engines, and carbon black production, LII may find application for measurements of:

(a) ambient atmospheric elemental carbon concentration,

(b) soot in pool fires, furnaces, and boilers,

(c) metal and metal oxide nanoparticles, and

(d) material synthesis.

Early LII research indicated the potential for an entirely new instrument for monitoring time-resolved nanoparticle emissions from combustion sources and was identified as one of the most promising technologies to emerge in the late 1990's.[69] The range of volume concentration measurements that have been demonstrated in a variety of applications exceeds 6 orders of magnitude, Figure 1-8.

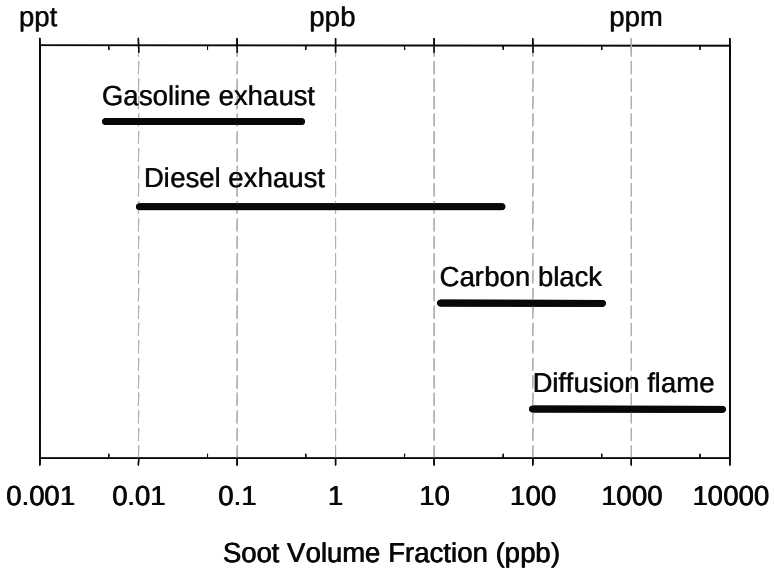

Figure 1-8. Numerous studies of soot detection illustrate the typical span of concentrations measured for a wide range of applications.

1.5.1. Diesel engines

Conventional LII has been applied by many to determine the mass concentration of particulates produced by diesel engines.[39, 75, 91, 92] Figure 1-9 illustrates the agreement between conventional LII and the AVL filter smoke number (FSN) over a wide range of particulate concentrations.[39] This good agreement is expected, as LII measures the soot concentration, and the FSN is related to the black smoke level, comparable quantities.

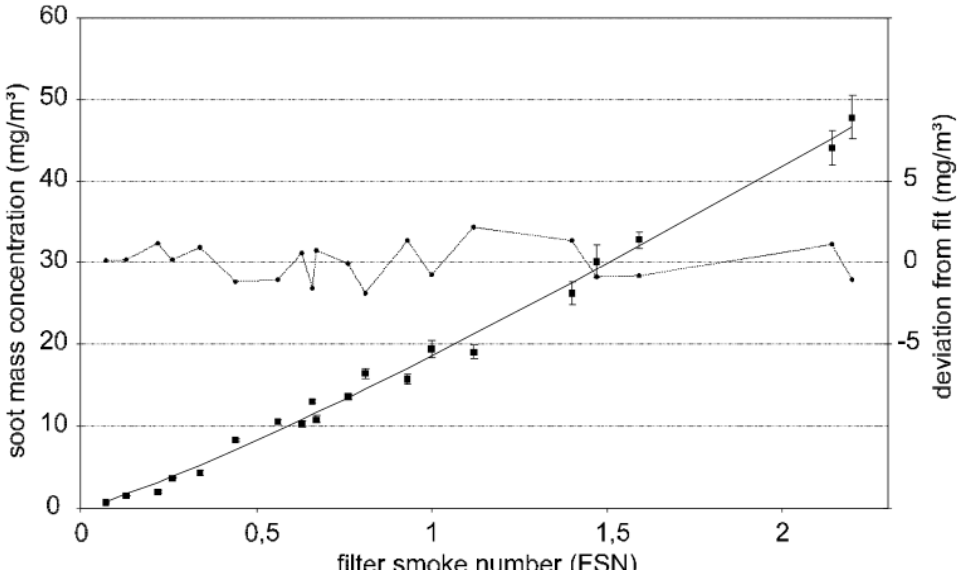

Figure 1-9. Soot mass concentration from LII measurements as a function of filter smoke number in the exhaust of a medium-duty diesel engine (Schraml *et al.*[39]).

Comparison of the particulate concentration data obtained from LII was in good agreement with gravimetric data simultaneously acquired, Figure 1-10.[93] The AVL steady-state simulation of the EPA transient test procedure was used in this example. Under this protocol, engine emissions were measured at steady speed/load conditions. The engine was varied from a low idle speed (600 RPM / 0 percent load) to the engine's rated speed and load (1800 RPM / 100 percent load).

A weighting scheme was designed to produce composite brake specific emissions to accurately predict the gaseous omissions obtained using the EPA transient test procedure. Since steady-state simulation does not accurately simulate transient engine behaviour, these composite PM emissions can only be expected to show the current trends due to engine transients. Some of the discrepancies between the gravimetric and LII results may be attributed to the fact that gravimetric sampling includes an organic fraction that does not contribute to the signal measured by LII and that the density of the particulates is required to convert the mass determined by the gravimetric filter methods to volume fraction for comparison with LII.

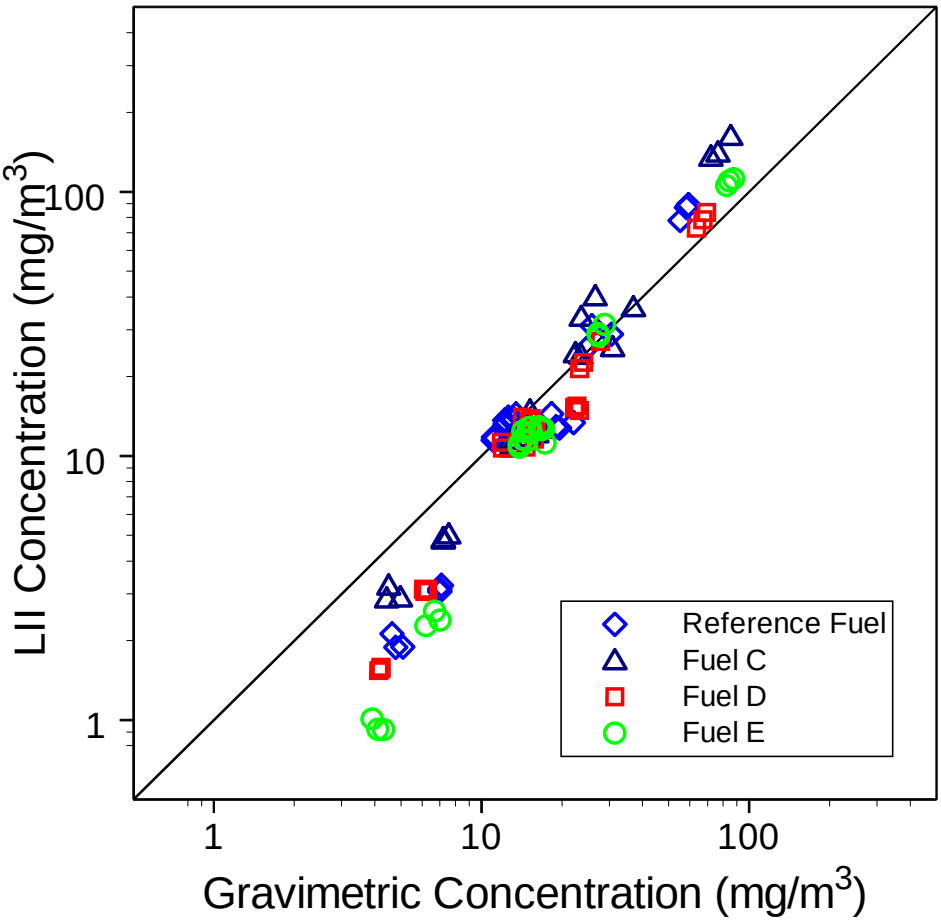

Figure 1-10. Soot particle concentration determined by the LII and gravimetric methods concurrently, for four different fuels (Smallwood *et al.*[93]).

1.5.2. Gasoline engines

Data were reported that demonstrate the LII technique's capability for measuring transient emissions, applied to the exhaust from a state-of-the-art production direct injection spark ignition engine.[94] The unmodified engine used a lean burn stratified charge combustion concept for some of its operating modes. Measurements were acquired over a series of transient driving cycles. Concurrent ELPI measurements were acquired for direct comparison. Dilution was unnecessary for the LII method since it responds to only the soot component of the particulates. Any condensed material including the organic fraction of the particulates and water do not contribute to the measured LII signal. The high-energy laser is anticipated to evaporate these volatile materials well before the significant portion of the LII signal is detected.

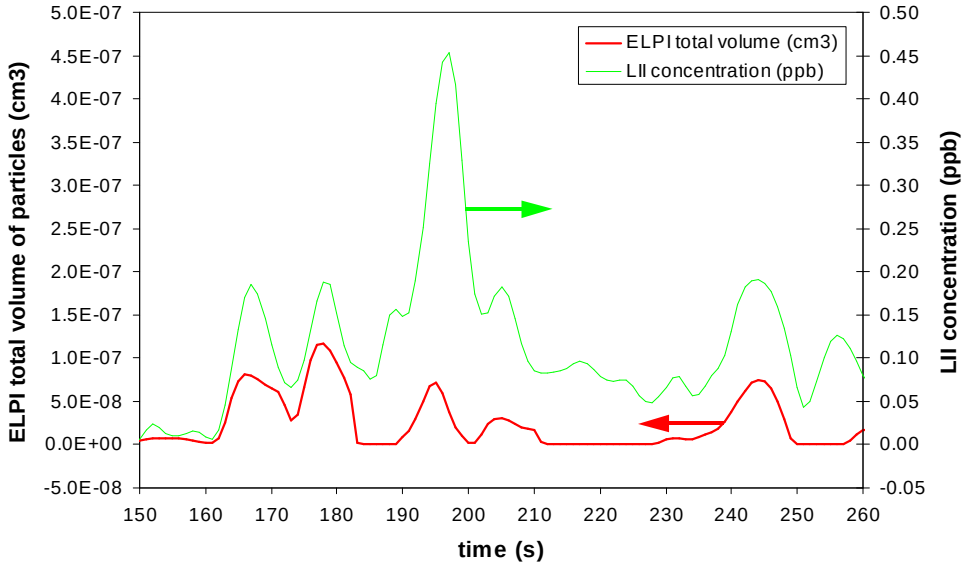

Figure 1-11. Relative temporal response and sensitivity of LII and ELPI (Smallwood et al.[94]).

Measurements using the ELPI instrument were made post dilution so the sampled stream experienced some cooling and consequently, the measured particulates are composed of soot and condensable organic species and trace elements. The ELPI instrument produces measurements at one-second intervals but appears to have a lower temporal response than the LII instrument, as shown in Figure 1-11. In this experiment LII was demonstrated to have sensitivity to concentrations as low as 5 ppt.[94]

1.5.3. Gas turbine engines

There has been heightened interest in the application of LII to measure soot concentrations in the exhaust of aviation gas turbines. These have been reported by Schäfer et al.,[95] Allen et al.[96] and Jenkins et al.[97] All have indicated that a measurement across a plume that is of the order of 1 m in diameter in a decidedly hostile environment is difficult. However, successful demonstrations of spatially resolved, real-time, in-situ LII measurements in a test cell environment have been reported.[97]

The spatial and temporal resolution of LII measurements in the plume of a gas turbine are shown in Figure 1-12, which illustrates the significant changes in the soot mass concentration that occur with rapid changes in engine power settings. Detailed

measurements of the particulate concentrations in the plume will assist designers in reducing particulate emissions, improving efficiency, and of significance to the military, minimizing the infrared radiation signature.

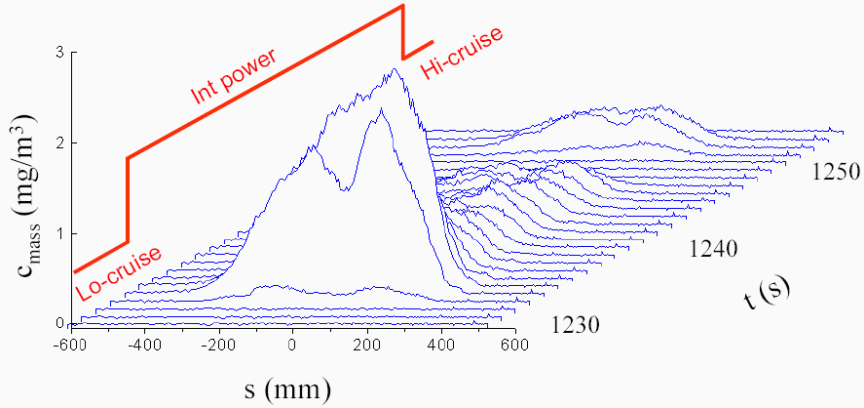

Figure 1-12. Transverse profiles of soot mass concentration in the exhaust plume of a gas turbine engine illustrating the effect of both low-to-intermediate and intermediate-to-low engine power changes (Jenkins et al.[97]).

1.6. FUTURE DEVELOPMENTS

A suite of high energy laser diagnostics (HELD) listed in Table 1-1 promises to offer detailed information about combustion generated particulate matter[98]. Currently the techniques other than LII are in their infancy in relation to making quantitative measurements of the properties of particulate emissions. Summaries of a number of these are presented below.

By performing LII and complementary elastic light scattering measurements[64] interpreted with Rayleigh-Debye-Gans polydisperse fractal aggregate theory,[99] characteristics of the aggregate size may be determined, including size distributions and other morphology-related properties of interest, assuming that the particles follow a log-normal distribution.[26]

Table 1-1. HELD techniques for PM measurements.

Diagnostic	Property measured
laser-induced incandescence (LII)	soot volume fraction and primary particle size
elastic light scattering (ELS)	total volume fraction
LII + ELS	aggregate size, number, and structure
laser-induced desorption (LID) + ELS (LIDELS)	volatile volume fraction
laser-induced breakdown spectroscopy (LIBS)	metallic ash (species and concentration)
laser-induced fluorescence (LIF)	composition

The volatile fraction of PM can be measured in situ, in real-time with laser-induced desorption/elastic light scattering, a new optical diagnostic.[100] This technique uses two light pulses. The first pulse heats the particulates, stimulates laser-induced desorption of the volatile fraction without initiating sublimation of the soot, and scatters light from the particulates. This elastic light scattering is proportional to the total PM volume. The second laser light pulse, of comparable energy to the first, scatters light from the soot that remains, providing an elastically scattered signal that is proportional to the volume of the remaining solid portion of the PM. The ratio of the second to the first measurements is then the quantitative solid volume fraction. Independent calibration would be required to obtain quantitative data for the volatile, solid, and total PM concentrations.

Laser-induced breakdown spectroscopy is a technique developed over the last two decades that has been applied to detect trace metal concentration in particulate matter.[101, 102] A focused high fluence laser beam produces a spark at the probe volume, creates a plasma, dissociates molecules to elemental atoms, and excites the atoms. Atomic emission is produced as the atoms relax from the excited states, and spectra can be collected. The intensity of the atomic emission lines can be related to the

concentration of the atomic species.

The combination of these techniques can provide *in-situ* real-time transient information about most aspects of particulate matter. Currently there is no complementary technique to provide information about the composition of the volatile organic fraction, which may be significant in terms of adverse health effects. However, encouraging developments may lead to success with the diagnostics discussed below.

Excimer laser fragmentation fluorescence spectroscopy can measure a number of chemical species at elevated temperatures with good sensitivity, selectivity, and time response, by focusing a UV pulsed laser beam to produce atoms or small fragments from larger compounds or particles that are normally non-fluorescing. It is showing promise in quantifying the relative concentrations of elemental carbon and volatile organic carbon.[71] It requires higher laser fluence than typically used with conventional LII (and much higher than with low fluence LII), yet less than the fluence applied to generate a plasma in laser-induced breakdown spectroscopy.

Small-angle X-ray scattering has been applied to study the formation of soot spherules during fuel pyrolysis. These results have measured the mean diameters and dispersion of primary particles for a polydisperse distribution in the range from 1.6 to 35.0 nm.[103] A complementary technique is small-angle neutron scattering, which uses contrast variation to preferentially highlight or mask specific molecules, allowing identification of specific species.[104]

1.7. SYNOPSIS

Despite the ubiquitous nature of nanoparticles, instrumentation for their real-time detection and characterization is inadequate and their physical and chemical properties remain poorly understood. The complexity of nanoparticles found in the atmosphere, due to the vast range of compositions, sizes, and geometries, is a severe challenge in terms of both nanometrology and evaluating the health and environmental impacts.

Particulate characterization is extending beyond mere mass, equivalent sphere diameter, and qualitative measurements available in the past. With the emergence of these new optical diagnostic techniques, detailed *in-situ* transient real-time characterization of

particulates is becoming possible. This detailed characterization includes measurements of soot volume and mass concentration, soot temperature, total particulate concentration, solid-to-volatile fraction, active surface area, primary particle diameter and distribution, and aggregate size and distribution. Furthermore, developments to provide particulate composition appear promising. Some of the techniques have the potential to provide accurate and precise on-line and real-time characterization that meets internationally recognized measurement standards.

These new capabilities are leading to: enhanced knowledge of particulate formation, growth, and oxidation; strategies for reducing particulate emissions at the source; evaluation of particulate filters and traps; improved understanding of the role of particulates in air quality and health; and new opportunities for process control in nanoparticle production. With the additional information provided by these laser-based techniques, regulators are now considering a broader range of measures than simply limiting the mass of particulates. Recently Europe has introduced legislation aimed at regulating the number of nonvolatile solid particulate matter emissions from vehicles.[20] LII is particularly well suited to the measurement of nonvolatile solid particles which are predominantly soot.

This new era of laser-based diagnostics has highlighted the longstanding need for better characterization of the optical and heat transfer properties of nanoscale particles such as soot and particulate matter, and it is anticipated that novel methods, also based on optical diagnostics, will arise to meet this challenge. Due to the complexity of the LII process, there are still open questions which limit the applicability and accuracy of this technique. To address these issues, a workshop series (International Discussion Meeting and Workshop on Laser-Induced Incandescence: Quantitative Interpretation, Modelling, Application) was initiated and has convened three times since 2005.[35] Major accomplishments that arose from the workshops were the identification of differences in the models of the LII process used to analyse experiments, the exchange of laboratory experimental techniques, and identification of various LII applications requiring different approaches of experimental setup and data analysis.[34, 55]

1.7.1. Goals of this Work

Progress is needed on the modelling, theory, experimental technique, and signal evaluation for laser-induced incandescence. The primary goal of this work was to improve upon the laser-induced incandescence technique specifically for the quantitative measurement of soot. This included the measurement of soot concentration, active surface area, and primary particle diameter. Particular attention was paid to improving the state of measurements for nonvolatile particulate matter emissions at or near ambient conditions, where the limitations of conventional LII are most apparent.

In order to achieve this goal a new variant of LII, autocompensating laser-induced incandescence (AC-LII), was developed. This required implementing a two-colour LII apparatus for performing two-colour pyrometry at low fluence conditions. This work focuses on development and optimization of the AC-LII experimental technique, the theory to support AC-LII and aspects of signal evaluation. The state-of-the-art model developed by Liu et al.[105] was adopted when required for comparison.

AC-LII overcame many of the limitations of conventional LII, but also presented new issues. Secondary goals included assessing and improving the performance of AC-LII under a range of conditions where soot measurements were required, enhancing the performance of the AC-LII technique, comparing AC-LII to competing instruments for performing particle measurements, and demonstrating the AC-LII technique to make measurements on a range of practical applications.

1.7.2. Outline of this Thesis

This thesis is written in seven sections. Sections 1 and 2 provide a rationale for soot measurements, a review of measurement methods, and an extended discussion of limitations of conventional LII, especially for nonvolatile particulate matter at ambient conditions. The majority of the thesis is in Section 3, which covers advances in laser-induced incandescence resulting from this work, primarily the development of autocompensating laser-induced incandescence. The state of the numerical model, the theory for AC-LII, development of the experimental technique, and signal evaluation to perform two-colour low fluence LII are discussed. Issues that were uncovered with AC-

LII and a significant enhancement to the sensitivity to allow measurement at atmospheric concentrations complete the section. An error analysis of the AC-LII technique is outlined in Section 4. The use of the AC-LII technique to measure particulates in a range of applications, including vehicle emissions, carbon black production, and urban air quality, is described in Section 5. Comparison of AC-LII to other frequently-used particle measurement techniques, and an extension to measure soot aggregate size distributions through the incorporation of elastic light scattering, is covered in Section 6. This work and implications for nanoparticle measurement are summarized in Section 7.

2. ISSUES REGARDING LII

Considerable effort is required to obtain reliable, accurate, and precise quantitative measurements with conventional LII. This effort requires optimization of the experimental technique in a combined approach that includes numerical simulation of the nanoscale nonequilibrium heat and mass transfer processes and rigorous data analysis to interpret the significance of acquired signals. This approach has most typically been applied assuming that the soot particles are monodisperse isolated spherules. However, it is known that soot forms aggregates, and that both the spherule size and aggregate size are distributed in practical applications.[34]

2.1. ISSUES WITH CONVENTIONAL LII

Although conventional LII is thought to be a reliable technique, there are many issues with the measurement that have not been addressed. These are grouped into experimental apparatus, numerical model, and signal evaluation topics, all of which are essential and important in determining the properties of nanoparticles with laser-induced incandescence. The issues are discussed in this section, and methods to address the issues will be discussed in subsequent sections.

Although the LII process is essentially nonintrusive, it is not completely non-perturbing as the laser light heating can be expected to affect the soot morphology and cause some sublimation during the short pulse of laser light. It is anticipated that the particulates undergo optical and physical property changes as a function of time, fluence, and their composition. The particles may become more structured (graphitized), and may become hollow shells as the sublimation occurs from the core outwards.[106]

2.1.1. Experimental Apparatus

Many aspects of the experimental configuration affect the results obtained with conventional LII. A typical apparatus is shown in Figure 2-1. This particular configuration includes a half-wave plate and thin film polarizer for energy control, a beam expander and cylindrical lens for creating a Gaussian sheet profile at the measurement location, and prompt and integrated detection of the LII signal.[50]

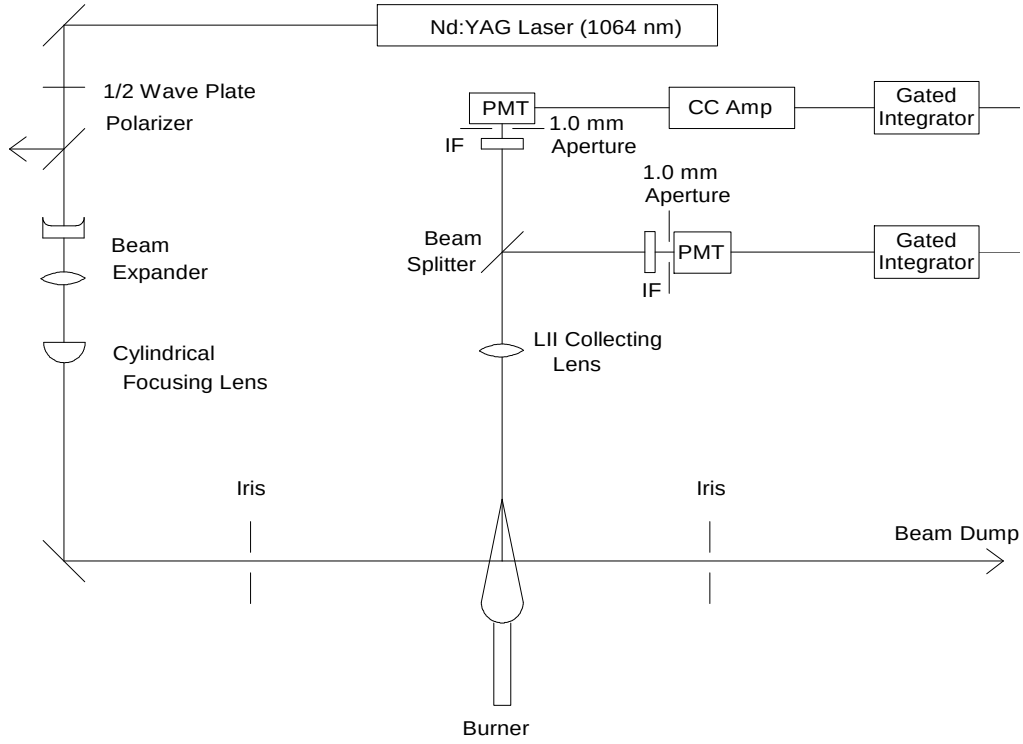

Figure 2-1. Apparatus for conventional LII with gated detection.

High laser fluence in the measurement volume, such that the detected LII emission from the soot reaches saturation, is desired with conventional LII. However, it has been shown that the laser profile (temporal and spatial) has a significant impact on the likelihood of obtaining an unwavering saturation condition.[74] Typical inhomogeneous laser spatial profiles are illustrated in Figure 2-2. A full-Gaussian profile results in signals which continually increase with increasing fluence, since increasing contributions from the wings of the laser beam more than compensate for loss of signal at the centre of the laser beam, due to significant sublimation of soot particles. Conversely, a homogeneous or 'top-hat' spatial profile (not shown) results in signals that rises to a maximum and then decreased with increasing fluence, as significant sublimation occurs for soot particles in all regions of the laser beam, with no offsetting increases from other regions. A Gaussian sheet spatial profile does achieve the elusive saturation condition (i.e., a range of fluences over which the measured signal is invariant with laser fluence), due to a balance between increasing contributions from the wings of the laser beam equalling the losses due to sublimation of the soot particles along the axis of the laser sheet, Figure 2-3. As a result, for most conventional LII

configurations, operating at high fluence is not sufficient to ensure that the LII signal magnitude will be independent of small changes in fluence.

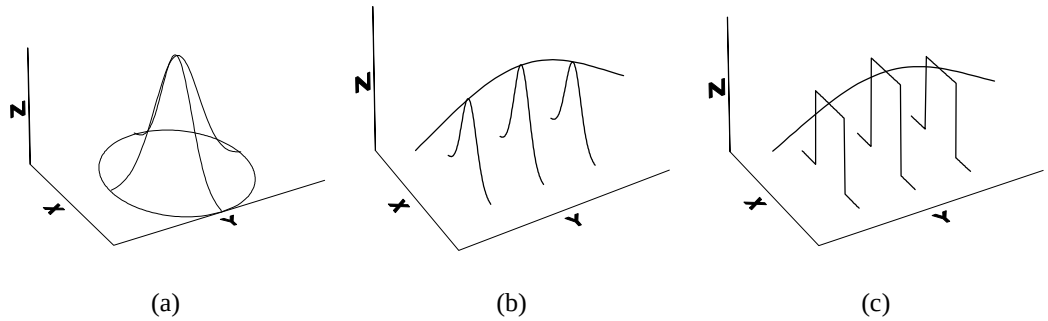

(a) (b) (c)

Figure 2-2. Laser beam spatial profile illustrations: (a) full-Gaussian (circle); (b) elongated Gaussian (sheet); and (c) 1-D Gaussian (near-homogeneous)

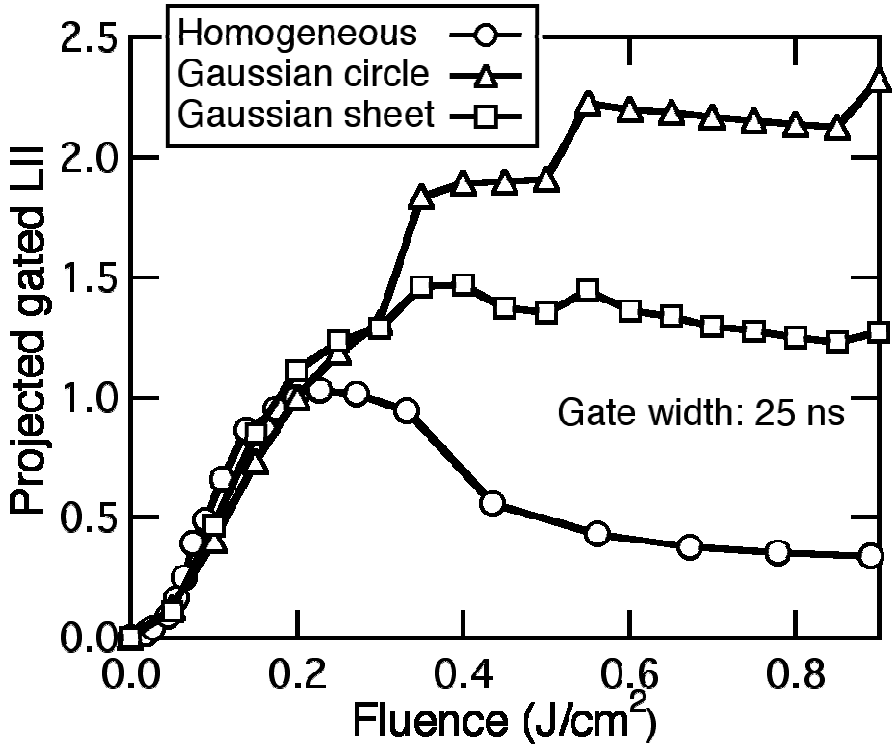

Figure 2-3. Impact of laser beam profile on the predicted LII signal for a range of fluences, with gated detection for a period of 25 ns around the peak of the laser pulse.[107]

As a reminder, conventional LII must be calibrated by applying the apparatus to a source of known concentration and correlating the relative LII signal to the alternate measure of concentration. Changes in the probe volume dimensions or changing from point measurements to quantitative two-dimensional measurements requires recalibration of the LII apparatus since the calibration coefficient only holds for the specific laser/detection configuration used when the initial correlation was performed. Similarly, any change in the detection timing strategy (*i.e.*, from gated to time-resolved, or variation in the duration or start of the gate) would impact the calibration. The selection of the excitation (laser) wavelength and the detection wavelength affect the interpretation of the LII signals, especially at high fluence.[34] This is primarily due to stimulating unwanted C_2, radical, and atomic emission, and laser-induced fluorescence of polycyclic aromatic hydrocarbons (PAH). Use of a longer wavelength laser results in a reduced interference from scattering. As many of these interfering processes are short-lived, on the order of the duration of the laser pulse, they are mitigated by delaying detection until after the end of the laser pulse.

In dense particulate fields, or those with exceptionally long optical path lengths, there are issues with attenuation of the laser light beam and trapping of the LII signal generated in the probe volume. In simple two-dimensional laminar flows these effects may be corrected for. However, in practical environments with turbulent flows, it is unlikely that an accurate correction could be applied.

Under any circumstances, the presence of condensed volatiles or other species other than soot can affect the relationship between the calibration and the measured LII signal. These species may affect the absorption properties of the soot particles, and require energy to evaporate them from the surface of the soot that would otherwise contribute to the heating of the soot particle. Similarly, any change in the ambient gas temperature can also affect the relationship between the calibration and the measured LII signal.

2.1.2. Numerical Model

Although an accurate numerical model is not essential to performing conventional LII measurements of soot concentration, one does aid in interpreting experimental results

and is necessary for determining primary particle diameter from the rate of LII signal decay. Areas of great uncertainty in the numerical models before this work began were numerous. They included the physical formulation of internal energy, laser heating, sublimation, conduction, and radiation models; temperature- and wavelength-dependent properties of soot; temperature- and ambient gas composition-dependent thermal accommodation coefficients; sublimation issues (mass accommodation coefficients for carbon clusters on particle surfaces, internal state distributions of desorbed or sublimed C_2, propensities for C_3 desorption or sublimation), aggregation effects on optical properties; and accuracy of the input conditions of the experimental apparatus.[34]

There is a wide range of uncertainty that occurs with numerical modelling of the LII process, Figure 2-4.[34] This presentation of results was tempered by peak normalization; the disparity in the absolute LII signals was far greater. All the calculations were performed for an identical laminar flame conditions, but each author applied their own model, with different physics and different input parameters for physical properties.

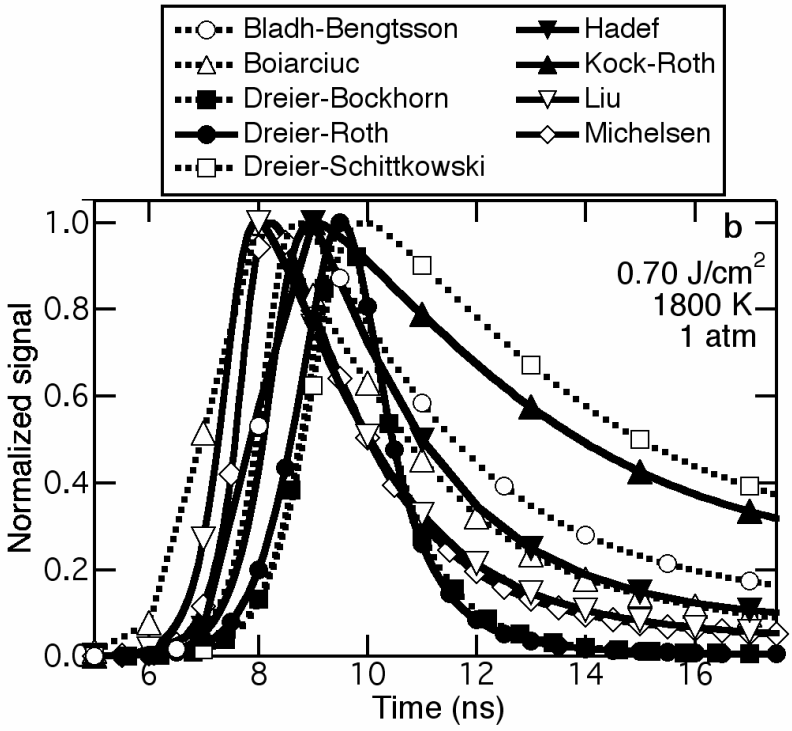

Figure 2-4. Comparison of nine LII numerical models, illustrating the disparity in predicted high fluence LII signals for soot at typical laminar flame conditions. The modelled results have been peak normalized.[34]

The rates of rise of the signal and the time of the maximum signal are significantly different, considering that the temporal profile of the excitation laser pulse was provided. The greatest discrepancy is in the decay of the signal, where the cooling mechanisms of sublimation and conduction dominate. Some models have virtually no signal at a time of 16 ns, while others are at as much as 60% of the peak signal at the same time. This comparative study provided impetus for groups modelling the LII process to attempt to improve the agreement between the models and thus to advance the understanding of the physical processes occurring in laser-induced incandescence.

2.1.3. Signal Evaluation

Typical signals obtained with conventional high fluence LII in a laminar diffusion flame are shown in Figure 2-5. The data demonstrate the accelerated rate of signal decay due to sublimation which occurs during the first 150 ns, followed by a relatively constant exponential decay over a period of several hundred nanoseconds or greater.

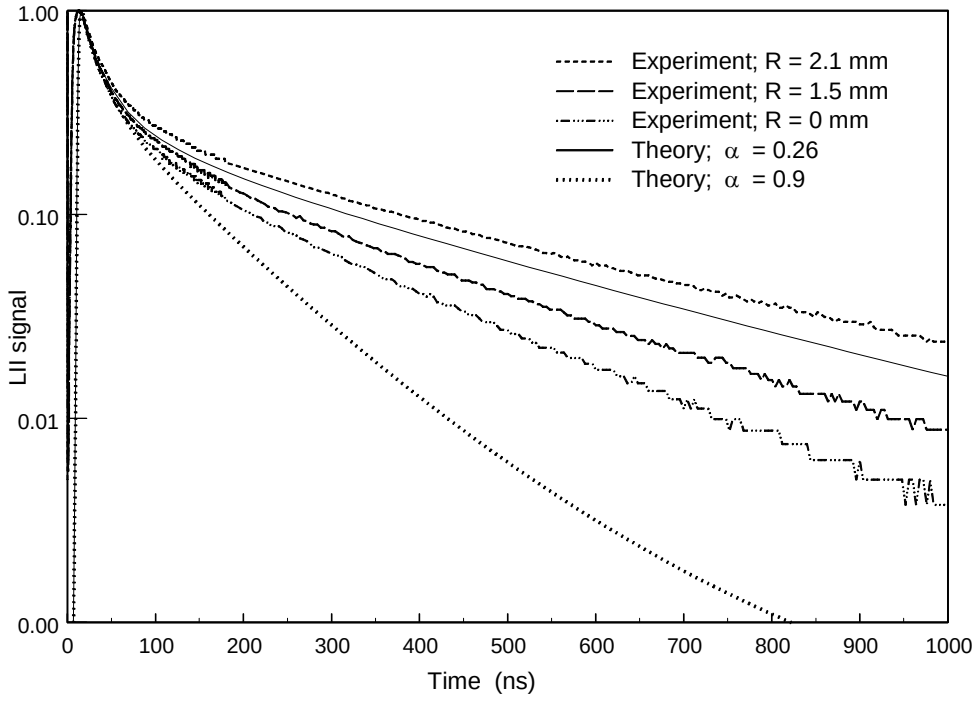

Figure 2-5. LII signal decay curves indicating variation in time constant in post sublimation (>150 ns) region. Measured and predicted values are shown for a range of radial positions at a height of 40 mm in an ethylene/air laminar diffusion flame.[50]

When conventional LII is calibrated with a source of known concentration and then measurements of an unknown source are made under identical conditions, the signal can be interpreted to give an accurate measurement of the unknown soot volume concentration. This is dependent on the soot particles being heated to the same peak temperatures for all LII measurements, so that the signal emitted from the soot is indeed proportional to the concentration. However, calibrating an LII apparatus using a flame with soot at high ambient temperature as the source of known concentration, and then applying LII using the same laser fluence to measure soot in a plume of lower ambient temperatures introduces inaccuracies due to different peak temperatures between the calibration and the measurement.[108] Furthermore, variation in the ambient pressure has an effect, as it impacts upon the sublimation temperature of elemental carbon.[54] The spatial light beam profile also affects the sensitivity of the LII signal to these variations in other parameters.[34] Even calibration in engine exhaust can result in errors, as the composition of the particulates change and the exhaust temperature changes as the engine conditions change, again resulting in different peak temperatures.

For particle sizing, the parameter of greatest interest to regulators and environmental and health researchers is the aggregate size. However, for sizing LII measures the surface are available for heat transfer (active surface area) and from this an effective primary particle diameter is determined. This effective primary particle diameter is functionally dependent on the soot primary particle diameter modified by the aggregate size through shielding effects.[109] Approaches to apply knowledge of the shielding effects in order to extract information on the aggregate size from LII are discussed in Section 3. Uncertainty in the value of the accommodation coefficient significantly affects the accuracy of the primary particle diameter determined with LII. Also, due to the significant sublimation which occurs, the particles shrink during laser heating and the initial cooling period. Also due to sublimation the particles become surrounded by a cloud of hot carbon vapour (Stephan flow), which reduces the diffusion to the particle and affects the heat conduction to the surrounding medium and therefore the cooling rate of the particles. This resulted in higher than expected particle temperatures after a high fluence laser light pulse.[53] These issues make it very difficult to model the physics of the transient sublimation and cooling of the particle, as it is unclear what the appropriate gas properties are as a function of temperature and time. Finally, the

assumption of monodisperse primary particles is unlikely to hold true for most practical combustion systems.

There are other parameters that affected signal evaluation. The temporal response of laser and detection system, if too slow, can bias the resulting measurements of both soot concentration and primary particle diameter.[73] The use of multipulse averaging will improve the signal-to-noise ratio, but will introduce a measurement bias to applications with unsteady concentrations of soot. Many practical environments also have broad distributions of the primary particle diameter and the number of primary particles per aggregate, which are not accounted for with the conventional approach of assuming monodisperse primary particles in the signal evaluation.

2.2. ADVANTAGES AND DISADVANTAGES OF WORKING WITH A FLAME TO DEVELOP LII

The vast majority of publications regarding the development of LII have performed *in situ* measurements in a laboratory flame, as demonstrated in a recent review.[34] The laminar diffusion flame (LDF) in Santoro or Gülder configurations is most frequently used for nonpremixed flames and the McKenna burner is most common for studies of rich premixed flames.[34] These laminar flames provide a near-ideal environment for LII, masking issues to be found in measurements of turbulent flames, post-flame soot, carbon black, and engine particulate emissions.

Although these laminar flames provide a near-ideal environment for development of the LII technique for the purpose of soot formation studies, where *in situ* measurements are required, they do not evaluate the performance of the technique over the full range of possible applications. As the objective of this work was to further develop LII so that measurements could also be performed to measure soot emissions, the performance of the technique at or near room temperature and with concentrations orders of magnitude lower than found in-flame required evaluation.

2.2.1. Advantages

The advantages of working with these flames are numerous. They provided steady laminar conditions, which allow the collection of multipulse averaged signals to improve the signal-to-noise ratio. The soot particles have undergone a common

temperature and chemical species history at a given location, which produces near-monodisperse primary particles and narrow distributions of aggregate sizes in comparison to turbulent environments. The high ambient temperature and atmospheric pressure result in a relatively slow decay of the LII signals, and do not permit organics and other volatile species to condense on the soot particles. Also, the high concentration of soot particles in these flames resulted in strong LII signals.

2.2.2. Disadvantages

For measurements in situations other than laminar flames, the opposite of some or all of the advantages described above are true. Development of LII for any of these applications is hindered by lack of knowledge of the technique under less than ideal conditions. Additionally, at the high temperatures found in flames, flame radiation becomes an issue but is relatively easy to discriminate against with familiar experimental techniques.[50] Other optical methods typically applied in flames, such as line-of-sight attenuation, require scattering correction in order to compare them to LII signals[67] When the soot concentration in flames approaches concentrations of 8 ppm or greater, signal trapping is found to lead to an error in the concentration.[110] At such high concentrations, both in-scattering and out-scattering must be considered, where the effect of scattering relative to absorption is found to be strongly dependent on the morphology of aggregated soot particles. For circumstances without independent sources of details on the morphology of the soot aggregates, it best to neglect both in- and out-scattering.[110]

3. ADVANCES IN LII

Laser-based measuring techniques are important tools for understanding soot formation and oxidation in flames and for the quantification and characterization of particulate emissions from energy generation, industrial, and mobile sources. Laser-induced incandescence (LII) offers many advantages and unique capabilities over existing measurement technologies. However, for this approach to mature into a reliable tool for the determination of particulate concentration and morphology, especially in practical applications such as the measurement of particulate emissions, the limitations of conventional LII had to be overcome. This required a novel approach to avoid the issues that have been identified with conventional LII. The novel approach that was developed was autocompensating laser-induced incandescence (AC-LII). AC-LII combined a low fluence approach to avoid sublimation with two-colour pyrometry to avoid many of the other issues described in the previous section.

The standard practice for measuring soot volume fraction in conventional LII is to calibrate the LII system in a steady-state flame where the concentration at the measurement point is determined using extinction measurements, or to correlate the measured signal levels obtained with LII to another measurement technique with the same source of particulates. An example would be to correlate the LII signals obtained in a diesel exhaust to either gravimetric filter measurements of mass, or to an AVL Smokemeter measurement of mass concentration. Unfortunately, these calibrations for conventional LII have to be repeated for each engine condition, as the condensed hydrocarbons on the particulates varies with engine conditions, and influences the LII signal. These calibrations are also susceptible to fluctuations in laser fluence, laser beam attenuation by the soot, and the local ambient temperature.

AC-LII is a novel technique which relies on absolute light intensity ($W/m^3 \cdot sr$) calibration of the LII detection system combined with physical theory of the emission propensity of soot aggregates to measure soot concentration rather than conventional calibration of the system response to a known soot source. This extends the capabilities of LII for making practical quantitative measurements of soot.

The absolute intensity method is a time-resolved approach that applies two-colour

pyrometry principles to determine the particle temperatures, relating the measured signals to the absolute sensitivity of the system as determined with a traceable source. The use of the absolute intensity approach provides for continuous *in situ* self-calibration of the LII technique due to continuous measurement of the soot temperature. The absolute intensity approach allows use of lower laser fluence, as there is no requirement to be in a saturation regime where the LII signal is independent of laser fluence. With lower laser fluence, the soot particles are heated to lower maximum temperatures, and the effects of sublimation including mass loss are mitigated.

The intention was to develop the new technique so that it was insensitive to changes in experimental conditions, such as a change in engine mode for diesel engines. The essential feature of this new technique was that it *automatically compensated* for any changes in the experimental conditions, including:

(a) fluctuations in local ambient temperature

(b) variation in laser fluence

(c) laser beam attenuation by the particulate matter

(d) desorption of condensed volatile material.

Thus, the most appropriate name for this new technique was autocompensating laser-induced incandescence (AC-LII). Any effect that caused a change in the peak temperature in the LII process and a corresponding change in the peak signal level, including the circumstances noted above, was compensated for with this technique, as the particle temperature was measured directly with two-colour pyrometry.

This section describes the development of the experimental technique for performing AC-LII, the state-of-the-art nanoscale heat transfer model that was applied to support the experimental research, aspects of the soot morphology that influence LII measurements, sources of uncertainty and approaches to mitigate them, issues that were discovered, and optimization to maximize the sensitivity of the technique. Overviews of these advances have been reported.[21, 111-113]

3.1. NUMERICAL MODEL

In LII measurements, soot particles are heated by a laser pulse to temperatures in the range of around 4000 K and emit thermal radiation (incandescence) which is detected. The process involves physical and chemical phenomena on very short time and length scales at very high temperatures. Theoretical models describing the LII process include different terms, *e.g.*, for laser absorption, heat conduction, vaporization, radiation or annealing. The state-of-the-art was presented in the review article of Michelsen et al.[55] Although the differences between existing LII models was reduced considerably compared to those in a previous model comparison,[34] they remained relatively large even at low laser fluences. The major cause for the discrepancies between different LII models at low laser fluences resulted from differences in the optical and thermal properties of soot used in the models, such as soot absorption function, soot density, and thermal accommodation coefficient. Much greater differences exist among the LII models in the soot sublimation sub-model at high laser fluences. Understanding of laser heating at high laser fluences remains a challenge and much greater theoretical, numerical, and experimental efforts are required.

In this study, a physical model that accurately describes the nanoscale heat and mass transfer processes in LII, the model of Liu *et al.*[105] optimized for low fluence, was applied to provide reliable interpretation of the LII experimental data.

3.1.1. State-of-the-Art Models

The Michelsen model[114] represented a breakthrough in the approaches to modelling the nanoscale heat and mass transfer processes relevant to laser-induced incandescence. Most models, including those of Melton,[44] Dasch,[45] and Hofeldt,[47] have followed the basic approach outlined by Eckbreth,[32] which relates the change in internal energy of the particle to the laser heating, and then cooling due to evaporation (more correctly, sublimation), convection, and radiation. Another model of significance is that developed by Bladh,[115-117] which follows the Liu model closely. The Liu model[105] applied in this study contrasts with the Michelsen model in that it considers only the most significant terms at a sophisticated level and addresses a more complex morphology relevant for soot particles. As Melton's is the most frequently referenced model, a comparison of the significant differences between the Michelsen model, the

Liu model, and the Melton model are presented in Table 3-1.

The Michelsen model specifically addresses structural changes in the carbonaceous particles by including phase-dependent properties and accounting for annealing. Many of the properties are also temperature and wavelength dependent, whereas the earlier models often ignored these dependencies. The Michelsen model also includes mechanisms for oxidation, melting, and annealing of the particles and nonthermal photodesorption of carbon clusters from the particle surface.

The significant elements of the Michelsen model are:

(a) at low fluences (less than 0.15 J/cm^2)

  (i) assumption of free-molecular flow conditions

  (ii) incorporation of a thermal accommodation coefficient and heat capacities more appropriate for high temperatures

  (iii) inclusion of annealing

  (iv) incorporation of an absorption coefficient more appropriate for aggregates;

(b) and at higher fluences (greater than 0.15 J/cm^2)

  (i) inclusion of annealing,

  (ii) inclusion of a fast photodesorption mechanism

  (iii) inclusion of temperature-dependent enthalpies of formation for multiple subliming clusters.

The model results indicate that oxidation, melting, temperature-dependent specific heat and density, and convective transport are less significant parameters in advancing the understanding of the heat and mass transfer processes relevant to laser-induced incandescence. Thus, most of these additional processes, as well as sublimation, are significant only for high fluence LII, where peak soot temperatures exceeded 4000 K.

Table 3-1. Advances in modelling of LII processes.

Property	Melton model[44]	Liu model[105]	Michelsen model[114]
Internal energy	Temperature-independent density and specific heat	Temperature-independent density and temperature-dependent specific heat	Temperature- and phase-dependent density and specific heat
Absorption	Wavelength-independent refractive index	Wavelength-independent absorption function	Wavelength- and phase-dependent absorption cross-section
Radiation	Wavelength-independent refractive index	Wavelength-independent absorption function	Wavelength- and phase-dependent emissivity
Sublimation	Kinetically controlled at all temperatures	Transition regime expression between kinetically controlled and diffusion controlled; equilibrium surface partial pressure	Diffusive/convective transport based on nonequilibrium surface partial pressures
	Single subliming species	Multiple subliming species based on vapour pressure data	Multiple subliming species based on vapour pressure data
	Mass accommodation assumed to be unity	Constant non-unity mass accommodation	Mass accommodation from measured values
Conduction	Transition between Knudsen/continuum regimes with isolated primary particles	Fuchs approach valid in the entire regime from free-molecular to continuum	Knudsen regime at low pressure / transition regime at high pressure with isolated primary particles
	Thermal accommodation coefficient, heat capacity ratio, and Eucken factor more consistent with low temperature data	Thermal accommodation coefficient based on low-fluence LII experiment in a laminar diffusion flame	Thermal accommodation coefficient based on high temperature data
		Temperature-dependent specific heat ratio	Temperature-dependent heat capacities
Oxidation	Not included	Not included	Based on measured rates
Annealing	Not included	Not included	Based on graphitization rates
Melting	Not included	Not included	Estimated from measurements of graphite melting by pulsed lasers
LII signal	Wavelength-independent refractive index	Wavelength-independent absorption function	Wavelength- and phase-dependent emissivity

However, Michelsen showed that even at low fluences melting and subsequent annealing to a more ordered form of carbon may be important processes, as they would have an effect on emissivity and the soot absorption function, as illustrated in Figure 3-1.

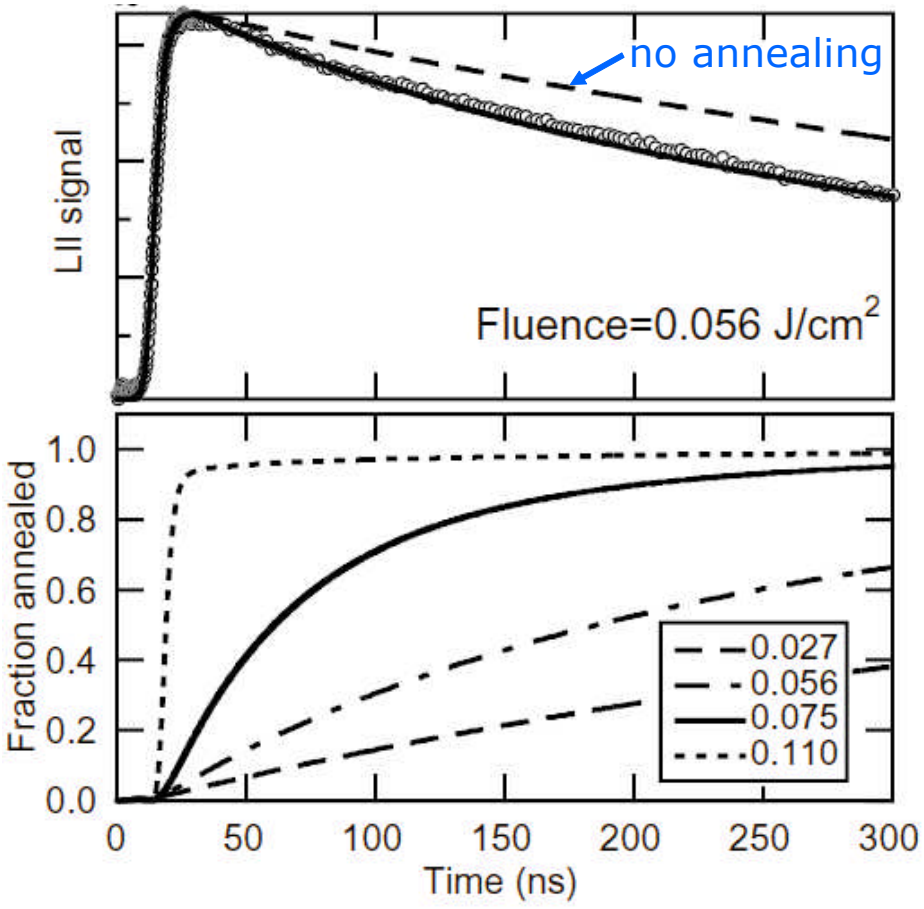

Figure 3-1. Accounting for annealing improves the fit to experimental LII signals obtained in a laminar diffusion flame at low fluence (top), and even at low fluences most of the particles eventually become annealed (bottom).[114]

One interesting aspect of low fluence LII discovered by Michelsen is that during the laser pulse, maximum LII signals are obtained at high fluences (>~0.2 J/cm^2) whereas during the decay, the greatest signals occur at lower fluences (peaking at ~0.1 J/cm^2 for a time 500 ns after the beginning of the laser pulse), as shown in Figure 3-2. This provides evidence of bias to larger primary particles in a polydisperse population, which is significant for most practical applications for LII.

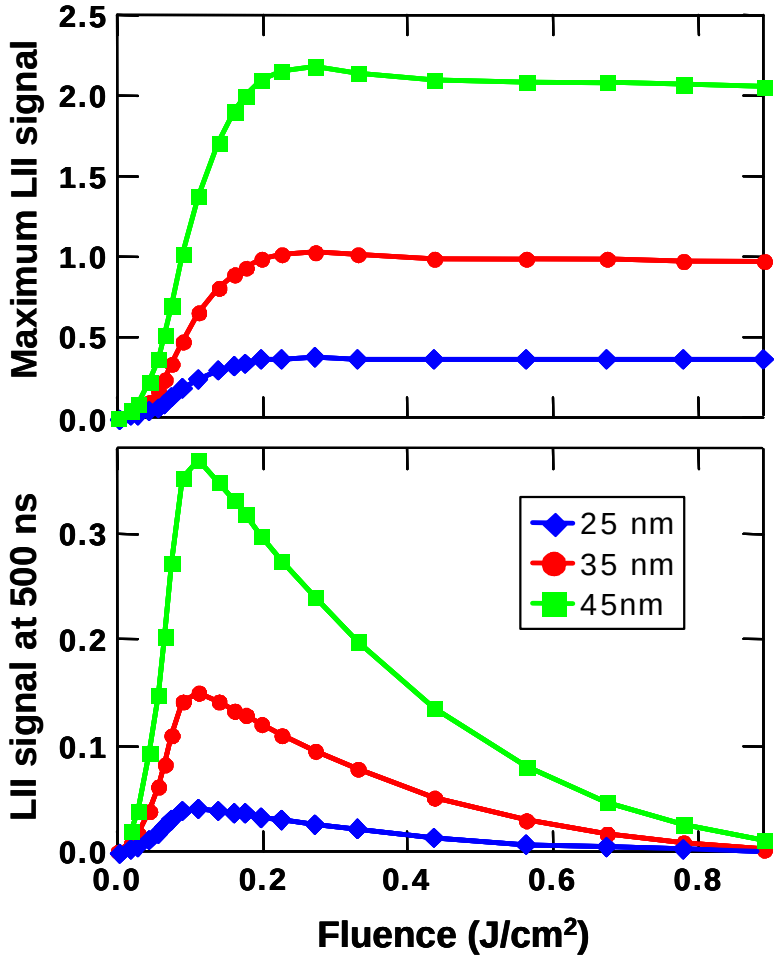

Figure 3-2. Maximum LII signals are obtained during the laser pulse at high fluences (>0.2 J/cm^2; top), whereas during the decay the LII signal peaks at low fluence (~0.1 J/cm^2; bottom).[114]

Current models have benefited from comparison exercises at three recent LII workshops. Specific test cases were developed for each workshop and multiple groups developing LII numerical models submitted their results for the comparison scenarios.

There was progress in improving the agreement amongst the models,[1, 2, 9] but there were still significant differences in the predictions at the most recent workshop, as illustrated in Figure 3-3 and Figure 3-4. The conclusions from the most recent workshop were that "*The individual models used within the LII community still do not reach agreement and have problems reproducing data. This holds for both low and high fluence which can be related to different treatment of the laser absorption, heat conduction and sublimation terms.*"[118]

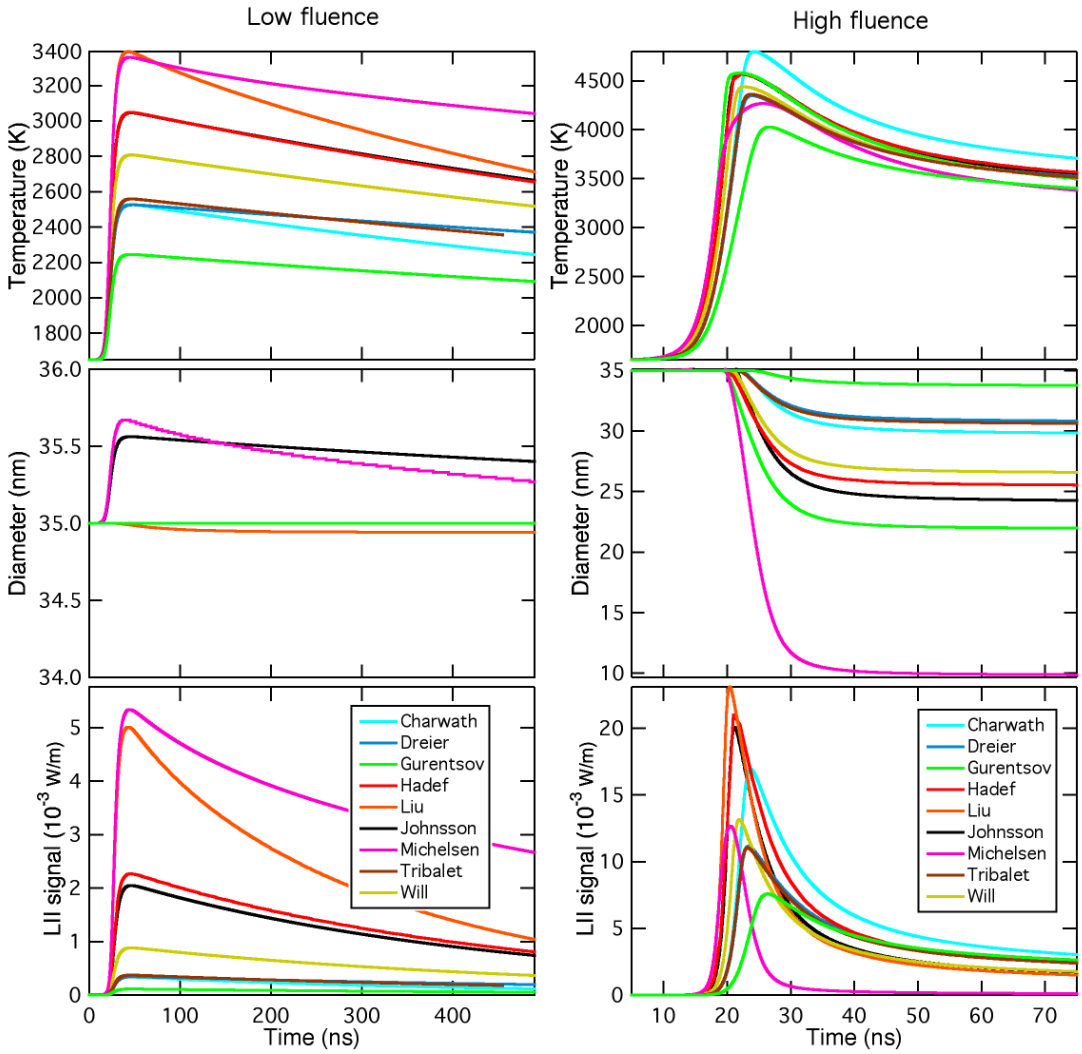

Figure 3-3. Comparison of nine LII numerical models, for monodisperse primary soot particles of 35 nm diameter in a flame at 1650 K and 1 bar. The laser was 1064 nm with a tophat spatial profile and a given near-Gaussian temporal profile, and detection was at 680 nm. Two fluences were compared, 0.1 J/cm^2 (low fluence, left) and 0.8 J/cm^2 (high fluence, right). Predictions of time-resolved particle temperature, diameter, and LII signal are shown.

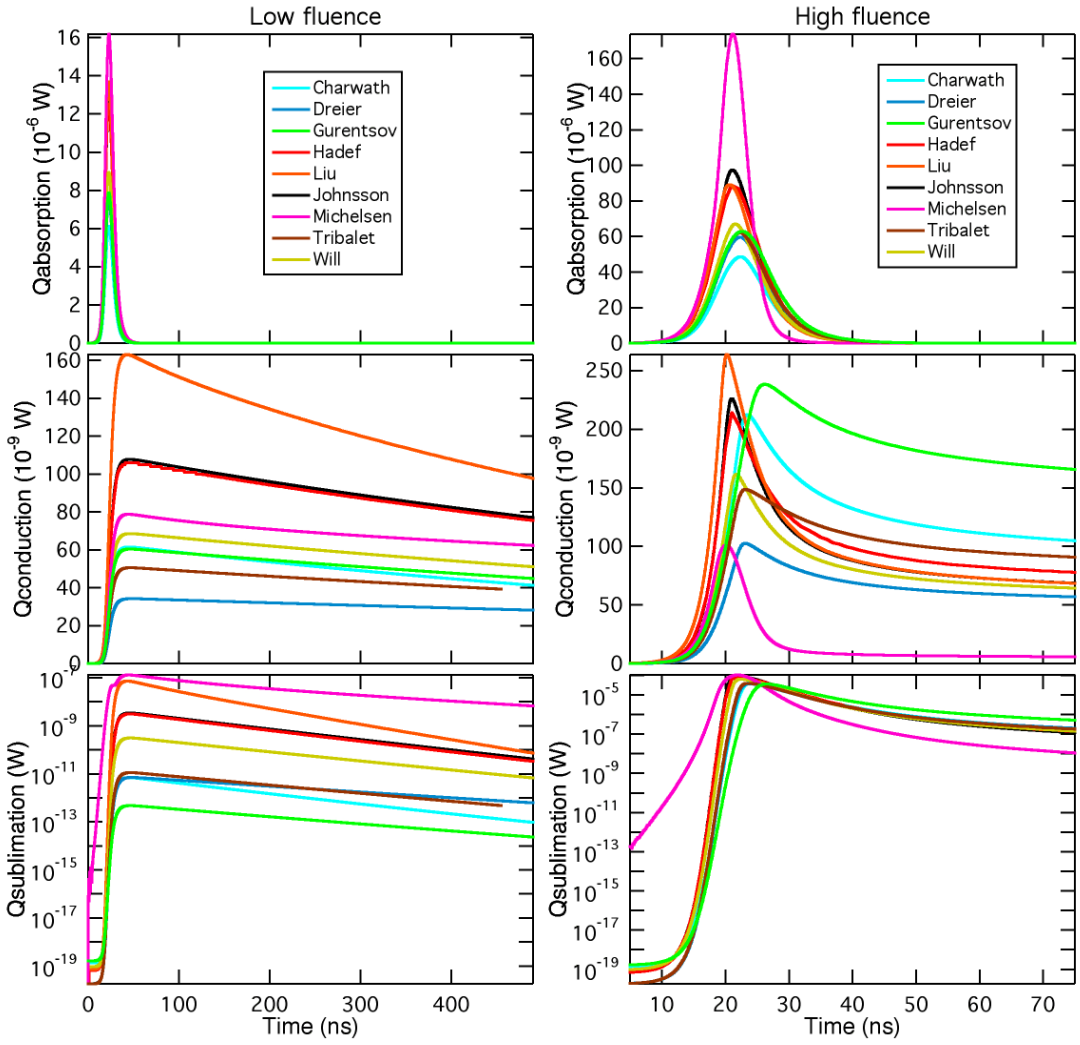

Figure 3-4. Comparison of nine LII numerical models, for same conditions as in Figure 3-3, illustrating differences in the heat transfer terms for absorption, conduction, and sublimation (low fluence, left; and high fluence, right).

The Liu model was used for comparison to experimental results generated in this work. The energy balance equation is the same as that presented in Eq. (1), as the Liu model was developed for low to moderately high laser fluences, where other physical and chemical processes such as photodesorption, annealing, and soot oxidation are unimportant. The terms for the rates of soot particle internal energy change, laser energy absorption by the particle, and heat loss due to soot sublimation are the same as those presented in Section 1.3.2.1. However, the properties have been substantially

updated, with temperature dependent data for all soot and surrounding gas parameters where available. New numerical model terms are presented for heat loss due to thermal radiation and for conduction heat loss from the particle to the surrounding gas. The basic features of the new conduction model are presented here, with further advances discussed in greater detail in the relevant sections later in the thesis.

3.1.2. Radiation Model

Radiation heat loss is included in the Liu model even though conduction heat loss is the dominant mechanism for low to moderate fluences. The radiation term is

$$\dot{q}_r = 8\pi^3 d_p{}^3 \bar{E}(m) \frac{k^5}{h^4 c^3} N_p \int_0^\infty \frac{t^4}{e^t - 1} dt \qquad (14)$$

where h and k are Planck and Boltzmann constants, respectively, c is the velocity of light, N_p is the aggregate size (number of primary particles per aggregate), and $\bar{E}(m)$ is an average value of $E(m)$ in the visible and near-infrared, wavelengths where heat loss due to thermal emission is most pronounced. An average value of 0.4 is assigned to $\bar{E}(m)$ and the integration results in a constant value of 24.886.

3.1.3. Conduction Model

The conductive cooling term uses a Fuchs approach[119] valid for all regimes from free-molecular to continuum. In laboratory flame environments the soot aggregates are generally smaller than the molecular mean free path length, λ_g. That is, the Knudsen number, Kn = λ_g/d_p is much greater than 1 and hence, the heat transfer coefficient is independent of the particle size. In other environments at lower ambient temperatures (or at higher pressures) such as engine exhaust, the mean free path is significantly shorter, and the Knudsen number is closer to 1. Therefore, a conductive cooling term that is valid for all applications is necessary.

The Fuchs approach, based on work by Filippov and Rosner[120] is applicable to the entire range of Knudsen numbers, from the free-molecular to the continuum regime. It involves finding the radius and temperature of a limiting sphere, which is defined such that inside this sphere heat conduction occurs in the free-molecular regime (between particle temperature T and the limiting sphere temperature, T_δ) and outside it heat

conduction is considered in the continuum regime (between the limiting sphere temperature T_δ and the gas temperature T_g). Inside the limiting sphere the heat conduction rate from the soot particle to the region within the limiting sphere is calculated using the free-molecular regime expression[120]

$$\dot{q}_c = \alpha\pi\left(\frac{D_{eff,fm}}{2}\right)^2 \frac{p_g}{2}\sqrt{\frac{8kT_\delta}{\pi m_g}}\frac{\gamma^*+1}{\gamma^*-1}\left(\frac{T}{T_\delta}-1\right) \tag{15}$$

where α is the soot particle thermal accommodation coefficient, $D_{eff,fm}$ is the diameter of a heat conduction equivalent sphere in the free-molecular regime calculated by DSMC (direct simulation Monte Carlo),[105] p_g is the gas pressure, m_g is the mass of the gas molecule, and γ* is the average value of the specific heat ratio defined as[120]

$$\frac{1}{\gamma^*-1} = \frac{1}{T-T_\delta}\int_{T_\delta}^{T}\frac{\mathrm{d}T}{\gamma-1} \tag{16}$$

In the region outside the limiting sphere conduction heat loss from the limiting sphere to the surrounding gas is calculated using the continuum regime expression[120]

$$\dot{q}_c = 4\pi\left(\delta+\frac{D_{eff,fm}}{2}\right)\int_{T_g}^{T_\delta} k_g \mathrm{d}T \tag{17}$$

where δ is the thickness of the boundary layer in the Fuchs approach. The validity of this model is supported in recent reviews of nanoparticle heat conduction theory.[121, 122]

3.1.4. Soot Absorption Function and Thermal Accommodation Coefficient

Knowledge of the soot absorption function, $E(m)$, is necessary in the determination of the concentration of soot using the AC-LII technique. Unfortunately, the reported values for $E(m)$ of soot used with LII vary from 0.179[60] to 0.4[109] which adds an uncertainty to the measurements. For soot particles, which are aggregates of relatively monodisperse spherical primary particles, Rayleigh-Debye-Gans (RDG) theory predicts that the absorption cross-section of a soot aggregate is equivalent to the sum of the absorption cross-sections of all the primary particles in the aggregate.[123] More accurate numerical simulation has confirmed that this is a reasonable approximation for the measurement of soot in flames.[124]

Knowledge of the thermal accommodation coefficient, α, of soot is critical in the determination of the specific surface area and primary particle diameter of soot using techniques based on time-resolved LII. The reported values of α for soot that are used with LII vary widely, from 0.07[125] to 1.[126] A recent evaluation of the methodologies behind these reported values determined that the most representative value of α for soot was 0.38.[127] Methods applying AC-LII to measure the soot absorption function and thermal accommodation coefficient are described in further detail in Section 3.6.1.

3.2. AC-LII SIGNAL EVALUATION

Autocompensating LII is based upon knowledge of the soot particle temperature, determined by optical pyrometry, and the concentration is determined from knowledge of the temperature and the measured absolute intensity. The temperatures and concentrations are time-resolved throughout the signal decay period, and the primary particle diameter is determined from the time constant of temperature decay in conduction phase of the particle cooling. This method offers advantages in that it is:

(a) NIST-traceable,

(b) not susceptible to: fluctuations in laser fluence; laser beam attenuation by the soot; or condensed volatiles on the particles, and

(c) knowledge of the ambient temperature is not needed to determine soot concentration.

Determination of the time-resolved absolute intensities, temperatures, and soot concentrations from measured signals at two wavelengths requires a sound physical theory. If two or more independent wavelengths λ are recorded, an average soot particle temperature across the laser light beam can be calculated by using the ratio of the observed signals (corrected for detection sensitivity) and the known soot particle absorption cross-sections. A single point calibration is made with a source of known radiance that is placed coincident with the measurement volume. This provides calibration factors η(λ) to relate the measured signals from incandescent soot to the absolute spectral intensities of the source (in $W/m^3 \cdot sr$)

$$\eta(\lambda) = \frac{V_{CAL}(\lambda)}{R_S(\lambda, T)} \tag{18}$$

where $V_{CAL}(\lambda)$ is the observed signal from the calibration source and $R_S(\lambda,T)$ is the spectral radiance of the calibration source. The calibration factor η accounts for the collection efficiency of the receiver and the detector responsivity at the detection wavelength λ.

The power radiated by a single particle of diameter d_p into 4π steradians is given by[128, 129]

$$P_p(\lambda) = \frac{8\pi^3 c^2 h}{\lambda^6}\left(e^{\frac{hc}{k\lambda T}} - 1\right)^{-1} d_p^3 E(m_\lambda) \tag{19}$$

The spectral radiance of the soot is dependent upon the power radiated by a single particle $P_p(\lambda,T)$ and the number of particles in the probe volume, $N_{PV} = n_p(w_b A_p)$, where n_p represents the concentration of primary particles in the probe volume, and the quantity in parentheses represents the volume interrogated, with w_b as the equivalent width of the laser light beam and A_p is the cross-sectional area of the probe volume as viewed by the detection system. The equivalent width of the laser light beam must be measured experimentally. Since this area is the same for both the calibration and the particle measurement, an equivalent spectral radiance for the particles in the probe volume R_p can be defined as

$$R_p(\lambda) = \frac{P_p(\lambda) n_p w_b}{4\pi} \tag{20}$$

which can be related to the observed signal from the particles $V_{EXP}(\lambda)$ by the calibration factor $\eta(\lambda)$, such that

$$\eta(\lambda) = \frac{4\pi \cdot V_{EXP}(\lambda)}{P_p(\lambda) n_p w_b} \tag{21}$$

The observed signal ratio at the two wavelengths $V_{EXP}(\lambda_1)/V_{EXP}(\lambda_2)$ can be converted to relative particle radiance using the calibration factors

$$\frac{P_p(\lambda_1)}{P_p(\lambda_2)} = \frac{V_{EXP}(\lambda_1)}{V_{EXP}(\lambda_2)} \frac{\eta(\lambda_2)}{\eta(\lambda_1)} \tag{22}$$

The ratio of the powers at two wavelengths radiated by a single particle is given by

$$\frac{P_p(\lambda_1)}{P_p(\lambda_2)} = \frac{\lambda_2^{\,6}}{\lambda_1^{\,6}} \frac{\left(e^{\frac{hc}{k\lambda_2 T}} - 1\right)}{\left(e^{\frac{hc}{k\lambda_1 T}} - 1\right)} \frac{E(m_{\lambda_1})}{E(m_{\lambda_2})} \tag{23}$$

Using the experimentally determined power ratio from Eq. (22), the known values of $E(m)$, and assuming all the particles in the probe volume are heated to the same temperature, Eq. (23) can be solved for T. It is the relative, not the absolute, magnitude of the particle absorption function at the two wavelengths that is important in determining soot particle surface temperature. For the work presented here, the values used for $E(m)$ are those determined by Krishnan et al.[130] and are referred to as Faeth values for $E(m)$, unless otherwise noted.

The particle (soot) volume fraction is given by

$$f_V = n_p \cdot \frac{\pi d_p^{\,3}}{6} \tag{24}$$

Expressing Eq. (19) in terms of $d_p^{\,3}$, and Eq. (21) in terms of n_p, and substituting into Eq. (24), the soot volume fraction is then

$$f_V = \frac{V_{EXP}(\lambda)}{\eta(\lambda) w_b} \frac{\lambda^6 \left(e^{\frac{hc}{k\lambda T}} - 1\right)}{12\pi c^2 h\, E(m_\lambda)} \tag{25}$$

The soot volume fraction has an inverse dependence on the absolute magnitude of the particle absorption function, $E(m)$.

As described in Section 1.3.2.4, the primary particle size is determined from the time constant of temperature decay in conduction phase of the particle cooling. The time-resolved temperature is determined from solving Eq. (23) for T. For low fluence LII, the dominant cooling mechanism for the soot particles is conduction to the surrounding gas. Eq. (12) is used to determine the time constant of the temperature decay, and Eq.

(13) is then applied to determine the primary particle diameter. The advantage in fitting the decay of temperature rather than the decay of the LII signal, as is common in high fluence time-resolved LII,[51, 53, 75] is that it requires less reliance upon the heat transfer models which have been demonstrated to have shortcomings.[54]

3.3. DEVELOPMENT OF THE EXPERIMENTAL LII TECHNIQUE

The absolute intensity method for performing LII experiments is a time-resolved approach that applies two-colour pyrometry principles to determine the particle temperatures, relating the measured signals to the absolute sensitivity of the system as determined with a traceable source. The time-resolution and temperature data are important for understanding the LII process and improving the associated nonequilibrium heat and mass transfer models.

Development of AC-LII required a well-characterized source of soot for comparison. Due to availability and a wealth of experimental and numerical simulation data on the flame, the Gülder burner was selected as the source of soot, always recognizing that the technique needed to work with particulate matter emissions as well as the flame. The burner is discussed below. In the sections that follow, the innovative features of the autocompensating laser-induced incandescence system developed for this work and the experimental apparatus used to perform AC-LII measurements, which have been recently documented,[112] are described.

3.3.1. Laminar Diffusion Flame Burner

Unless specified otherwise, all mention of laminar diffusion flame refers to a Gülder burner, which produces a laminar coflow ethylene diffusion flame at atmospheric pressure.[67] Briefly, the burner consisted of a central fuel steel tube with an inner diameter of 10.9 mm and outer diameter of 12.7 mm surrounded by a coannular air nozzle with an outer diameter of 100 mm and an inner diameter of 89 mm. The ethylene flow rate was 3.23 cm^3/s (0.194 SLPM) and the air flow rate was 4733 cm^3/s (284 SLPM), which resulted in a visible flame height of about 65±2 mm. A photograph of the flame is shown in Figure 3-5.

Figure 3-5. NRC ethylene/air co-flow laminar diffusion flame.

This flame had been extensively characterized at NRC, including the measurement of soot volume fraction with two-dimensional line-of-sight attenuation (2D-LOSA),[67] the measurement of soot surface temperature and soot volume fraction with spectral soot extinction (SSE),[131] coherent anti-Stokes Raman spectroscopy (CARS) to determine flame temperature, and LII measurements. At a height of 42 mm in the 65 mm tall flame, the radial profile of soot concentration is flat out to a radius of 2 mm, as shown

in Figure 3-6, and the variation with change in height is minimal.[67] This height was selected for comparisons, as it was the location that demanded the least spatial resolution from the LII experimental apparatus. Thus, all the LII experiments in the present work were carried out at a location 42 mm above the burner exit, on the burner centreline. The gas temperatures at this location, as measured with CARS and averaged over the central 3 mm is 1730 ± 25 K.[132] This result has been confirmed with SSE measurements.[131]

Thermophoretic sampling of the soot was performed at the 42 mm height/centreline location with a standard technique.[8, 9] Transmission electron micrograph (TEM) imaging was performed on the collected samples and image processing was applied to determine the soot morphology.[133] A sample image is shown in Figure 3-7 to illustrate the variation in soot morphology that is present in the well-controlled environment of

the laminar diffusion flame. Note that there are distributions of both the primary particle diameter and the number of primary particles per aggregate.

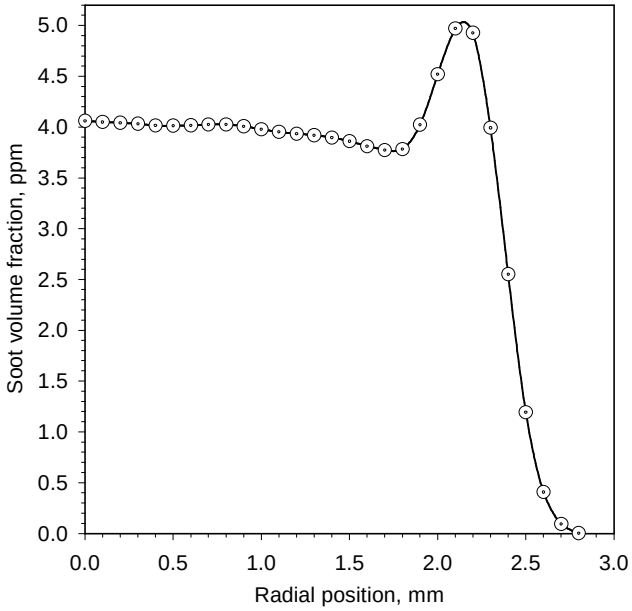

Figure 3-6. Radial soot profile at 42 mm above the burner exit and on the flame centreline in the laminar diffusion flame from 2-D LOSA measurements at 577 nm.[67]

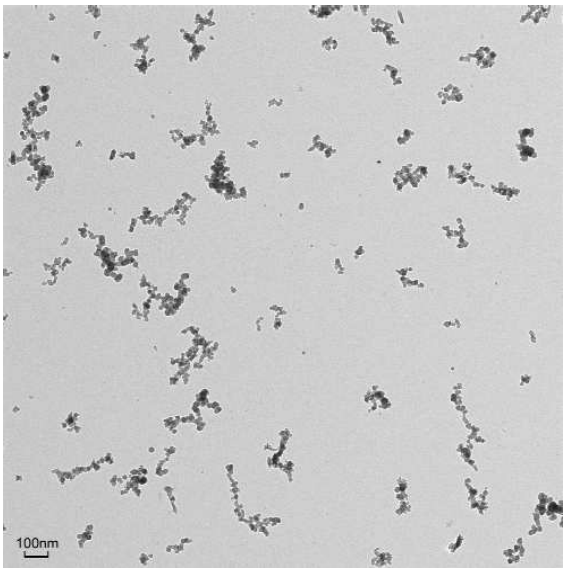

Figure 3-7. A typical TEM image of soot particles obtained by thermophoretic sampling at the sampled at the 42 mm height/centreline location of the laminar diffusion flame.[133]

3.3.2. Absolute Calibration

The absolute intensities of the time-resolved signals were determined by calibration of the spectral sensitivity of the detection system with an extended source of known spectral radiance or irradiance as was discussed in Section 3.2.

Three absolute intensity calibration techniques were evaluated. The first used a strip filament tungsten lamp spectral radiance standard.[128] The second used an integrating sphere coupled with a calibrated spectrometer as a spectral radiance standard. The third used radiation from a quartz halogen spectral irradiance standard scattered off the surface of a Lambertian surface. To compare and contrast the three techniques, a two channel demultiplexer receiver described later in Section 3.3.6.1 was implemented. With all three methods, for each wavelength there was a calibration factor $\eta(\lambda)$ in $W/V \cdot m^3 \cdot sr$, relating the absolute intensity in $W/m^3 \cdot sr$ to the photomultiplier tube (PMT) signal in volts.

3.3.2.1. Strip Filament Lamp Radiance Calibration

The radiance calibration was based upon a General Electric tungsten filament microscope illuminator lamp. The lamp was complete with a traceable spectral radiance temperature calibration determined by comparison to a secondary standard photoelectric pyrometer, which resulted in a polynomial fit of lamp current to spectral radiance temperature. The lamp had a 2 mm wide filament which limits the size of the probe volume to 2 mm for the 1:1 imaging configuration, since the calibration required all of the probe volume to provide a source of radiation.

The lamp calibration data provided a brightness temperature, the temperature of a blackbody source with equivalent radiance at a given lamp current at the calibration wavelength. Because tungsten is a non-blackbody source the brightness temperature had to be translated into an actual filament temperature. Using a function that defines the spectral radiance of a non-blackbody source, the spectral radiance at each demultiplexed channel centre wavelength was calculated for the applied current related filament temperature.

The calibration was performed at three different lamp currents (9.0, 10.0 and 11.0

Amps) with a precision current power supply, and the results were averaged. A light chopper complete with custom single slot blade running at 100 Hz was used to limit the DC saturation of the PMTs. Calibrated Schott neutral density filters were also inserted in the optical path to limit the signal on the PMTs. This arrangement is shown schematically in Figure 3-8.

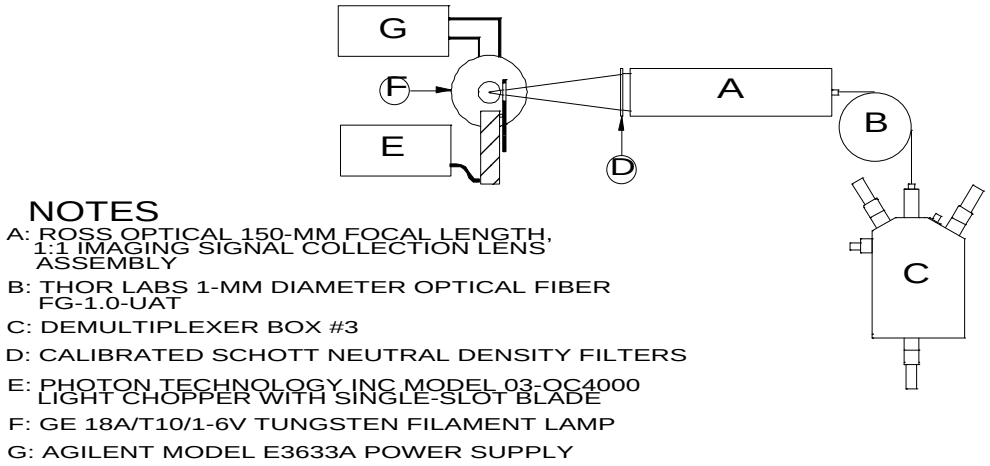

Figure 3-8. Setup for radiance calibration with either a tungsten strip filament lamp (shown) or an integrating sphere.

The strip filament lamp was calibrated for a point on the centre of the filament. Detailed spatially-resolved measurements showed that the absolute intensity decreases by as much as 5% as one approached the edges of the filament, likely due to temperature variation across the filament. This was a source of error that must be considered.

3.3.2.2. Quartz Halogen Lamp Irradiance Calibration

The irradiance calibration was based upon using radiation from a 200-Watt quartz halogen spectral irradiance standard scattered off the surface of a Lambertian surface. The lamp was a General Electric 200-Watt lamp with a coiled tungsten filament enclosed in a quartz glass envelope having an iodine rich atmosphere. The lamp was provided with a traceable irradiance calibration determined by comparison against two irradiance secondary standards. The Lambertian surface was an Ocean Optics 32 mm diameter PTFE white plastic diffuse reflectance standard. This calibration method using

the 32-mm diameter surface also allowed for larger LII probe volumes, as the technique would no longer be limited by the 2 mm width of the strip filament. The lamp was operated at a DC current of 6.500 Amps, and with a filament temperature of approximately 3000K. The calibration units for irradiance are $\mu W/cm^2 \cdot nm$. The arrangement for the irradiance calibration is shown schematically in Figure 3-9. As per the calibration requirements, the white Lambertian surface was located 43 cm from the lamp, and was oriented normal to the lamp. This arrangement also required a light chopper complete with custom single slot blade running at 100 Hz to limit the DC saturation of the photomultiplier tubes (PMTs), and calibrated Schott neutral density filters were inserted in the optical path to limit the signal on the PMTs.

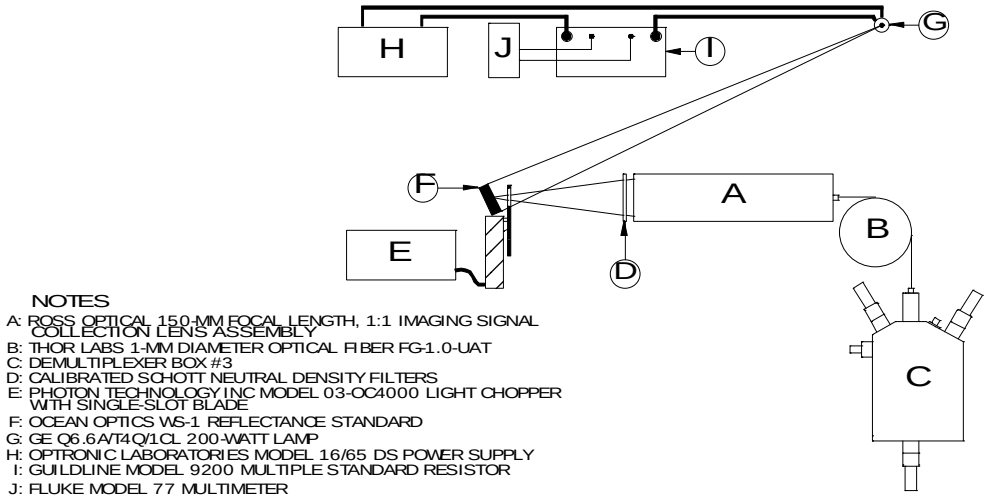

Figure 3-9. Setup for irradiance calibration with quartz halogen lamp and Lambertian surface.

3.3.2.3. Integrating Sphere Radiance Calibration

To overcome the limitations of the strip filament lamp and provide a larger source which would allow for a larger probe volume if necessary, an integrating sphere was examined as a possible calibration source. A Sphere-Optics Model SR-3A radiance source with a 25 mm exit port diameter was used. This was provided with a coupled spectrometer, and it was the spectrometer that had the traceable calibration, so that any deviation in the lamp performance did not alter the reported spectral radiation. The

integrating sphere used a quartz halogen bulb as its illumination source. The exit port of the SR-3A source was placed at the focal point of the LII signal collection optics. The lamp was operated at 4.167 A, and the radiation attenuating iris was set to a position that decreased lamp output entering the sphere by ~50% from its maximum. A light chopper complete with custom single slot blade running at 100 Hz was used to limit the DC saturation of the PMTs. Calibrated Schott neutral density filters were also inserted in the optical path to limit the signal on the PMTs.

3.3.2.4. Comparison of Radiance and Irradiance Calibrations

The three calibration methods produced similar results. The agreement is better than 15% at the two wavelengths (Table 3-2), lending confidence to using any of the three techniques for calibration. As the integrating sphere and the irradiance standard had much larger areas and therefore larger probe volumes could be calibrated, they offered advantages. Further, the spectrometer attached to the integrating sphere allowed continuous monitoring of the spectral emission of the illuminating bulb, so that any deterioration was detected and corrected for. Thus, the integrating sphere was determined to be the preferred source for calibration of the LII instrument.

Table 3-2. Comparison of Radiance and Irradiance Calibration Techniques.

Wavelength (nm)	397.1 nm	782.5 nm
Strip Filament Lamp Radiance Calibration Factor, $\eta(\lambda)$ ($W/V \cdot m^3 \cdot sr$)	2.208×10^{10}	4.285×10^{10}
Irradiance Calibration Factor, $\eta(\lambda)$ ($W/V \cdot m^3 \cdot sr$)	2.273×10^{10}	4.166×10^{10}
Integrating Sphere Radiance Calibration Factor, $\eta(\lambda)$ ($W/V \cdot m^3 \cdot sr$)	2.703×10^{10}	4.344×10^{10}
Average ($W/V \cdot m^3 \cdot sr$)	2.395×10^{10}	4.265×10^{10}
Coefficient of Variation (COV)	11.2%	2.1%

3.3.3. Two Colour LII

Two-colour pyrometry was applied to measure soot particle temperature history in the LDF. The blackbody radiation intensity I_b as a function of wavelength λ is given as

$$I_{b\lambda} = \frac{2c^2h}{\lambda^5}\left(e^{\frac{hc}{k\lambda T}} - 1\right)^{-1} \tag{26}$$

The radiation intensities I_p emitted by a spherical soot particle of diameter d_p as a function of wavelength are the blackbody intensities modified by the particle emissivity as

$$I_{p\lambda} = I_{b\lambda}\varepsilon_p = \frac{8\pi c^2h}{\lambda^6}\left(e^{\frac{hc}{k\lambda T}} - 1\right)^{-1} d_p E(m) \tag{27}$$

The particle emission intensities were calculated for d_p = 30 nm, a representative soot primary particle diameter, and a constant $E(m)$ of 0.4 for the UV-VIS-NIR spectral range. The calculated blackbody and particle emission intensities at temperatures relevant to LII applications from 2500 K to 4500 K are shown in Figure 3-10. As the wavelength increased, the particle emission intensity was further reduced compared to the blackbody emission intensity, due to the particle emissivity being inversely proportional to the wavelength. At temperatures above 4000 K, the particle emission intensity did not vary significantly in the spectral range considered. At lower temperatures the particle emission intensity increased as the wavelength increased in this spectral range.

During the course of this work, several other researchers have adopted variants of the two-colour LII approach,[134-137] including performing simultaneous two-colour LII and two-dimensional LII,[138] but have not adopted the principles of AC-LII.

Typical time-resolved low fluence LII calibrated signals at two wavelengths are shown in Figure 3-11. These illustrate the common features found in LII signals, including a rapid rise in signal on the order of the duration of the laser pulse, slow decays, and the longer wavelength signal having a greater maximum amplitude and slower decay than the shorter wavelength signal. Specific to low fluence LII, there was no evidence of a

rapid drop in LII signals immediately after the peak signal, common in high fluence LII due to sublimation. The near-monotonic exponential decays were characteristic of measurements performed in the LDF. It can be observed in Figure 3-11 that greater separation of the two wavelengths to be used for two-colour LII would result in greater sensitivity to change in the soot particle temperature.

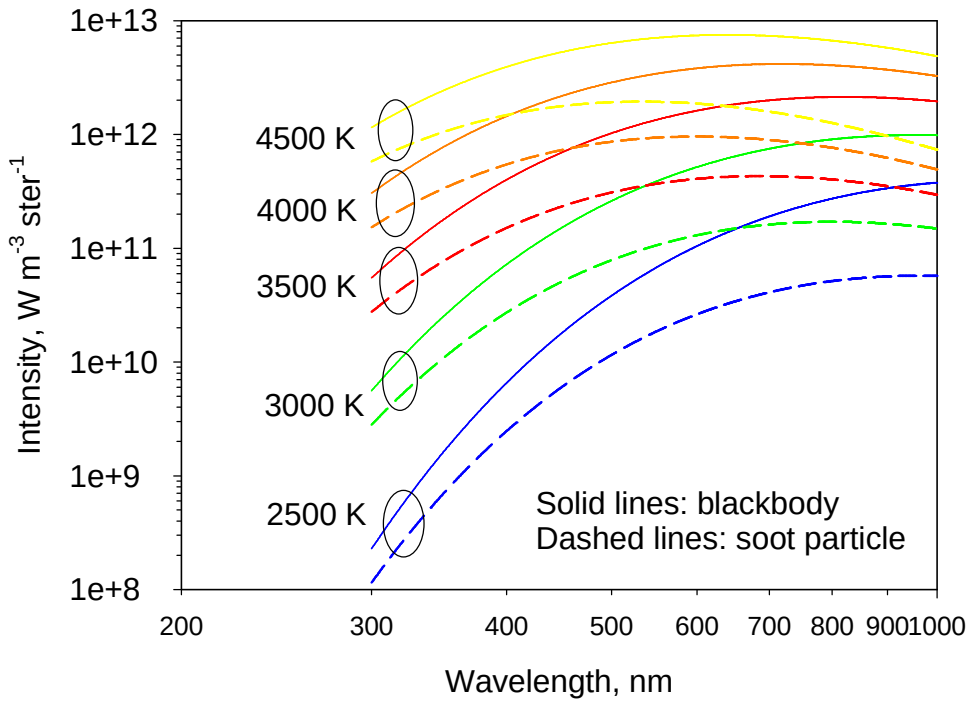

Figure 3-10. Blackbody and soot particle emission intensity for a range of temperatures encountered in LII over the UV-VIS-NIR spectral range. Soot particles are calculated for d_p = 30 nm and $E(m)$ = 0.4.

As described in Section 3.2, using Eqs. (22), (23) and the LII calibrated signals at two wavelengths, the soot particle temperature was determined. The temperatures were time-resolved, as the calculation was performed at each interval in the acquisition of LII signal data. The temperatures for the signals shown in Figure 3-11 are shown in Figure 3-12. This illustrated the common features found for LII soot particle temperatures, including a rapid rise in temperature on the order of the duration of the laser pulse, and a slow decay in the temperature, asymptotically approaching the surrounding gas temperature. Specific to low fluence LII, the peak temperature was less than 4000 K and there was no evidence of a rapid drop in temperature immediately after the peak signal,

common in high fluence LII due to sublimation. The near-monotonic exponential decay in the soot particle temperature was characteristic of measurements performed in the LDF.

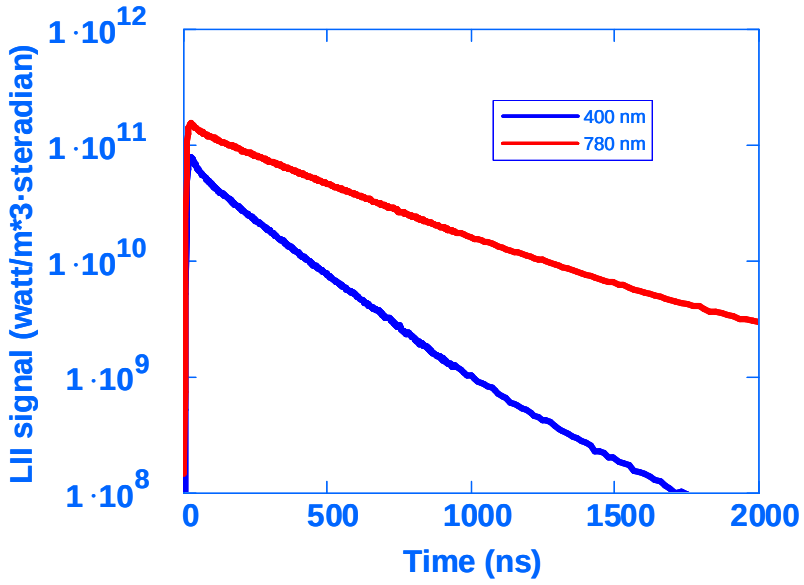

Figure 3-11. Absolute LII signal intensities during the transient heating and cooling of soot particles.

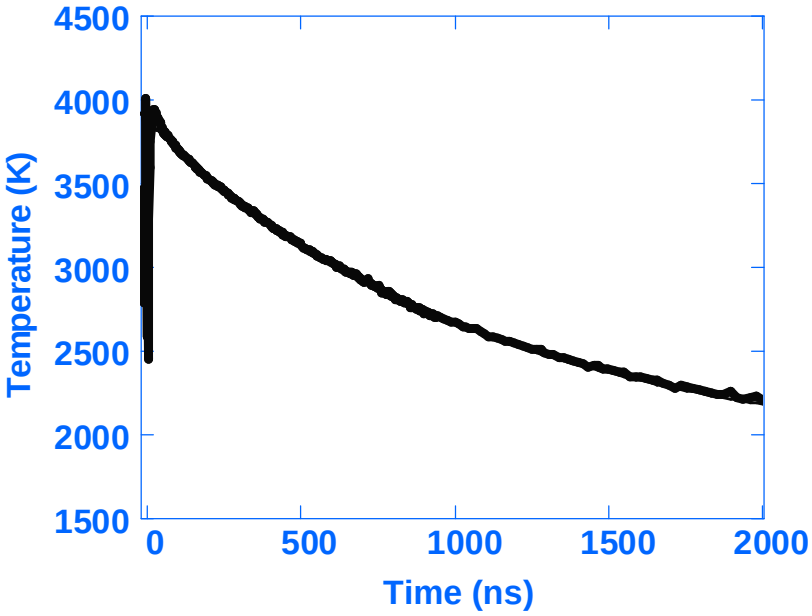

Figure 3-12. Determination of soot particle temperature during the transient heating and cooling of soot particles.

3.3.4. Low-Fluence LII

Conventional LII is performed using sufficient laser light fluence to ensure that the soot particles are heated to temperatures greater than that required for the sublimation of carbon (~ 4000 K). This is done so that the LII signal is notionally independent of the laser fluence, and hence particle temperature does not need to be measured. Typically, a laser light fluence considerably greater than 0.2 J/cm^2 for 1064 nm excitation is used. The laser light fluence required to reach a high fluence condition is proportional to the wavelength, so a laser light fluence greater than 0.1 J/cm^2 would be sufficient to reach high fluence for 532 nm excitation. The application of high fluence LII is based on the assumption that mass loss from sublimation does not affect the measurement of soot concentration. However, as shown in Figure 3-13, mass loss from laser heating and subsequent sublimation was significant in the high fluence condition. This was confirmed in a separate study of simultaneous LII and time-resolved light scattering.[139]

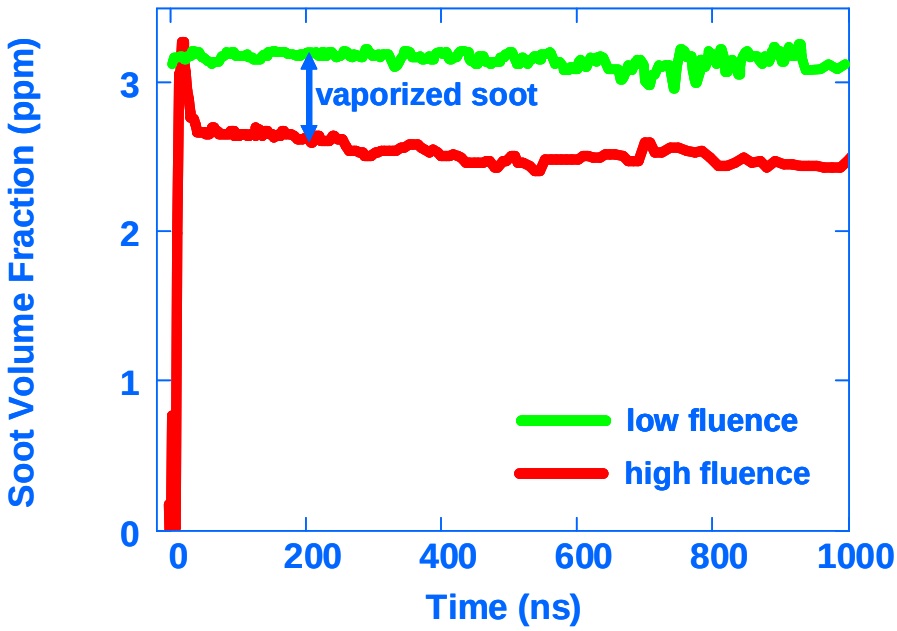

Figure 3-13. Real-time measurements of soot volume fraction showing no sublimation at low fluence and ~20% volume change at a higher fluence, occurring within 50 ns of the beginning of the laser pulse.

In the low fluence condition, the soot concentration measured with LII remained constant throughout the temperature decay period up to 1000 ns after the laser pulse. In

the high fluence condition, 20% of the soot concentration was removed during and shortly after the laser pulse, within the first 50 ns. This illustrated a distinct advantage of the low fluence LII approach, as it did not significantly alter the concentration of the soot particles that are the subject of the measurement.

With the low-fluence LII technique, the particles were heated to temperatures below the temperature at which significant sublimation occurs. Quantitative low fluence LII can only be performed in conjunction with the absolute intensity calibration, as the absolute intensity method provides a direct measure of the particle temperature.

3.3.5. Uniform Spatial Beam Profile

As the intensity of LII signals depends upon the particle temperature, accurate measurements demanded uniform heating of all particles in the probe volume. If uniform heating is not achieved, as with a Gaussian spatial profile, then the soot particles in the probe volume reach dramatically different peak temperatures, and interpretation of the resulting signals is exceedingly difficult.

To achieve uniform heating of the soot particles, a true top-hat (homogeneous) laser spatial profile is required. There are multiple methods of beam homogenization, including the use of diffractive optical elements. A relatively simple technique was demonstrated to inexpensively optimize the uniformity of the laser beam at the probe volume:

(a) a rectangular aperture was used to pass just the central, most uniform, portion of the laser light beam,

(b) a relay lens was used to relay image the aperture plane to the probe volume, mitigating diffraction effects from the aperture, and

(c) an iris was used in the detection optics to restrict the field-of-view to the central portion of the rectangular laser light beam. The iris allows us to vary the probe volume size, and thus signal intensity.

The resulting near-top-hat spatial profile for a 532 nm multimode Nd:YAG laser is shown in Figure 3-14. Similar results were obtained for a 1064 nm multimode Nd:YAG

laser, where the spatial standard deviation over the central 2 mm (region imaged by the detection system) was less than 6%. The width of the laser light beam in the probe volume defined the depth-of-field of the detection system, as soot particles not illuminated by the laser light beam were not heated and did not contribute to the measured LII signal. The use of a rectangular aperture rather than a circular one ensured that the depth-of-field was uniform for all regions imaged by the detection system. This allowed precise definition of the probe volume dimensions, including the equivalent width of the laser light beam, w_b, necessary for determination of the soot concentration as expressed in Eq. (25).

The laser light beam spatial profile was assumed to be uniform in the direction of the laser-beam propagation. This was considered to be defensible for most applications, but would be invalid in highly-attenuating applications such as in high-pressure heavily sooting flames.[140]

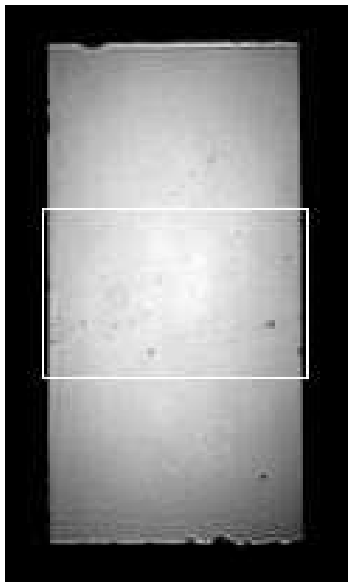

Figure 3-14. Measured laser spatial profile of a tophat laser beam. The image is a 50-pulse average from a multimode Nd:YAG laser operating at 532 nm, passing through a 1.5 × 3.0 mm^2 aperture, and relay imaged to the detection volume with 1:1 magnification. The pixel size of the beam profiler was 17.1 × 19.7 μm^2. The spatial standard deviation of the intensity over the region detected by the LII receiver (indicated by the white rectangle) was 9.4%.

3.3.6. Implementation

The features of the autocompensating laser-induced incandescence technique described above, including two-colour pyrometry, low fluence excitation, absolute intensity calibration, and relay imaging of a rectangular aperture were combined in an experimental apparatus to further investigate the capabilities of AC-LII. Subsequently, the innovative features were licensed to Artium Technologies, an instrumentation company, which produced an easy-to-use automated version of the laboratory experimental apparatus. Both systems were used in this work to make measurements, with the Artium system used primarily for some of the applications covered in Section 5, and they are described below.

3.3.6.1. Laboratory LII System

A schematic diagram of the laboratory autocompensating laser-induced incandescence system is shown in Figure 3-15. It was configured for portability and was referred to as Mobile II, as it was intended not only for use in the laboratory to make measurements in the LDF, but also to be taken to other laboratories for measurements of soot particles in practical applications.

A Big Sky UltraCFR multimode pulsed Nd:YAG laser, operating with 60 mJ/pulse at 20 Hz and 1064 nm, was used as the excitation source. As a multimode laser, it produced a quasi-top-hat laser beam spatial profile in the near field. This beam profile is shown at the left in Figure 3-16 to illustrate the laser output which was stretched with a cylindrical lens to form a mini-sheet. This demonstrated that attempting to create a more homogeneous spatial profile with a simple solution was ineffective. The laser was equipped with an electro-optic q-switch to produce a laser light pulse with a smooth profile of 7 ns FWHM (full-width at half of maximum) duration. A half-wave plate (to rotate the plane of polarization) in combination with a thin film polarizer (angle-tuned to transmit horizontally polarized radiation) was used to adjust the laser energy as required. A second half-wave plate was used to return the plane of polarization of the transmitted laser light beam to vertical.

Low fluence LII, ~ 0.1 J/cm^2 (= 1.0 mJ/mm^2) was typically employed to limit the peak temperatures to ≤4000 K, ensuring that negligible soot sublimation occurred.

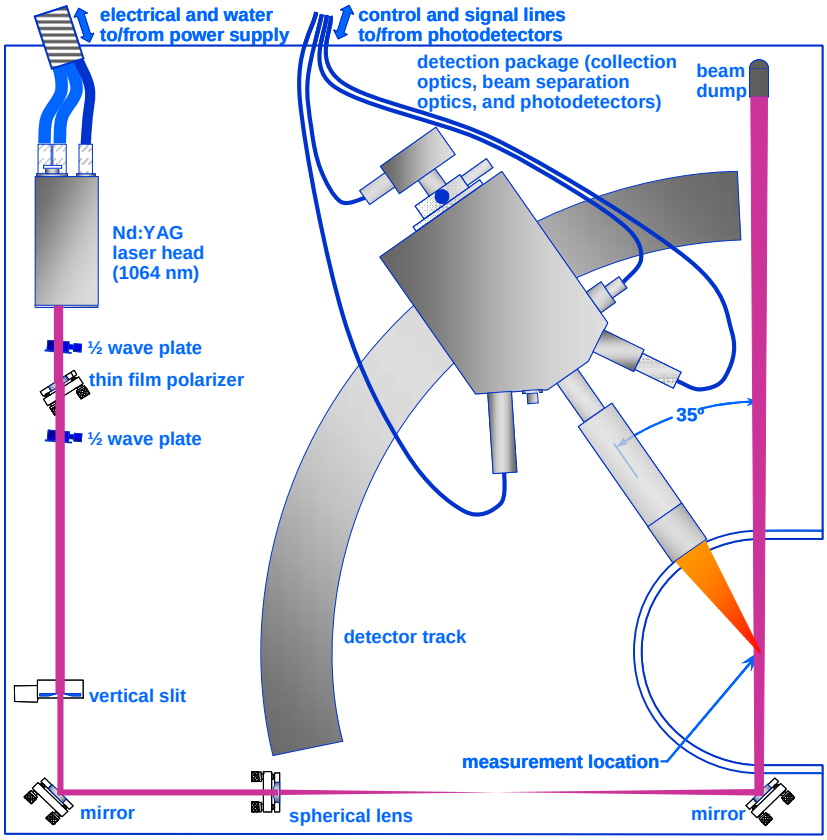

Figure 3-15: Top-view schematic of the AC-LII optical apparatus.

To ensure that the soot particles were heated to a uniform temperature throughout the sample volume, care was taken to make the spatial distribution of the laser fluence as uniform as possible throughout the probe volume. This was done as described in Section 3.3.5, where the laser beam was directed through a rectangular aperture to block all but the central, most homogeneous portion of the beam. A relay imaging lens was positioned such that the laser light beam profile at the aperture was imaged to the probe volume. This relay imaging of the aperture ensured that diffraction from the edges of the slit was minimized, and resulted in a nearly perfect top-hat distribution of fluence, so that there was uniform irradiation of the particles. This was confirmed by measuring the spatial beam intensity profiles in the probe volume with a Coherent BeamView system, shown at the right in Figure 3-16. This demonstrated that the relay imaging of an aperture was effective in creating a homogeneous spatial distribution.

The LII signal from the centre of the laser light beam in the probe volume was imaged at 1:1 magnification onto 2 mm diameter aperture, which was direct-coupled to a two-

channel demultiplexer detector box, as illustrated in Figure 3-17. The aperture defined the diameter of the region illuminated by the laser light beam that was imaged onto the photodetectors. The imaging system was arranged such that the imaging axis was at an angle of 35 degrees from the forward direction of the laser beam. This angle nearly doubled the depth-of-field of the probe volume relative to a 90 degree collection angle, improving the sensitivity by a similar factor. Thus the probe volume in the flame was a slanted cylinder of diameter 2 mm with a mean length of 4.9 mm.

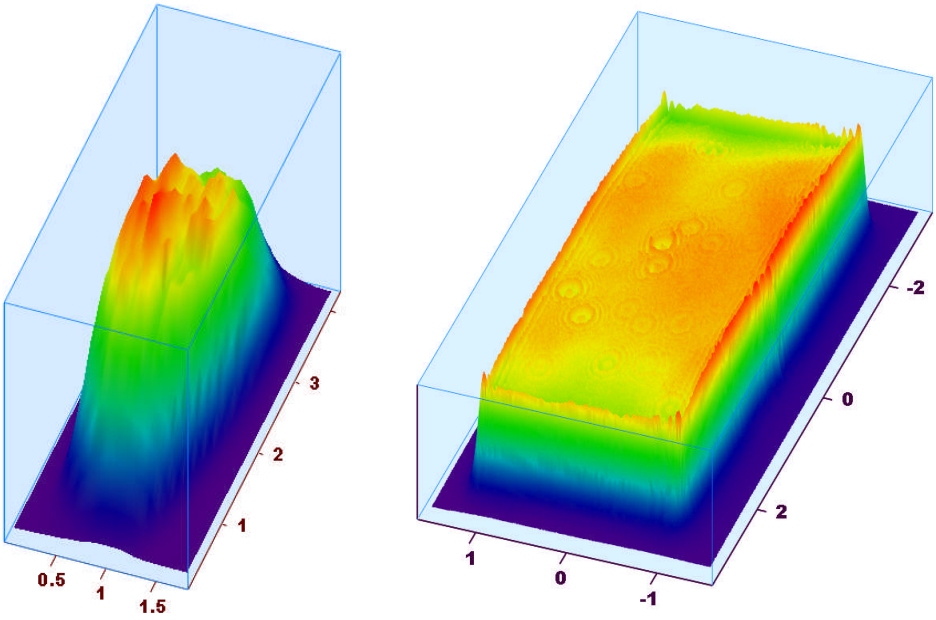

Figure 3-16. Measured spatial profiles of the laser light beam at the probe volume from a multimode near-top-hat laser: stretched with a cylindrical lens to form a sheet (left); and apertured and relay imaged to form a rectangular profile (right).

A two channel demultiplexer was used to separate the incandescent light into two wavelengths for performing the two-colour pyrometry measurements and subsequent signal evaluation to determine soot concentration and primary particle diameter, as displayed in Figure 3-18. An evaluation of the spectral response of available photodetectors, dichroic mirrors, and interference filters, was performed along with the desire to maximize overall sensitivity and precision of the temperature measurement over the temperature range relevant to LII (2500 K to 4500 K). This resulted in

selection of ~400 nm and ~780 nm as the two detection wavelengths. The lower wavelength channel had greater demands, as it was required cover a measurement range

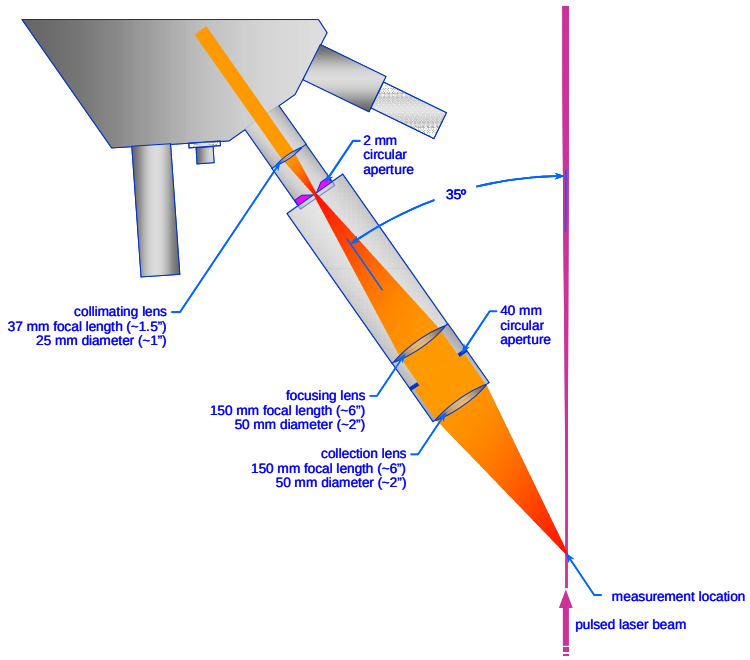

Figure 3-17. Details of collection optics for Mobile II AC-LII apparatus.

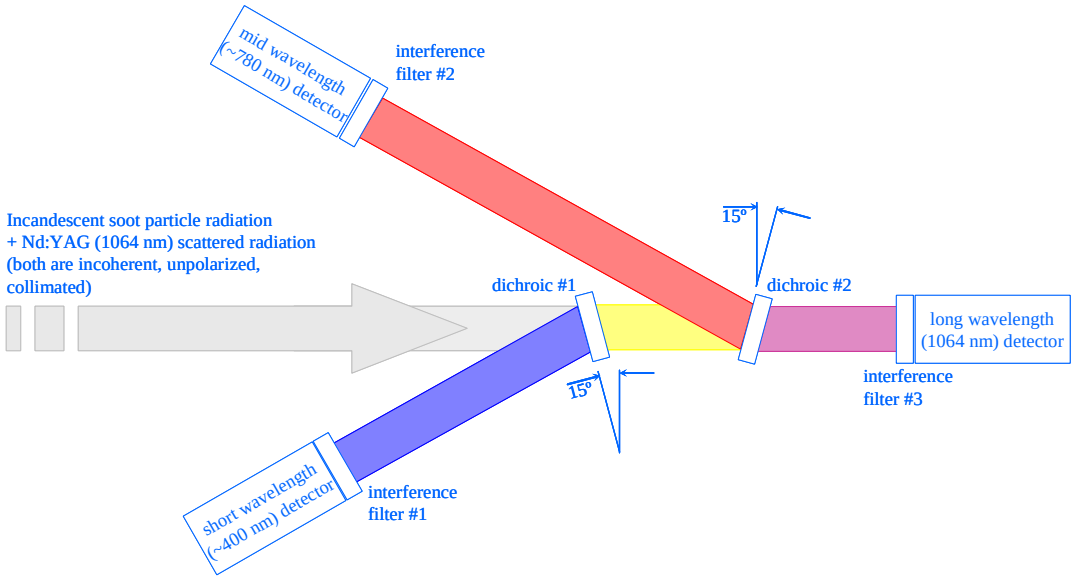

Figure 3-18. Details of optics inside demultiplexer receiver for Mobile II AC-LII apparatus, showing separation of wavelengths and optional detection of scattered laser radiation.

of ~3 orders of magnitude as the soot temperature dropped from 4500 K to 2500 K, whereas the higher wavelength channel was only required cover a measurement range of ~1.5 orders of magnitude, as shown in Figure 3-10. The 400 nm and 780 nm channels used a Hamamatsu H5783-03 bialkali photomultiplier module and a Hamamatsu R7400U-50 photomultiplier tube, respectively. These photomultipliers had rise times of 1-2 ns. The Hamamatsu photomultipliers could be operated with bias voltages of 400 V to 1000 V, with a commensurate change in gain of over two orders of magnitude. This provided flexibility to balance the peak signals on the two detectors, and to adjust the overall sensitivity to the concentration of soot particles being measured. Further adjustment in sensitivity was provided by inserting calibrated neutral density filters in the collection path immediately before the collection lens attached to the demultiplexer.

The collimated radiation entering the demultiplexer box was incident upon a CVI long wave pass dichroic beamsplitter, which reflected the ~400 nm radiation onto a CVI bandpass filter with a centre wavelength near 400 nm, a 40 nm FWHM bandpass, and a peak transmission of 35%. The radiation that is transmitted by the first CVI dichroic beamsplitter was incident upon a second long wave pass CVI dichroic beamplitter, which reflected the ~780 nm radiation onto an Oriel bandpass filter with a centre wavelength near 780 nm, a 10 nm FWHM bandpass, and a peak transmission of 45%. Lenses were used to focus the radiation onto the photodetectors with a diameter at the focal planes of 4 mm. The longest wavelength radiation was transmitted to a beam dump (optionally a third detector channel for 1064 nm detection of scattered radiation was implemented, but this was not typical).

Transient signals from the photomultipliers were recorded with a 500 MS/s oscilloscope, typically recording 400 shot averages, and subsequently transferred to a computer for further signal analysis.

A sampling cell was used for LII measurements whenever the source could not be inserted directly into the probe volume region. Typically this was used for practical applications, where the sample of particulates was drawn with a slight vacuum to the measurement location. This cell provided a window for introducing the laser beam to the probe volume, a second window for signal collection and for transmitting the laser

beam to a beam dump, and a third window orthogonal to the laser beam for viewing and alignment, as displayed in Figure 3-19. With this optical cell, the laser sheet was centred 2 mm from the open end of the tube carrying the sample of particulates.

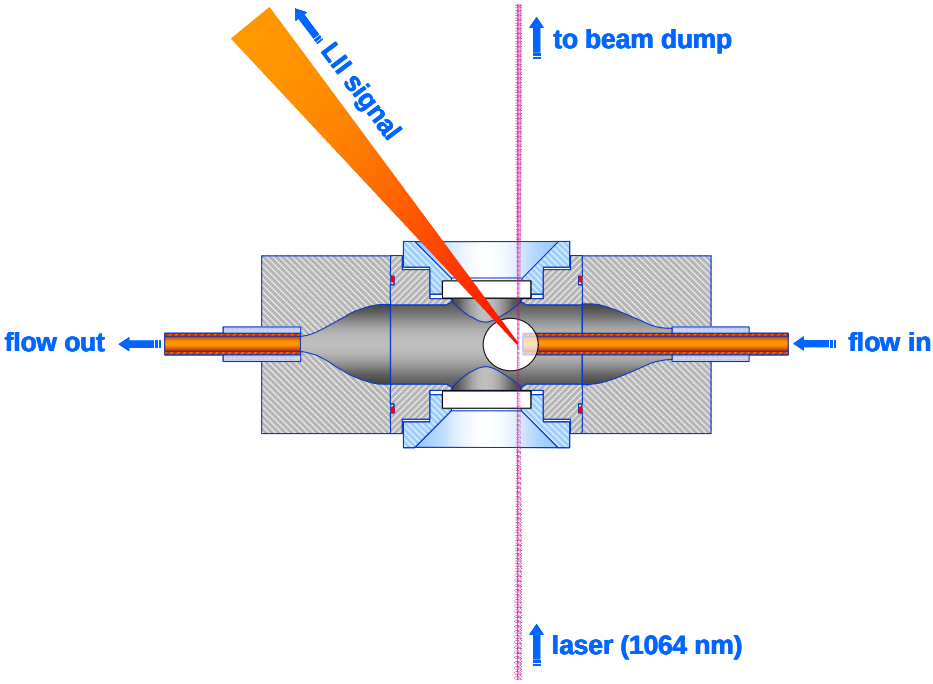

Figure 3-19. Schematic top view of optical cell used for sampling practical (non-laboratory flame) applications where the particulates were drawn from the source of emissions to the measurement location.

3.3.6.2. Commercialization

A fully-integrated, portable system was developed by Artium Technologies Incorporated for soot particulate characterization in various applications, utilizing the key innovations of AC-LII. A schematic layout of the system is presented in Figure 3-20. This system consisted of many of the same features as the Mobile II system developed as part of this work. These include a pulsed Nd:YAG laser, operating with 60 mJ/pulse at 20 Hz and 1064 nm; a half-wave plate, thin film polarizer, and second half-wave plate to adjust the laser energy and return the plane of polarization to vertical; and a rectangular aperture followed by a relay lens. This resulted in a top-hat laser light beam spatial profile at the probe volume, which deliberately ensured that the soot

particles were heated to a uniform temperature. Also as with Mobile II, low fluence LII, ~0.1 J/cm^2, was employed to limit the peak soot temperatures to ≤4000 K, ensuring that negligible soot sublimation occurs. A photodetector was used to measure the transmitted laser energy as a monitor of the window cleanliness.

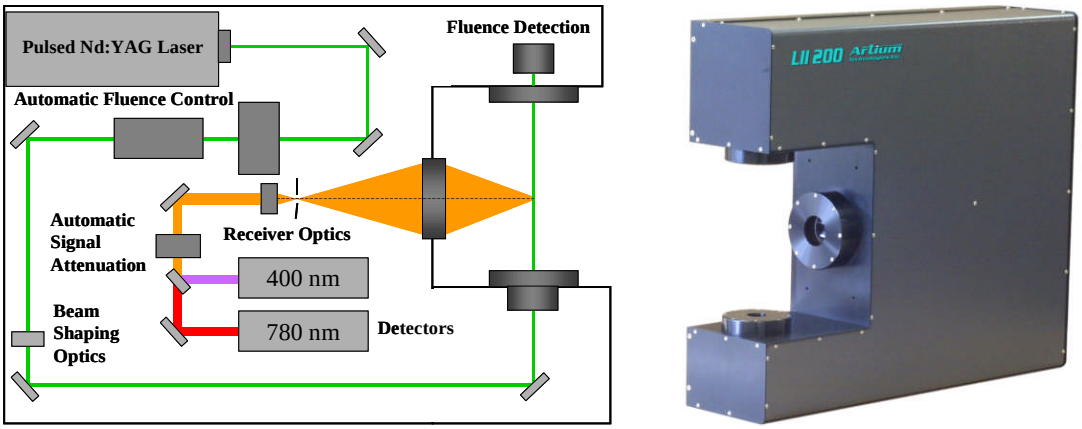

Figure 3-20. Schematic layout and photograph of an AC-LII commercial instrument.

The LII signal from the centre of the laser beam is imaged onto an aperture, which is coupled to a two-channel colour separation and detection unit. The collected LII signal is colour separated and independently recorded by two photomultipliers, equipped with narrowband interference filters centred at 400 nm and 780 nm, respectively. The bias voltage on the photomultipliers plus an automatic light attenuation system are all controlled by software, which provided wide dynamic range detection. The transient signals from the photomultipliers are recorded by a high speed data acquisition board at 10 ns intervals and subsequently transferred to a computer for further automated analysis. The AIMS software program provided with the LII 200 instrument performed the same calculations as were applied to the signals acquired with the Mobile II instrument. An optical cell for sampling the measured particulates was used with the Artium LII 200 instrument.

3.4. INITIAL RESULTS

AC-LII was demonstrated in the LDF with the Mobile II apparatus. Measurements were made on centreline and at the standard height of 42 mm. The temporal variation of LII intensities detected at the two wavelength bands and the resultant soot particle

temperatures are shown in Figure 3-21. A constant value of $E(m)$ was used in calculating the temperatures, which only depend on the ratio of $E(m)$ at the two wavelengths. The value of $E(m)$ used for this demonstration was 0.26.[60] For a measured temperature range of ~ 2500 K to 3750 K, the 400 nm detector was required to cover a range of signals of about 220:1, whereas the 780 nm detector only needed to cover a range of signals of about 20:1. There was little noise observed in the 400 pulse average signals collected for this condition even at 1600 ns after the laser pulse, when the signals have decreased significantly.

The measurements were made for a range of fluences, and temperature decay results for the ultralow fluence condition of 0.35 mJ/mm^2, the low fluence conditions of 0.95 mJ/mm^2 and 1.30 mJ/mm^2, and the moderate to high fluence conditions of 1.65 mJ/mm^2 and 2.12 mJ/mm^2 are shown in Figure 3-22. The peak soot particle temperatures achieved for these five fluences were 2405 K, 3519 K, 4007 K, 4245 K, and 4423 K, respectively. Note that for the lowest fluence of the five, this was only a ~700 K increase above the flame temperature at this location. The soot concentration, reported as a soot volume fraction, f_V, for the same five conditions is shown in Figure 3-23. In general, the four lowest fluences resulted in approximately the same measurement of soot concentration over the first 500 ns after the peak of the laser pulse.

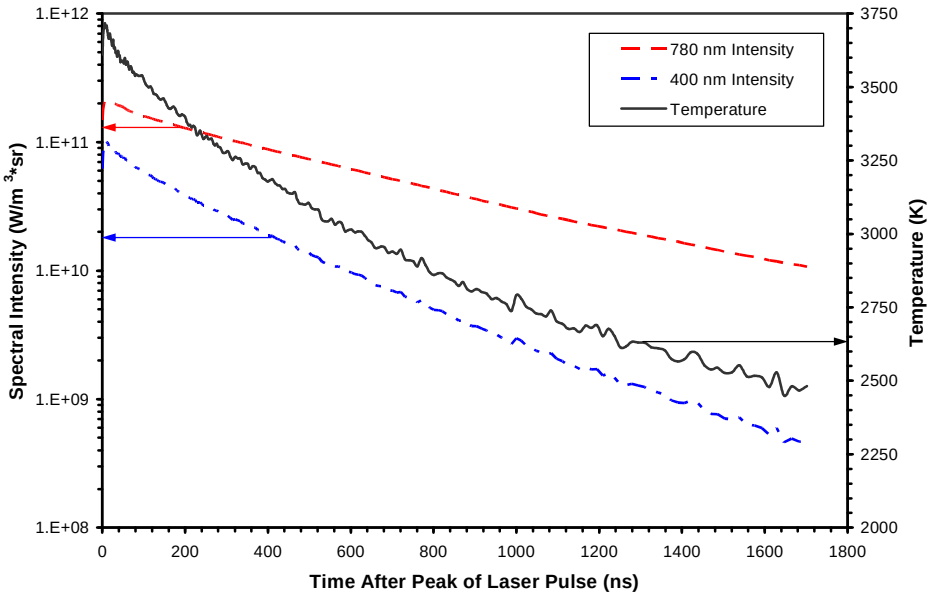

Figure 3-21. The absolute LII signal intensities detected at 400 nm and 780 nm and the resultant soot temperature for a fluence of 1.06 mJ/mm^2.

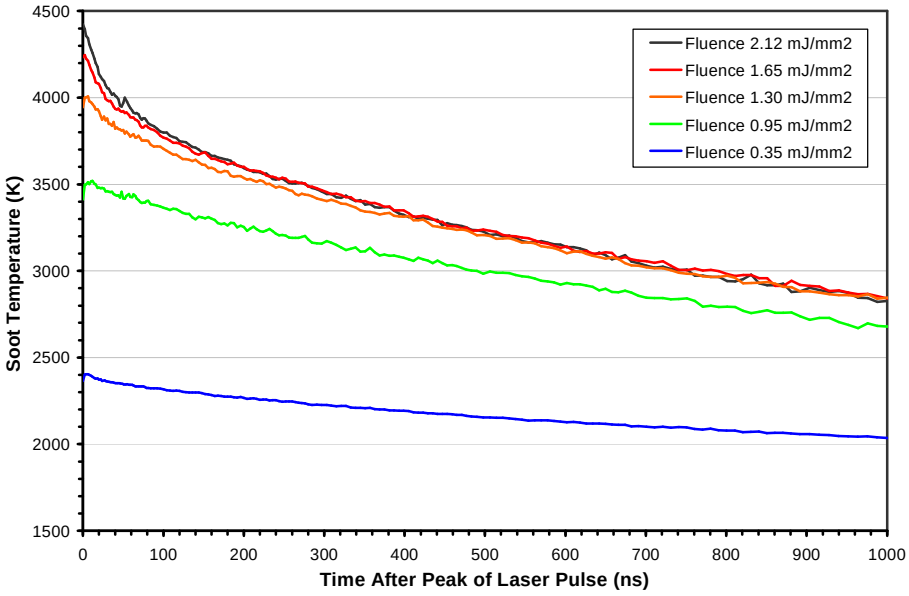

Figure 3-22. Soot particle temperature decays measured using the AC-LII technique. Measurements were made in the LDF on centreline at a height of 42 mm, for five different values of laser fluence.

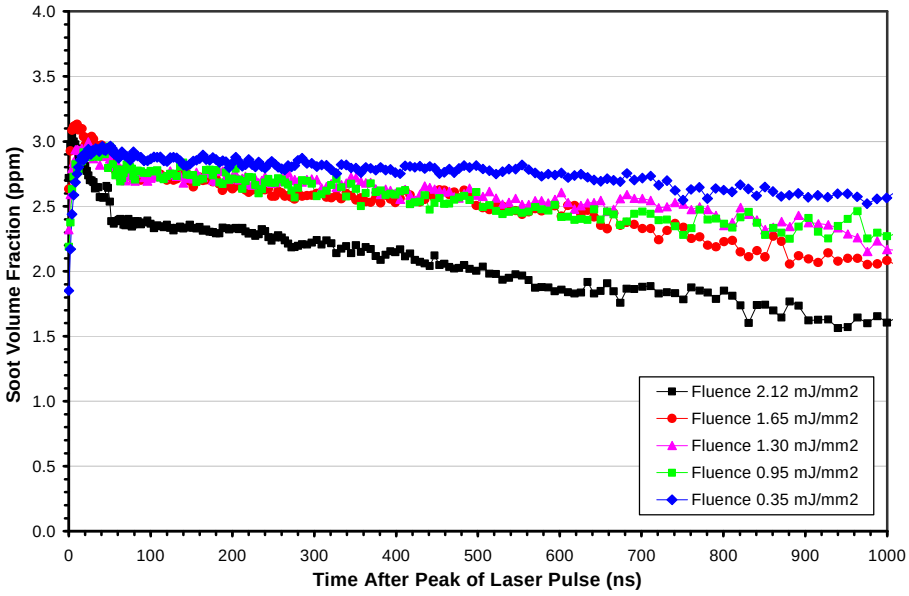

Figure 3-23. Soot volume fraction measured using the AC-LII technique during the decay period of the LII signal. Measurements were made in the LDF on centreline at a height of 42 mm, for five different values of laser fluence.

The highest fluence demonstrated evidence of significant sublimation, indicating this measurement was indeed in the high fluence regime. Within the first 50 ns after the peak of the laser pulse, the soot particles had lost 20% of their volume. It should be noted that at later times, especially more than 500 ns after the peak of the laser pulse, the measured concentrations were decreasing with increasing time. This effect was most apparent for the highest fluence and least apparent for the lowest fluence. This variation at long times was investigated further and is reported in Section 3.5.2.

A more complete range of fluences, from 0.12 mJ/mm^2 to 2.12 mJ/mm^2, was studied and the results are summarized in Figure 3-24 to Figure 3-27. This range spanned the entire low fluence regime, as well as reaching ultralow fluence levels where the peak temperature was only marginally above the flame temperature, and moderate to high fluence levels where sublimation was beginning to occur. The demands on the detection system were apparent, with the 400 nm detector required to respond to peak signals that varied over nearly five orders of magnitude, as shown in Figure 3-24.

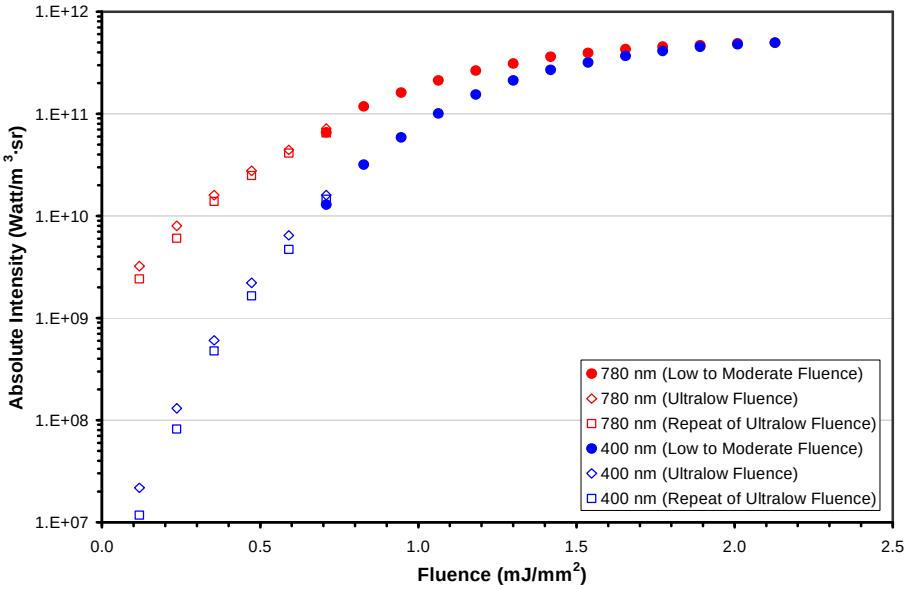

Figure 3-24. Peak absolute intensity recorded with the 400 nm and at 780 nm detectors on the Mobile II AC-LII system, for a wide range of fluences that extended above and below as well as spanning the low fluence regime. Data was acquired in the LDF on centreline at a 42 mm height.

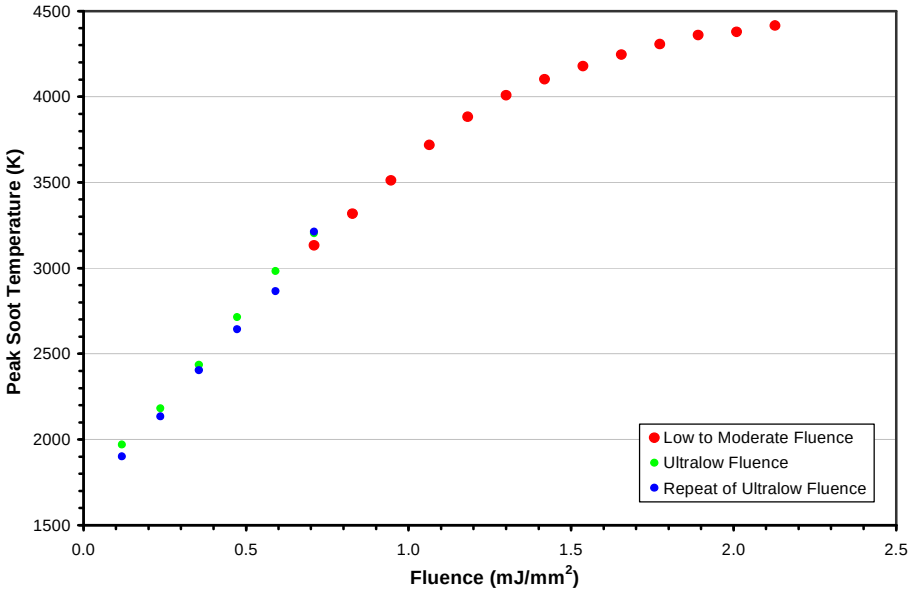

Figure 3-25. Peak soot temperatures calculated from the time-resolved data recorded on the Mobile II AC-LII system, for the range of conditions described in Figure 3-24.

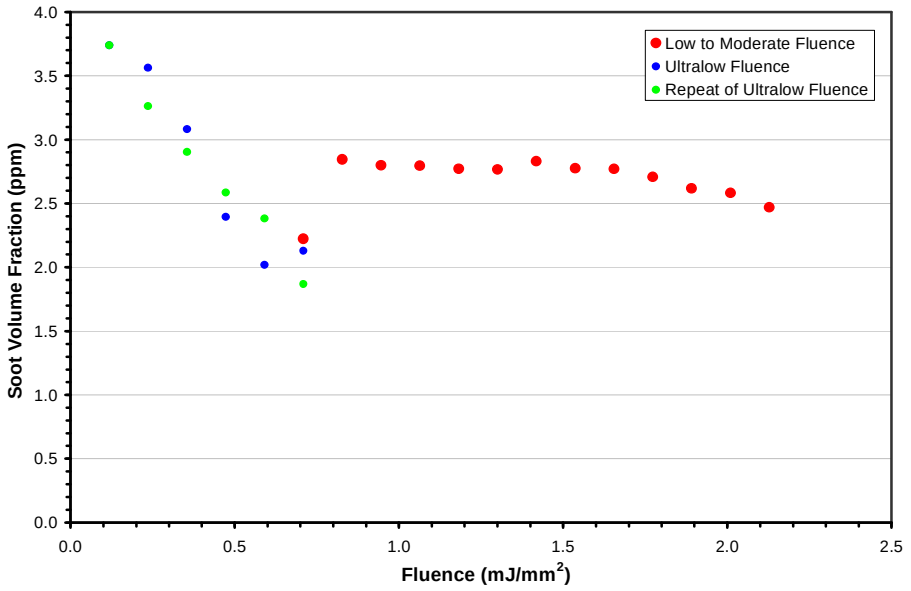

Figure 3-26. Soot volume fractions calculated from the time-resolved data recorded on the Mobile II AC-LII system, for the range of conditions described in Figure 3-24. f_V was calculated as a mean of the time-resolved f_V over the interval from 40 to 120 ns after the peak of the laser pulse.

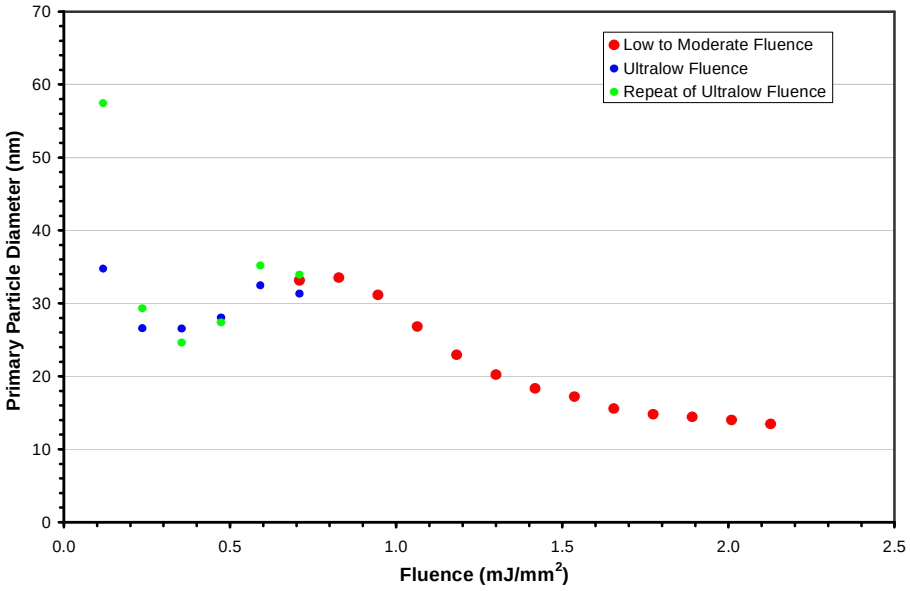

Figure 3-27. Primary particle diameters (d_p) calculated from the time-resolved data recorded on the Mobile II AC-LII system, for the range of conditions described in Figure 3-24. The d_p was calculated from a least-mean-squares best-fit to the time-resolved decay of T-T_{gas} over the interval from 40 to 120 ns after the peak of the laser pulse.

The time-resolved peak soot particle temperatures recorded from the LDF ranged from 1901 K (only 200K above the flame temperature) to 4414 K at the highest fluence. As displayed in Figure 3-25, at higher fluences the rate of increase in peak temperature was diminished, as sublimation during the laser pulse was simultaneously cooling the soot particles while the laser was heating them. The values of f_V shown in Figure 3-26 over the full range of fluences demonstrated the limitations of the AC-LII technique. At low fluences, in the range 0.8 to 1.6 mJ/mm^2, AC-LII performed as predicted, and reported identical concentrations independent of the fluence. In this range the measured soot concentration over the interval of 40 to 120 ns after the peak of the laser pulse was 2.79 ± 0.03 ppm independent of laser fluence or soot temperature. At higher fluences, > 1.7 mJ/mm^2, the reported concentrations decreased with increasing fluence, as predicted due to sublimation. However, at low fluences, < 0.7 mJ/mm^2, the reported concentrations were erratic, as they dropped suddenly at 0.7 mJ/mm^2 and then increased with decreasing fluence. The measurements at these ultralow fluences were repeated and found to exhibit the same behaviour. Possible reasons for this behaviour, including

the assumption of isolated monodisperse primary particles, were explored and are reported later in this section.

The time-resolved temperature decays were used to determine the primary particle diameters by applying a least-mean-squares best-fit to the decay of the temperature difference between the soot particle temperature and the flame temperature over the interval from 40 to 120 ns after the peak of the laser pulse. The results are shown in Figure 3-27, which demonstrate that there was only a very limited fluence range for which the measured d_p was constant. This narrow range of fluences was from 0.6 to 1.0 mJ/mm^2, where the measured d_p was 33.0 ± 1.4 nm independent of laser fluence or soot temperature. If the lowest fluence is ignored, as the temperature difference was too small for an accurate measurement to be made, then for fluences in the ultralow range d_p increased from ~ 25 nm to ~ 34 nm with increasing fluence. From the low fluence range through to the high fluence range d_p decreased from ~ 34 nm to ~ 14 nm. At moderate to high fluences, the sublimation process was expected to result in a decrease in the primary particle diameter. The behaviour at ultralow fluences and at moderate fluences was not anticipated. Possible reasons for uncertainties in measuring d_p were explored and are reported later in this section.

The AC-LII approach was demonstrated to be able to repeatably measure the soot concentration in the LDF and return the same value for a wide range of varying fluences. The validity of the AC-LII technique was less certain at ultralow fluences of ~ 0.7 mJ/mm^2 or lower, and while the technique reported valid results above the sublimation threshold of ~ 2.0 mJ/mm^2, it demonstrated that substantial sublimation is occurring at these fluences. It was recommended not to perform AC-LII in the high fluence regime. Overall, the AC-LII technique has also been demonstrated to work reliably over a wide range of peak soot particle temperatures, as was anticipated.

The precision of the AC-LII technique was evaluated in the soot emitted from a quenched flame burner. This was the Gülder burner with radial air jets placed at a height of 42 mm above the burner to quench the flame at that point. It resulted in a relatively steady stream of soot emitted from the tip of the quenched flame. Measurements were performed with Mobile II on this stream of particulates with 500 single shot data sets acquired. The results for soot concentration were f_V = 0.1524 ±

0.0082 ppm, Figure 3-28. Similar results were obtained for the primary particle diameter, which was measured as 31.38 ± 1.63 nm, Figure 3-29. This was a COV of 5.4% for f_V and 5.2% for d_p, indicating the level of precision that was obtained with these single shot measurements. It is anticipated that flame measurements, such as in the LDF, would result in higher levels of precision as the quenched flame was not a steady as the LDF, with a times series drift in concentration appearing over the course of the experiment. The greater soot concentration in the LDF would also contribute to improved signal quality and would be expected to aid in optimizing the precision.

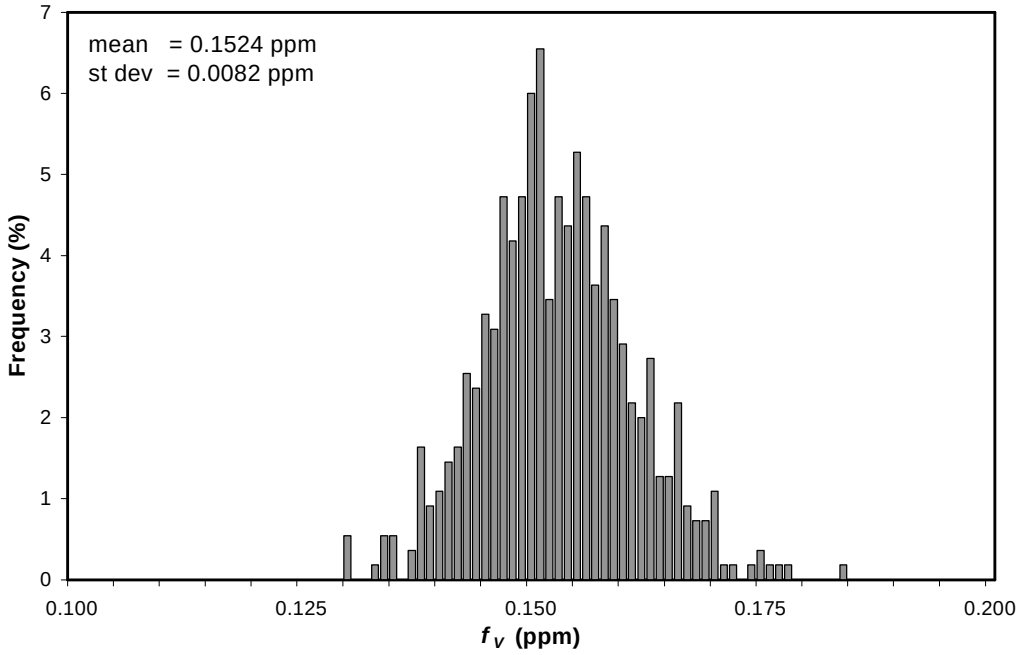

Figure 3-28. Precision of AC-LII in measuring f_V. Single shot data acquired above a quenched LDF.

The measurements in the LDF burner confirmed the correct operation of the novel AC-LII system. However, as it was developed for practical applications, an example of measurements performed in the exhaust of a heavy duty diesel engine is provided. Further examples of applications are discussed in Section 5. Results of a comparison between the soot mass concentration determined by AC-LII and the US EPA (United States Environmental Protection Agency) standard gravimetric particulate matter (PM) mass concentration corrected to remove the volatile fraction are shown in Figure 3-30.

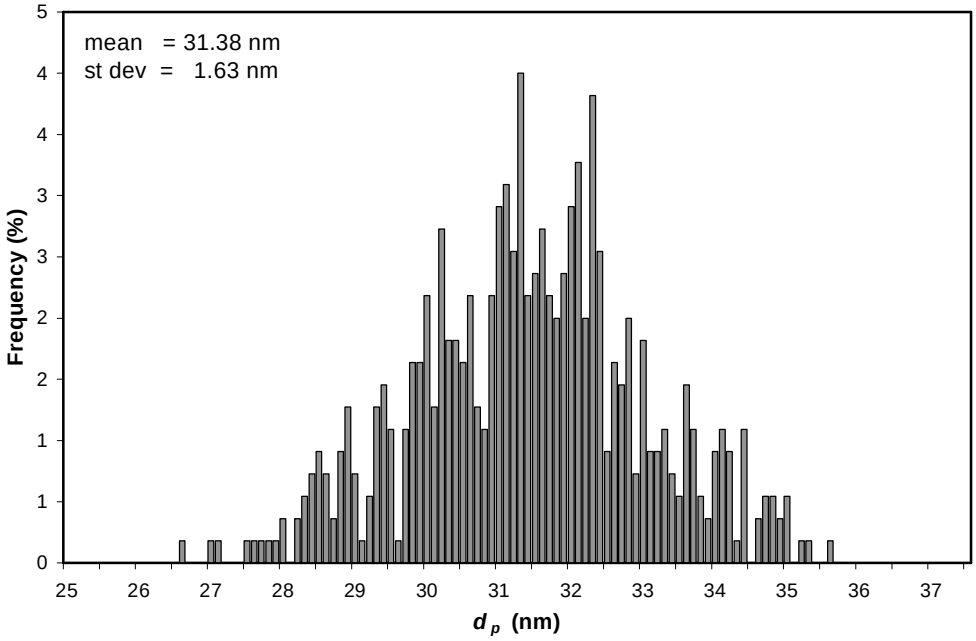

Figure 3-29. Precision of AC-LII in measuring d_p. Single shot data acquired above a quenched LDF.

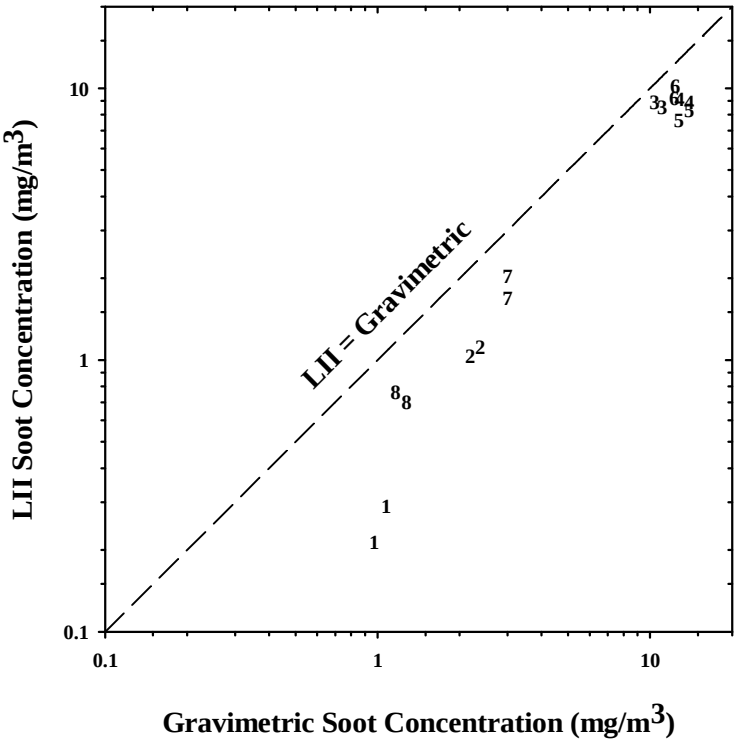

Figure 3-30. Comparison between AC-LII soot concentration and gravimetric assessment of non-volatile particulates concentration for a heavy duty diesel engine.[141]

Two repeats of each of the eight steady-state modes in the AVL eight-mode steady-state simulation are illustrated, with the numeral indicating the mode number. The soot concentrations measured by LII were consistently lower than those measured by the gravimetric method. The difference could have been due to the solvent extraction technique used to remove the volatiles from the filters used for the gravimetric measurements. However, the experimental differences might also have been due to the AC-LII technique, such as the choice of $E(m)$. This is discussed in further detail in later in this section. The differences did highlight the difficulty of making comparative measurements, as there was experimental error and uncertainty with all measurements, including those that are derived from certified reference standards.

3.5. IMPACTS OF AGGREGATION, AND PRIMARY PARTICLE DIAMETER AND AGGREGATE SIZE DISTRIBUTIONS

Soot particles in general form fractal-like structures (aggregates) with some bridging between the primary particles.[9, 123, 142] To improve the understanding of soot morphology, and to improve the interpretation of LII signal or temperature decays, the simple isolated sphere concept used to determine primary particle diameter (the mean or distribution of the diameter) needs to be improved upon. It has been well established that for any morphology other than isolated and monodisperse primary particles, the decay of the LII signal or temperature will not follow a single exponential behaviour due to the variation in cooling of particles of different primary particle diameters and/or different aggregate sizes.[105, 125, 143-147]

This section summarizes recent results in measuring the full particle distribution parameters for soot sampled in the laminar diffusion flame, an increasingly complex treatment of the soot morphology from a numerical modelling perspective, and techniques to determine the distribution parameters using a combined numerical/experimental approach. All of the numerical approaches described have been developed for low fluence LII, allowing the uncertainties in the models due to significant soot sublimation to be ignored.

The development of AC-LII was an essential component to the rapid development and increasingly sophisticated approaches of the modelling treatment of the morphology of

the soot particles. This was due to the availability of high quality low fluence time-resolved soot temperature data.

3.5.1. TEM Determination of Soot Morphology

Optical diagnostics for soot require a reliable description of soot morphology obtained independently for calibration and/or estimation of optical properties of soot. As soot aggregates consist of polydispersed carbon nanoparticles, there is a need to characterize the distribution of the primary particle diameter d_p and the distribution of the number of primary particles per aggregate N_p. Analysis of aggregated soot particles with imaging from a transmission electron microscope (TEM) offers an opportunity to provide characteristic data for these distributions. However, although physical sampling techniques have been frequently used to determine soot morphology, for flame measurements it must be recognized that the sampling probes interfere with the flame and potentially lead to erroneous results.

Soot aggregates acquired by thermophoretic sampling from a height of 42 mm on the centreline of the laminar diffusion flame were reported by Tian *et al.*[133] The diameters of the primary particles were represented by an arithmetic mean diameter, $\bar{d}_p$ = 29.2 nm and a standard deviation of $\sigma_{d,g}$ = 7.1 nm. Based on fitting a normal distribution to the data, the fit parameters were $\bar{d}_p$ 28.3 nm and $\sigma_{d,g}$ = 6.5 nm. These results are in agreement with those previously reported at comparable heights in similar laminar diffusion flames.[9, 148] In the same study, a lognormal distribution represents the data for N_p well with N_g = 23.2 and $\sigma_{N,g}$ = 4.15, for a lower limit of N_p > 5, where N_g is the geometric mean of N_p and $\sigma_{N,g}$ is the geometric standard deviation. This high quality data on the distributions of d_p and N_p will assist in the development of optical techniques to assess the morphology of soot particles.

Subsequently, the study was extended by applying a new image-processing method, the relative optical density (ROD) method.[149, 150] With this method, the number of primary particles in each individual aggregate was determined by not only the projected area but also the optical density distribution within the projected area of the aggregate. As such, it attempted to address the three-dimensional nature of the aggregates. Unlike the conventional statistical method applied in analysis of TEM images of soot, ROD was

independent of empirical constants based on correlations or numerical simulations. The number of primary particles per aggregate, N_p, of each object was calculated using ROD. The reported values for the log-normal fit of N_p was N_g = 31.4 and $\sigma_{N,g}$ = 5.08 with a lower limit of $N_p > 5$. However, the quality of fit was poor for large N_p. As a result, the data from the statistical projected area method were considered to be the more accurate data.

Finally, the data analysed with the statistical projected area method was re-analyzed and fit with an improved least-mean-squares fit function optimized for log-normal distributions. The lognormal distribution function for primary soot particle diameters is

$$p(d_p) = \frac{1}{d_p \sqrt{2\pi} \ln \sigma_{d,g}} \exp\left[-\left(\frac{\ln(d_p / d_g)}{\sqrt{2} \ln \sigma_{d,g}} \right)^2 \right] \tag{28}$$

and the log-normal distribution function for the number of primary particles per aggregate is

$$p(N_p) = \frac{1}{N_p \sqrt{2\pi} \ln \sigma_{N,g}} \exp\left[-\left(\frac{\ln(N_p / N_g)}{\sqrt{2} \ln \sigma_{N,g}} \right)^2 \right] \tag{29}$$

This final analysis resulted in a lognormal distribution fit to the data with d_g = 28.9 nm, $\sigma_{d,g}$ = 1.26, N_g = 25.9 and $\sigma_{N,g}$ = 4.42 when a lower limit of $N_p > 5$ was applied. These final results were preferred for subsequent analyses of aggregation effects, as this was the best overall fit to the experimental data, and did not display the double-log-normal behaviour. This final fit to the data is shown in Figure 3-31 for the distribution of primary particle diameters and for the distribution of number of primary particles per aggregate. The results for the aggregate size distribution from the three methods are presented in Table 3-3.

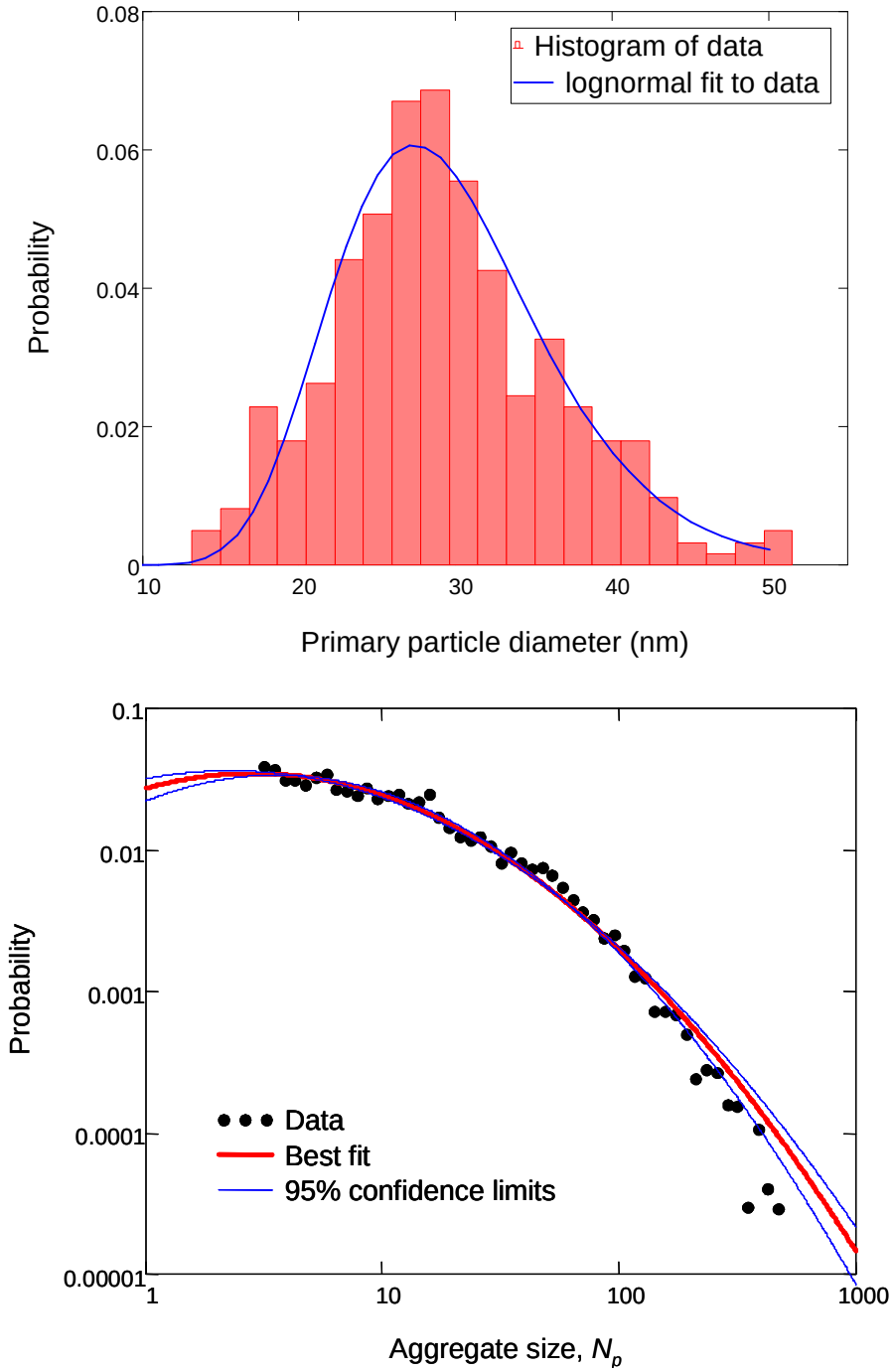

Figure 3-31. Probability distributions of primary particle diameters, d_p (above), and the number of primary particles per aggregate, N_p (below), with a lower cut-off limit of $N_p > 3$, determined from analysis of TEM images and displayed with log-normal fits to the distributions.

Table 3-3. Comparison of ROD and statistical methods for determination of aggregate size distributions from TEM images.

Log-Normal Distribution Parameter	Relative Optical Density (ROD) Method	Statistical Projected Area Method	
		Initial	Final
N_g	31.4	23.2	25.9
$\sigma_{N,g}$	5.08	4.15	4.42

3.5.2. Advances in Numerical Modelling of Polydispersity Effects

The Liu model has become increasingly sophisticated, as it has incorporated shielding effects due to aggregation for monodisperse d_p and monodisperse N_p,[109] polydisperse d_p and monodisperse N_p,[146] monodisperse d_p and polydisperse N_p,[144] and finally polydispersed d_p and N_p.[105] The key findings from the results of this continual development are summarized below. Details of the formulation of the new models can be found in the relevant references.[105, 109, 144, 146] The effects of ambient temperature and pressure were included in the studies.

As prior and some current modelling in the LII community assume isolated primary particles, they ignore shielding and bridging effects that reduce the active surface area available for heat transfer in aggregates. Shielding refers to the surface area of primary particles hidden within the aggregate that is no longer available for heat transfer. Bridging refers to the loss of surface area as primary particles fuse with one another. The reduction in surface area by shielding was estimated by comparing the active surface area (the surface are available for energy transfer) to the total surface area of all primary particles in an aggregate.

3.5.2.1. Monodisperse Primary Particle Diameter and Aggregate Size

The shielding effect was first studied for the simplified case of monodisperse primary particles and monodisperse aggregates, for a range of aggregate sizes. In all cases it was

reported that for the ratio of heat transfer areas of aggregated particles to non-aggregated particles, the shielding effect varied little with N_p for $N_p > 50$. However, it did provide a dramatic reduction in the surface area, as shielding reduced the area by nearly a factor of two for large aggregates. If the reduction in surface area was not accounted for, it would result in an overestimation of the primary particle diameter when using Eq. (13) by an equivalent factor, nearly two for this example. This is a significant finding for measurement of the primary particle diameter with LII.[109]

3.5.2.2. Monodisperse Primary Particle Diameter and Polydisperse Aggregate Sizes

The theory of shielding was advanced by including distributions of the aggregate sizes. The shielding effect not only reduces the heat transfer rate per unit surface area of soot particle but also causes a nonuniform temperature distribution within an aggregate after the laser pulse. When the temperature of soot particles in the laser probe volume is nonuniform, two-colour optical pyrometry provides a weighted average or effective particle temperature. A uniform spatial laser energy profile was considered, so any non-uniformity in soot particle temperature was due to the aggregate size dependent heat conduction process. It was found that the temperature of soot particles in smaller aggregates decays faster than that of particles in larger aggregates due to the shielding effect, which effectively reduces the surface area-to-volume ratio of larger aggregates. The shielding effect is significant for smaller aggregates and becomes progressively less significant for very large aggregates. The peak particle temperature is only slightly dependent on the primary particle diameter d_p and the aggregate size N_p.

When results calculated at low ambient temperature were compared to the results of those calculated for a flame, the difference in temperature history between the large and small aggregates was much more significant, and the peak particle temperature was found to be somewhat sensitive to the aggregate size, with the peak particle temperature increasing slightly with the aggregate size.

The temporal decays of the effective particle temperatures of log-normal distributed aggregates exhibited significant nonlinearity, while the decay curve of the monodisperse aggregates was still quite linear. The much slower decay of the effective particle temperature of the log-normal distributed aggregates was due to the significant

contribution from the tail of the log-normal distribution where the aggregate sizes are very large and their temperatures are much higher, though they have very small distribution probability. Physically, the thermal radiation intensity from the particles in the laser probe volume at later times is dominated by a small number of very hot and very large aggregates. Unlike in the flame case, where an approximation of the mean aggregate size seemed sufficient to estimate the primary particle diameter based on the temporal decay curve of the effective particle temperature, a detailed knowledge of the aggregate size distribution is required for the low ambient temperature case for determining the primary particle diameter using the temporal decay curve of the effective particle temperature.[144]

3.5.2.3. Polydisperse Primary Particle Diameters

This study isolated the effect of the primary soot particle diameter distribution and only considered laminar diffusion flame conditions, where aggregate effects would be minimized. The temperature decay of polydisperse primary soot particles was found to depart from the single exponential behaviour found with monodisperse particles. This departure was found to increase over time with the decay rate gradually decreasing, and for a fixed $\sigma_{d,g}$, the degree of departure from linearity increases with increasing d_g. It was also noted that the experimentally determined initial temperature decay rate can be used unambiguously to obtain the Sauter mean diameter of the soot particle ensemble.[146] Application of a perturbation analysis to this inverse problem demonstrated that recovery of the size distribution was most sensitive to the uncertainty in the thermal accommodation coefficient, and also to measurement noise.[151]

3.5.2.4. Polydisperse Primary Particle Diameters and Aggregate Sizes

The approaches presented above were somewhat idealized, and in response, a strategy that considered both the primary particle diameter and the aggregate size will be polydisperse was reported, and included conduction heat transfer in the transition and continuum regimes as well as the more common free molecular regime. It was reported that neglect of the polydispersity of either the primary particle diameter or the aggregate size leads to overestimate of the temperature decay of the soot particle ensemble. Results indicated that the polydispersity of d_p should in general be taken into account in the calculation of soot particle temperature, while the importance of the polydispersity

of N_p depended on in which regime the heat conduction process had taken place.

The results had significant implications in using time-resolved soot temperature for primary particle diameter sizing: primary particle diameter cannot be adequately retrieved without detailed knowledge of the aggregate size distribution. In practical applications, the aggregate size distribution of the nanoparticles to be sized using time-resolved LII is not known *a priori* and the time-resolved soot temperature alone is insufficient to determine the primary particle diameter.[105]

3.5.2.5. Elevated Pressures

At elevated pressure, the heat conduction between soot particles and the surrounding gas shifts from the free-molecular to the transition regime. Consequently, the rate of conduction heat loss from the soot particles increases significantly with pressure. The lifetime of laser-induced incandescence (LII) signal has been shown to be significantly reduced as the pressure increases.[140, 152-155] The numerical study found that as pressure increases, the soot particle temperature not only decays more rapidly after the peak value but also reaches a lower peak temperature. The significantly reduced peak particle temperature is an indication that laser energy absorption and heat conduction loss occur simultaneously towards the end of the laser pulse. This situation is different from that encountered at atmospheric pressure where laser energy absorption and heat conduction processes can be essentially separately in time.

With increasing pressures, the initial temperature decay rate became increasingly sensitive to the distributions of both d_p and N_p. These results suggest that the LII based particle sizing techniques developed at atmospheric pressure, where heat conduction takes place in the free-molecular regime, become less useful at elevated pressures where heat conduction occurs in the transition regime.[140]

3.5.3. Measuring Distribution Parameters of Primary Soot Particle Diameter

The model for polydisperse primary particle diameters described above was combined with AC-LII to measure d_g and $\sigma_{d,g}$. The model assumed isolated spherical primary soot particles, and thus that non-uniformity in soot particle temperature is due to the distribution of the primary soot particle diameter. The effective temperature used in this

study was

$$T_e = \frac{hc}{k}\left(\frac{1}{\lambda_2} - \frac{1}{\lambda_1}\right) / \ln \frac{\int_1^\infty p(d_p) d_p{}^3 \exp(-hc / k\lambda_1 T) \mathrm{d}d_p}{\int_1^\infty p(d_p) d_p{}^3 \exp(-hc / k\lambda_2 T) \mathrm{d}d_p} \tag{30}$$

where λ_1 and λ_2 are the two wavelengths used for detection and only the distribution of d_p was considered. The effective temperature for the more complete description of requires a double integration over the distributions of both primary particle diameter and the size of aggregates, and is[105]

$$T_\mathrm{e} = \frac{hc}{k}\left(\frac{1}{\lambda_2} - \frac{1}{\lambda_1}\right) / \ln \frac{\int_1^\infty \int_0^\infty p(N_\mathrm{p}) N_\mathrm{p} p(d_\mathrm{p}) d_\mathrm{p}{}^3 \exp(-hc / k\lambda_1 T) \mathrm{d}d_\mathrm{p} \mathrm{d}N_\mathrm{p}}{\int_1^\infty \int_0^\infty p(N_\mathrm{p}) N_\mathrm{p} p(d_\mathrm{p}) d_\mathrm{p}{}^3 \exp(-hc / k\lambda_2 T) \mathrm{d}d_\mathrm{p} \mathrm{d}N_\mathrm{p}} \tag{31}$$

As this study was performed in the LDF, the model assumed free molecular regime conditions. AC-LII was used to provide experimental data for the peak soot particle temperature, T_{max}, and the initial rate of soot particle cooling, dT_e/dt. With these two terms, the Sauter mean diameter d_{32} was determined from a derivation of Eq. (15),

$$\left.\frac{dT_e}{dt}\right|_{t_\mathrm{max}} = -\frac{(T_{max} - T_\delta)}{d_{32}} \frac{3\alpha p_g}{4\rho_s c_s T_\delta} \sqrt{\frac{8kT_\delta}{\pi m_g}} \left(\frac{\gamma^* + 1}{\gamma^* - 1}\right) \tag{32}$$

which is only valid for free-molecular regime.

The procedure was to start with an initial estimate of $\sigma_{d,g}$ typical for soot in a laminar diffusion flame (*i.e.*, $\sigma_{d,g} = 1.2$), then d_g was calculated from $d_{32} = d_g \exp[2.5(ln\sigma_{d,g})^2]$. Once d_g was estimated, then T_e was calculated at a time delayed from the time t_{max} for a range of $\sigma_{d,g}$ values. This calculated value for T_e was matched to the experimental value, which resulted in a new $\sigma_{d,g}$, and then the process was iterated until convergence was obtained. An example from the laminar diffusion flame is shown in Figure 3-32 and Figure 3-33. The resulting distribution parameters for primary particle diameter in the LDF were $d_g = 31.43$ nm and $\sigma_{d,g} = 1.30$.

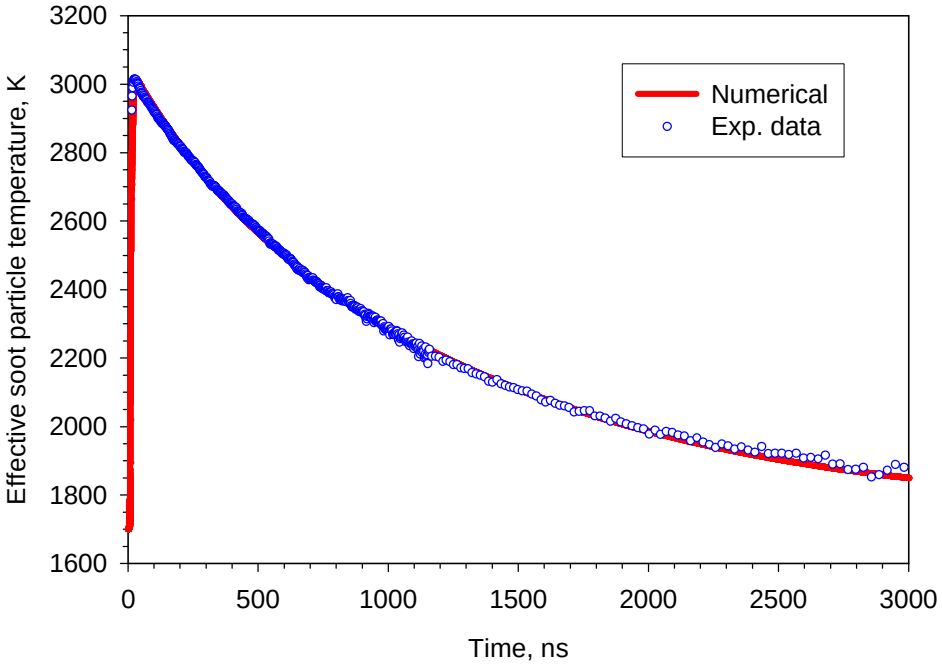

Figure 3-32. Comparison of the predicted effective soot particle temperature with the experimental soot particle temperature in the LDF.

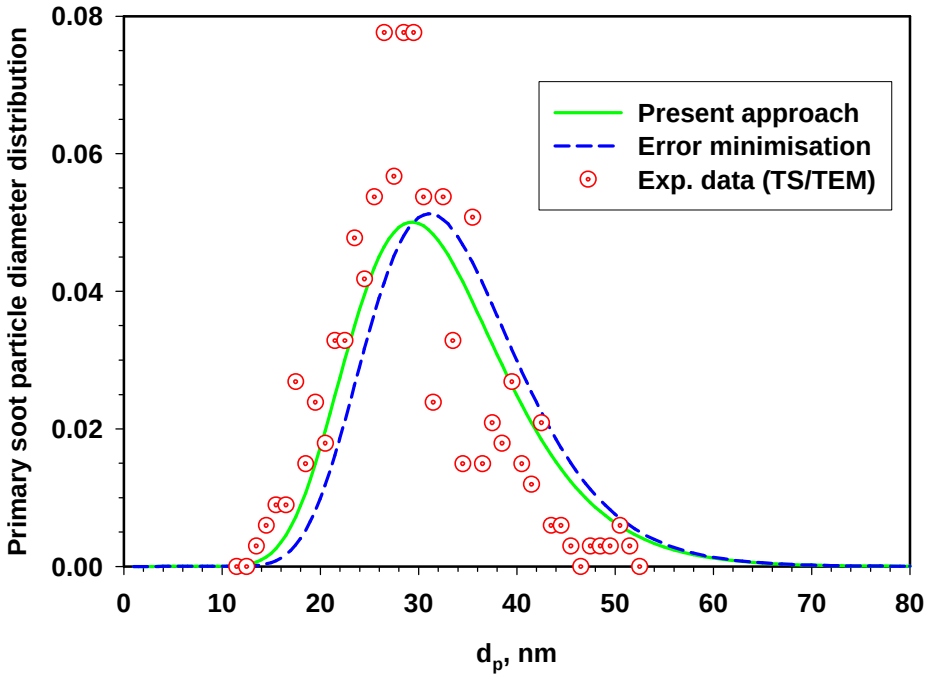

Figure 3-33. Comparison of combined experimental/numerical approach (present), error minimization approach,[146] and TEM data.[133]

The d_p distribution parameters obtained by this approach was similar to and in better agreement with the TEM data than that reached by the error minimization method proposed by Liu et al.[146] This approach was consistent with the multi-variable optimization technique used by Lehre *et al.*,[125] but is simpler and computationally more efficient. The combined AC-LII/numerical modelling approach was shown to resolve log-normal distribution parameters for primary particle diameter in the LDF. However, extension of the method to low ambient temperatures and including aggregate size effects remain topics for further study.

3.5.4. Effect of Aggregate Size Distribution on Soot Volume Fraction

Reimann *et al.*[156] observed that particle size influenced the measurement of soot concentration with LII. With AC-LII, it is possible to determine the time-resolved soot volume fraction, f_V, during the decay of the LII signal. Observation of f_V with time during the decay has shown that it is not constant in all situations. Data acquired in a diesel exhaust and with carbon black remains relatively constant for a period of ~500 ns, whereas the data acquired in a laminar diffusion flame appears to remain constant for the entire decay. This may be due to the fact that the width of the distribution of aggregate sizes is much larger in a diesel exhaust and with carbon black than in a laminar diffusion flame. The laminar diffusion flame has a narrow distribution due to all particles at the same location experiencing the same chemistry and temperatures, whereas the practical applications have high levels of turbulence, ensuring a well-mixed collection of particles.

Over time, the smallest aggregates cool most quickly, and the larger aggregates contribute greater proportion to the LII signal due to their higher relative temperature. Eventually, all particles reach the ambient temperature, and the soot volume fraction returns to its initial value. This is difficult to achieve at low ambient temperatures, as the natural luminosity of the particles is below the detection limit of the LII system.

Results obtained in a laminar diffusion flame with 1700 K initial temperature are shown in Figure 3-34. The effect of small aggregates cooling first was simulated with the Liu model using parameters for the size distribution of aggregates based on data reported by Köylü *et al.*[148] and by Tian *et al.*[133] The theory predicts the correct trend, but the time

and magnitude are not correct. This was due to lack of inclusion of primary particle diameter distribution in the theory, and to the assumption of air properties in the conduction cooling term rather than flame intermediates. Also, the initial period of experimental data showed some evidence of sublimation, which was not ideal for this comparison. Further study is required at a lower fluence level. Nonetheless, there was qualitative agreement between the theory and the experiment, supporting the concept that the variation in f_V during the cooling period was due to the distribution of aggregate sizes.

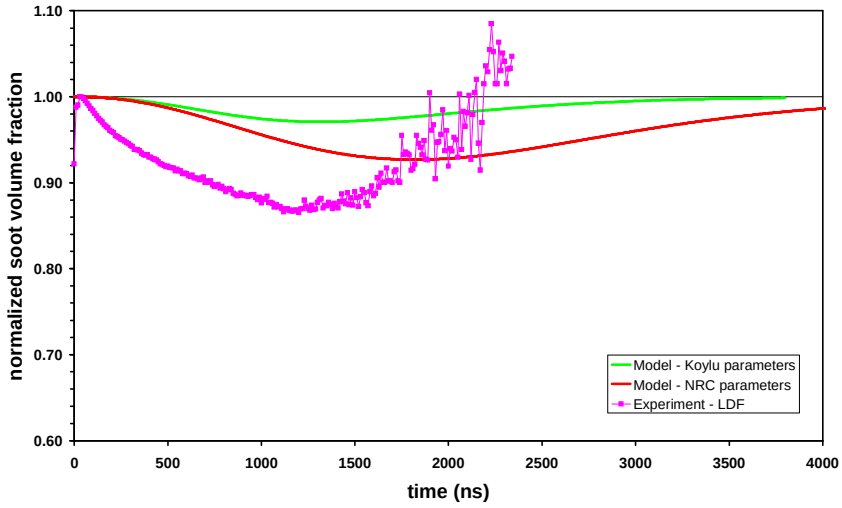

Figure 3-34. Effect of aggregate size distribution on soot volume fraction in a laminar diffusion flame.

This could potentially be used to determine the aggregate size distribution parameters by fitting theory to experimental results. An example applied to carbon black is shown in Figure 3-35, where three different combinations of N_g and $\sigma_{N,g}$ were demonstrated. The data was not used to fit N_g and $\sigma_{N,g}$ in this example.

The carbon black, with wider aggregate size distribution, and at 300 K, showed a marked departure from the initial soot volume fraction, and does not recover before the signal approaches the detection limit around 1000 ns. However, once again the theory predicted the qualitative trends of the experiment. Based on this example, it may be possible to fit the aggregate size distribution parameters from the temporal behaviour of the LII f_V measurement.

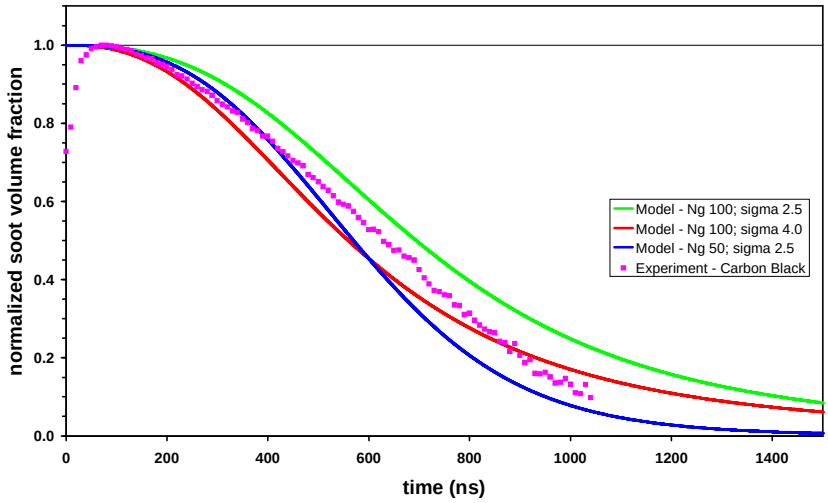

Figure 3-35. Effect of aggregate size distribution on soot volume fraction for carbon black at room temperature.

3.6. IMPROVEMENTS IN KNOWLEDGE OF SOURCES OF SIGNIFICANT UNCERTAINTY

The primary sources of uncertainty in determining the soot concentration and primary particle diameter were acknowledged to be the soot absorption function and the thermal accommodation coefficient, respectively.[34] The soot absorption function was a critical optical property of flame-generated soot that determined the amount of laser energy absorbed by soot, as shown with Eqs. (3)-(5). The large uncertainties have lead some researchers to assume that the laser heating of soot and the subsequent cooling could be separated temporally.[157] However, this approach was not valid since the laser heating of soot and the subsequent cooling occurred simultaneously, especially at elevated pressures. This approximation would not be required if accurate values of the soot absorption function were available. An improved knowledge of the value of the soot absorption function would benefit not only the further development and application of LII, but also soot measurements using laser extinction and soot spectral emission, since the soot absorption function was also required for those techniques. In AC-LII the dominant cooling mechanism was conduction. A key parameter of the conduction model was the thermal accommodation coefficient, as shown with Eq. (15). Much like the soot absorption function, there was great uncertainty in an accurate value for this critical parameter and thus there was a pressing need to determine its value with respect

to the conditions encountered in AC-LII.

3.6.1. Determination of Soot Absorption Function and Accommodation Coefficient

It was known that the peak soot temperature was highly dependent on the soot absorption function, $E(m)$, and that the temperature decay rate was dependent on the thermal accommodation coefficient, α. A combined approach of theoretical analysis and experimental particle temperature measurement was applied to determine $E(m)$ and α. This was done by varying $E(m)$ to fit the experimental maximum temperature observed in a laminar diffusion flame, and by varying α to fit the experimental decay rate.[109]

The peak soot temperature, T_{max}, occurs at a time $t_{\max}$ near the end of the laser pulse when the heat loss rate starts to dominate the laser energy absorption rate as

$$T_{max} \approx T_g + \frac{6\pi E(m) F_0}{\lambda \rho_s c_s} \int_0^{t_{max}} q(t) dt \tag{33}$$

The temporal decay rate of soot temperature is inversely proportional to the active surface area of the aggregate available for heat transfer. After the laser pulse, the soot temperature decay rate is entirely controlled by the heat loss rate of soot aggregates to the surrounding gas, as

$$\frac{\mathrm{d}ln(T - T_g)}{\mathrm{d}t} = -\frac{3k_g \alpha(\gamma + 1)}{2 f \lambda_g \rho_s c_s d_p N_p} \left(\frac{N_p}{f_a} \right)^{1/\varepsilon_a} \tag{34}$$

Results of the analysis using this approach are displayed in Figure 3-36. The illustrated comparison of experimental and numerical effective soot particle temperatures was performed in the LDF. The experimental soot particle temperature was determined assuming a linear variation of $E(m)$ with wavelength. The numerical particle temperatures were calculated for different values of $E(m)$ and α, with a primary particle diameter d_p = 29 nm, a mean number of primary particles per aggregate N_p = 42, and the prefactor and exponent of Brasil et al.[158] was used to simulate the shielding effect upon the heat transfer rate due to aggregation.[109]

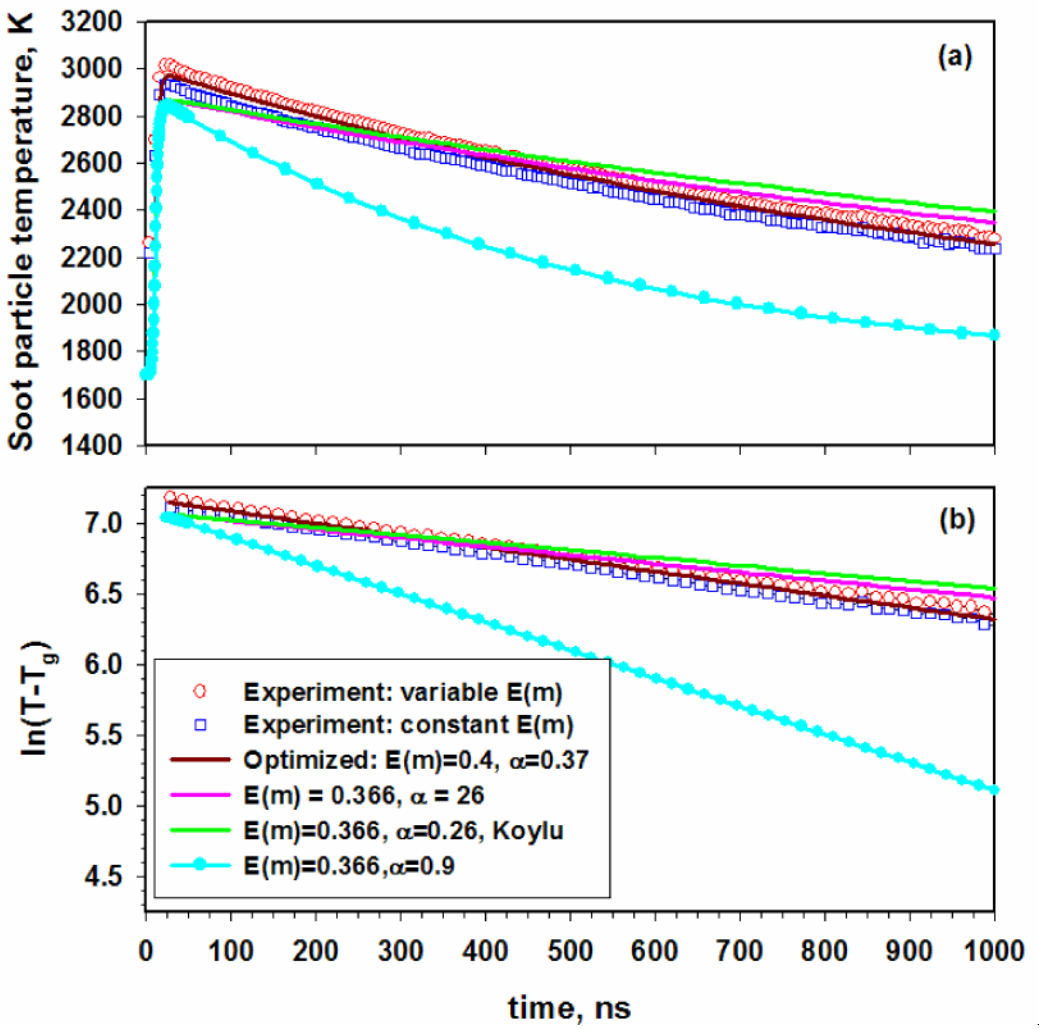

Figure 3-36. Comparison of experimental and numerical effective soot particle temperatures: (a) fit *E*(*m*) to match peak experimental temperature; and (b) fit α to match slope of temperature decay.

For this example, the best fit result was $E(m) = 0.4$ and $\alpha = 0.37$. Note that this was an illustration of use of the technique, and does not suggest that these were necessarily the best values to be used universally for future experiments.

Subsequently, Therssen *et al*. performed low fluence LII measurements at 532 nm and 1064 nm for a range of fluences and peak temperatures, and by matching the data at the two wavelengths, determined that the assumption of constant *E*(*m*) between these wavelengths was valid.[159]

Further investigation was initiated to determine the most appropriate value of the soot absorption function, $E(m)$, to use with AC-LII over a range of wavelengths. The sources of data from the literature were assessed to determine reliable values for $E(m)$ in order to compare them to values derived from LII experiments as described above. It was common to calculate $E(m)$ from the soot refractive index, which is quite uncertain, resulting in large uncertainty in the resulting absorption function.

Although knowledge of the refractive index was a sufficient condition for deriving $E(m)$, it was not a necessary one. There were many direct experimental determinations of the absorption function that resulted from comparison of optical absorption, by measuring attenuation corrected for scattering, with subsequent collection of the soot for gravimetric determination that were far more reliable.[57, 130, 142, 160-162] However, the variation amongst the reported $E(m)$ from these references that have applied the absorption/gravimetric method was typically ±30%. The LII method described above has the further advantages that it was a totally independent measurement that did not require *a priori* knowledge of the particle scattering or the soot density.[109]

This further investigation involved examining the measurement of the experimentally determined peak soot temperature in greater detail. For this experiment a frequency doubled Nd:YAG laser was used for excitation in an AC-LII configuration, and the source of soot remained the centreline position at a 42 mm height in the LDF. The experimental peak soot temperature was estimated by fitting the temperature variation over an interval of 60 ns to an exponential, with starting times of 12 ns and of 30 ns after the peak of the laser pulse. Any difference in temperature between the two would have indicated significant cooling over the short interval between 12 ns and 30 ns. The results are shown in Figure 3-37. As expected, at high fluence where sublimation was occurring, there was a considerable difference between the two soot temperatures at times of 12 ns and 30 ns after the peak of the laser pulse. Also as expected, at low fluence the soot temperatures at the two times were indistinguishable since very little cooling to the ambient gas occurs during the first 30 ns, especially at the high ambient temperatures in the LDF.

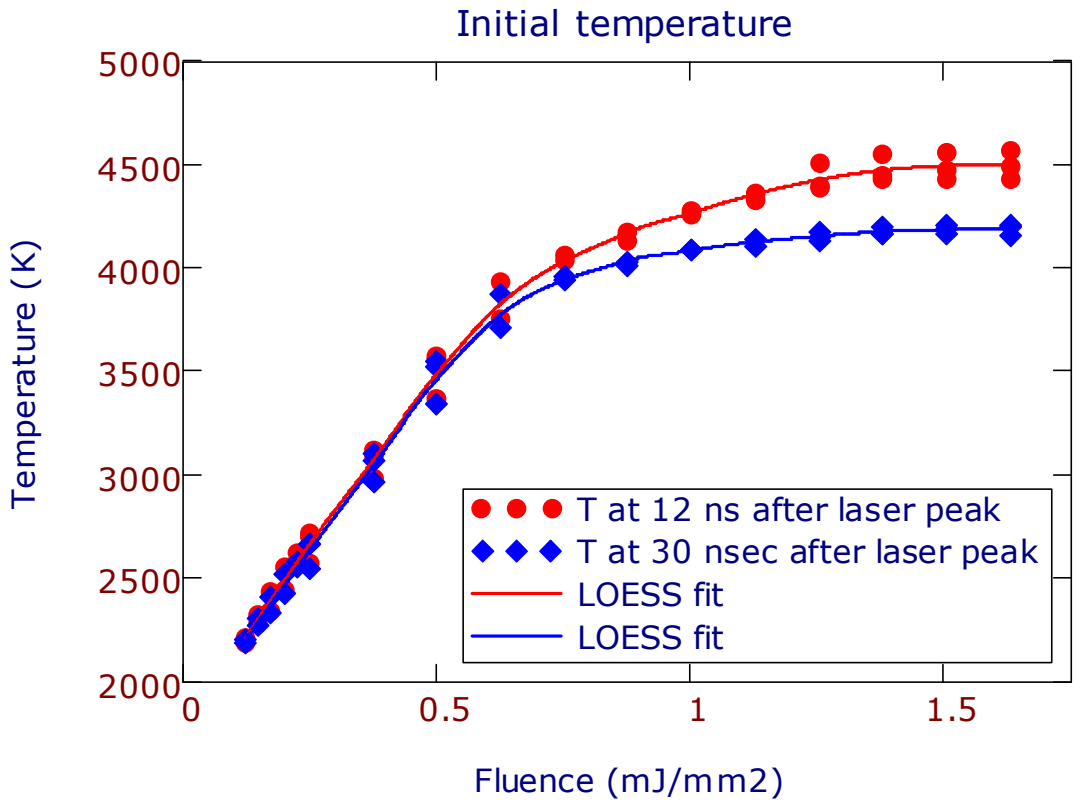

Figure 3-37. Initial temperatures as a function of laser fluence, defined at times 12 ns and 30 ns after the peak of the laser pulse.

As the soot particle temperature was measured before any significant cooling occurred, the following energy balance equation was applied

$$\int_{T_g}^{T_i} \frac{1}{6} c_s(T)\, \rho_s \mathrm{d}T = F_0 \frac{\pi E(m)}{\lambda} \tag{35}$$

where T_i was the initial soot particle temperature after heating, at either 12 ns or 30 ns after the peak of the laser pulse. The soot heating term was integrated from the flame temperature to the observed initial soot particle temperature using temperature dependent specific heats for the soot particle. The soot heating term was equated to the laser energy absorbed, which is the product of the laser fluence, the primary particle cross-section, and the absorption efficiency and is shown in simplified form in Eq. (35).

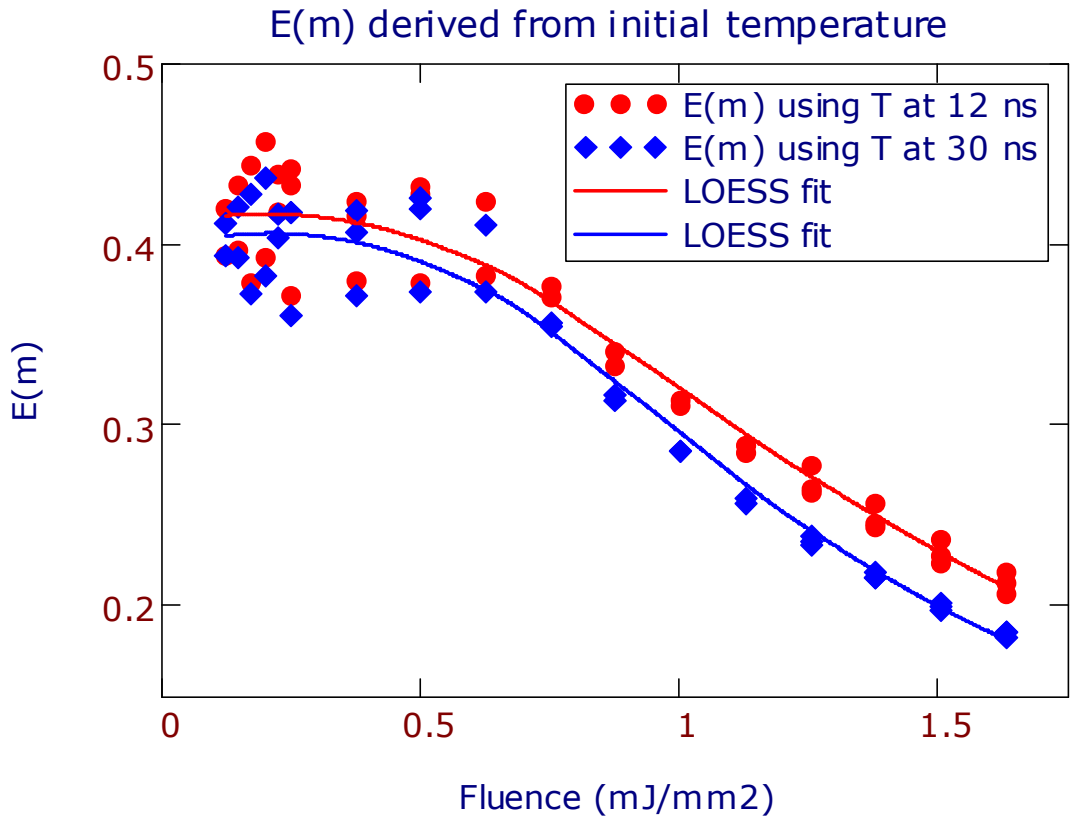

Figure 3-38. *E*(*m*) at 532 nm derived from LII initial temperatures, defined at times 12 ns and at 30 ns after the peak of the laser pulse.

Eq. (35) was then solved with the initial soot particle temperatures displayed in Figure 3-37 to determine $E(m)$. As illustrated in Figure 3-38, at low fluence the difference between $E(m)$ values derived from the initial temperatures at 12 ns and at 30 ns after the laser pulse was negligible, further indicating that very little cooling was occurring during this time interval. The low fluence $E(m)$ values obtained from the temperatures 12 ns after the laser pulse were therefore considered to be reliable estimates of $E(m)$ at 532 nm. Note that there was considerable spread in the data, which reflected the uncertainties in measuring the laser energy, and in calculating the fluence from the measured laser light beam spatial profiles.

The low fluence results for the data derived from the initial soot temperatures at 12 ns after the peak of the laser pulse, up to a fluence of 0.6 mJ/mm^2, were averaged to produce a measurement of $E(m) = 0.41 \pm 0.03$ for the 532 nm wavelength. Similar

experiments could be conducted for other wavelengths, to further determine the relationship between $E(m)$ and wavelength. 1064 nm was an obvious choice, but with the recent data of Therrsen *et al.*[159], it was concluded that such an experiment would be redundant.

It has been convincingly established that careful AC-LII experiments at low fluence under well-controlled conditions can be used to measure unambiguously the soot absorption function so essential to quantitative measurements of soot concentration with LII. A method for determining an effective accommodation coefficient by comparing numerically calculated temperature decays to experimentally determined decays has also been demonstrated. This approach, with further refinement and investigation, showed promise for improving the measurement of primary particle diameter for all forms of time-resolved LII.

3.7. ISSUES WITH AUTOCOMPENSATING LII

An issue that affected all LII measurements, conventional and AC-LII, was discovered during this work. It was the impact of laser fluence on the local medium surrounding the soot particles. The magnitude of the issue and possible solutions were investigated. Despite the advantages presented by AC-LII, deficiencies unique to this technique were uncovered. Two issues that were not resolved despite multiple investigations were a brief period of anomalous cooling immediately following laser heating, which affected the determination of active surface area and primary particle diameter, and a fluence dependence of the measurement of soot volume fraction. The investigations are described in the following sections.

3.7.1. Effect of Laser Fluence on Surrounding Gas

A key element of the LII theory was that one of the dominant cooling mechanisms in LII was conduction to the surrounding gas. A series of detailed experiments in a laminar diffusion flame confirmed this effect and illustrated how the LII process perturbs the medium.

For these experiments, a laser was employed with 1064 nm excitation and a quasi-top-hat beam, and detection was recorded on the 780 nm channel. The probe volume

location was at the standard 42 mm height on centreline in the LDF. 1000 pulse averages were recorded to minimize the noise, and detection at two different gain settings on the photomultiplier was employed in subsequent experiments to maximize the measurement range. The data recorded at high and a low gain were spliced together in post-processing. The background intensity due to the natural luminosity of the flame was subtracted, providing a reference zero condition.

By 8 μs after the laser pulse, the absolute intensities asymptotically reached a range of constant final values for the different laser excitation energies, Figure 3-39. As the laser energy was increased from 1 mJ to 5 mJ, there was a steady increase in the absolute intensities at all times, from the initial signal rise to the final and constant intensity. The 7.5 mJ data had a higher peak intensity (not shown) and then decayed more rapidly due to sublimation, but eventually concluded in a higher final intensity than the 5 mJ data. The 12.5 mJ and 20 mJ data had more pronounced sublimation (not shown) and showed marked decreases in the final intensity.

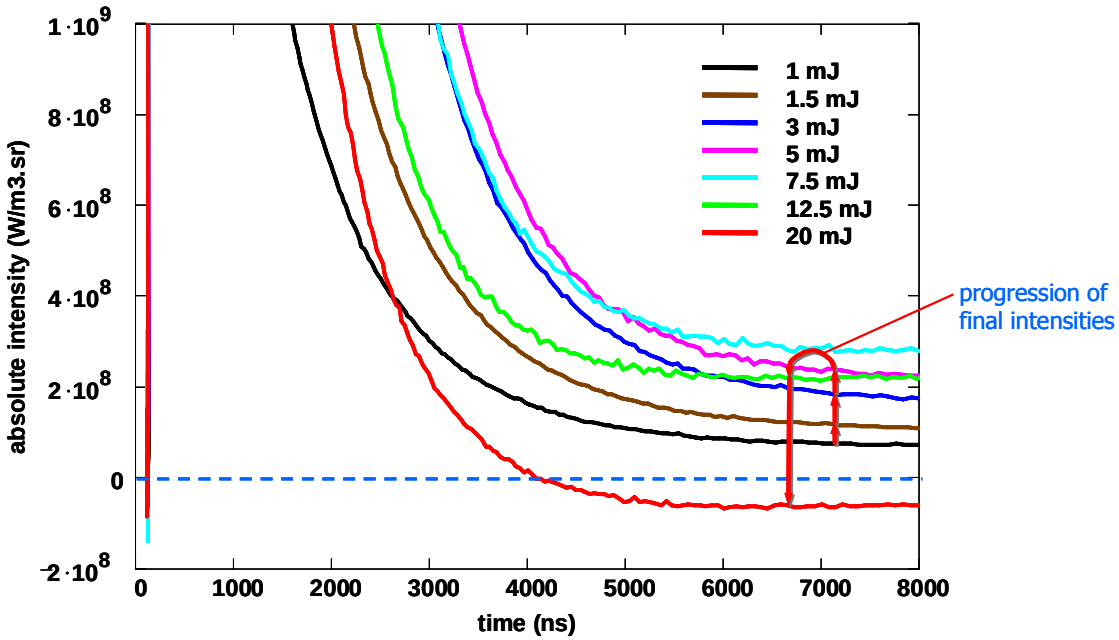

Figure 3-39. Effect of laser fluence on absolute intensity in a laminar diffusion flame.

This behaviour was consistent with soot particles transferring heat to the surrounding

gas, as was demonstrated by the return to different final intensities (and thus different final temperatures) for the 1 mJ to 7.5 mJ data. At the highest energies, the sublimation was so great that even with heating of surrounding gas, the total intensity was less than the initial background radiation from the flame. This was due to sublimation of the soot which reduced the total concentration of particles contributing to signal, thus reducing the total absolute intensity produced by the soot particles.

The laser energy, initially absorbed by the soot, appeared as local gas heating once local thermal equilibrium was established. When the product of the absorbed fluence and soot concentration was sufficiently high, then this heating was significant. The local heating was not dissipated during the time scale of LII cooling, on the order of one to several microseconds, and had to be accounted for when measured soot cooling rates were interpreted.

As a result of this initial study, a more detailed investigation was undertaken with AC-LII. The steps were to develop a theoretical prediction of the local gas heating, compare it to measurements, develop a correction for local gas heating, demonstrate the necessity of applying this correction to measured soot cooling rate data, and compare the corrected cooling rate data to theoretical predictions.

For the predicted local gas heating, the laser energy absorbed per unit volume by the soot particles was the product of the primary particle absorption cross-section, $\pi d_p^2/4$, the absorption efficiency, $4\pi d_p E(m)/\lambda$, the laser fluence, F_0, and the number density of primary particles, $6f_V/\pi d_p^3$. The temperature rise in the gas due to laser heating, ΔT was then given by equating the energy absorbed by the soot particles to the change in the volumetric heat capacity of the surrounding gas, as

$$\int_{T_g}^{T_g+\Delta T} \frac{c_V(T)\, p_g\, m_g}{RT}\,\mathrm{d}T = \frac{F_0\, 6\pi E(m)\, f_V}{\lambda} \tag{36}$$

where the volumetric heat capacity of the surrounding gas was $c_{Vvol} = c_V p_g m_g/RT_g$, c_V was the temperature-dependent heat capacity of the gas (assumed to be air) defined per unit mass, m_g was the molecular weight of air (taken as 28.96 g/mole), p_g was the gas pressure, R was the universal gas constant and T_g was the gas temperature. This resulted

in a calculated heating coefficient of 77 K/(ppm_{soot}mJ/mm^2). This was predicted to produce a nearly 300K increase in the ambient gas temperature in the LDF for a soot concentration of 4.0 ppm and a laser fluence of 1.0 mJ/mm^2, as shown in Figure 3-40.

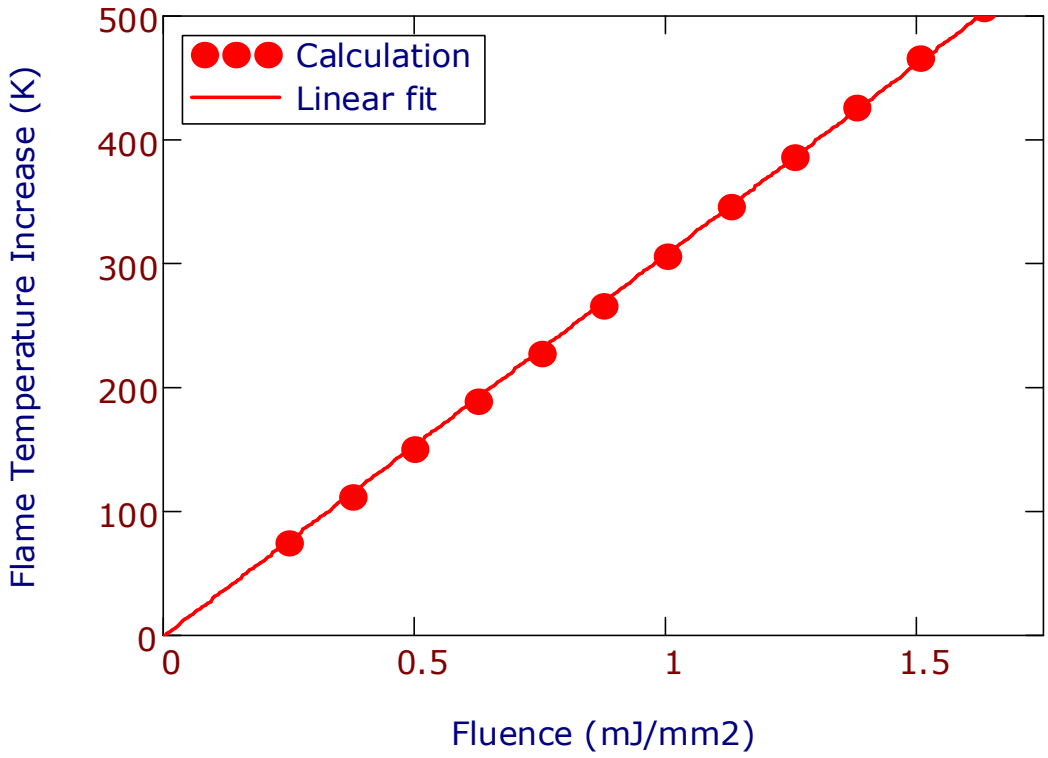

Figure 3-40. The temperature rise of the flame due to laser heating as a function of laser fluence in the LDF for a concentration of 4.0 ppm.

Experimental temperatures for comparison were obtained from measurements that were performed in the laminar diffusion flame at the standard centreline location at a height of 42 mm. As noted earlier, the CARS temperature at this location was 1730±25 K. For this experiment a frequency doubled Nd:YAG laser was used for excitation in an AC-LII configuration. The soot absorption function, $E(m)$ at the laser wavelength of 532 nm was 0.41 and the measured soot volume fraction was 4.0 ppm. The AC-LII temperature decay was fit to an exponential and the final temperature was derived from the asymptotic value. As mentioned above, the measurement of the experimental decays require a large AC-LII intensity dynamic range and necessitated assembling data acquired at more than one gain level on the photomultipliers. Examples of the resulting measurements are shown in Figure 3-41 for a low and a moderate-to-high fluence. In

the low fluence case, the asymptotic final temperature was 1780 K, only slightly above the initial flame temperature. However, even for a moderate fluence level, the asymptotic final temperature was 2140 K, over 400 K above the initial flame temperature, a significant level of heating to the local gas.

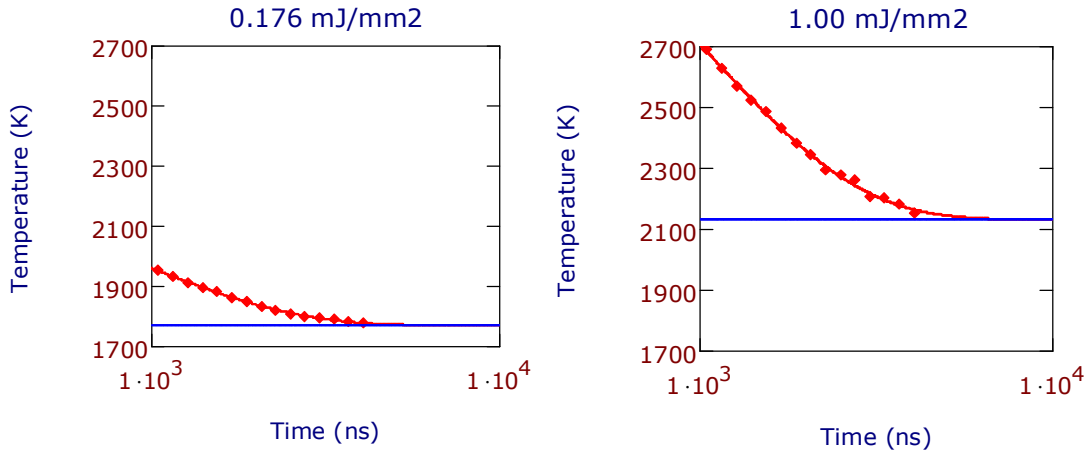

Figure 3-41. Tail of experimental temperature decays asymptotically approaching local gas temperature for low (left) and moderate (right) fluences.

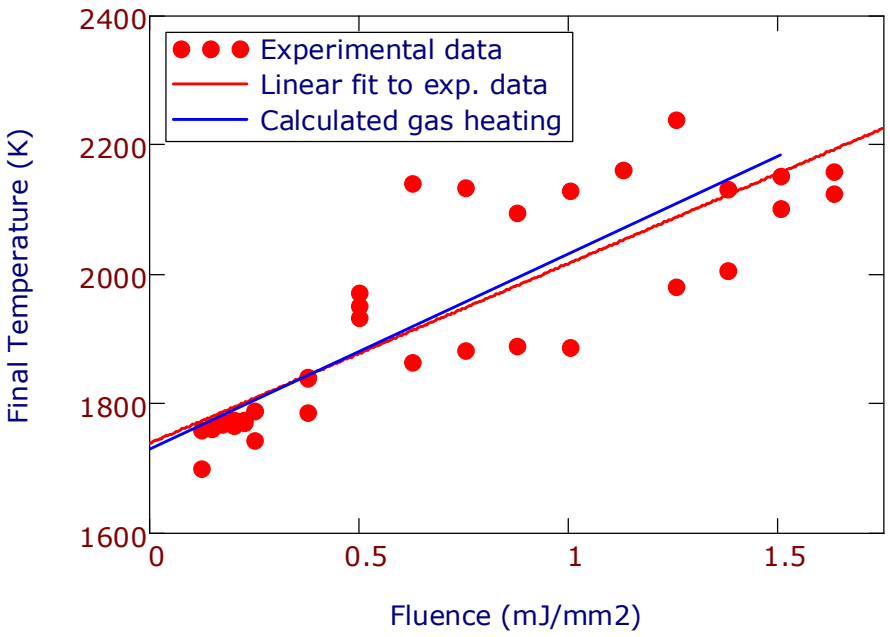

Figure 3-42. Comparison of predicted to observed local gas temperature.

These experiments were repeated for a wide range of low, moderate, and high fluences

from 0.1 to 1.7 mJ/mm^2. The asymptotic final temperatures that resulted from these experiments are shown in Figure 3-42. The least-mean-squares fit to this experimental data closely matched the prediction based on Eq. (36). Despite the scatter in the results, the agreement between the predicted and experimental final temperatures was unexpectedly good, especially in consideration of the assumptions inherent in the predicted values. The impact of the change in final gas temperature on the soot cooling rates will be examined in Section 3.7.2.

The observed local gas heating was in agreement with theoretical predictions, as the increases in final intensity were supported by model results for the final temperature as a function of laser fluence. This issue is unlikely to be relevant to applications where the particles are in a gas at much lower temperature, such as in a diesel exhaust, where there is no contribution from natural luminosity. However, this exercise does demonstrate that LII perturbs the medium, and that there may be cases where this effect must be considered.

3.7.2. Anomalous Cooling

Closer examination of the initial cooling rates, such as those shown in Figure 3-22, revealed that the initial decay rate for the moderate to high fluence data was less pronounced than was expected from models of cooling due to sublimation, shown in Figure 3-3. For example, the numerical results from the Liu model showed a drop of ~1000 K, from ~4500 K to ~3500 K over the first 50 ns after the peak of the laser pulse at the high fluence condition. However, the experimental results in Figure 3-22 only decreased from 4423 K to 3968 K over the same interval, a drop of 455 K, less than half of the model prediction. This anomalous cooling warranted further investigation.

For this study, experimental temperatures were obtained from measurements that were performed in the laminar diffusion flame at the standard centreline location at a height of 42 mm and the temperature obtained with CARS at this location was 1730±25 K. A frequency doubled Nd:YAG laser operating at 532 nm was used for excitation in this experiment in an AC-LII configuration, and the lower wavelength detector was fit with an interference filter centred at 450 nm with a bandwidth of 62 nm FWHM. The soot absorption function, was considered constant over the visible and near-infrared

wavelength range.

The cooling rates for the soot particles were modelled for comparison to the experimental data. The numeric calculations are based on the Liu model and include sublimation.[163] Primary particle diameter and aggregate size effects on the cooling rate were modelled with integration over distributions of both, which were assumed to be lognormal, with data from TEM analysis reported in Section 3.5.1. The gas composition and properties in the flame were taken from a numerical simulation of the ethylene-air laminar diffusion flame which included detailed gas-phase reaction mechanism and complex thermal and transport properties.[164]

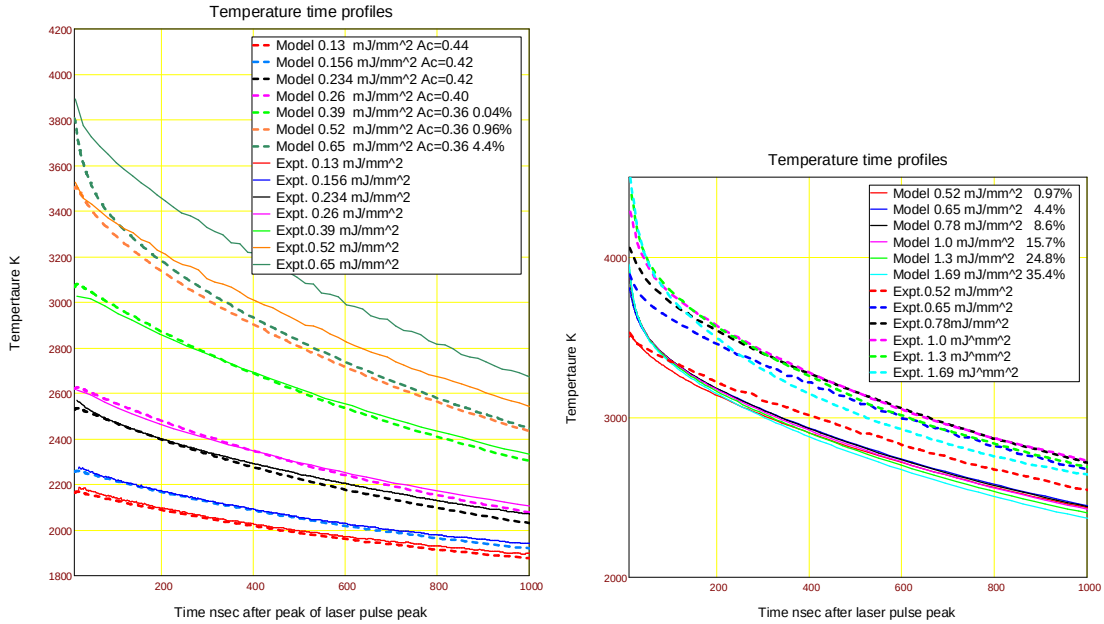

Figure 3-43. Experimental and numerical soot particle temperature decays for low to moderate fluences (left) and moderate to high fluences (right).

A comparison of the experimental and numerical results for a wide range of fluences is shown in Figure 3-43. For the numeric calculations $E(m)$ at the laser wavelength of 532 nm was 0.4, which provided a good prediction of the initial soot temperature results from the low to moderate fluence experiments. The model prediction of the fraction of soot removed due to sublimation was calculated and is shown in Figure 3-43 for the cases where the quantity was non-negligible. The thermal accommodation coefficient was a fit parameter for the low to moderate fluence numeric calculations, and was found

to drop from $\alpha = 0.44$ to $\alpha = 0.36$ with increasing laser fluence and initial soot particle temperature. It was postulated that this could be due to the fact that the vibrational degrees of freedom that would contribute to heat capacity with increasing temperature were less effective than the translational degrees of freedom were in cooling the soot particles.

The low fluence data was well-described by the model for the first 1000 ns of the temperature decay. However, as sublimation became non-negligible at higher fluences, the model and experiment began to diverge, as displayed in Figure 3-43, and the model seriously underestimates the experimental temperature decay. However, the rates of decay appeared similar beyond the first 100 ns after the peak of the laser pulse, and it was only in the first 100 ns that the anomalous cooling behaviour occurred. The data were reanalyzed to investigate the cooling rates as a function of the soot particle temperature. The experimental cooling rate results, shown in Figure 3-44, displayed a discontinuity between the low fluence data and the high fluence data. Within each of the two groups of data, the cooling rates were remarkably similar, except for the initial cooling rate for the low fluence data. However, once below temperatures where sublimation was known to occur (< 3200 K), the cooling rates for high fluence and low fluence experiments were expected to agree.

The difference was hypothesized to be due to the local heating of the surrounding gas in high fluence LII, discussed in Section 3.7.1. The local gas heating was calculated with the simple model in Eq. (36) and this was applied as a correction to the flame temperature. The experimental data for cooling rates was re-evaluated as a function of the difference between the soot particle temperature and the corrected local gas temperature, as shown in Figure 3-45.

This resulted in cooling rates for the high fluence data that were consistent with those for low fluence data at temperatures below the sublimation threshold. Inspection of Figure 3-45 showed that at low fluence there was a period of anomalous cooling before the cooling rates converged. The high fluence cooling rates diverged with this approach, which was likely due to increasing errors in the assumptions of the simple model of gas heating that was used.

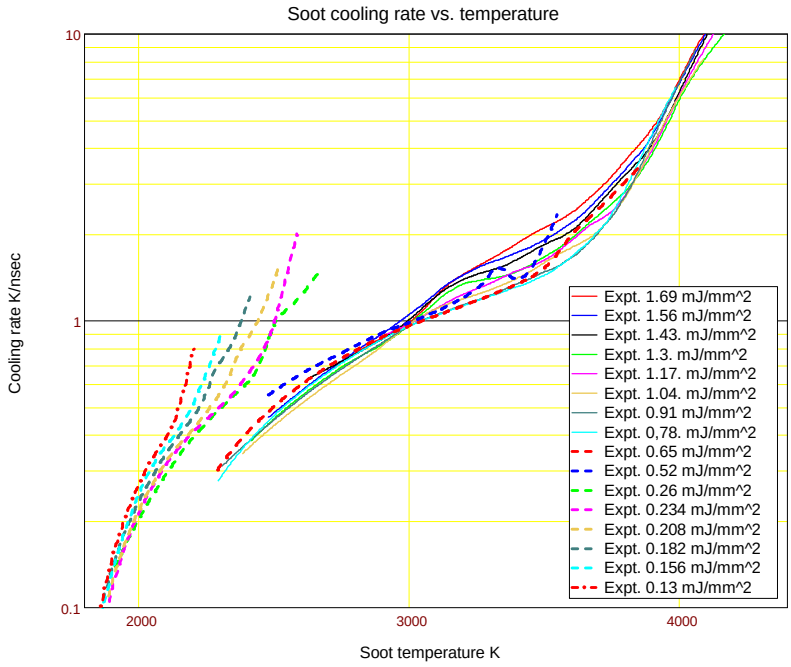

Figure 3-44. Experimental soot particle temperature cooling rate results for a broad range of fluences encompassing low to high fluence LII, as a function of the soot temperature.

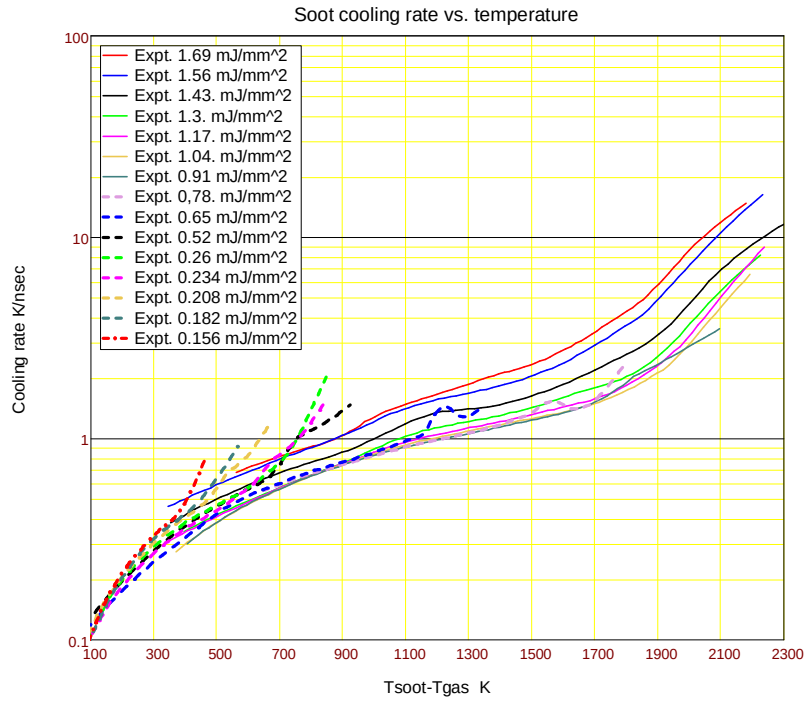

Figure 3-45. Experimental soot particle temperature cooling rate results as a function of the difference between soot temperature and corrected local gas temperature.

For instance, at high fluences where a large fraction of the soot was removed through sublimation, there would be chemical energy transferred to the carbon sublimation species which was not accounted for by the local gas heating model.

The Liu model was applied in order to compare the predictions of soot particle cooling rate to the experimental measurements, and the results are shown in Figure 3-46. There was good agreement between the experimental results and the model predictions in the regime dominated by heat conduction to the surrounding gas. The close agreement between the model results in the range 500 K < $T - T_g$ < 900 K indicated that aggregate size effects on the cooling rate are small, as the assumptions used in the aggregate model became less valid for moderate to high fluences. However, this may have been due to the relatively small aggregates in this flame at 1730 K, and may be different for larger aggregates and lower ambient temperatures, such as those found in particulate emissions from engines.

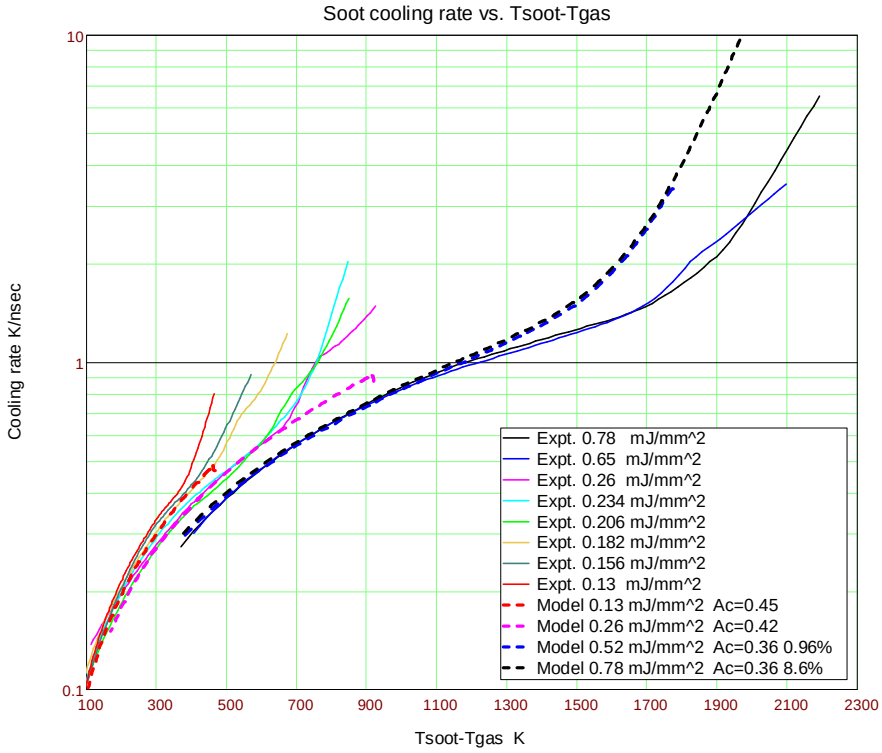

Figure 3-46. Comparison of model and experimental soot particle temperature cooling rate results as a function of the difference between soot temperature and corrected local gas temperature.

The anomalous cooling behaviour at all fluences is apparent. Furthermore, the model vastly overpredicts the soot particle cooling rate in the sublimation regime, with predicted cooling rates that were as much as 4 times greater than the observed cooling rates. This was not due to experimental limitations, as the most rapid signal decay observed had a time constant of ~ 35 ns, over 40 times the measured photomultiplier response time of 1.8 ns. A possible cause for the failure of the model predictions in the evaporative regime was the neglect of gas-dynamic effects of sublimation species.[165] For instance, pulsed heating of macroscopic targets indicated the sublimation species that left the surface with a high velocity normal to the surface reached a Boltzman equilibrium in as little as three collisions, then the initial sublimation species momentum was converted to a gas dynamic expansion, and with sufficient sublimation flux a shock front formed close to the surface.[165] Compared to the Liu model this would have resulted in a reduced cooling rate and an eventual return of sublimation species to the surface.

Further research was required to discover the mechanism(s) responsible for the anomalous cooling and the overprediction of the sublimation cooling rates, but was not attempted as part of this work.

3.7.3. Variation in Measured Concentration with Laser Fluence

Low fluence LII measurements in the LDF reported the a soot concentration that was independent from fluence over the range 0.8 to 1.6 mJ/mm^2 with the Mobile II AC-LII system operating with a 1064 nm excitation laser. Initially, it was assumed that measurements in this range would be accurate for all applications. However, it was discovered that the independence from fluence was not valid for all situations. This was first observed in measuring the particulate emissions from a diesel engine, and was dramatic in that the reported soot concentrations varied from a factor of ~ 6 from the lowest fluence to moderate fluence where the effects of sublimation began to interfere. The effect was a positive one, with the measured concentration increasing as fluence increased up to the sublimation threshold, as shown in Figure 3-47.

To investigate further, a reliable steady source of particulates a low ambient temperature was required. An inverted flame burner[166] was designed and implemented to provide

such a source. This burner was demonstrated to produce soot with soot insignificant quantities of condensed volatiles, and thus it eliminated the presence of volatiles in the diesel exhaust as a possible source for the dependence of the measured AC-LII soot concentration on fluence.[166] Detailed AC-LII measurements were performed on particulates sampled from the exhaust of this burner.

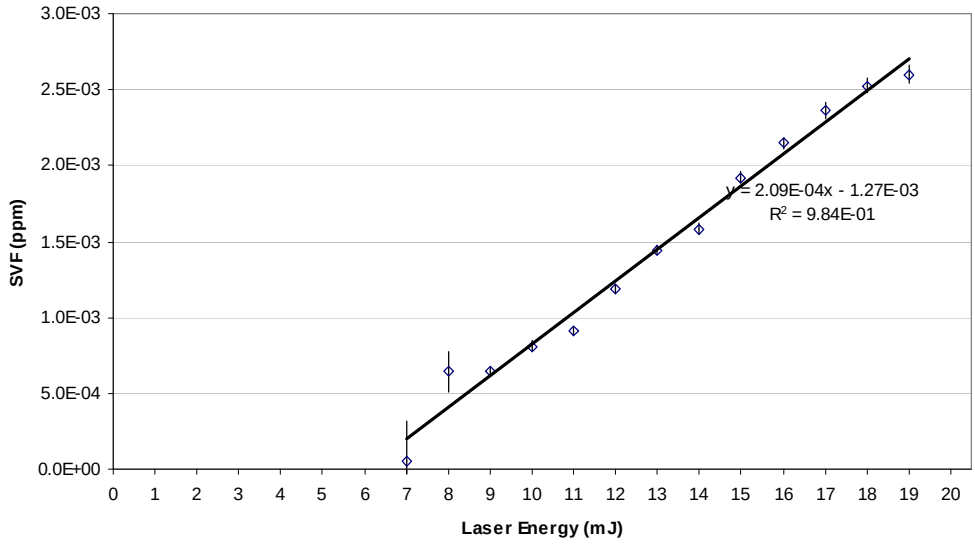

Figure 3-47. Variation in measured soot concentration from a heavy duty diesel engine as a function of the laser fluence, recorded with the LII 200 instrument.

The results shown in Figure 3-48 were obtained with the Artium LII 200 instrument, which demonstrate that the effect was real and reproducible. The horizontal error bars in Figure 3-48 represent the uncertainty in measuring the laser energy, and the vertical error bars represented a single standard deviation of the single shot LII measurements of concentration. The peak temperatures for these measurements are shown in Figure 3-49. These peak temperatures demonstrated the expected behaviour, increasing with fluence up to the sublimation threshold and then asymptotically reaching a plateau. The vertical error bars represent a single standard deviation of temperature.

The data obtained from the inverted flame burner confirmed the results obtained earlier in the diesel engine particulate matter emissions, and it indicated that the presence of volatile species in the diesel exhaust was not a contributing factor.

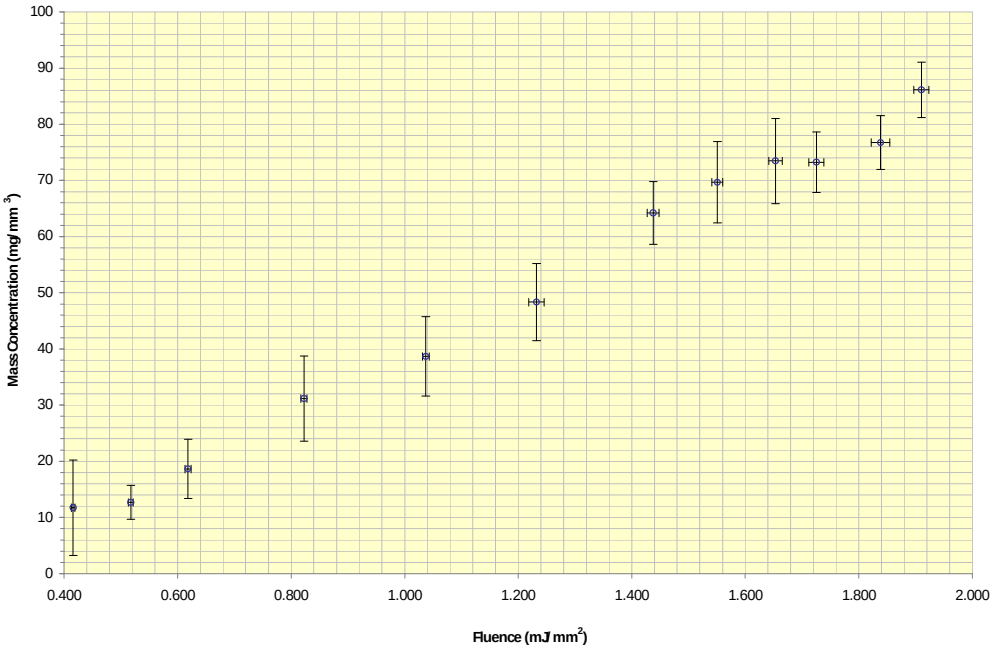

Figure 3-48. Soot concentration as measured with AC-LII in a constant source of low temperature soot as a function of laser fluence.

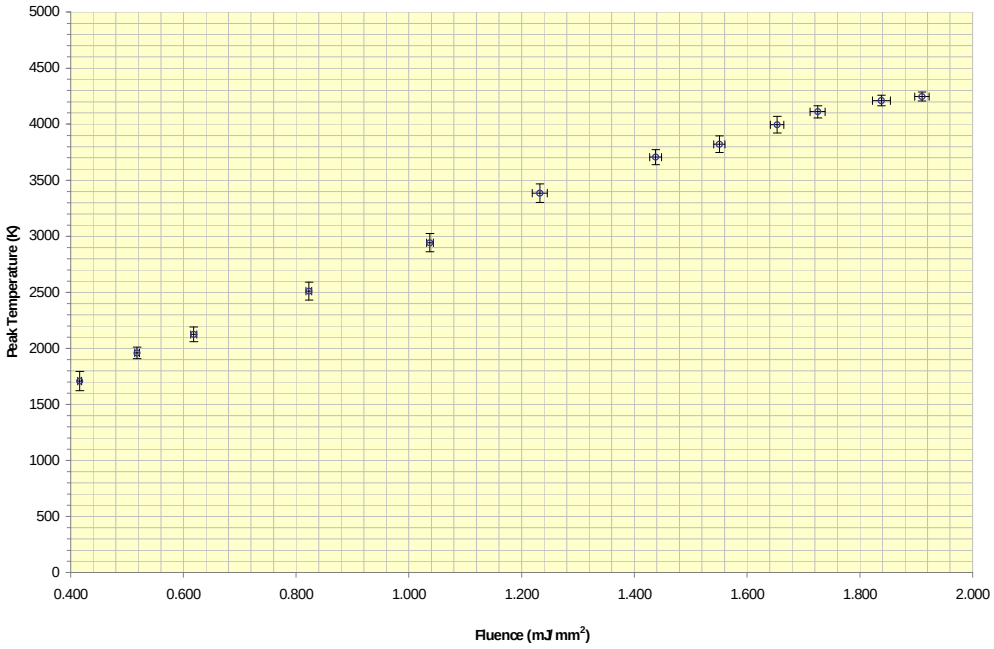

Figure 3-49. Peak soot particle temperatures as measured with AC-LII in a constant source of low temperature soot as a function of laser fluence.

It was important to identify a reason for the difference between the measurements performed in a flame and those performed at low ambient temperatures. Possible issues related to the calibration or performance of the experimental instrument were ruled out through detailed examination of the performance of the components. Further research was required to discover the mechanism responsible for the variation of measured concentration as a function of fluence, but was not attempted as part of this work. Several possible causes for this behaviour were postulated, including

(a) a change in $E(m)$ due to the pulsed laser itself that does not occur with soot measured at flame temperatures *in situ* in the LDF due to the increased degree of heating required for soot particles at low ambient temperatures

(b) a change in $E(m)$ due to the cooling process for mature soot that does not occur with soot measured *in situ* in the LDF

(c) a change in $E(m)$ due to the presence of coatings, possibly condensed volatiles (despite the findings of Stipe *et al.*[166]) or water

(d) severe agglomeration of the soot aggregate particles while cooling, such that the Rayleigh-Debye-Gans assumption is far from valid

(e) coupled with (d) above, explosion of the particles into smaller fragments at higher laser fluences, as found in Beyer *et al.*[79]

(f) surface effects due to exhaust lines, hoses, etc.

(g) other sampling effects due to dilution, sample transit time, etc.

The above list was not exhaustive, but did indicate the complexity of the issue. Possible experiments conceived for future work to address (a) and (b) above included: monitoring the attenuation through the sample volume with a continuous line-of-sight optical attenuation experiment before, during, and after heating the particles in the sample volume with a pulsed laser for a range of fluences; and applying a double-pulse laser in a pump-probe configuration to study the effect of preheating the particles on the subsequent AC-LII signal for a range of fluences for each of the pump and probe lasers.

As a valid explanation for this variation in soot concentration measurement was not discovered, it was recommended that measurements of soot concentration with AC-LII should be performed at moderate fluence, such that the peak temperature was just below the sublimation threshold. This produced the maximum soot concentration, which was shown to have the best agreement with measurements of concentration performed with other techniques, discussed in Sections 5 and 6.

3.8. HIGH SENSITIVITY LII

The race towards cleaner engines, including the introduction of diesel particulate filters (DPFs) on diesel engines and the advent of low temperature combustion (LTC) technologies such as homogeneous charge compression ignition (HCCI), resulted in soot levels dramatically lower than they were a decade ago. Also, with the knowledge that black carbon (BC) is a significant contributor to global warming, environmentalists were demanding the ability to measure black carbon in the atmosphere at levels dramatically lower than those found in the emissions from the production of energy with fossil fuels. These requirements led to the need to develop LII systems that were orders of magnitude more sensitive than Mobile II, which had a detection limit of 5 ppt (~ 10 $\mu g/m^3$). The target for this task was to improve the overall sensitivity of the AC-LII technique by two orders of magnitude, to a new detection limit of 0.05 ppt, which is approximately equivalent to 0.1 $\mu g/m^3$ or 100 ng/m^3, which is a 100-fold improvement in sensitivity over the Mobile II AC-LII system. This needed to be accomplished while maintaining the low fluence and two-colour pyrometry features of auto-compensating laser induced incandescence, and the system needed to be portable/mobile so that demonstration field measurements could be performed.

The design approach involved assessing all aspects of the AC-LII instrument, including the laser and beam generation optics, the sampling cell, the receiver collection optics, the receiver filters and dichroics, the photodetectors, the signal detection and digitization electronics, and the signal analysis software. The high sensitivity laser-induced incandescence (HS-LII) system incorporated many changes relative to the Mobile II AC-LII system, while retaining the essential feature of low fluence two-colour LII.

For signal generation, the concept was to generate an LII signal over the largest possible volume that could be detected with the receiver. For any given concentration, this would maximize the incandescent signal generated. The Big Sky Ultra CFR Nd:YAG laser (50 mJ/pulse @ 1064 nm) used on Mobile II was replaced with a Big Sky CFR 200 Nd:YAG laser (200 mJ/pulse @ 1064 nm). This allowed creation of a laser light beam 4 times larger in cross-sectional area while maintaining the same fluence, due to the greater energy of the CFR 200 laser. For beam shaping, the rectangular aperture and single lens relay imaging used with Mobile II to create a uniform beam profile at the probe volume of ~3 x 5 mm (15 mm^2) in cross-section was abandoned. With HS-LII a taller laser sheet was desired in the probe volume and the layout was constrained to be compact for portability. Instead of the relay imaging approach, a mix of cylindrical and spherical lenses was used to create a collimated sheet with a quasi-top-hat profile. This laser light sheet overfilled a rectangular slit aperture, which trimmed this laser sheet to a cross-section of 2 mm wide by 28 mm tall (56 mm^2) just before the laser beam entered the sample cell.

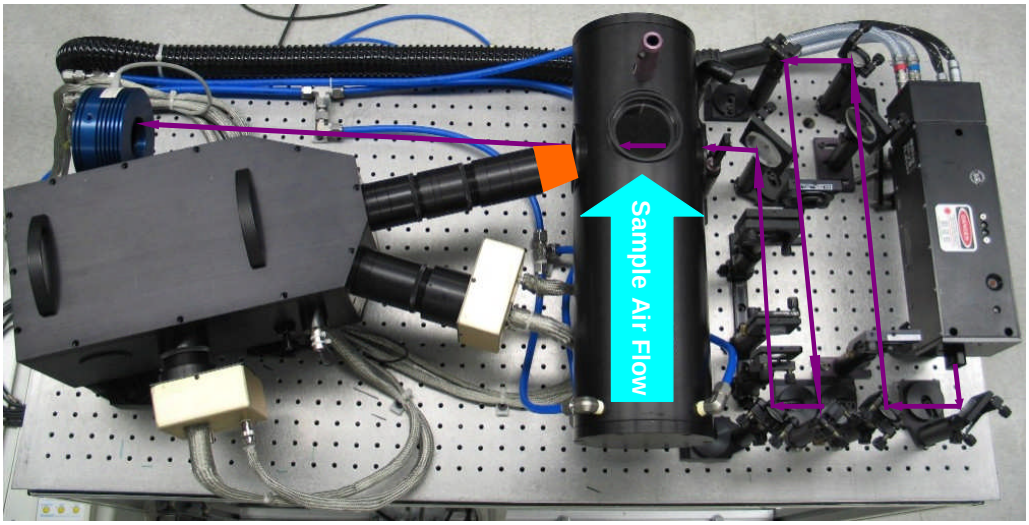

Figure 3-50. Optical layout of high sensitivity system (HS-LII). The path of the laser beam is indicated by the violet line, the orange region indicates the incandescence collected by the receiver, and the blue arrow indicates the direction of the sample air flow in the sample cell.

The sample cell was also designed to maximize the probe volume for LII signal generation. It was created with a 100 mm diameter flow path and with flow

straighteners to ensure plug flow and uniform distribution of the particulates. Sample air or exhaust was drawn through the sample cell with a vacuum pump. The sample flow rate and laser repetition rate were set to ensure that a fresh sample was in the probe volume for each laser pulse. The configuration of the beam generation optics, sample cell, and optical receiver is shown in Figure 3-50.

The fundamental principal used in the receiver design was to use the Lagrangian Invariant principle to constrain design of collection optics and receiver, as preservation of this property is essential for a lossless optical system. Briefly, this principle states that L, the minimum product of numeric aperture, NA, and aperture diameter, $2r$, cannot be improved upon:

$$L = NA_1 \times 2r_1 = NA_2 \times 2r_2 = \text{constant} \tag{37}$$

where the numeric subscripts simply refer to different elements in the optical path.

The probe volume diameter was based on the maximum practical Lagrangian invariant of receiver optical system, and was limited by the divergence of the collimated incandescent light through the optical paths in the receiver. An 8 mm aperture was used in the collection optics path and 1:2 demagnification by paired collection lenses was used to create a 16 mm diameter region imaged at the probe volume. The crossing angle between laser sheet and the receiver collection axis was minimized in order to maximize the length of the signal generation region in the direction of propagation of the laser light beam. However, this angle was constrained by practicality, as an angle of 15° with an *f*/4 imaging lens just allowed the laser beam to pass by the collection optics without entering the receiver. This resulted in a probe volume that was elliptical in shape, 50 mm long by 16 mm tall, and 2 mm deep.The HS-LII receiver, shown in Figure 3-51, was designed with interference filters that were 50 mm diameter, an improvement over the 25 mm diameter filters used in the Mobile II system. To further improve light throughput, larger bandwidth interference filters were used, with a 50 nm bandwidth on the high wavelength channel and a 60 nm bandwidth on the low wavelength channel. Additionally, to increase the signal levels collected, the centre wavelength of the lower wavelength “blue” channel was increased from 397 nm on Mobile II to 445 nm on HS-LII. At 2500 K, this results in more than doubling the soot

particle spectral radiance emission, as shown in Figure 3-10. For the higher wavelength "red" channel, the centre wavelength was decreased from 782 nm on Mobile II to 753 nm on HS-LII to better fit the optimum quantum efficiency of the photomultiplier tubes that were used with the HS-LII system. Interference filters with > 90% transmission over the desired bandpass and blocking at other wavelengths from 300-1100nm from Semrock, plus a dichroic with > 90% transmission/reflectance at the desired wavelengths, were used. The relative transmission of interference bandpass filters which demonstrated higher throughput in HS-LII in comparison to Mobile II is shown in Figure 3-52.

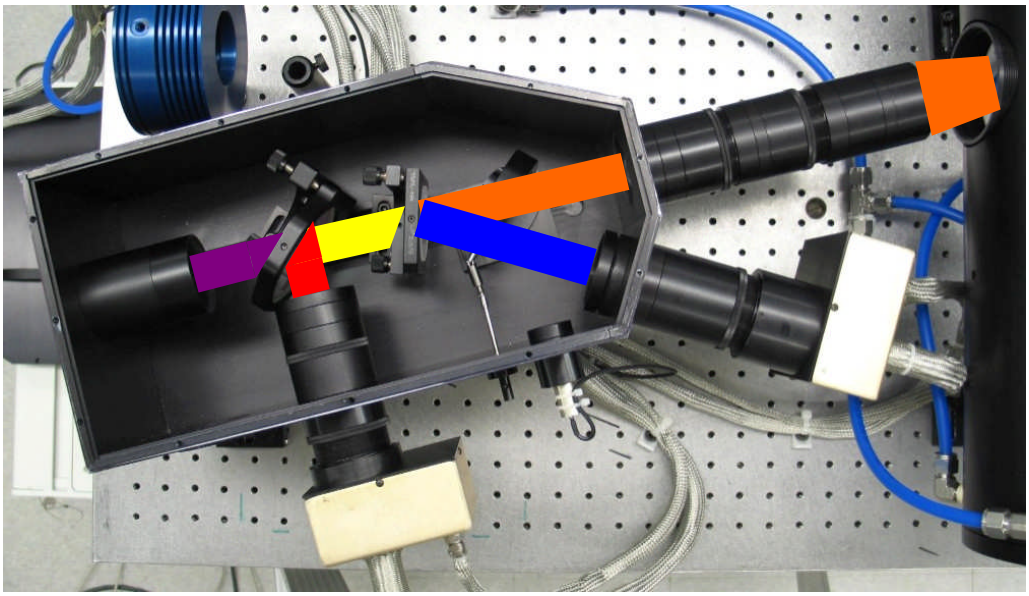

Figure 3-51. Optical path through high sensitivity receiver. Incandescent radiation indicated by orange, radiation reflected towards 450 nm detector in blue, radiation reflected towards 750 nm detector in red, and violet indicating longer wavelength incandescence plus scattered laser radiation entering beam dump.

New Hamamatsu large area PMTs were used, with a model R1924A on the 445 nm channel and a R5900U-20 on the 753 nm channel. These had an active area of more than 18 mm diameter, in comparison to the 8 mm diameter photomultipliers used on Mobile II. With progress in the optoelectronics field, new photocathode materials with equal or greater cathode radiant sensitivity were selected, as shown in Figure 3-53.

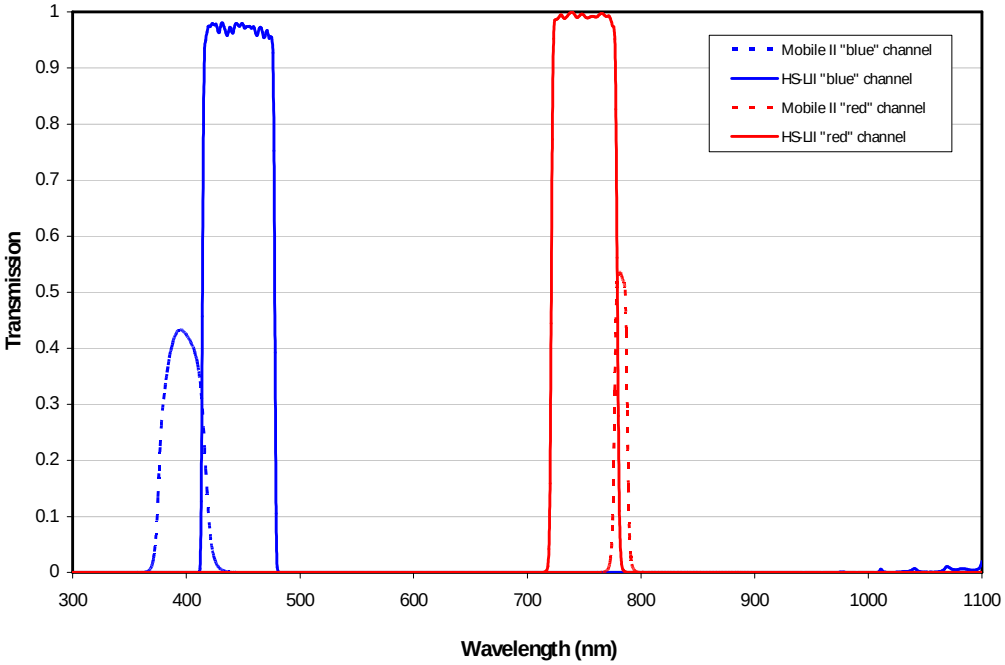

Figure 3-52. Relative transmission of interference bandpass filters with the areas under the curves demonstrating higher throughput in HS-LII.

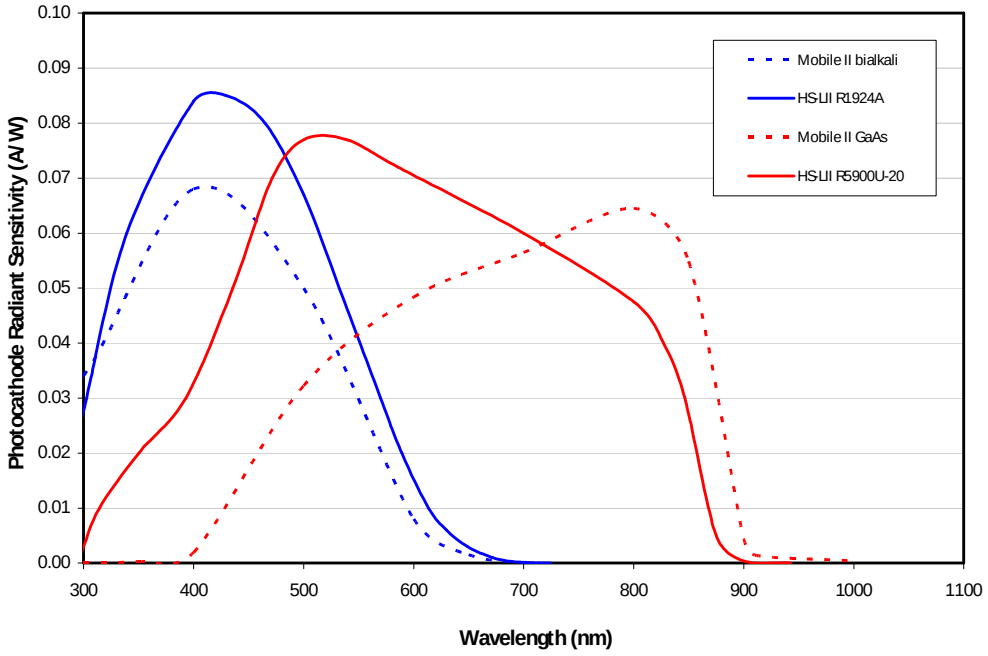

Figure 3-53. Photomultiplier response for the two systems being compared. Note that the GaAs PMT in use on Mobile II is no longer available, but the Super-20 PMT on HS-LII has nearly the same performance for the wavelengths in use.

Initial attempts at signal detection and digitization led to undesirable interference, despite careful electronic design and extensive use of shielding. Artium Technologies, which designed and manufactured the commercial LII-200 instrument, custom designed the final electronics used in the HS-LII system. Maximum noise rejection was achieved by utilizing single ground plane electronics, which integrated the photomultiplier tube signal detection, photomultiplier tube bias voltage power, signal preamplifiers, and signal amplifiers. This was coupled with differential signal cables to the high speed analogue-to-digital converter which was housed in a stand-alone PC computer. The Artium Technologies AIMS signal analysis software from the LII 200 instrument was used with the HS-LII system. The software had multi-pulse averaging added as a feature, and it was utilized when required to mitigate noise in signals.

Table 3-4. Comparison of Sensitivity for the Two AC-LII Systems

System	λ_1 (nm)	Radiance Calibration Factor, $\eta(\lambda)$ (Watt/Volt·m^3·sr)	Increase relative to Mobile II	λ_2 (nm)	Radiance Calibration Factor, $\eta(\lambda)$ (Watt/Volt·m^3·sr)	Increase relative to Mobile II
Mobile II	397	$2.54 \cdot 10^{10}$	–	782	$4.22 \cdot 10^{10}$	–
HS-LII	445	$9.14 \cdot 10^{5}$	27,800x	753	$1.36 \cdot 10^{7}$	3100x

After calibration, the HS-LII system was demonstrated to have far exceeded the target of an improvement in performance of two orders of magnitude, as can be observed from the data presented in Table 3-4. Measurements have been performed that have recorded measurable concentrations below 20 ng/m^3, which were 600 times lower than the sensitivity limit of the Mobile II AC-LII system. These levels were produced by HEPA-filtering laboratory air so that very little black carbon remained in the sample. These levels are far lower than the requirements stated by environmental researchers and engine manufacturers as the targets for their needs. An example where HS-LII was applied to measure black carbon content as part of an urban air quality study is shown in Figure 3-54. These advances which have extended the sensitivity limit of LII from the

mg/m^3 sensitivity required for tailpipe emissions measurements for vehicles to ng/m^3 levels required for ambient air monitoring of black carbon nanoparticles have been recently documented.[167, 168]

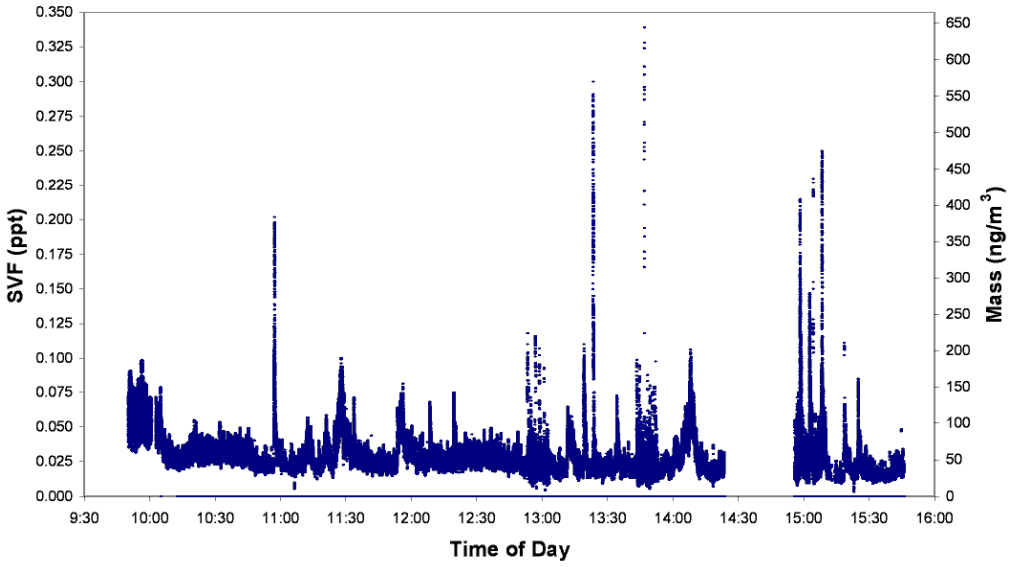

Figure 3-54. HS-LII data recorded from ambient air, demonstrating the capability of measuring concentrations far below the 0.1 mg/m^3 target.

4. ERROR ANALYSIS

This section provides details on the systematic and random sources of error and their importance in determining the soot concentration and primary particle diameter with autocompensating laser-induced incandescence. Issues raised in Section 3.7, such as uncertainties in determined d_p due to local gas heating and anomalous cooling (which were common to all LII methods) or uncertainty in measured f_V due to a variation with fluence (an AC-LII specific issue) are not addressed as these remain outstanding issues.

4.1. LIMITATIONS AND SOURCES OF ERROR

Differences between the volume concentration of soot measured with AC-LII and the total PM measured with other techniques can be attributed to several factors. These factors include: uncertainty in relating soot volume fraction to the relevant property of the PM measured by the other techniques; uncertainties in the AC-LII technique; and uncertainty and errors introduced by the other techniques.

The uncertainties in the absolute intensity approach to LII are primarily due to uncertainty in the soot refractive index at elevated temperatures. In particular, one must know the relative value of $E(m)$ at the two wavelengths to correctly determine the temperature, and the absolute value of $E(m)$ to determine the concentration once the temperature has been determined. The relative value of $E(m)$ at the two wavelengths based on the best available data of Krishnan et al.[130] increases ~20% with wavelength over the range 400 nm – 800 nm. However, recent results from Snelling et al.[131] indicate that over the visible to near-infrared range the relative value of $E(m)$ is constant. Sensitivity analysis indicates that a change in the relative value of $E(m)$ of this magnitude will result in an increase in the soot volume fraction of the order of 50%. Similarly, sensitivity analysis on the absolute value of $E(m)$ indicates a 1:1 correspondence, such that a 20% uncertainty in the magnitude of $E(m)$ leads to a 20% uncertainty in the soot volume fraction. Furthermore, $E(m)$ may vary with temperature as the soot structure may be altered as it is heated by LII, and if present, condensed organic species may also affect the soot absorption function.

A minor uncertainty which also affects the accuracy in a systematic manner is in the

knowledge of the effective centre wavelength of the light detection system for each of the two wavelengths. As the temperature of the source changes, whether it is the calibration lamp or the heated soot particles, the effective centre light wavelength of the combination of the dichroic mirror, interference filter, and detector response varies in a nonlinear yet predictable manner. This systematic inaccuracy is greatest for short wavelengths, low temperatures, and large bandwidths, reducing monotonically with increasing temperature. The error is less than 5%, and could be corrected for with an iterative approach to the data analysis.

In order to compare with mass concentration, the bulk density of the particulates was required to convert the volume fraction measured with LII. An average density for dry soot (1.9 g/cm^3) was used, although there is a wide range in the densities reported in the literature, up to that for graphite (2.26 g/cm^3).

As the primary particle diameter determined from the cooling rate is proportional to the surface area per unit volume (specific surface area) available for conduction, it was an "effective" or "apparent" size. In addition, the current AC-LII standard software analysis treats the particles as individual monosized primary particles, without accounting for the effects of primary particle size distribution and aggregate size discussed in Section 3.5. Due to shielding (dense clusters) and bridging (greater than point contact) of particles in an aggregate, the available specific surface area is substantially reduced, resulting in an apparent primary particle size that is significantly larger than the size measured with techniques such as transmission electron microscopy (TEM). Also, the size distributions of both primary particles and aggregates have been demonstrated to have an impact upon the primary particle size measurements.

Another significant uncertainty is the thermal accommodation coefficient α, which is often ignored (i.e., assigned a value of 1) or arbitrarily assigned a value of 0.9, which may be suitable for equilibrium conditions at room temperature. The thermal accommodation coefficient is the efficiency of heat transfer between gas molecules and a condensed body when gas-surface collisions occur in the free-molecular regime. The value of 0.26 determined by Leroy et al.[62] for carbon under nonequilibrium conditions at elevated temperatures was the preferred value for AC-LII until the application of AC-

LII experiments coupled with modelling produced the new value of 0.37. However, it is unknown whether this value is valid for the full range of experimental conditions encountered. This uncertainty may affect the accuracy of the primary particle sizing, but neither the precision, nor the relative comparison of the primary particle sizes obtained for different engine conditions.

With anomalous cooling affecting the early stages of the signal decay, and polydispersity effects affecting the later stages of the decay, there is a narrow time interval for performing high quality AC-LII measurements, Figure 4-1. That interval is the period where the decay in the temperature difference between the soot particle and the ambient gas can be fit to a single exponential. In this illustration the optimum interval is 50 – 100 ns after the peak of the laser pulse. The selection of the interval start and end times is likely to be dependent on the experimental conditions. The error in determining primary particle diameter will be affected by the time of the analysis interval when performing AC-LII measurements.

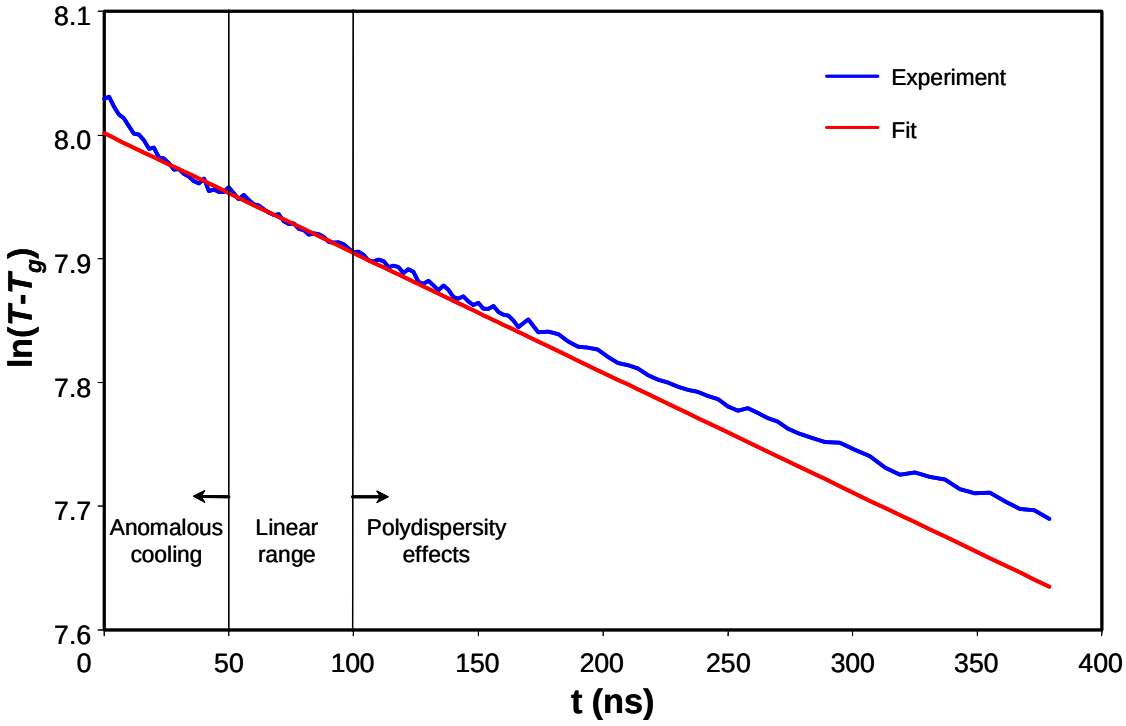

Figure 4-1. Experimental AC-LII temperature difference decay and a single exponential fit to the interval between 50 ns and 100 ns after the peak of the laser pulse.

As uncertainties in $E(m)$, accommodation coefficient, and particle density only affect the analysis of AC-LII data (and do not require changes to the experimental configuration), previously obtained results can easily be updated as new information becomes available for these quantities.[169]

Some sources of error in LII have been avoided through careful instrument design. Selection of the laser wavelength and detector bandpass wavelengths were made to avoid the photochemical and sublimation species interferences noted by others.[65, 72, 137, 170] This was aided by the use of low fluence, as others have noted that these interferences only become significant at high fluences.[72, 171] Effects noted due to the temporal response of the detection system[73, 107, 172] are less significant due to the continuous measurement of temperature with AC-LII,[112] as it is not essential to capture the peak intensity, which is desirable with conventional LII.

4.2. LIMITATIONS DUE TO THE OPTICAL APPARATUS

The properties of the following parameters need to be known in advance. Any uncertainty in any of these translates into inaccuracies in the LII measurement. The parameters include:

(a) calibration source

  (i) radiance or irradiance calibration

(b) optics

  (i) absolute neutral density filter transmission

  (ii) relative dichroic mirror reflectivity

  (iii) relative interference filter transmission

(c) electronics

  (i) relative photodetector sensitivity

  (ii) photodetector gain

(iii) amplifier gain

(d) dimensions of probe volume

(e) laser spatial fluence profile

Errors in the calibration source have been discussed in Section 3.3.2, and are likely to be of the order ±10%.

4.2.1. Optics

The weak signal generated at the lower wavelength places great demands on the detection system. Ideally one wants to follow the decay of the LII signal from a high of near 4000K (where sublimation becomes significant) to below 2500K, where there is little signal remaining. It has been demonstrated that while there is a drop of greater than one order of magnitude in spectral radiance at 780 nm for this temperature decrease, there is nearly a three orders of magnitude drop in spectral radiance at 400 nm. This places great demands on the detection system.

As common collection optics and optical path are used for both calibration and experiment, analogous to common mode rejection in detection of electronic signals, all the geometric terms involved in a conventional calibration procedure become redundant.

However, the wavelength calibration of all the elements in the optical path is required. Figure 4-2 shows the profiles of the interference filter transmission and dichroic mirror reflectance in the demultiplexer receiver for the 400 nm channel used with the Mobile II AC-LII system. The convolution of these with the bialkali photomultiplier quantum efficiency provides the overall spectral responsivity of the detection system. All of these elements must be considered, as well as "neutral" density filters or other optics which may be placed in the light path.

The net system response as a function of wavelength must be integrated over the relevant passband. This integral can be approximated using an equivalent filter representation. The centre wavelength, λ_C, of this equivalent filter is defined as the wavelength which splits the integral in Eq. (38) into two equal parts. The response of the equivalent filter, τ_{max}, is taken as the system response at the centre wavelength and

the bandwidth, Δ_f, is defined by requiring the integrated response of the equivalent filter to match the exact integral as shown in Eq. (38)

$$\Delta_f \cdot \tau_{max} = \int_{\lambda} \tau(\lambda)\, d\lambda \quad at\ \lambda_C \tag{38}$$

where $\tau(\lambda)$ is the product of the transmission characteristics of the optical filters and the spectral detector response.

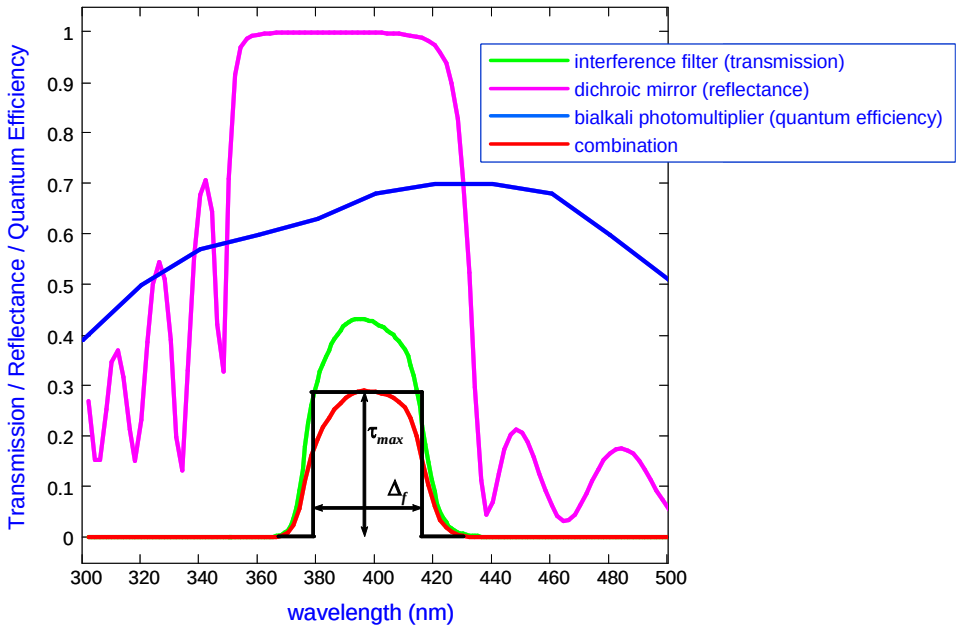

Figure 4-2. Responsivity of 400 nm channel of demultiplexer receiver.

The error in using this approximation instead of the full integration is worst for the 400 nm channel, but is not significant except for temperatures below the AC-LII detection limits. The error of the equivalent filter approximation is shown in Figure 4-3, where the equivalent filter approximation is compared to the exact integral. The error in the temperature range 2500K – 4000K is less than 3%. The error for the 780 nm channel is far less, as the particle radiation spectral distribution is relatively flat across the bandwidth of the filter/mirror/PMT combination, as shown in Figure 3-10.

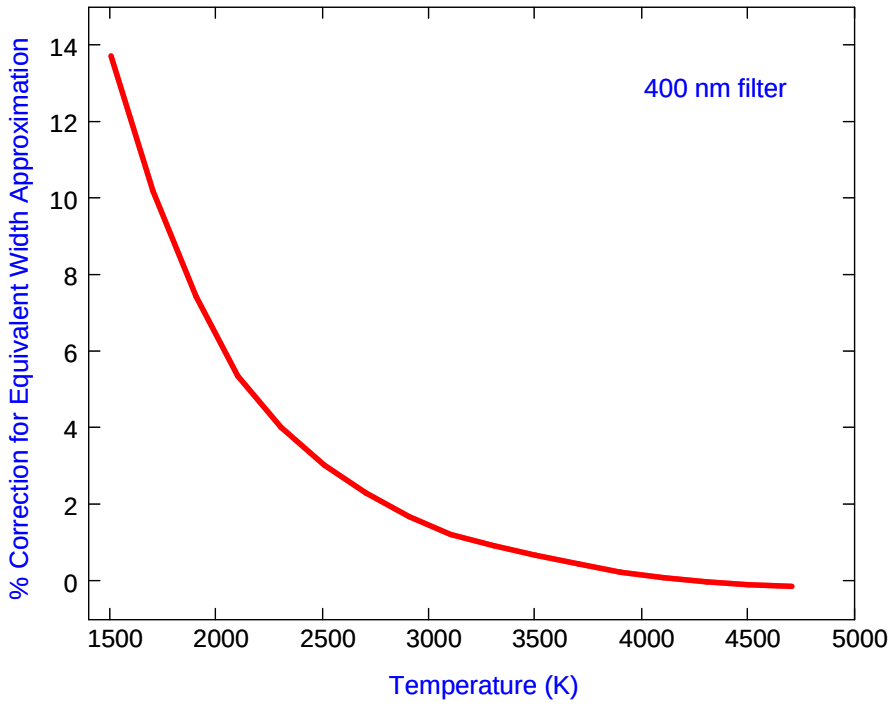

Figure 4-3. Error in assuming an equivalent bandwidth for the spectral responsivity of the 400 nm channel.

4.2.2. Electronics

The relative photodetector sensitivity has been discussed in conjunction with the optical elements. The photodetector gain and the amplifier gain must also be calibrated, and are relatively simple to acquire, as each depends only on the applied voltage. Modest errors may be anticipated from inaccuracies in performing these calibrations.

4.2.3. Dimensions of the Probe Volume

The dimensions of probe volume can be determined from the geometry of the intersection of the laser beam and the optical path defined by the collection optics. This will be determined by the laser beam dimensions, the crossing angle between the laser bean and the collection optics, the aperture size in the collection optics, and the magnification ratio of the collection optics. Modest errors may be anticipated from inaccuracies in measuring these quantities.

4.2.4. Laser Spatial Fluence Profile

The laser spatial fluence profile can have a significant impact on the LII measurement, as contribution from the lower intensity "wings" can become significant as the fluence is increased for non-top-hat laser beams. An example is presented in Figure 4-4, which is calculated for a quasi-top-hat spatial profile. The calculation was performed for an ambient temperature of 300K. This result was calculated based on the measured spatial profile in the probe volume (without the use of an aperture and relay imaging).

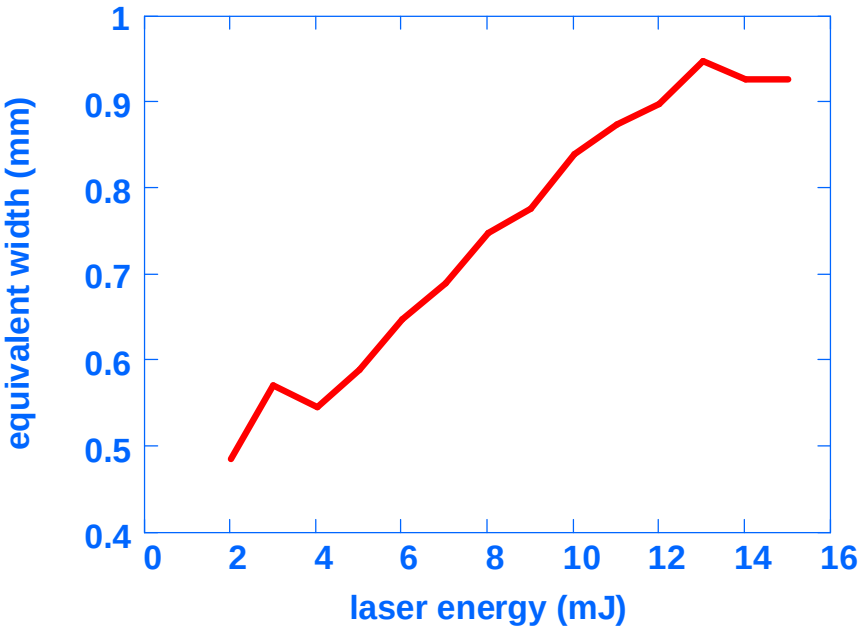

Figure 4-4. Variation in equivalent width of laser beam with laser energy for a quasi-top-hat laser profile.

This example illustrates that an error of as much as a factor of two could be made by not measuring and optimizing the laser light beam spatial profile. The approach used in AC-LII to homogenize the laser light beam was shown to be highly effective and mitigated the potential error due to nonuniform illumination of the soot particles. Use of a lees homogeneous spatial light profile, such as a Gaussian beam, would increase the error.

4.3. UNCERTAINTIES IN THE SOOT ABSORPTION FUNCTION

The uncertainties in the absolute intensity approach to LII are primarily due to uncertainty in the soot refractive index at elevated temperatures. In particular, one must know the relative value of $E(m)$ at the two wavelengths to correctly determine the temperature, and the absolute value of $E(m)$ to determine the concentration once the temperature has been determined.

There was a large database on the optical properties of soot and graphite in the literature. Some of the most relevant work for soot included light extinction with gravimetric calibration,[57, 130, 173, 174] photoacoustic spectroscopy,[161] and UV-VIS-NIR mass specific absorption.[162] The graphite data was based upon *ex situ* measurements of refractive index (RI),[175] UV-VIS-NIR mass specific absorption,[162] and scattering and extinction.[176, 177] The absorption function data for graphite was predominantly below a value of 0.25, whereas the data for soot was mostly above the value of 0.25. Due to this distinct separation, it was recommended that data on absorption function for graphite should not be used for LII measurements of soot.

The high quality absorption function, $E(m)$, data for soot is shown in Figure 4-5. There is obviously considerable uncertainty in both the absolute value of $E(m)$ and its variation with wavelength. A loess fit to some of the data is presented, showing a slightly increasing characteristic with wavelength over the 350-1000 nm range.

The LII derived value was somewhat higher than most of the gravimetric determinations, but the agreement was considered satisfactory given the assumptions made and experimental uncertainties of the two techniques. In summary, for the visible and near-infrared portion of the spectrum, $E(m)$ has no significant wavelength dependence and $E(m) = 0.32 \pm 0.08$ based on an analysis of the above data. In a recent review of all available data, undertaken to elucidate the absorption function for black carbon in the atmosphere, a reported best estimate was equivalent to $E(m) = 0.40 \pm 0.06$ at 550 nm.[178] This is in excellent agreement with the LII determined value of $E(m) = 0.41$ at 532 nm and is not statistically different from the analysis of the data in Figure 4-5. As a result, the use of $E(m) = 0.41$ is recommended along with the assumption that it does not vary over the VIS-NIR wavelength range.

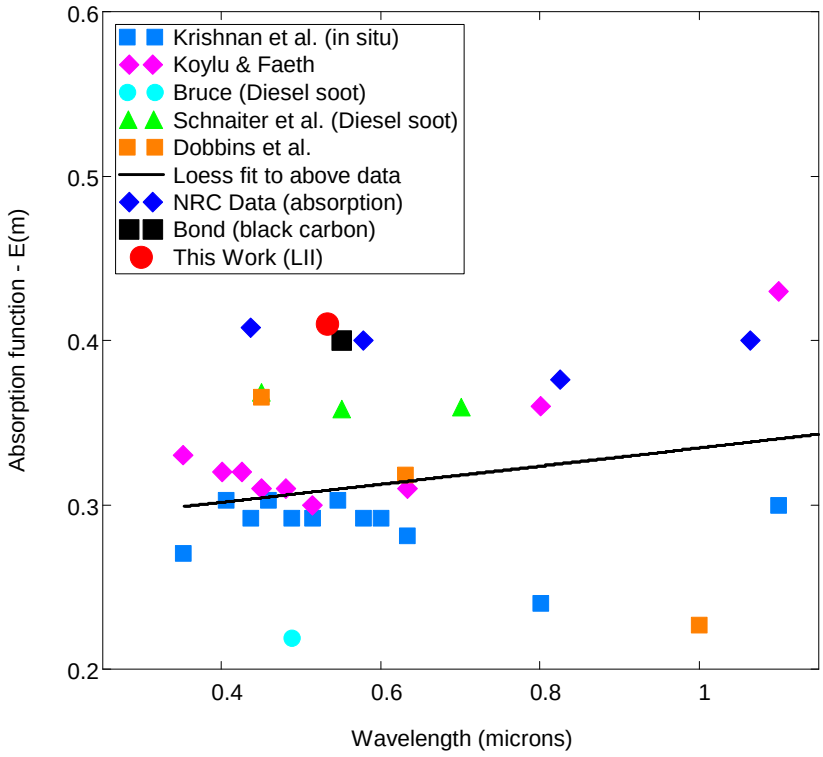

Figure 4-5. Absorption function, *E*(*m*), data for soot.[57, 109, 130, 142, 160-162, 178]

The effects of changes in $E(m)$ on the measured soot concentration were investigated. The error in soot concentration produced by an error in $E(m)$ is

$$\frac{d}{d\ln\left(E(m)_{\lambda_{low}}\right)}\ln\left(f_V\right)=\frac{\lambda_{low}}{\lambda_{high}-\lambda_{low}} \tag{39}$$

and

$$\frac{d}{d\ln\left(E(m)_{\lambda_{high}}\right)}\ln\left(f_V\right)=\frac{-\lambda_{high}}{\lambda_{high}-\lambda_{low}} \tag{40}$$

where λ_{low} and λ_{high} refer to the lower and upper detection wavelengths, respectively. Combining Eqs. (39) and (40), the resulting change in soot concentration when either or both values of $E(m)$ were changed was

$$\frac{f_{V_1}}{f_{V_0}}=\left(\frac{E(m)_{\lambda_{low}1}}{E(m)_{\lambda_{low}0}}\right)^{\frac{\lambda_{low}}{\lambda_{high}-\lambda_{low}}}\left(\frac{E(m)_{\lambda_{high}1}}{E(m)_{\lambda_{high}0}}\right)^{\frac{-\lambda_{high}}{\lambda_{high}-\lambda_{low}}} \tag{41}$$

where the subscripts 0 and 1 referred to the initial and final values of f_V and $E(m)$. The net impact was that an increase to the value of $E(m)$ at the upper detection wavelength decreased the reported soot concentration whereas an increase to the value of $E(m)$ at the lower detection wavelength increased the reported soot concentration, and the proportional effect was greater at the upper wavelength than at the lower wavelength.

A physical explanation of the different f_V errors resulting from uncertainties in the low and high wavelength $E(m)$ values can readily be seen from the fact that the error in relative value of $E(m)$ at the two wavelengths determines the temperature, and the absolute value of $E(m)$ then determines the concentration once the temperature has been obtained. Thus an increase in the $E(m)$ value at low wavelength decreases the derived temperature, partially offsetting the reduction of f_V resulting from the higher $E(m)$. For the higher wavelength and increase in $E(m)$ leads to a higher derived temperature thus augmenting the effect of the higher $E(m)$ value in reducing f_V.

Further work is essential to improve the knowledge of both the relative value of $E(m)$ at the two wavelengths and the absolute value of $E(m)$ over the range of conditions anticipated with LII. This will lead to greater confidence in the reliability of the LII measurements.

4.4. MULTIPULSE AVERAGING

The noise inherent in LII signals could be mitigated by the use of multipulse averaging in situations where a fast time response for the measured properties was not required. Seldom was data required at greater than a 1 Hz rate, even in transient engine emission measurement experiments. Often, in steady-state experiments, such as a laminar flame, the measurement period could last much longer. With the 20 Hz laser typically used in AC-LII, a 1 Hz measurement interval allowed averaging of 20 single shot pulses, and only 1 minute was required to collect a 1200 pulse average in steady state experiments. A study of several thousand single shot LII acquisitions of ambient laboratory air was used to demonstrate the improvement offered by multipulse averaging, Figure 4-6. The coefficient of variation, COV, which is the standard deviation normalized by the mean, was calculated for several thousand single shot measurements of soot concentration and primary particle diameter. The data was reanalyzed with multipulse averaging from 2

up to 1600 pulses per average. If the noise in signal is dominated by photomultiplier shot-noise then the theoretical improvement in the COV given by (1/number of pulses per average)$^{0.5}$ and is shown in Figure 4-6 for comparison.

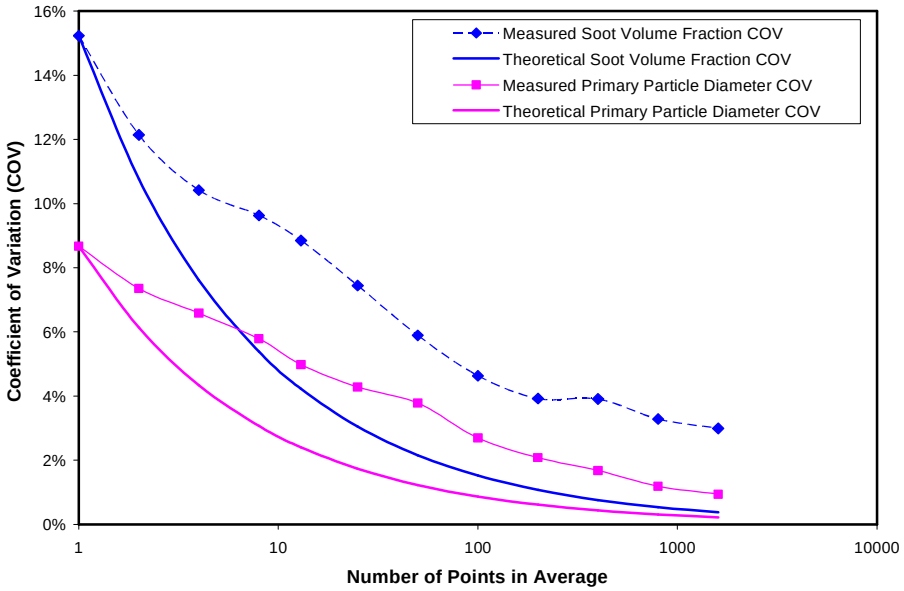

Figure 4-6. Reduction in the coefficient of variation for the soot volume fraction and the primary particle diameter through multipulse averaging of single-shots LII signals. Dashed lines are measurements; solid lines are theoretical improvement relative to single shot data.

Although the experiments did not demonstrate the full theoretical improvement possible form multipulse averaging, they did show that the use of averaging does reduce the COV dramatically. The failure to obtain the full theoretical improvement can be attributed to real variations in the soot LII response, and to variations in the concentration of black carbon in the laboratory over the duration of the experiment. This effect was used for two benefits in AC-LII, as it reduced the noise in the results relative to single shot data, and it allowed extraction of valid measurements from data that was too noisy to be analyzed on a single shot basis. These benefits are illustrated in Figure 4-7 and Figure 4-8, respectively. At low concentrations very few single shot data points result in a valid measurement, but with multipulse averaging the validation rate can be improved dramatically.

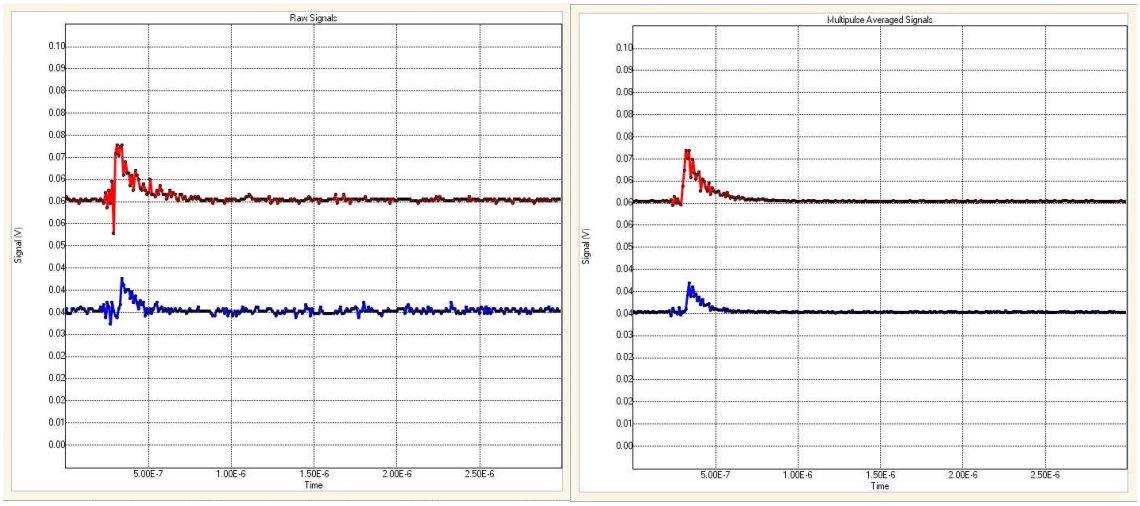

Figure 4-7. Quality of signals at a concentration of 289 ng/m^3 obtained with HS-LII. Single pulse (left) and 50-pulse average (right), demonstrating the reduction in noise possible with multipulse averaging.

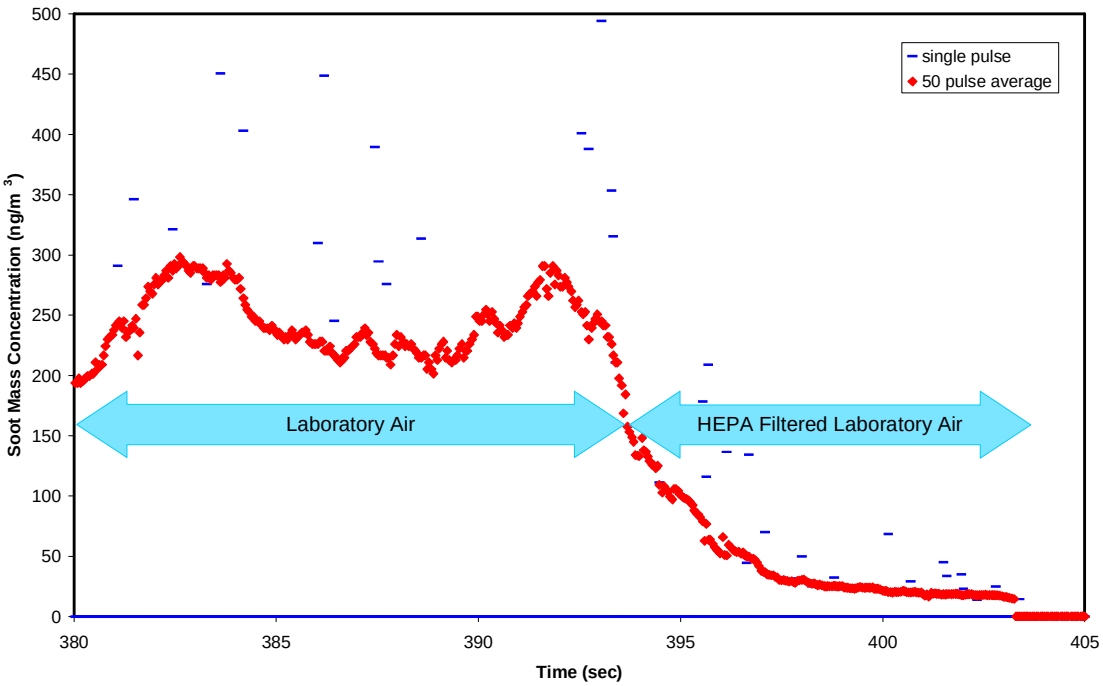

Figure 4-8. HS-LII detection of indoor atmospheric particulates. Blue dashes are single-shot data; red diamonds are 50 shot multipulse averages.

5. APPLICATIONS OF AUTOCOMPENSATING LII

As part of the research performed for this work, measurements were made with AC-LII in many applications. These have resulted in numerous publications and/or presentations[21, 28, 69, 113, 140, 141, 179-185], but only a few selected examples are presented here to illustrate the use of AC-LII. These were chosen to establish that AC-LII does provide the features and corresponding benefits that it was anticipated to when this work was initiated. It has been demonstrated in a wide range of applications, with university, industry, and government partners collaborating on the research. AC-LII was applied to measure soot in conditions that extended from: high vacuum to high pressure; room temperature to flame temperature; in-laboratory to on-road; steady-state to transients requiring greater than 1 Hz response; raw exhaust to dilute exhaust; concentrations from ng/m^3 to g/m^3; and primary particle diameters from 5 to 100 nm.

5.1. DIESEL EXHAUST – CHASSIS DYNAMOMETER

Chassis dynamometer measurements of diesel soot with the Artium LII 200 instrument were performed with a number of other researchers from Cranfield at the Millbrook Proving Grounds, UK.[180] The vehicle tested was a large SUV and a standard transient test cycle developed by Millbrook was followed. The results demonstrate that AC-LII has ample time resolution and measurement range to meet the needs of particulate measurements on transient driving cycles, Figure 5-1.

For this trial, the soot concentration ranged from a low of 0.05 ppb to a high of 965 ppb, all while the Artium LII 200 was operated in an unattended, fully automated mode. This represented a measurement range of ~ 20,000:1. Data supplied by the Millbrook researchers allowed the calculation of instantaneous exhaust volume flow, so that an integrated mass over the driving cycle could be determined. This AC-LII result provided time resolved particulate measurements for the chassis dynamometer transient driving cycle with a level of quality that was previously unobtainable.[180]

Closer inspection of a portion of the results confirmed that the majority of the particulate mass accumulated over the driving cycle is generated during acceleration transients, Figure 5-2. The sharp rise in soot concentration occurs at the beginning of

each acceleration during the driving cycle, and there is a corresponding step-rise in the cumulative mass associated with the sharp rise in instantaneous soot concentration.

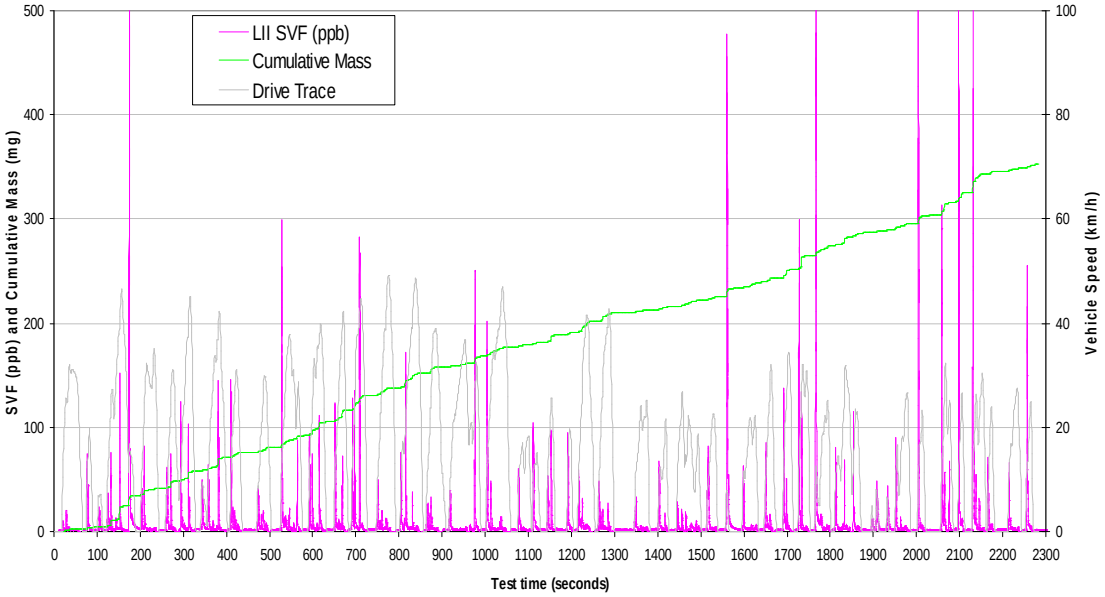

Figure 5-1. AC-LII measurement of soot concentration from a diesel vehicle operating on a standard chassis dynamometer driving cycle.

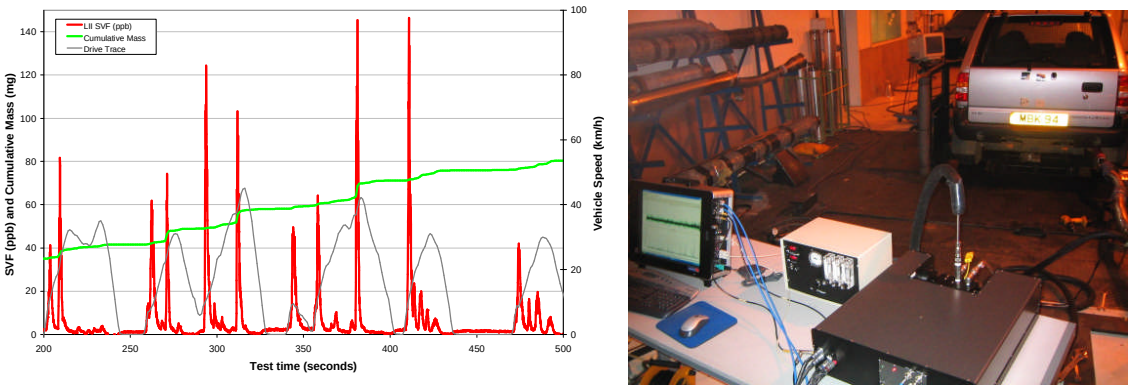

Figure 5-2. Detail of results presented in Figure 5-1 (left) and the Artium LII 200 instrument in the chassis dynamometer test cell with the SUV vehicle (right).

The 20 Hz operation of the LII 200 instrument provided definition of transient events that were previously unattainable. Between 410 s and 420 s in this drive cycle, the variation in soot concentration resulting from 5 gear changes was identifiable. At 380 s

in this drive cycle, the concentration rises from 2.5 ppb to 145 ppb in 1.3 s. Instruments operating at a 1 Hz or slower rate would miss some, if not all, of this rapid rise in concentration. The 20 Hz time resolution was found to be necessary in order to adequately capture the cumulative concentration of soot.

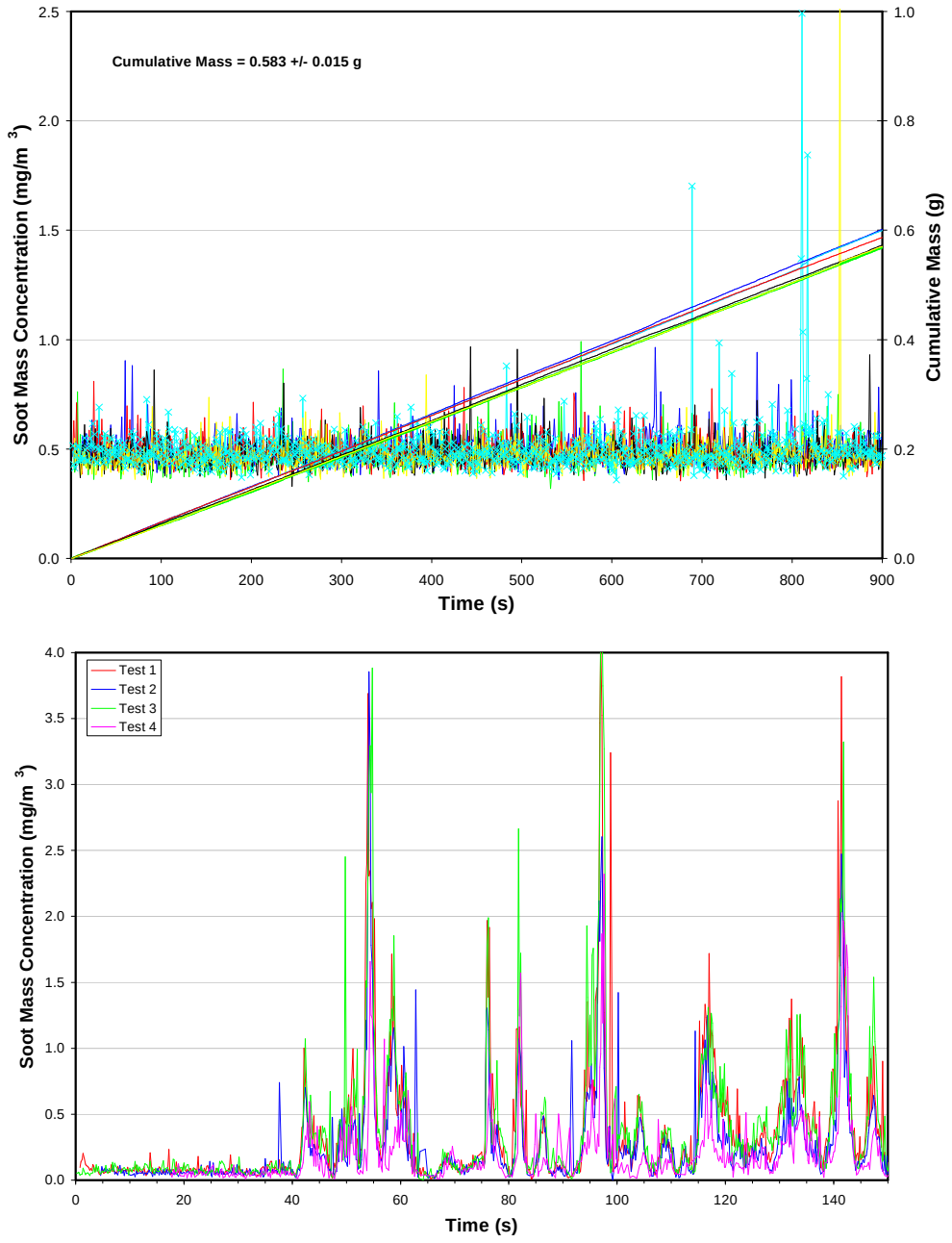

Figure 5-3. Repeatability of AC-LII measurements of soot concentration from the exhaust of a heavy duty diesel engine, steady-state (above) and transient (below).

A study was performed with John Deere and Artium Technologies at the John Deere Engineering Center in Waterloo, IA, USA to investigate the repeatability of AC-LII. The Artium LII 200 instrument was used with a heavy duty diesel engine running steady-state and EPA standard off-highway transient cycles. Both the steady-state and transient data showed a high level of repeatability, Figure 5-3.

The steady-state experiments were repeated 6 times, with a coefficient of variation of 2.6%, which was considered excellent, considering the variability of engine operation, even on a chassis dynamometer.

Chassis dynamometer measurements of diesel soot were also carried out in collaboration with Artium Technologies and the California Air Resources Board (ARB) at the ARB facility in Los Angeles, CA, USA.[179] These experiments were performed on a heavy duty truck mounted on the chassis dynamometer, and were part of a larger study to assess the suitability of portable emissions measurement systems (PEMS) to measure compliance with the EPA's not-to-exceed (NTE) regulation.[179] The specific goal of the trials was to evaluate the performance of a number of gaseous emissions instruments from competing manufacturers. However, a number of particulates instruments were also participating in the trials. The particulates were sampled on board the CE-CERT mobile emissions laboratory from the University of California, Riverside, which has a full CVS (constant volume sampling) dilution tunnel. Other particulates measurements included the standard gravimetric technique, the Dekati Mass Monitor, the AVL Photoacoustic Soot Sensor, and the TSI DustTrak. AC-LII measurements were performed with the Artium Technologies LII 200 instrument.

Results for one of the NTE conditions are shown in Figure 5-4, illustrating that the 7 repeats at each of 3 conditions did not produce the steady-state engine condition that was anticipated for these NTE tests. Instead, the soot concentration was observed to gradually decrease from test to test, and only increased when the next condition requiring greater load was initiated. As the maximum sampling rate of the other PM instruments was 1 Hz, a 1 Hz running average of the AC-LII data was superimposed over the 20 Hz data, illustrating the loss of detail by sampling at such a reduced rate. The 1 Hz data does not span the range of extremes nor does it show the shot-to-shot variability in the soot concentration evidenced by the 20 Hz data.

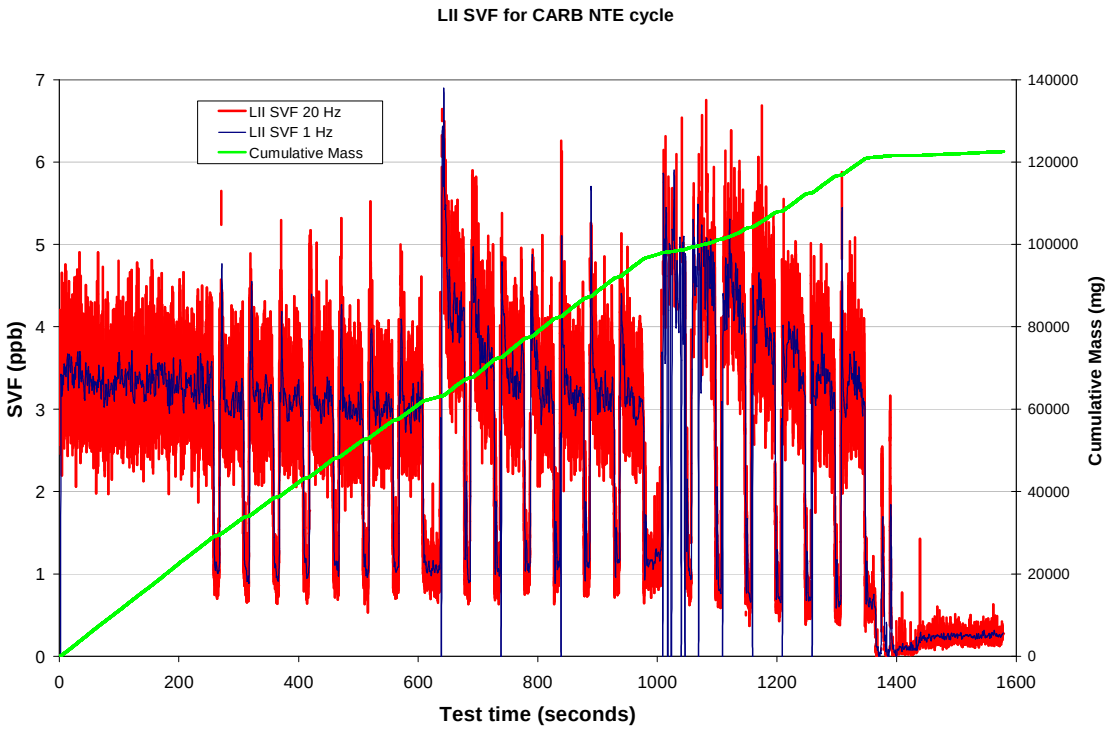

Figure 5-4. AC-LII data from a heavy duty truck operating under EPA not-to-exceed conditions, sampling exhaust from a CVS dilution tunnel.

During these tests, a large number of conditions were run for comparison of the particulate measurement instruments to the gravimetric filter data that was acquired. Results from the competing instruments were not made available. The AC-LII data was poorly correlated to the total particulate matter mass emission rate determined from the gravimetric filters, Figure 5-5. However, the filters were processed to remove the volatile compounds and reweighed, which resulted in data that was reported by CE-CERT as an EC mass emission rate. This had a positive correlation of 0.85 with the mass emission rate of soot measured by AC-LII. Significantly, the slope of the fit between the AC-LII results and the EC results was 0.99, indicating almost perfect agreement between the two. This was the best agreement in terms of accuracy recorded for concentration measurements with AC-LII compared to another technique.

This study was performed for the California Air Resources Board and resulted in a report that indicated that AC-LII was particularly suited to the real-time monitoring of particulate emissions from diesel-powered vehicles.[179]

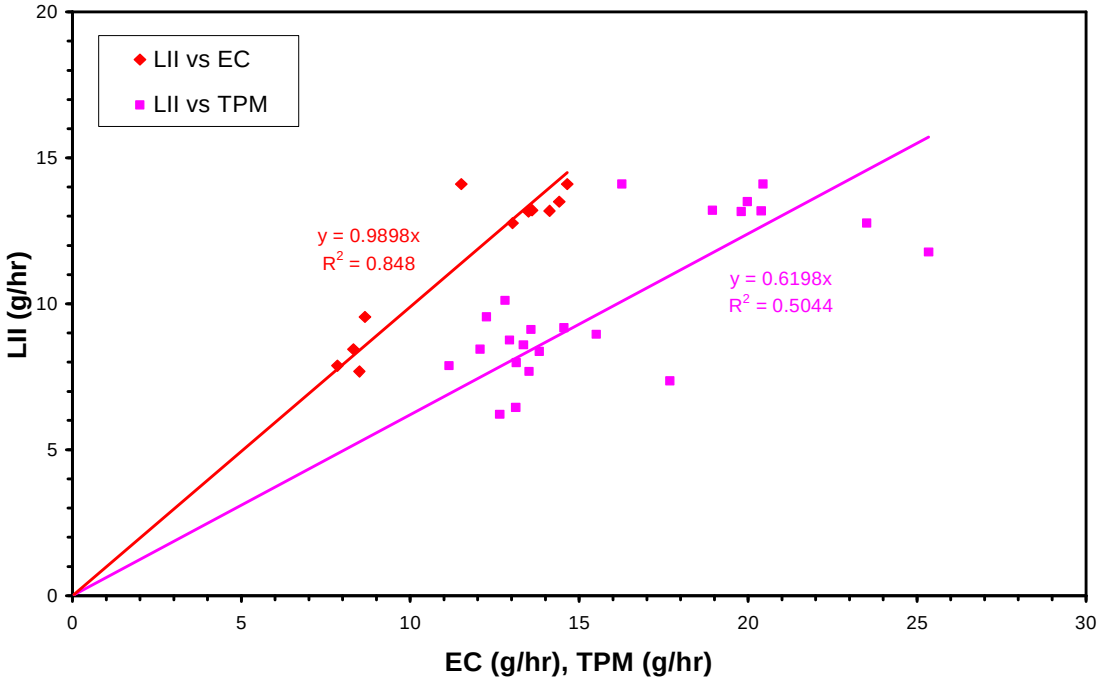

Figure 5-5. AC-LII measurements of soot emissions from a heavy-duty truck on a chassis dynamometer compared to total particulate matter (TPM) and nonvolatile particulate matter (EC) emissions.

5.2. DIESEL EXHAUST – ON-ROAD

In collaboration with Artium Technologies, Sandia National Laboratories, and Chevron, a study was undertaken to demonstrate that it was possible to obtain real-world on-road emissions on board a compact automobile.[183] The Artium LII 200 instrument and ancillary equipment were installed in the trunk and fold-down back seat area of a 2002 Volkswagen Jetta with a 1.9 liter TDI diesel engine. The equipment consisted of a mini-tower PC, flat-screen monitor, laser power supply, ejector pump and compressor to extract exhaust from the tailpipe through a sampling tube clamped to the tailpipe, and a generator to power the instrument, fit easily into the Jetta. The exhaust sampling line and the vent lines from the ejector pump and generator were routed through the opening of the trunk lid left slightly ajar, Figure 5-6.

An OBD-II scan tool interface was used to access the vehicle and engine speeds for recording by a dedicated notebook PC as the vehicle was driven around several loop

routes in the vicinity of the Sandia National Laboratories California site in Livermore, CA, USA. These measurements were then time-matched with the AC-LII measurements to obtain a synchronized data set correlating time-resolved PM emissions with vehicle operating conditions that included accelerations from a stop, hill climbing, and freeway driving.[183]

Figure 5-6. On-road measurements of diesel particulate emissions in a compact automobile.[183]

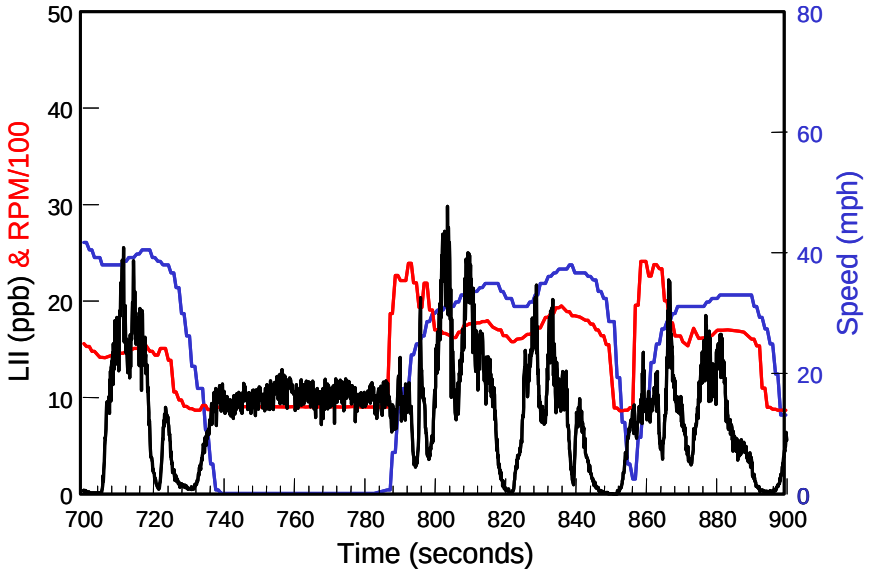

Figure 5-7. On-road demonstration of AC-LII to measure particulate emissions.

As expected the results show a direct link between changes in engine speed and particulate emissions, Figure 5-7. The results indicated that the AC-LII instrument is very capable for mobile measurements of soot particulates, even in a relatively small vehicle. This created the opportunity for further detailed trials to characterize real-world in-use soot particulate emissions from vehicles.

A second collaboration with the California Air Resources Board and Artium was undertaken in an on-road evaluation of the real-world emissions from a range of heavy duty trucks.[184] Once again, CE-CERT was providing their mobile emissions laboratory, this time as a rolling laboratory trailer to be towed by the range of trucks. The experiments were performed near the ARB facility in Stockton, CA, USA and consisted of a driving loop primarily on freeways in the central California valley. Each truck was driven over the ~1.5 hour route twice, and three different trucks (representing three major engine manufacturers) were evaluated.

AC-LII data was collected continuously during each pass over the test route, and filters for gravimetric analysis were collected over 12 periods during the test, Figure 5-8. As before, this illustrates the capability of AC-LII in terms of a large measurement range, high sensitivity, and superior time response. The real-time response provides unparallel resolution for discretizing transient events during real-world driving.

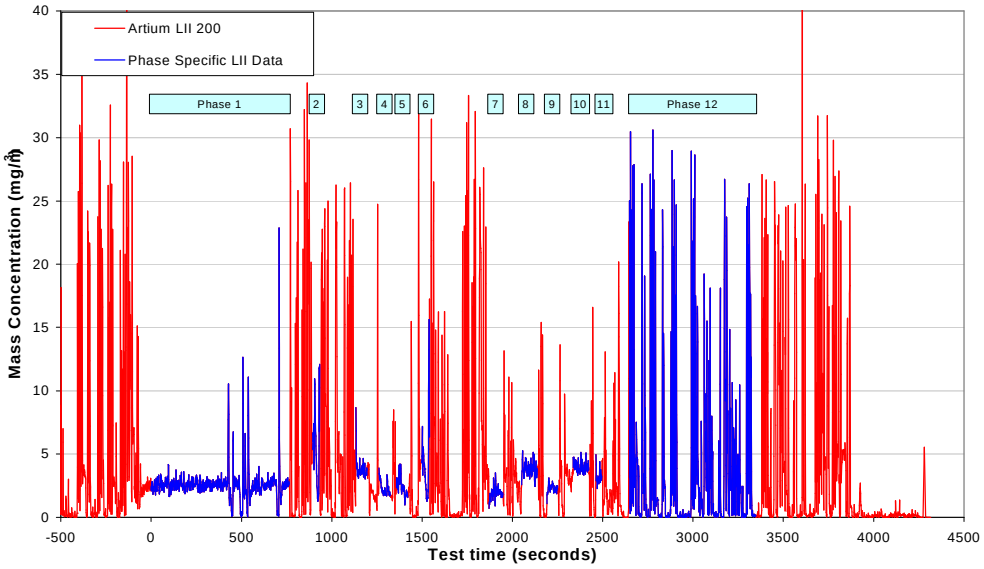

Figure 5-8. On-road measurement of heavy duty diesel exhaust from a tractor-trailer truck.

The AC-LII data was reasonably correlated to the total particulate matter mass emission rate and the EC mass emission rate determined from the gravimetric filters for these on-road measurements, Figure 5-9. The latter, which had the volatile compounds removed, only had a positive correlation of 0.73 with the mass emission rate of soot measured by AC-LII. However, the slope of the fit between the AC-LII results and the EC results was 0.94, indicating good agreement between the two. This was another demonstration of the relative accuracy of the AC-LII technique in a real-world application.

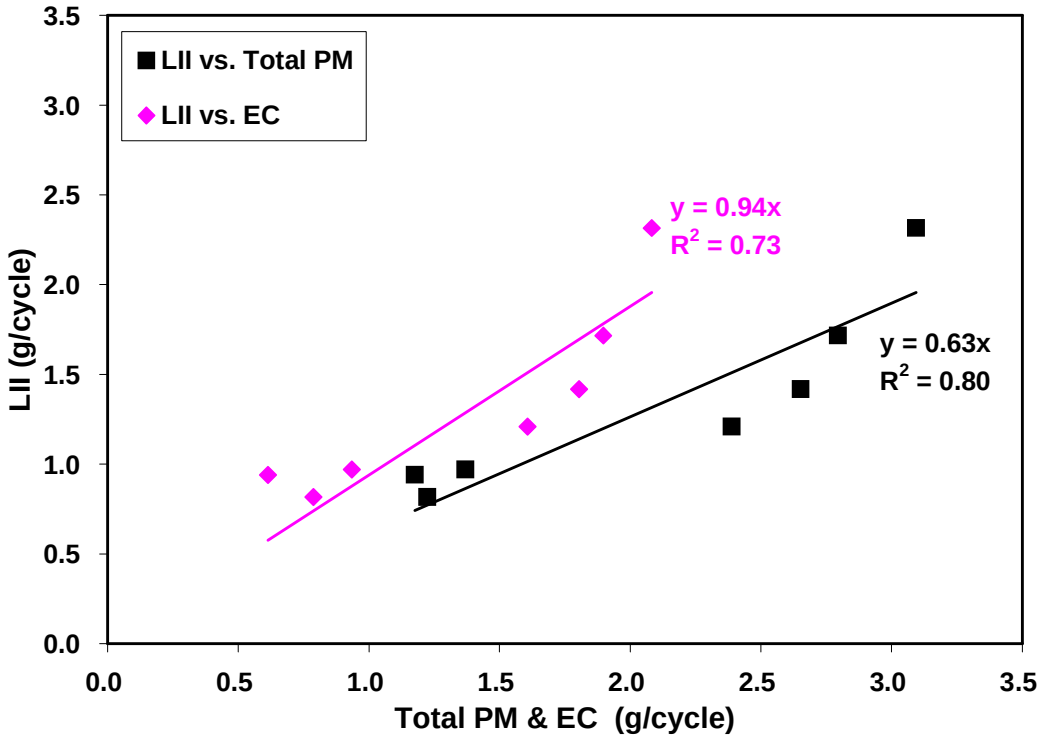

Figure 5-9. Real-time AC-LII measurements of soot emissions from a heavy-duty truck during on-road testing compared to total particulate matter (TPM) and nonvolatile particulate matter (EC) emissions.

5.3. GAS TURBINE EXHAUST

Measurements of soot from a gas turbine were performed with the Artium LII 200 in collaboration with a major gas turbine manufacturer. Due to the confidential nature of these experiments, results may not be shown. Each experiment was performed for a period of 60 s at a laser repetition rate of 20 Hz, during which time typically greater than 1190 single-shot data points which could be processed were acquired. This was a

data validation rate of greater than 99%. Time series and histograms of the primary particle diameter and soot volume fraction were recorded. The data demonstrated that the condition being measured was steady during the test period, with some variation on a shot-to-shot basis. The experiment was repeated three times for each condition.

These steady-state experiments were performed for a series of five different engine conditions. A comparison between the mass concentration determined by AC-LII and the smoke number determined from the SAE ARP 1179 Test Method was made. The smoke number technique is the accepted standard in the aviation industry. It involved collection of particulates from the gas turbine exhaust on filter paper, followed by a reflectance measurement to determine the smoke number. The results illustrated that the AC-LII technique produced much greater repeatability in comparison to the smoke number method, as the error bars were much smaller for the AC-LII results. As expected, the comparison showed the AC-LII measurement of concentration varied according to a power law relationship with the smoke number. The relationship produced a good degree of correlation.

5.4. CARBON BLACK PRODUCTION

The surface area of aggregated nanoparticles, related to the primary particle size, is a key parameter in the production of carbon black. As AC-LII only measures the elemental carbon portion of the particulates, it has been recognized as a potential method for measuring carbon black in a process control application. A comparison of samples drawn from a carbon black reactor and analyzed with conventional LII[38] and with AC-LII[181] to those simultaneously acquired for subsequent analysis with standard laboratory methods has been recently reported. Another unique approach was the investigation of the performance of LII on carbon black suspended in a liquid, where the conduction cooling is much more rapid.[186]

The carbon black specific surface area, *S*, can be expressed as

$$S_{CB} = \frac{\text{surface area}}{\text{mass}} = \frac{\pi \int_0^\infty d_p{}^2 p\left(d_p\right) \mathrm{d}d_p}{\rho_{CB}\left(\frac{\pi}{6}\right) \int_0^\infty d_p{}^3 p\left(d_p\right) \mathrm{d}d_p} = \frac{6}{\rho_{CB} d_{32}} \tag{42}$$

or

$$S_{CB}\left[m^2/g\right]=\frac{6000}{\rho_{CB}\left[g/cm^3\right]\ d_{32}\left[nm\right]} \tag{43}$$

where d_{32} is the Sauter mean diameter (SMD) and $p(d_p)$ is a probability distribution function. As the size determined by AC-LII is proportional to the surface area per unit volume, it should be related to d_{32} as

$$S_{CB,LII}=\frac{6000}{1.8\ d_{p_{LII}}} \tag{44}$$

where d_{pLII} is the apparent primary particle diameter determined by AC-LII, 1.8 g/cm^3 is a typical density for carbon black particles, and $S_{CB,LII}$ is expressed in m^2/g.

A collaborative study was performed with Columbian Chemicals Company and Artium Technologies, using the Mobile II AC-LII system to make measurements of the carbon black extracted from a reactor at one of their industrial plants in North Bend, LA, USA.[181] AC-LII specific surface area distributions were measured for two carbon black reactor conditions. The normalized specific surface area (NSSA) was calculated by assigning the specific surface area equal to the independently measured statistical thickness surface area (STSA) value at 100 using the following relation

$$NSSA=1.955\cdot\frac{6000}{1.8\ d_{p_{LII}}}=\frac{6517}{d_{p_{LII}}} \tag{45}$$

These normalized specific surface area distributions demonstrate that the 95% confidence intervals on the mean of the NSSA is approximately 0.1%, Figure 5-10. The width of the distributions of NSSA, as measured by a single standard deviation, is approximately 1% of the mean value. In all cases the AC-LII data correlated well with the standard surface area measurement techniques, exhibiting the correct trends with changes in reactor operating conditions and a high degree of correlation with STSA (an established physical measure of specific surface area) as illustrated in Figure 5-11. However, variation in the AC-LII data was significantly less than the STSA data over the range studied, which indicated that AC-LII was not as sensitive to the change in

surface area as was the STSA technique.[181]

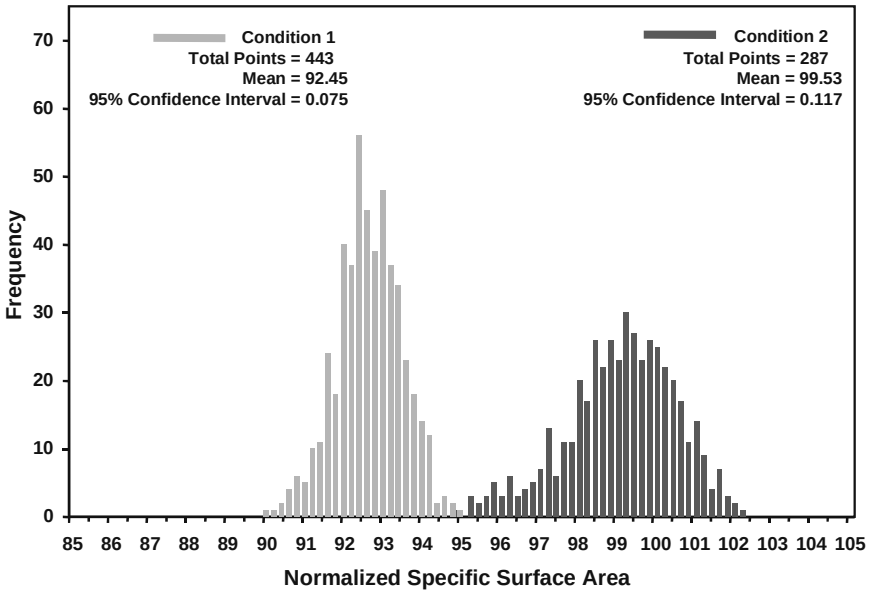

Figure 5-10. NSSA distributions for two different carbon black reactor conditions.

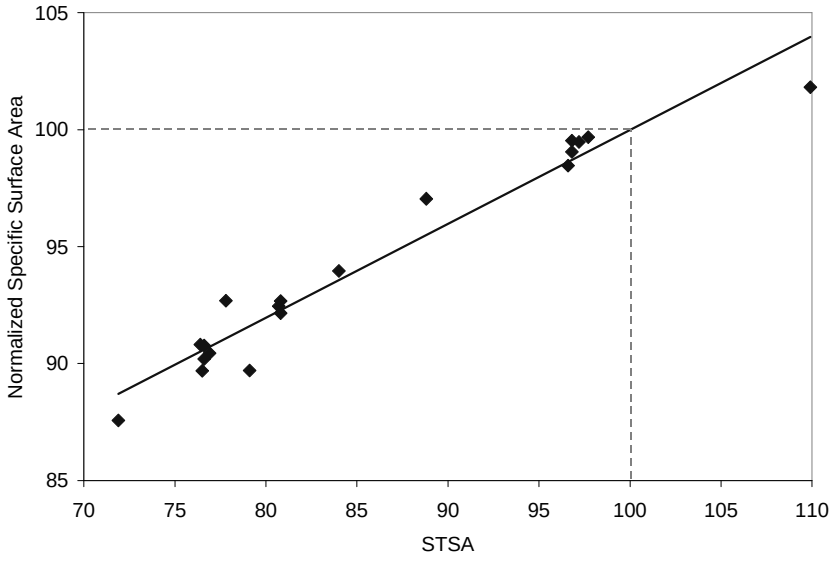

Figure 5-11. NSSA (as determined by AC-LII) is highly correlated with STSA.

Columbian Chemicals has actively pursued investigation of the use of AC-LII for process control in its plants as a result of the positive outcome of this study.

5.5. AMBIENT MEASUREMENTS

The high sensitivity laser-induced incandescence (HS-LII) system was deployed on an Environment Canada mobile platform known as CRUISER (Canadian Regional and Urban Investigation System for Environmental Research), which was being used to perform a detailed examination of how polluted air masses change as they move from urban to rural areas and across political boundaries, along with a number of related objectives. CRUISER is bristling with instruments to measure common gaseous pollutants (ozone, sulphur dioxide, nitrogen oxides, carbon monoxide, carbon dioxide, and volatile organic compounds) as well as the total mass, sizes and numbers, and chemical composition of particulates. The PM instrumentation in addition to HS-LII includes an aerosol mass spectrometer (AMS), TEOM®, CPC, SMPS, aethalometer, optical dust counter, photoacoustic instrument, and gravimetric sampling. The CRUISER mobile laboratory is shown in Figure 5-12.

Figure 5-12. Environment Canada CRUISER mobile emissions measurement laboratory, with the sampling probe raised.

A study in collaboration with Environment Canada was performed in the city of Ottawa, ON, Canada to illustrate the impact of combustion emissions on the black carbon concentration in the urban atmosphere.[182] HS-LII data acquired in a suburban park

demonstrated the low concentration of black carbon present in a traffic-free area, Figure 5-13. The average late afternoon black carbon concentration in this area was 0.47 μg/m^3. In contrast, measurements performed in the urban core, on a transit bus mall during the morning rush hour produced much higher concentrations of black carbon, Figure 5-14. At this location the lowest levels of black carbon were concentrations on the order of 2 μg/m^3 and frequently the air contained levels as high as 8 μg/m^3.

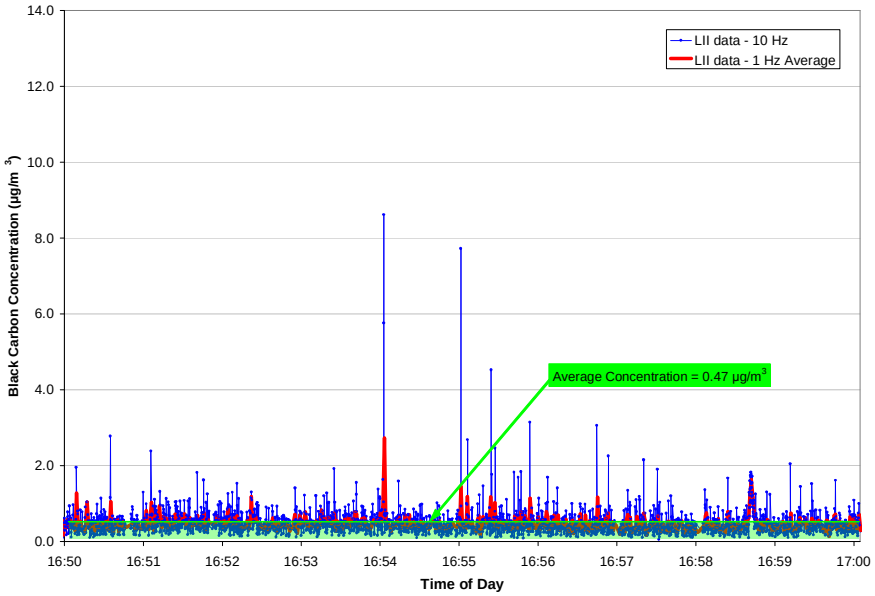

Figure 5-13. HS-LII data recorded in a residential park area.

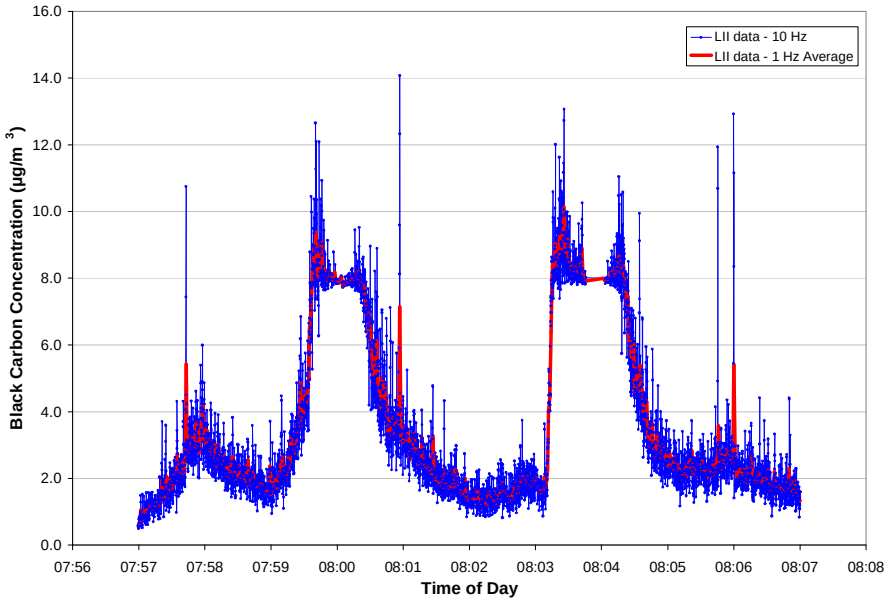

Figure 5-14. HS-LII data recorded roadside in an urban transit bus mall.

These measurements confirmed the sensitivity and measurement capabilities of the HS-LII for making ambient measurements of atmospheric black carbon nanoparticles, and have been recently documented.[182]

5.6. PRIMARY PARTICLE DIAMETER LIMIT

Support was provided to a study of the sooting propensity of dimethyl ether. Although a DME flame has a very visible yellow tip in a laminar diffusion burner, Figure 5-15, it presented difficulties when attempts were made to measure it with line-of-sight attenuation. The soot attenuation was very low and a precise measurement of the soot concentration was not possible. AC-LII measurements with Mobile II were conducted to confirm the presence of soot.

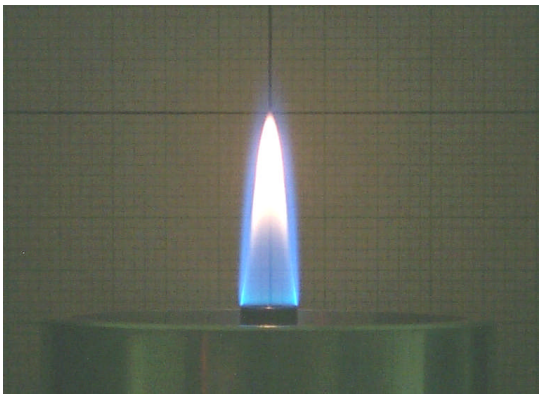

Figure 5-15. Photograph of dimethyl ether (DME) laminar diffusion flame.

The visible yellow-orange region of the flame extends from a height of about 27 mm to 43 mm above the nozzle exit on the centreline. AC-LII measurements were performed at heights of 31 and 35 mm. At the 31 mm height, the concentration was 5.9 ± 0.3 ppb, almost three orders of magnitude lower than in the ethylene LDF at the standard 42 mm centreline position. The primary particle diameter recorded at this location was 4.1 ± 0.5 nm. At the height of 35 mm, the concentration was 22.1 ± 0.8 ppb and the primary particle diameter was 5.8 ± 0.1 nm. These were the smallest primary particle diameters ever recorded with AC-LII, but do not represent a lower limit for the technique. Rather, they are simply the smallest soot particles that have been encountered in measurements with AC-LII.

6. CHALLENGES AND ENHANCEMENTS

There were many instruments for measuring various characteristics of particulate matter, aerosols, and nanoparticles in the marketplace. These instruments were competing for regulatory, monitoring, development, and research applications. As AC-LII measures the soot concentration and primary particle diameter, and there was limited interest in measurements of primary particle diameter from the end use communities, comparisons were made to techniques that are commonly used to determine particle concentration. These included the gravimetric filter method, a regulatory requirement for diesel and gasoline engine emissions, the filter smoke number, the scanning mobility particle sizer, and the photoacoustic soot sensor. Of these, only the photoacoustic soot sensor offered real-time temporal response that was demanded by engine developers and was provided by AC-LII. Most regulations included total particulate matter, whereas AC-LII and other LII techniques responded only to the soot component of PM. However, demand for the measurement of the non-volatile fraction of PM was emerging. AC-LII was a strong candidate for the direct measurement of nonvolatile PM. The comparisons required some modification to the results produced by the other techniques, such as removal of the volatiles from the gravimetric filters for a direct assessment of AC-LII.

Comparison of techniques was difficult, as each technique measured a different characteristic of the particulates, and sampling methods were often different between AC-LII and the techniques it was being evaluated against. Additionally, most of the other techniques are proprietary, with little public knowledge of the detailed physics used to perform the measurements, and no opportunity was found to verify the manufacturers' claims of remarkable accuracy and precision.

There was an additional demand to determine the aggregate size distribution of the nanoparticles from a health and environmental perspective. To address this, the possibility of coupling elastic light scattering with AC-LII to determine aggregate size distributions was investigated as an enhancement to the AC-LII technique. Integrating AC-LII with other diagnostics will also improve the reliability and broaden the utility of AC-LII for the characterization of complex, transient problems such as measurements

for particulate emissions.

6.1. COMPARISON TO COMPETING PARTICLE MEASUREMENT TECHNIQUES

Comparisons to other measurement techniques were made with either Mobile II or the Artium LII 200 instrument as the AC-LII system. In all cases the particulates were measured in a sampling cell on the AC-LII system used, after being transferred from the source through a sampling line.

6.1.1. Gravimetric

For regulatory purposes, particulate matter emissions were defined as the mass of the matter that could be collected from a diluted exhaust stream on a filter. This included the organic compounds that condensed at lower temperatures, but the temperature was maintained sufficiently high (~ 50°C) to avoid the condensation of water. This measurement provided the time-averaged PM emissions over the period during which the particulates were collected on the filter, which made measurements of the transient behaviour of PM emissions impractical. Since the collected PM and other condensed material on the filter agglomerated, it was also impractical to determine the particulate size and size distribution. As diesel engines improved, the quantity of PM generated was reduced, pushing the gravimetric technique nearer to its sensitivity and reproducibility limits. In spite of its drawbacks and limitations, the gravimetric filter technique was the recognized regulatory test method throughout Europe, North America, and Japan for diesel and gasoline vehicles, engines and fuels.

AC-LII was compared to the gravimetric filter technique for a heavy duty diesel single cylinder research engine on an engine dynamometer operating over the AVL 8-mode steady state test procedure. This was performed in collaboration with researchers at the National Research Council Canada (NRC) in Ottawa, ON, Canada.[141] The AC-LII measurements and the gravimetric filter measurements were performed simultaneously, with one filter acquired for each of the eight engine modes and the entire test procedure performed two times. The Mobile II instrument was used for the AC-LII measurements. The engine emissions were diluted with a commercial particulate sampling system (Sierra Instruments Inc., model BG-2). The average AC-LII mass

concentration over the period for which the filters were acquiring PM loading was reported. The comparison of the AC-LII mass concentration to the mass concentration calculated from the gravimetric filter masses is shown in Figure 6-1.[141] The soot mass concentrations measured by the AC-LII method were lower than the PM mass concentrations measured by the gravimetric method at all eight modes. This result was anticipated because the gravimetric method measured the total particulate mass, whereas the AC-LII method measured only the soot mass concentration. Subsequently, the filter samples were subjected to a solvent extraction procedure to remove the volatile material and re-weighed. The resulting mass concentrations were compared to AC-LII as shown previously in Figure 3-30.

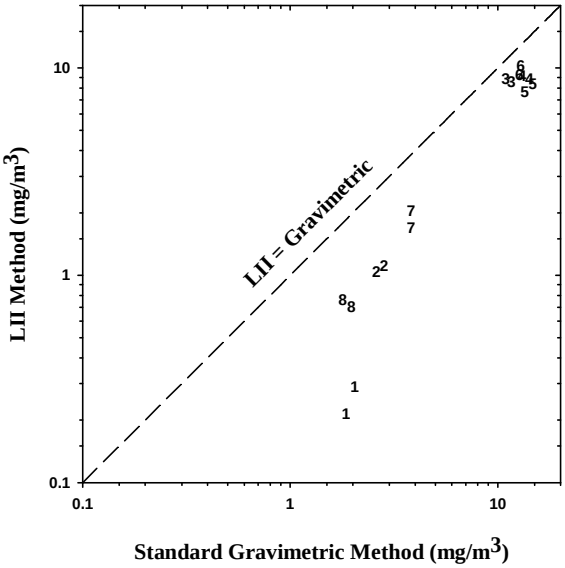

Figure 6-1. Comparison between the mass concentration of soot determined by AC-LII and the concentration of total particulate matter determined by the gravimetric filter method for eight steady state modes on a heavy duty diesel engine. Numerals refer to the mode number.

Although the soot mass concentrations measured by the AC-LII method were still lower than the nonvolatile mass concentrations measured by the gravimetric method, there was a marked improvement in the agreement. The largest difference existed at Mode 1, which is an engine idle condition and produced the lowest quantity of PM of the eight modes. As such, it was at the measurement limit of the gravimetric technique, and the results had large uncertainty. With the more recent discovery that the concentration

measured with AC-LII varied with laser fluence, discussed in Section 3.7.3, it was possible that these measurements were performed with a lower than optimum laser fluence. Unfortunately, at the time these measurements were made the laser fluence was not recorded.

More recent comparisons to the gravimetric technique, performed with a heavy duty diesel engine on an engine dynamometer in collaboration with Cummins and Artium Technologies at the Cummins Technical Center in Columbus, IN, USA.[187] The Artium LII 200 instrument was used for these AC-LII measurements. The measurements were performed on engine emission samples extracted from a constant volume sampling (CVS) dilution tunnel. Modes 1 and 3 were repeats of a high load condition, and modes 2 and 4 were repeats of a low load condition. For these experiments, the volatiles were removed from the filters by supercritical fluid extraction (dry PM). These results demonstrated good agreement at the high load conditions, where about 40% of the total PM was removed as volatiles, Figure 6-2. The total PM at each mode, as well as the brake specific PM emissions, are shown for reference only. However, at the low load conditions, where about 80% if the total PM was removed as volatiles, the AC-LII method was substantially lower than the gravimetric determination of nonvolatile mass.

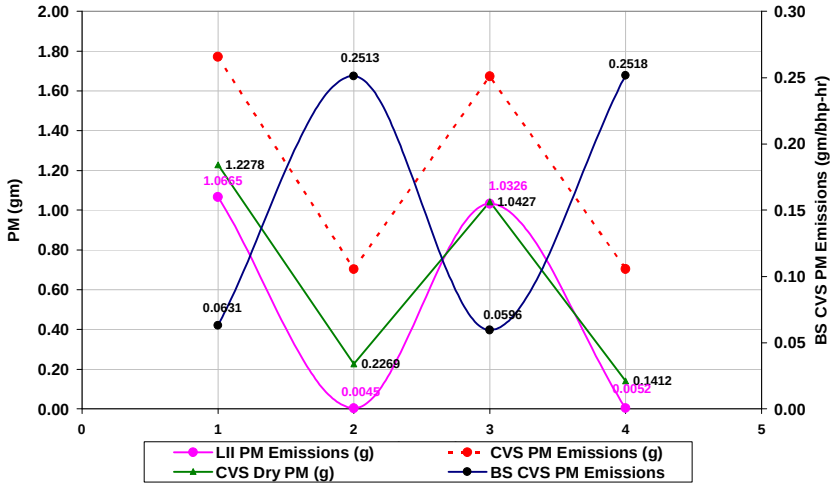

Figure 6-2. Comparison between the mass of soot determined by integrating AC-LII measurements and the mass of dry particulate matter determined by the gravimetric filter method for two steady state modes on a heavy duty diesel engine. The mode number is indicated on the horizontal axis.

Effort was still required to demonstrate that the soot concentration measured by AC-LII was equivalent to the nonvolatile mass measured gravimetrically, and remained a subject for future work. As the techniques were measuring different properties, there may be no reason to have expected complete agreement. The methods for removing the volatiles from filters were laden with problems, plus there was the added difficulty that the filter technique was reaching its measurement limits with these clean diesel engines. These uncertainties, combined with the uncertainties in measurements made with the AC-LII technique, limited the ability to reach complete agreement.

6.1.2. Filter Smoke Number

Comparisons were also made between the AC-LII instrument and the AVL smoke meter for a heavy duty diesel single cylinder research engine on an engine dynamometer operating over the AVL 8-mode steady state test procedure at NRC in Ottawa, ON, Canada.[141] The AVL smoke meter (AVL LIST GmbH, model 415) operates by measuring the reflectance of a filter paper, through which a fixed volume of exhaust gas has passed, to determine the degree of blackening. This reflectance measurement was claimed by the manufacturer to be indicative of the soot loading rather than the total particulate matter. The AC-LII measurements and the filter smoke number (FSN) measurements were performed simultaneously, with one FSN measurement acquired for each of the eight engine modes and the entire test procedure performed two times. The Mobile II instrument was used for the AC-LII measurements. The AVL smoke meter FSN measurements were converted to a mass concentration with a correlation function provided by AVL for the smoke meter. The results shown in Figure 6-3 indicate very good correlation between the two measurements over 2.5 orders of magnitude variation in soot concentration.[141] The solid line in Figure 6-3 represents the regression fit to the data and the dashed line represents perfect agreement between the two methods. Numerals on the graph indicate the data points for each mode of the AVL 8-mode steady state test procedure.

The most significant discrepancies between the AC-LII and AVL smoke meter determinations of mass concentration were at the lowest concentrations, where the AVL smoke meter was at its sensitivity limit, and had limited measurement resolution. This demonstrated a distinct advantage of AC-LII, which had high sensitivity to low soot

concentrations.

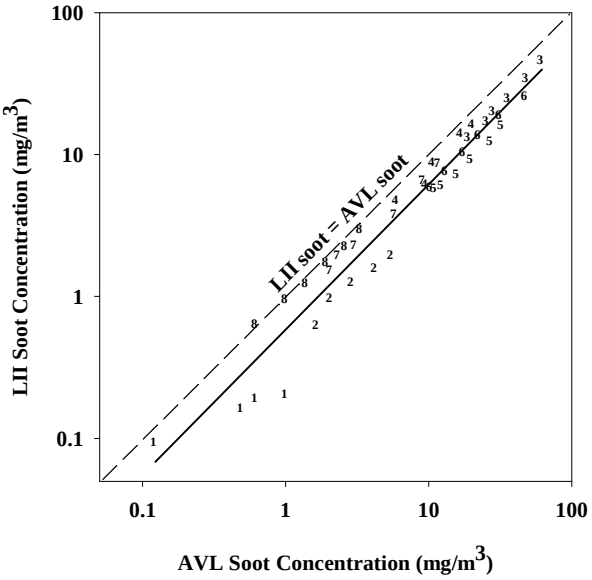

Figure 6-3. Comparison of the soot concentration measured with AC-LII and the AVL smoke meter for the AVL 8-mode steady state test procedure on a heavy duty diesel engine. Numerals refer to the mode number.

6.1.3. Scanning Mobility Particle Sizer

The effects of aggregation in diesel particulate emissions were investigated using two contrasting techniques, autocompensating laser-induced incandescence and the scanning-mobility particle sizer (SMPS). The SMPS[188] was essentially an automated version of a differential mobility analyzer (DMA)[189] and was used by many researchers studying particulate emissions. While AC-LII gave a direct measure of the soot concentration, the SMPS measured the mobility diameter of the total particulate matter. A quantitative comparison of these two techniques, for which there was no evidence in the literature, was performed. During the course of this work a comparison between conventional LII and SMPS emerged that studied sampling effects and laser heating effects on the measured size distribution.[190] Significant detail on the comparison is provided in the sections below as the SMPS was claimed to be capable of measuring volume and mass concentration, and this was discovered to be invalid. This research was performed in collaboration with Sandia National Laboratories and Artium Technologies at Sandia's laboratory in Livermore, CA, USA, with the Mobile II AC-LII

instrument.[28]

6.1.3.1. Experimental

6.1.3.1.1. Engine

The measurements were made on a 1996 Volkswagen 1.9-L TDI diesel engine on an engine dynamometer. The steady-state speed and load operating conditions that were investigated and the variation in exhaust gas recirculation (EGR) for each operating condition are summarized in Table 6-1. The carbon content of diesel PM increases dramatically with EGR, from levels of about 50% to as much as 90% by mass,[191] which made EGR an interesting variable in performing the comparison.

Table 6-1. Steady-State Engine Conditions

Engine Speed (RPM)	Load (N•m)	EGR Range (%)
1100	53	1 – 44
	63	0 – 40
	75	0 – 37
1500	52	2 – 30
	66	0 – 26
	81	0 – 16
2000	53	3 – 36
	63	0 – 34

The engine exhaust was sampled just downstream of the turbocharger and was diluted as dilution was required for the SMPS instrument, which was limited in the number concentration of particles it could measure. The AC-LII and SMPS measurements were performed simultaneously. The AC-LII optical sample cell was heated to prevent water condensation on the windows.

6.1.3.1.2. Scanning mobility particle sizer

For the measurement of PM size distributions, under steady-state conditions, the SMPS was considered by some to be the instrument of choice.[26] The SMPS worked on the principle of using an electric field to laterally move the charged particles in a laminar flow. For a polydisperse aerosol, the strength of the electric field determined the size of particles extracted through a small slit to produce a monodisperse aerosol that flowed to a condensation particle counter to obtain the particle concentration. The electric field strength was scanned so that a polydisperse aerosol was separated into as many as 64 discrete size bins for each decade of particle diameter. A typical scan time was one minute. A TSI SMPS Model 3936L25, with DMA (differential mobility analyzer) Model 3081 and CPC (condensation particle counter) Model 3025A-S, was used.

The response of small, charged particles in an aerosol to an electric field was very fast, such that PM-size particles reached their terminal velocity in less than a microsecond.[24] As a consequence, the mobility of particles through the gas was independent of particle density and governed only by the drag force on the particle given by Stokes law. This behaviour was characterized by a particle's electrical mobility Z_p, defined as

$$Z_p = \frac{neC}{3\pi\mu D_m} \tag{46}$$

where n was the number of elementary charges on the particle, e was the elementary charge, C was the Cunningham correction factor for non-continuum effects, μ was the gas viscosity, and D_m was the particle mobility diameter. It was inherent in this definition, as well as in the calibration of an SMPS, that the particles were spherical. Because this was not the case for PM aggregates, the size measured was presumed to be the diameter of an equivalent sphere having the same drag as the aggregate.

6.1.3.2. Theory: Space-filling Volume Fraction

In general, the equivalent sphere defined by the mobility diameter as measured by SMPS had considerably greater volume than was actually contained in a PM aggregate due to the presence of voids within the equivalent sphere. By defining a space-filling volume fraction ν_s, it followed that the volume of the aggregate V_a occupied by bulk material contributing significantly to the mass of the particle was

$$V_a = \nu_s \pi D_m^3 / 6 \,. \tag{47}$$

This definition assumed that the void volume consisted of the interstices between primary particles, but neglected their porosity. As such, V_a also represented the volume to which AC-LII is sensitive. When comparing SMPS measurements to measurements of the PM volume (or mass) concentration, this effect was taken into account.

A similar issue occurs when measurements made with an ELPI were compared with SMPS results. The ELPI separated particles by inertial impaction, and thus gave a measure of effective aerodynamic diameter, or particle mass. Ahlvik *et al.*[192] and Maricq *et al.*[193] used concurrent ELPI and SMPS measurements to estimate an effective density correction for diesel PM mobility size measurements. Their results are shown in Figure 6-4 reformulated as a space-filling volume fraction, which was used as a correction factor for mobility-volume, where the solid line was an empirical fit to their data of the form

$$\nu_s = 0.58\left(3 - log_{10} D_m\right)^{2.4} + 0.013 \tag{48}$$

for 56 nm $\leq D_m \leq$ 1000 nm. The constant 0.013 in Eq. (48) was an offset estimated by assuming that in the limit of large D_m the mobility-volume correction factor should asymptotically approach a value compatible with the fractal characterization of aggregates. This analysis suggested that a mobility diameter of 400 nm for an aggregate actually contained only about 10% space-filling material.

To estimate whether this result was reasonable, these results were converted to a fractal dimension following the analysis of Köylü et al.[148] The number N_p of primary particles of diameter d_p in a soot aggregate was expressed as

$$N_p = k_L \left(\frac{L_{ag}}{d_p} \right)^{D_f} \tag{49}$$

where k_L was a fractal prefactor and L_{ag} was the maximum dimension of an aggregate (Feret's diameter) obtained from transmission electron microscopy (TEM). Eq. (49) was reformulated to give

$$\nu_s = k_L \left(\frac{D_m}{d_p} \right)^{D_f - 3} \tag{50}$$

for $D_m \geq d_p$, where it was assumed that D_m was analogous to L_{ag}. Köylü *et al.*[148] measured d_f and k_L for a number of positions along a flame centreline and report average values of 1.72 and 1.44, respectively. Because the primary particle diameter d_p varied with position in the flame, and directly influenced the value for k_L, the median value of d_p=26 nm found by Köylü *et al.*[148] was chosen for this analysis. Using the values just cited, evaluation of Eq. (50) for D_m=1000 nm gave ν_s=0.013, the offset used in Eq. (48).

An alternate approach for determining the space-filling volume fraction that also accounts for the fractal nature of the aggregates was presented by Wang and Sorensen.[194] Their method treated the particulates as diffusion-limited cluster aggregates (DLCA), and offered a more rigorous solution, as it had the correct limit as the number of primary particles in the aggregate approached one, and only followed a true fractal behaviour when the number of primary particles in the aggregate exceeded ~60.[195] In the small aggregate case, the mobility diameter was found to depend only upon the primary particle diameter and the number of primary particles per aggregate,

$$D_m = d_p N_p^{0.44}; \qquad N_p \leq 60 \tag{51}$$

whereas in the large aggregate case the fractal dependence was exhibited as

$$N_p = k_0 \left(\frac{D_m}{0.7 d_p} \right)^{D_f}; \qquad N_p > 60 \tag{52}$$

where $k_0 \approx 1.3$ and the fractal dimension was 1.75.[195] Equations (51) and (52) were reformulated to give

$$\nu_s = N_p^{-0.33}; \qquad N_p \leq 60 \tag{53}$$

$$\nu_s = 4.6 N_p^{-0.71}; \qquad N_p > 60 \tag{54}$$

Results for Eqs. (48), (50), and (53) and (54) are presented in Figure 6-4, together with the measurements of Ahlvik *et al.*,[192] Maricq *et al.*,[193] and McMurry *et al.*[196] These data suggested that the larger the PM aggregate, the greater the void fraction. The

measurements of McMurry *et al.*[196] with an aerosol particle mass analyzer (APM) were for urban atmospheric aerosols, which were hypothesized to consist of aggregate soot. McMurry *et al.*[196] note that Ahlvik *et al.*[192] found "effective densities" for diesel soot that were significantly higher than their measured values, which may have been due to the technique for determining these values. The method of Wang and Sorensen[194] also considered Knudsen number effects, which were not addressed in the references that led to Eqs. (48) and (50).[148, 192, 193] The Knudsen number was important in determining the diffusive transport properties of fractal aggregates, and thus their diffusive mobility.

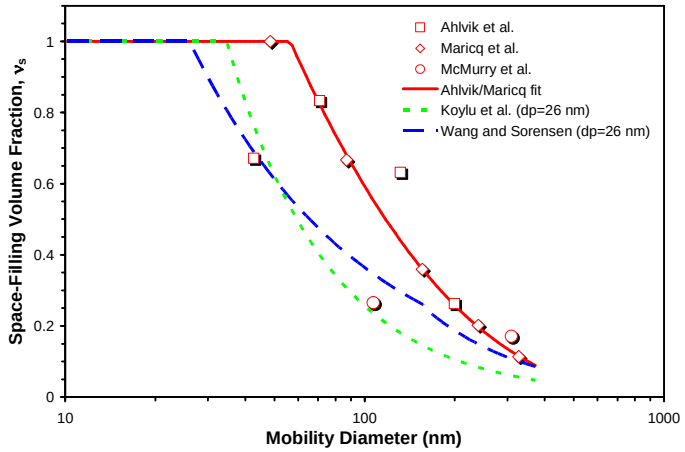

Figure 6-4: Estimates of the space-filling volume fraction from SMPS/ELPI/APM measurements (symbols; solid line for Eq. (48)) fractal analysis (dotted line for Eq. (50)), and DLCA analysis (dashed line for Eqs. (53) and (54)).

Klingen and Roth[197] used scanning electron microscopy to investigate the exhaust PM from a prechamber diesel engine and found fractal dimensions that varied from 1.12 to 1.2, which were considerably smaller than the values used for Figure 6-4. In contrast, Skillas *et al.*[198] found fractal dimensions ranging from 2.2 to 2.8 for a diesel electrical power generator, which were considerably larger than the values used for Figure 6-4. They used concurrent inertial low-pressure impactor and differential mobility analyzer measurements to obtain their results. Lee *et al.*[199] presented results that supported the use of the fractal dimensions and primary particle sizes selected for the above analyses, as they found similar values from TEM analyses of particulate samples extracted from

diesel exhaust over a wide range of engine operating conditions.

6.1.3.3. Results

6.1.3.3.1. SMPS Results

Typical size distribution results from the SMPS are presented in Figure 6-5 for the 1100 RPM, 63 Nm torque engine condition and a range of EGR rates. The solid lines indicate the analytic log-normal distribution obtained from the measured geometric mean D_g and standard deviation $\sigma_{D,g}$. Integration of the area under the distributions gave the cumulative volume fraction, as shown in Figure 6-6(a) for the data in Figure 6-5. In Figure 6-6(b) the same calculations are shown, except corrected for the space-filling volume fraction in the SMPS mobility diameter as expressed by Eq. (48). This reduced the volume fraction by approximately a factor of four. Similar effects were observed for the corrections for void volume expressed in Eqs. (50), and (53) and (54), shown in Figure 6-6 (c) and (d), respectively. Subsequent results did not have this correction applied, except when explicitly stated.

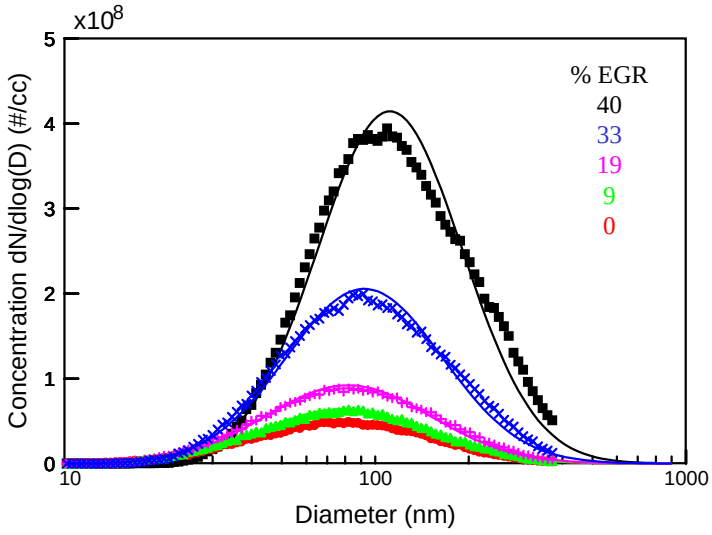

Figure 6-5: SMPS measurements (symbols) of particle size compared with log-normal distributions (lines).

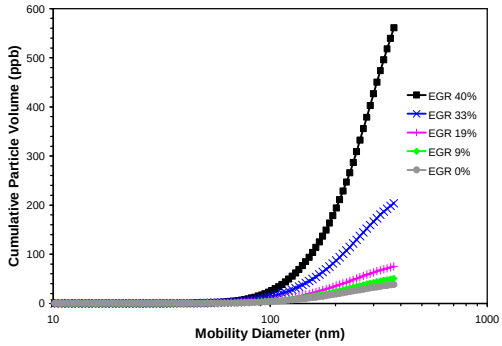

(a) Uncorrected for mobility-volume voids

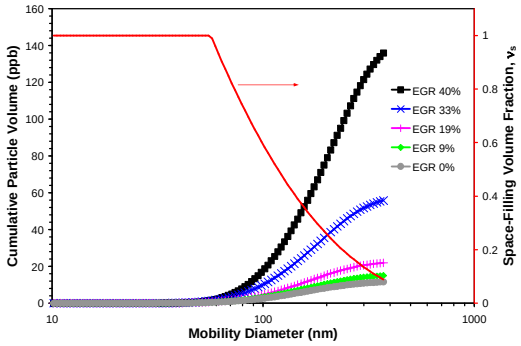

(b) Corrected for mobility-volume voids using Eq. (48)

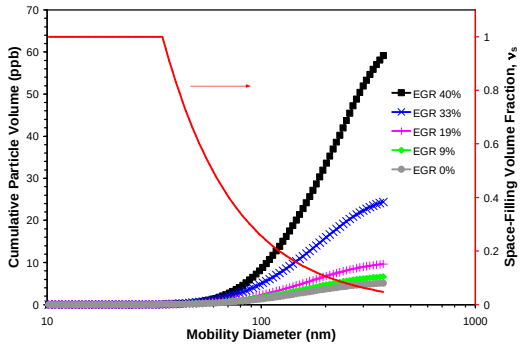

(c) Corrected for mobility-volume voids using Eq. (50)

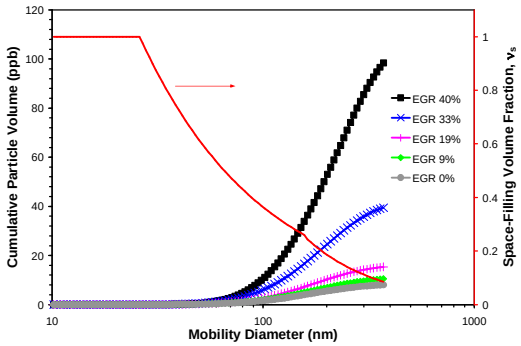

(d) Corrected for mobility-volume voids using Eqs. (53) and (54)

Figure 6-6: Cumulative volume fraction determined from the SMPS data in Figure 6-5(b) (1100 RPM, 63 N·m torque).

6.1.3.3.2. AC-LII Results

The AC-LII measurements were obtained for 400-pulse averages, resulting in a 20 second acquisition period for each steady-state engine operating condition. Soot concentration measurements obtained from AC-LII for all engine speed, load, and EGR conditions investigated are presented in Figure 6-7. With increasing EGR the soot concentration gradually increased up to an EGR rate of 20-25%, beyond which the soot emissions rapidly increased.

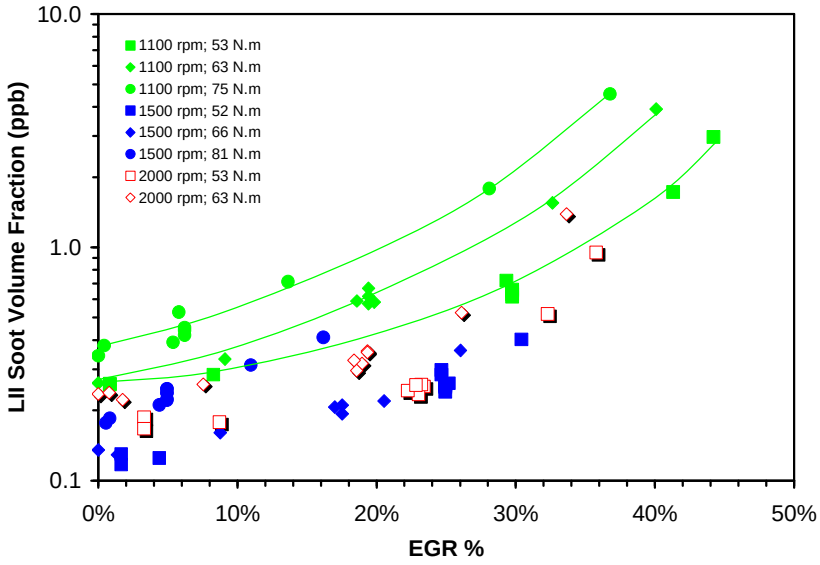

Figure 6-7: Soot concentration as determined by AC-LII at various EGR rates, for a range of engine speeds and loads.

6.1.3.3.3. AC-LII vs. SMPS results

The AC-LII and SMPS volume fractions acquired for all engine conditions were directly compared in Figure 6-8. The raw, uncorrected data showed a near-linear behaviour over a range of nearly two decades, but a significant difference in magnitude. A best fit to the data resulted in a correction factor of 12.7 that was applied to reduce the SMPS measurements to values comparable to the AC-LII results. The standard error of this correction factor was less than 2%, indicating the degree of consistency between the two techniques. This implied that there was a strong relationship between the physical quantities actually measured by the two techniques. The mobility-volume corrections proposed by Eqs. (48), (50), and (53) and (54), also shown in Figure 6-8, did not fully account for the differences between SMPS and AC-LII, particularly for the smaller volume fractions. In addition, their application significantly increased the overall scatter of the measurements and introduced non-linear behaviour. In contrast, simply dividing the SMPS measurements by the factor of 12.7 yielded a far better result, suggesting that the aggregates were not fractal-like throughout the entire size range, which was consistent with the DLCA formulation presented by Wang and Sorenson[194] that only showed a true fractal behaviour for large aggregates.

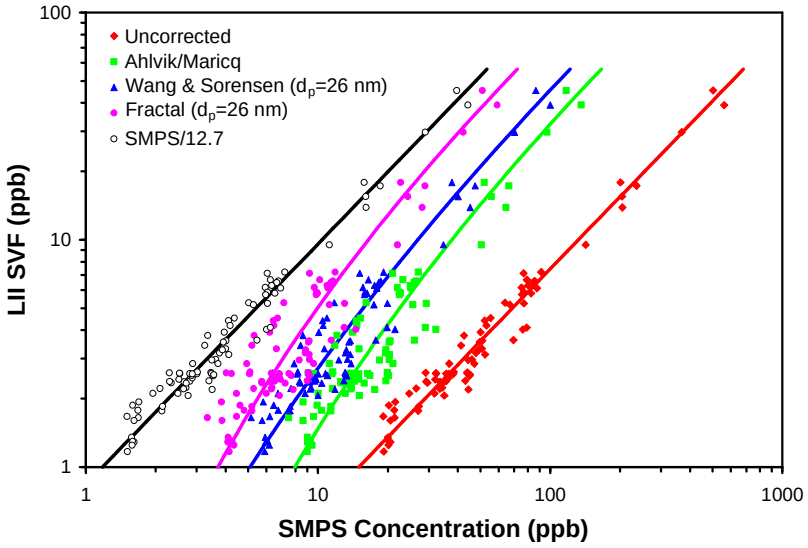

Figure 6-8: Comparison of AC-LII and SMPS volume fraction measurements, together with corrected measurements using Eqs. (48), (50), and (53) and (54), and a scaling factor of 12.7. The lines are quadratic fits performed in the log domain.

An alternate interpretation of the data shown in Figure 6-8 was that the corrected results (fractal and DLCA analyses) revealed the expected trends between AC-LII and SMPS measurements. If, as shown by Ladommatos *et al.*,[191] the mass percentage of volatiles decreased from ~50% with no EGR to <10% with high EGR, there should have been a nonlinear trend of larger SMPS measurements relative to AC-LII at low PM concentrations. The low concentrations corresponded to low EGR levels, where a higher proportion of volatiles was anticipated than at higher EGR levels. However, the space-filling volume fraction correction had the opposite effect of larger corrections to the SMPS measurements at high PM concentrations corresponding to larger mobility diameters. These offsetting effects could have resulted in the appearance of the near-linear behaviour of the uncorrected AC-LII and SMPS results shown in Figure 6-8, even though there was no physical reason for such a relationship.

In summary, it was determined that the fractal nature of the aggregate morphology must be accounted for with SMPS measurements. The equivalent sphere based on the mobility diameter grossly overestimated the volume of particulates. SMPS correction algorithms for aggregated particles were formulated, resulting in substantial reductions

in the measured volume fractions. Although the AC-LII and SMPS measurements were consistent with each other for all the engine conditions, the uncorrected results for the SMPS concentrations were greater than those for AC-LII by a factor of 12.7.

6.1.4. Photoacoustic

Instruments such as the aethelometer and photoacoustic soot spectrometer claim to respond only to black carbon, but have recently been discovered to suffer interference from the presence of condensed volatile species.[200] AC-LII also claimed to have the selectivity to measure the concentration of soot particles in the presence of volatiles. A comparison between the DRI Photoacoustic Instrument and HS-LII was performed on atmospheric particulates sampled from ambient air in an urban location at the laboratories of Environment Canada in Toronto, ON, Canada.[182]

The experiments were conducted on the CRUISER mobile laboratory vehicle (described in Section 5.5) in a stationary location. The instruments available on CRUISER included an Aerodyne AMS aerosol mass spectrometer which is capable of identifying and quantifying the species and concentration, respectively, of volatile aerosol particles. CRUISER was also equipped with a thermodenuder, which was a device for heating aerosols and stripping away the volatile compounds. An automated valve was installed in the particulate sampling line to alternate between sending fresh sample or thermodenuded sample to the measurement instruments at 5 minute intervals. The thermodenuder removed 50-80% of the volatiles, as measured by the AMS. The AMS results were averaged. presenting just one data point for each 5 minute interval. This is illustrated in Figure 6-9, where the concentrations of organics, sulphates, and nitrates as measured by the AMS were dramatically lower at alternate 5 minute intervals, when the sample was passed through the thermodenuder.

The photoacoustic instrument and HS-LII were operated simultaneously, sampling from the same line as the AMS. The results for the photoacoustic instrument are shown in Figure 6-9, where it was observed that the photoacoustic signal followed the same 5 minute interval pattern as the AMS. This indicated that despite the claim that the photoacoustic instrument only responded to black carbon, it was clearly influenced by the presence of volatile species.

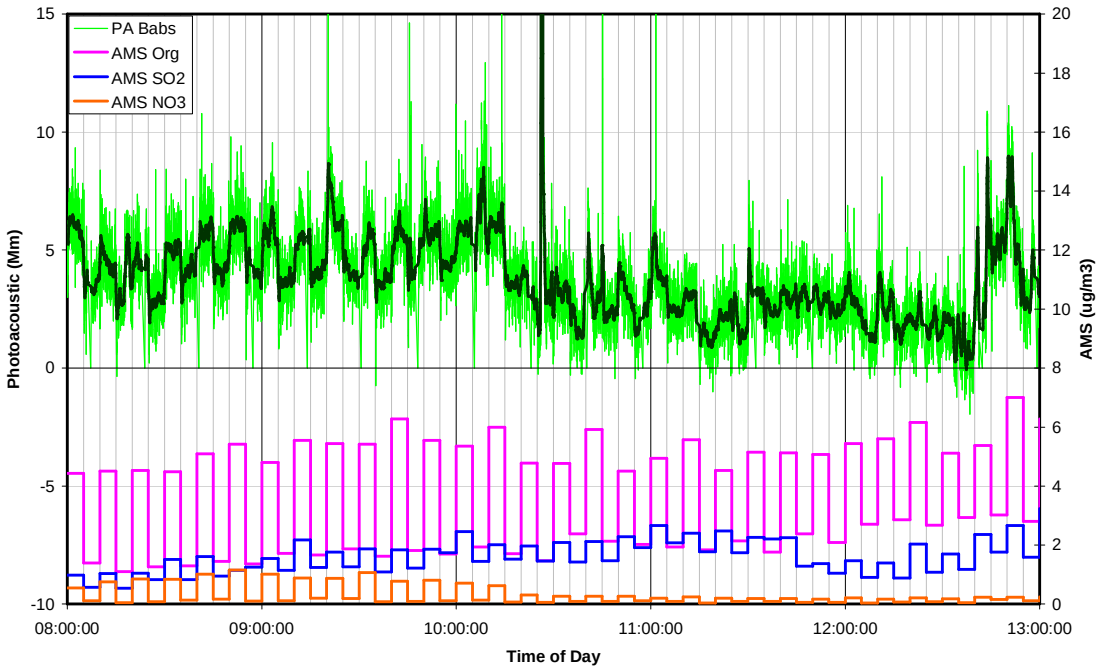

Figure 6-9. Photoacoustic instrument measurements of black carbon in an urban environment compared with AMS measurements of volatile species, alternating with and without a denuder at 5 minute intervals.

The HS-LII measurements were averaged at 1 minute intervals, and due to problems with the laser power supply, a continuous stream of data could not be acquired. However, sufficient data was recorded to demonstrate that the HS-LII instrument was not affected by the sudden changes in volatile concentration that were observed with the photoacoustic instrument. The HS-LII data is shown in Figure 6-10. The concentrations recorded by HS-LII were in the range 0.03 to 0.3 μg/m^3 over the five hours of data presented, and the combination of organic, sulphate, and nitrate volatile species were in the range of 6-8 μg/m^3 over the same period when not being removed by the thermodenuder. Throughout this experiment the black carbon concentration was less than 5% of the volatile concentration, yet the measurement of black carbon with HS-LII was as expected, unaffected by the overwhelming presence of volatiles.

Both instruments reported a long term drift in the atmospheric concentration of black carbon, as the concentration gradually declined between 10:00 and 12:30, and rose more quickly between 12:30 and 13:00.

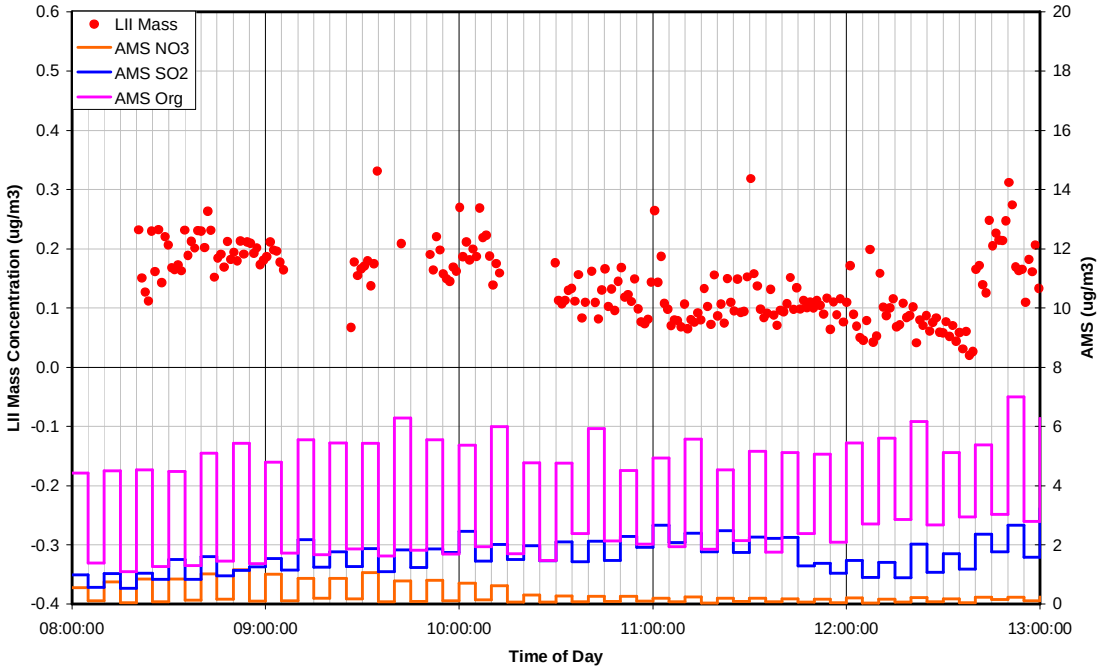

Figure 6-10. HS-LII measurements of black carbon in an urban environment compared with AMS measurements of volatile species, alternating with and without a denuder at 5 minute intervals.

To further verify that AC-LII has high selectivity and responds directly to the concentration of soot, a series of measurements were performed at Southwest Research Laboratories in San Antonio, TX, USA. The soot concentration as measured by the Artium LII 200 instrument was compared to the elemental carbon (EC) concentration measured with the Sunset Laboratory Carbon Aerosol Analysis Field Instrument, which used the NIOSH 5040 thermo-optical method[201] to determine the EC concentration. The source of particles was a Jing Ltd. mini-CAST soot aerosol generator, which produced a repeatable stream of soot particles at near-ambient temperatures and a wide range of concentrations.

The LII 200 was operated at 20 Hz for the duration of each collection by the Sunset Laoratory instrument, which varied from 60 s at the highest concentrations to over 2000 s at the lower concentrations. The results of the measurements are shown in Figure 6-11. The data from the LII 200 instrument demonstrated excellent linearity with the EC concentration determined by the NIOSH 5040 method, which further confirmed that

AC-LII responded directly to soot particles.[182] The LII data was about 30% high than the EC data at all concentrations, which indicated that there was a need for improvement in terms of the calibration constant or the $E(m)$ used with the LII 200 instrument.

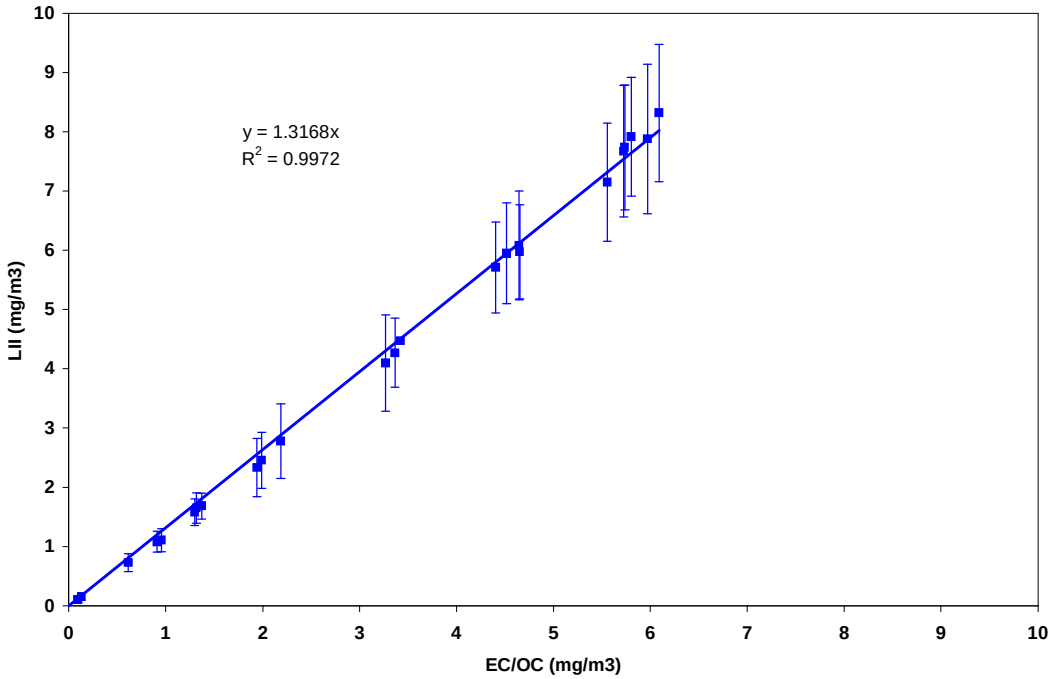

Figure 6-11. AC-LII measurements of soot concentration compared to elemental carbon concentration determined by the NIOSH 5040 method. Error bars represent a single standard deviation of the single shot AC-LII measurements.

6.2. LASER LIGHT SCATTERING TO MEASURE AGGREGATE SIZE

The combination of auto-compensating laser-induced incandescence (AC-LII) measurements and laser elastic light scattering (ELS) measurements optimized for aggregates had the potential to simultaneously determine the aggregate size distribution, the mean primary particle diameter, soot volume fraction, and the active surface area for an ensemble of nanoparticles at the probe volume of the instrument with a single measurement. This was a significant enhancement in the capability for the real-time characterization of soot nanoparticles, as details of the morphology of soot/black carbon aggregates were necessary to assess the health and environmental impacts of these nanoparticles.

6.2.1. Development

Elastic light scattering (ELS) employing Rayleigh-Debye-Gans polydisperse fractal aggregate (RDG-PFA) theory to interpret scattered laser light is an appropriate technique for the study of soot aggregates.[202] In the RDG-PFA approach, the aggregate differential scattering cross-section, σ_{ag}

$$\sigma_{ag} = N_p^{\,2} \frac{\pi^4 d_p^{\,6} F(m)}{4\lambda^4} S(q, R_g) \tag{55}$$

was defined in terms of the number of primary particles per aggregate, the primary particle diameter, the scattering function, $F(m)$, and the structure factor, $S(q,R_g)$. The structure factor was a function of the fractal radius of gyration, R_g and the scattering vector, $q(\theta)$

$$q(\theta) = \frac{4\pi}{\lambda} \sin\left(\frac{\theta}{2}\right) \tag{56}$$

where θ is the scattering angle. The structure factor $S(q, R_g)$ was calculated numerically using the confluent hypergeometric approach,[202] which assumed a Gaussian fractal cut-off. For a distribution of aggregates the scattering cross-section was integrated over an appropriate distribution function. The lognormal distribution where N_g was the geometric mean aggregate size and $\sigma_{N,g}$ was the distribution width was an appropriate distribution function for N, the number of primary particles per aggregate. To derive N_g from the ratio of soot scattering to AC-LII intensity and the known soot scattering and absorption functions a distribution width $\sigma_{N,g}$ was assumed.

Sorensen[202] had shown that a self preserving or scaling distribution gave a more accurate description of the higher moments that describe scattering than did a lognormal distribution. A self preserving distribution was theoretically predicted from solving the aggregate coagulation equations over a wide range of conditions, and an aggregating system would develop a self preserving scaling distribution. Lognormal distribution moments with a width of $\sigma_{N,g} \sim 2.5$ were in best agreement with the scaling distribution up to the third moment, which provided a reasonable approximation for the true distribution width. This was confirmed with experimental evidence for flame soot where $\sigma_{N,g} \sim 2.6$, used for subsequent analysis

The volumetric scattering coefficient, C_{vol}, was dependent upon the scattering function which had a relatively high uncertainty (with complex index of refraction m)

$$C_{vol} = N_{ag}\sigma_{ag} = \int_1^\infty p(N_p) N_p{}^2 \frac{\pi^4 d_p{}^6 F\left(m_{532}\right)}{4\lambda^4} S\left(q, R_g\right) dN_p \frac{f_V 10^{-6}}{\frac{\pi d_p{}^3}{6} N_g \exp\left(0.5 \ln\left(\sigma_{N,g}\right)^2\right)} \tag{57}$$

However, the $F(m)/E(m)$ ratio at 532 nm for soot has been summarized with $F(m_{532})/E(m_{532}) = 1.1$ for a wide range of flame conditions, and this ratio has far less uncertainty.[130] Also, the soot volume fraction from AC-LII was inversely proportional to the value of the absorption function, $E(m)$, assumed at the AC-LII wavelengths. This allowed substitution of the value of $E(m)$ and the ratio $F(m)/E(m)$ at 532 nm to replace the lack of knowledge of the absolute values of the coefficients. The volumetric scattering coefficient was then

$$C_{vol} = \int_1^\infty p(N_p) N_p{}^2 \frac{\pi^4 d_p{}^6 F\left(m_{532}\right)}{4\lambda^4 E\left(m_{532}\right)} S\left(q, R_g\right) dN_p \frac{f_V 10^{-6} E\left(m_{532}\right)}{\frac{\pi d_p{}^3}{6} N_g \exp\left(0.5 \ln\left(\sigma_{N,g}\right)^2\right)} \tag{58}$$

For this analysis $E(m)$ was assumed constant from 400 to 780 nm. The apparatus for the combined AC-LII/ELS technique is shown in Figure 6-12. This was a variant of the Mobile II design which utilized a frequency-doubled 532 nm Nd:YAG laser, added collection optics and a fibre-optic transfer cable so that signals were recorded from a near-forward or a near-backward location, and added a 532 nm detector and associated dichroics and interference filters to the demultiplexer. The 532 nm wavelength was selected to increase the scattered laser light, and due to the availability of higher sensitivity detectors, both relative to 1064 nm.

This technique was applied to the laminar diffusion flame. The AC-LII and ELS measurements were performed sequentially in this investigation. The volumetric scattering coefficient was measured for near-forward scattering ($\theta = 35°$) and near-backward scattering ($\theta = 145°$), as shown in Figure 6-13 over a range of low to moderate fluence conditions.

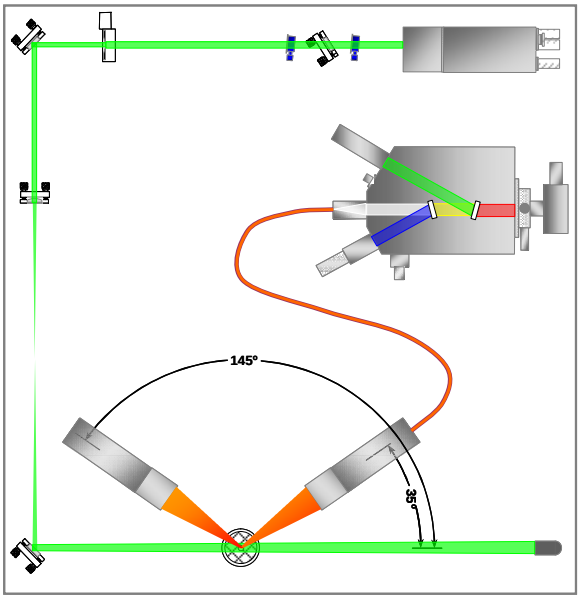

Figure 6-12. Combined AC-LII and ELS apparatus

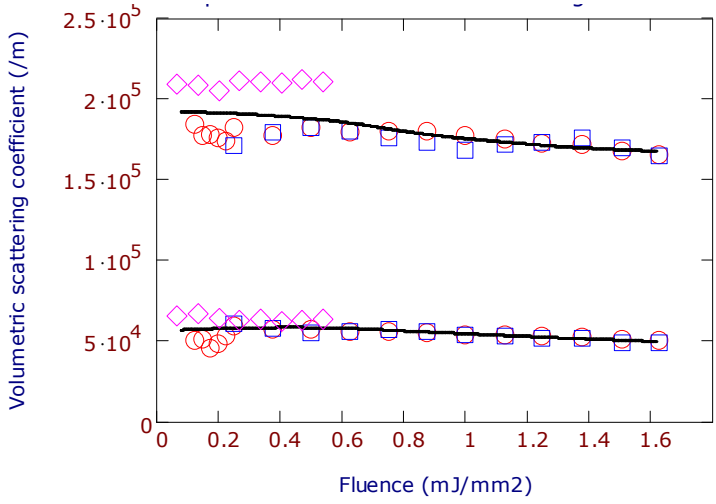

Figure 6-13. The volumetric scattering coefficient for near-forward scattering (35°, upper curve) and near-backward scattering (145°, lower curve) for three identical experiments in the LDF.

The results indicated that there was little effect of fluence on the scattering measurement, as the forward-to-backward ratio was relatively constant except at fluences below 0.3 mJ/mm^2. The forward-to-backward ratio gives an independent estimate of aggregate size and requires no *a priori* knowledge of the scattering function.

Analysis was performed to predict N_g from the scattering measurements. The data from AC-LII and forward scattering resulted in an average measured low fluence C_{vol}/f_V ratio of 1.91 at 35°. With a primary particle diameter from TEM analysis and also measured with AC-LII of 29 nm, the predicted N_g ~ 18, as shown in Figure 6-14. The near-backward scattering data was also analyzed, and it was found that it was insensitive to N_g but varied with d_p (not shown).

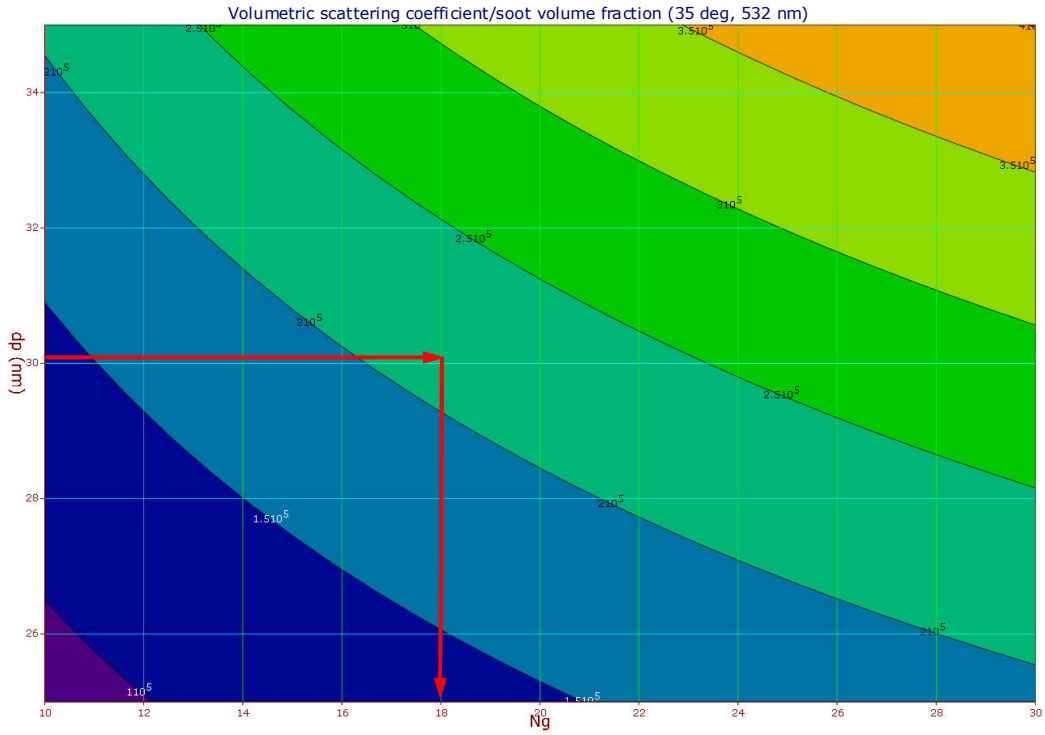

Figure 6-14. Volumetric scattering coefficient/soot volume fraction, C_{vol}/f_V , ratios calculated for a range of d_p and N_g values typical for soot in the LDF. Red arrows indicate experimental data for d_p and C_{vol}/f_V. Colour contours indicate d_p and N_g pairs producing a constant ratio.

Similar analysis was performed for the data from forward/backward scattering ratio which resulted in an average ratio of 3.25 at 35° and 145°. With the same primary particle diameter of 29 nm, the predicted N_g ~ 19, as shown in Figure 6-15.

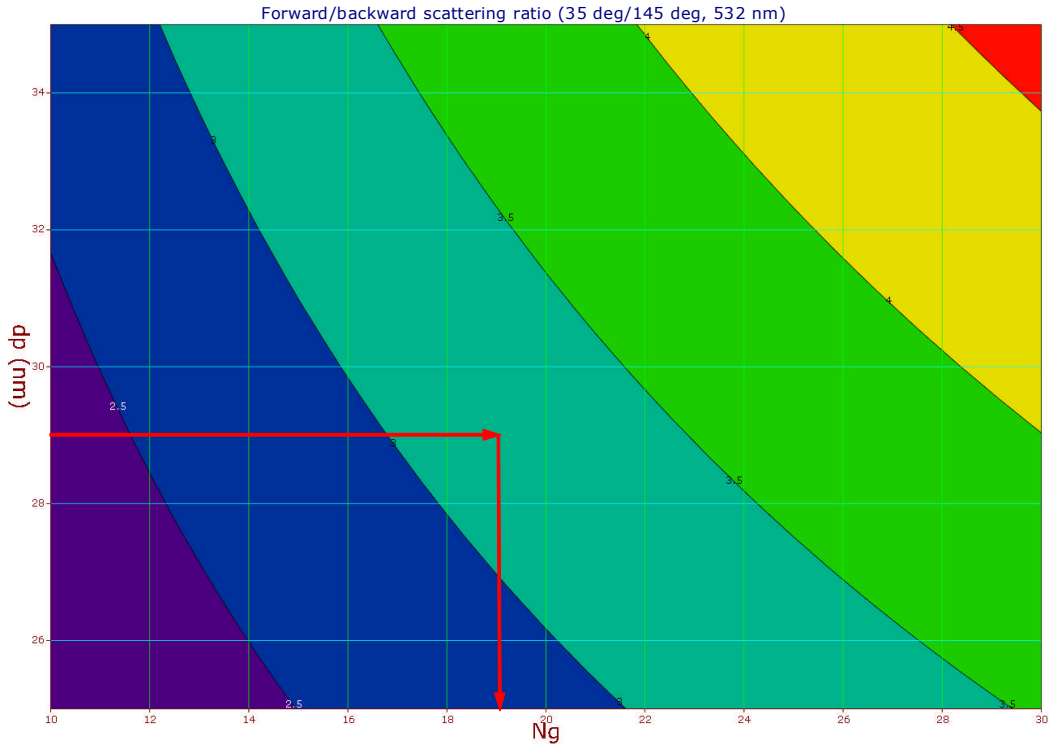

Figure 6-15. Forward/backward ratios of the volumetric scattering coefficients calculated for a range of d_p and N_g values typical for soot in the LDF. Red arrows indicate experimental data for d_p and the forward/backward scattering ratio. Colour contours indicate d_p and N_g pairs producing a constant ratio.

The N_g results from these preliminary scattering measurements are in reasonable agreement with the TEM-derived N_g value of 21 primary particles per aggregate. It has been demonstrated that an estimate of the mean aggregate size of an assumed lognormal distribution of aggregates can be derived based on the ratio of laser scattering to LII signal, or from the forward/backward scattering ratio.

Many issues remain to be resolved with the development of a combined AC-LII/scattering technique for measuring soot morphology. They include:

(a) Simultaneous measurement of the AC-LII and scattering signals to ensure that the same nanoparticles in the probe volume are being assessed by both techniques.

(b) Extending the range of applicability of the RDG-PFA theory to particles as large as several hundred nanometres in size. This requires changing the laser wavelength from 532 nm to 1064 nm so that the size parameter, x_p, of the nanoparticles will be less then 1 over a wider range of sizes.

(c) Optimization of forward and backward scattering angles requires investigation to determine the appropriate angles for use in measuring combustion-generated aggregated soot nanoparticles.

(d) Scattering responds to all the particles in the probe volume, whereas AC-LII only measures the soot particles. A method of removing volatile particles from the sample without affecting the soot aggregates is required.

(e) The use of an optical sampling cell with windows for practical applications poses challenges for the scattering technique due to secondary scattering of laser light from the window surfaces, and requires investigation.

(f) It is possible that sampling procedures to bring the particulate sample to the probe volume affect the soot aggregates. Such effects, such as coagulation and agglomeration need to be studied.

6.2.2. Demonstration Application

6.2.2.1. Aggregate Morphology with AC-LII and Elastic Light Scattering

Despite the limitations noted above, a preliminary application of simultaneous combined AC-LII/ELS was made.[203] This required the many assumptions noted above, including assumed fractal parameters, assumed a lognormal distribution of N_p, and assumed a value for $\sigma_{N,g}$. Although this is a large number of assumptions, there may be enough evidence to support these assumptions in some circumstances.

In this approach, the near-forward 35° 532 nm scattering was recorded with the AC-LII data. One difference from the study in the LDF was that the results were iterated, using the N_g determined from the C_{vol}/f_V ratio to correct the value for d_p determined from LII (assuming monodisperse primary particles). This was performed using the normalized surface area available for heat transfer.[109] With the new estimate of d_p a new value for

N_g was determined from the C_{vol}/f_V ratio, and the process was repeated until convergence was obtained.

These preliminary results are for data acquired in the exhaust of a direct-injection spark-ignition (DISI) engined automobile. The vehicle was subjected to a load of 3 hp on a chassis dynamometer, and the engine was held at a constant 1700 RPM. The scattering detector was calibrated by measuring the scattering from HEPA-filtered air as a reference value.

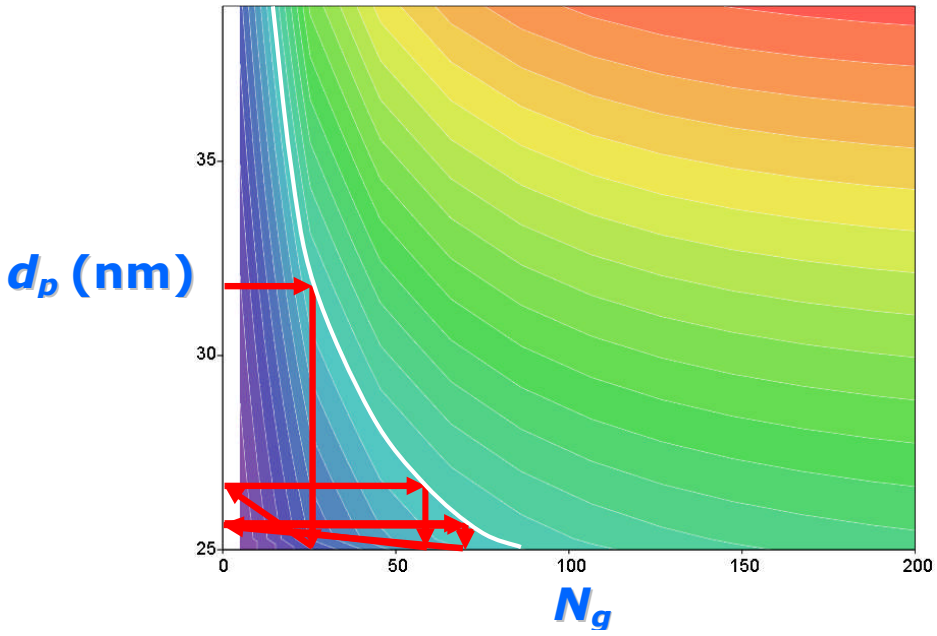

Figure 6-16. Preliminary determination of N_g and an aggregate size corrected value for d_p, using iteration, based on combined AC-LII/ELS. Red arrows indicate the iterative values. Colour contours indicate d_p and N_g pairs producing a constant ratio.

The results are shown in Figure 6-16, where the contours are for constant soot/air scattering ratios for a range of values of N_g and d_p, at a constant soot volume fraction of 0.72 ppb which was determined by AC-LII in the DISI exhaust. The white line signified the contour for the value of 172 measured for the C_{vol}/f_V ratio in this experiment. The resulting distribution of number of primary particles per aggregate is shown in Figure 6-17. For this example, the final result was f_V = 0.72 ppb, d_p = 25.7 nm, N_g = 42, and N_{ag} = 9.1 x 10^5/cm^3. The latter term is the number concentration of

aggregate soot particles.

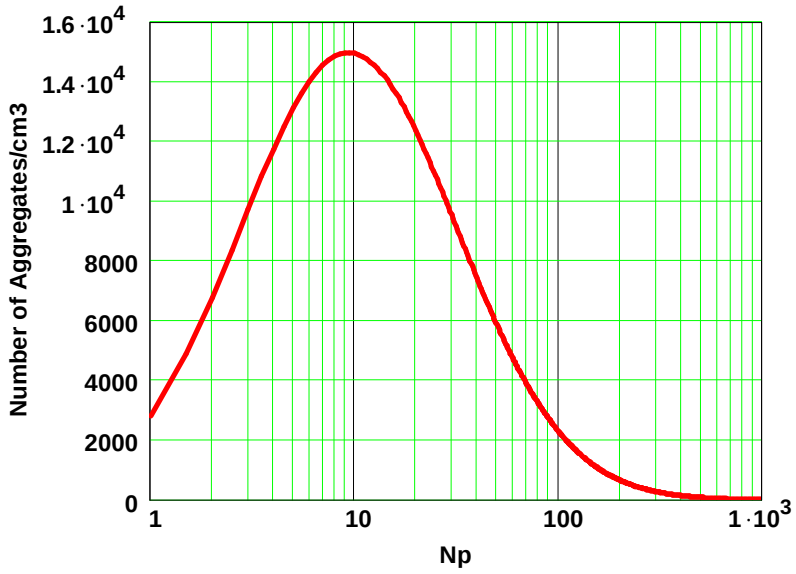

Figure 6-17. Distribution of number of primary particles per aggregate determined by combined AC-LII/ELS.

This example was a proof-of-concept, and much further work is required to understand the implications of the many assumptions involved. The opportunity exists to combine inverse analysis of the AC-LII temperature decays, which have been demonstrated to be sensitive to the distribution parameters of the primary particle diameter and the aggregate size, with AC-LII determination of the soot concentration and its variation over the temperature decay period, and with elastic light scattering determination of the relationship between N_g and d_p. With a full suite of analytical tools and high quality data, it could be possible with all of the above data to reduce the number of assumptions that were required to make the current analysis possible.

7. SUMMARY

The health and environmental consequences of nanoparticles, and soot in particular, were becoming an increasing concern for researchers, regulators, and policymakers in many fields. As a result, government regulations for combustion-generated emissions and for air quality standards have focused on reducing the mass of these emissions. Recently, regulations have evolved that specifically target nonvolatile nanoparticle emissions, which are primarily soot.

The need for substantially improved instruments to quantify nanoparticle characteristics was firmly established, as the instruments in use did not have the capabilities to meet the emerging measurement demands. The principles of operation of the instruments in use are often poorly known, and their accuracy is dependent on correlation with other measurements of nanoparticles. Laser-induced incandescence (LII) showed promise as it was a species selective technique that measured the concentration and primary particle diameter of soot nanoparticles with good sensitivity at low concentrations.

The implementation of conventional high fluence LII was demonstrated to have shortcomings. It relies on a correlation with other soot particle measurements to determine the concentration. This correlation is dependent on the LII signal being in a saturation regime where the signal does not vary with fluence. However, it was shown that such a regime does not exist, as the variation in signal with fluence is highly dependent on the laser light beam spatial profile, and the appearance of a saturation threshold is due to the loss of LII signal in some regions of the probe volume being replaced by increased signal in other regions. This sensitivity to fluence causes high fluence LII to be susceptible to measurement errors due to variation in the ambient temperature, laser energy, the presence of condensed volatiles on the soot particles, and attenuation of the laser beam by particulate matter. Conventional high fluence LII also causes substantial sublimation of the soot nanoparticles, reducing their concentration substantially during and shortly after the laser pulse, making it an intrusive optical diagnostic technique.

A new approach to LII was proposed to retain the species selectivity and sensitivity benefits of conventional high fluence LII while addressing the shortcomings. This

approach was autocompensating laser-induced incandescence (AC-LII) which is a two-colour low fluence implementation of LII. AC-LII uses a physics-based approach for calibration, with the spectral radiance of a traceable source used to calibrate the optical sensitivity of the instrument. Three traceable calibrations sources were implemented, and after careful comparison, an integrating sphere with a coupled spectrometer was selected as the preferred source due to its large and uniform illuminated area. The thermal emission of the soot particles, which is dependent on the soot particle temperature and concentration, was then measured at two wavelengths. Two-colour pyrometry was used to determine the soot particle temperature, and with the temperature and the absolute intensity of the soot particle incandescence, the concentration was determined. By measuring the decay of the temperature, the active surface area available for conduction heat transfer was measured, and from this the primary particle diameter was inferred.

The use of low-fluence ensures that substantial sublimation of the soot was avoided. The direct measurement of soot particle temperature was necessary to permit the use of low fluence, as the LII signal varies dramatically with fluence in the low fluence regime. However, by measuring the temperature, the technique automatically compensates for any effect that could cause a change in the peak soot particle temperature reached during the LII process, including variations in fluctuations in local ambient temperature, laser energy, attenuation, and desorption of condensed volatile material. A method to generate a homogeneous laser light beam spatial profile was implemented. This was used to ensure that all soot particles were exposed to the same laser fluence and thus heated to the same peak temperature.

Development of conventional LII focused on measurements made in laminar flames, such as the laminar diffusion flame (LDF). While measurement in laboratory flames is necessary for the understanding of soot formation and oxidation, where conventional LII has made a contribution, there was a greater need for measurements at many other conditions, especially at much lower ambient temperatures and concentrations. Use of an LDF for development of AC-LII presented advantages, as it was a stable high concentration source of soot particles that resulted in the generation of high quality low noise AC-LII signals. The narrow aggregate size distribution and primary particle

diameter distribution allowed the use of the isolated or monodisperse primary particle assumptions in the numerical models. This combined with the high flame temperature enabled straightforward evaluation of the temperature decay to infer primary particle diameter measurements. However, the LDF also presented disadvantages for complete development of AC-LII as a technique for other applications, as many practical sources of particulates such as combustion emissions are unsteady, with much lower soot concentration, much lower ambient temperatures, and much wider distributions of primary particle diameter and aggregate size.

Development of the AC-LII technique and application to the LDF demonstrated that the hypothesis of measurement of soot concentration independent of fluence was valid over a wide range of low to moderate fluences up to the sublimation threshold. However, subsequent studies at lower ambient temperatures revealed that this hypothesis was no longer true, and that for accurate concentration measurements under these conditions the fluence must be at the sublimation threshold. The mechanism responsible for this difference was not elucidated, and remains an issue for further investigation. Other issues that were uncovered are common to all forms of LII, not just AC-LII. They were the impact of laser fluence on the temperature of the surrounding gas, which affects the conduction cooling rate and therefore the determination of primary particle diameter, and an anomalous cooling behaviour in the first 50 ns of the temperature decay after the peak of the laser pulse. The relatively simple model for low fluences for correcting the former issue was presented, but the latter remains an open topic for further study.

Application of a state-of-the-art numerical model of the nanoscale heat and energy transfer processes enabled extension of the signal evaluation from the initial assumption of monodisperse isolated primary particles to more credible morphologies. The effects of aggregation on the measurement of soot concentration were shown to be important at low ambient temperatures. The impacts of polydispersity of primary particle diameter and of the number of primary particles per aggregate were investigated separately and ultimately in combination. This was demonstrated to have a modest impact on measurements performed in the LDF due to the high ambient temperature and the relatively narrow parameter distributions. However, it was demonstrated that due to the broader distributions and lower ambient temperatures, measurements in practical

applications are significantly affected, both for the determination of soot concentration and primary particle diameter. It is recommended that signal evaluation begin immediately after the anomalous cooling period but before distribution effects become dominant, *i.e.*, in the period approximately 50-100 ns after the peak of the laser pulse. Enhancement of the AC-LII method by combining it with elastic light scattering (ELS) to determine the mean aggregate size and improve the determination of the mean primary particle diameter was explored and a proof-of-concept employing simultaneous AC-LII and near-forward scattering was successfully demonstrated.

The major sources of uncertainty in all variants of LII are the soot absorption function, $E(m)$, for the determination of soot concentration, and the thermal accommodation coefficient, α, for the determination of primary particle diameter. Methods were presented for the analysis of AC-LII signals acquired in the LDF where the morphology of soot and the ambient conditions are well-known, to determine the value of $E(m)$ at the laser wavelength and the value of α.

Optimization of the AC-LII technique to improve the sensitivity was performed, resulting in a high sensitivity autocompensating laser-induced incandescence (HS-LII) system. This was demonstrated to measure concentrations as low as 20 ng/m^3, far lower than atmospheric concentrations of black carbon, and therefore suitable for almost any application where low soot concentrations are anticipated.

As there are many instruments for measuring the concentration of nanoparticles, AC-LII was compared to several of the key competitors. AC-LII was shown to have high selectivity to measuring soot, unlike other instruments that also claimed this capability. In comparison to gravimetric filter measurements of total particulate mass from engine emissions, AC-LII typically produced lower concentrations, even after the filters were treated to remove volatile compounds. This could be due to the uncertainty in $E(m)$, aggregation effects, or to differences between the nonvolatile residue on filters and soot. Further investigation of these differences is recommended.

Based on the advances due to the unique innovations in AC-LII, a commercial instrument employing the features of AC-LII developed in this work was produced under licence by Artium Technologies. This instrument, the Artium LII 200, offered the

advantages of AC-LII in a highly automated and portable format suitable for field measurement campaigns. Several applications using the Artium LII 200 or HS-LII were described, demonstrating the versatility of AC-LII in a wide variety of practical applications.

AC-LII was found to be capable of measuring the soot volume fraction, mass concentration, active surface area, and an effective primary particle diameter accurately with high precision, sensitivity, repeatability, and time response. Examples include sensitivity to ng/m^3 concentration levels and primary particle diameters as low as 5 nm. AC-LII is ideal for the measurement of the concentration of soot without interference from other species, and represents a major advancement in instrumentation for nanoparticle characterization.

REFERENCES

1. M. Faraday, Lectures on the Various Forces of Matter and on the Chemical History of a Candle (Griffin, Bohn and Company, London, 1863).

2. R. Weeks and W. Duley, "Aerosol-Particle Sizes from Light Emission During Excitation by TEA CO_2 Laser Pulses," *Journal of Applied Physics* **45**, 4661-4662 (1974).

3. "Oxford English Dictionary", retrieved 1 Oct 2008, http://dictionary.oed.com.

4. J. Seinfeld, "Atmospheric Science: Black Carbon and Brown Clouds," *Nature Geoscience* **1**, 15-16 (2008).

5. K. Kohse-Höinghaus and J. B. Jeffries, eds., *Applied Combustion Diagnostics*, Taylor and Francis, New York (2002).

6. "Air Quality Criteria for Particulate Matter," U.S. Environmental Protection Agency Paper No. EPA 600/P-99/002aF-bF,Washington, DC, USA (2004).

7. H. Bockhorn, ed., *Soot Formation in Combustion*, Springer-Verlag, Berlin (1994).

8. C. M. Megaridis and R. A. Dobbins, "Morphological Description of Flame-Generated Materials," *Combustion Sci. Technol.* **71**, 95-109 (1990).

9. R. A. Dobbins and C. M. Megaridis, "Morphology of Flame-Generated Soot as Determined by Thermophoretic Sampling," *Langmuir* **3**, 254-259 (1987).

10. M. Frenklach, "Reaction Mechanism of Soot Formation in Flames," *Physical Chemistry Chemical Physics* **4**, 2028-2037 (2002).

11. J. H. Seinfeld and S. N. Pandis, Atmospheric Physics and Chemistry: From Air Pollution to Climate Change (John Wiley and Sons, 1998).

12. "Nanoscience and Nanotechnologies: Opportunities and Uncertainties" (Joint Report from the Royal Society and Royal Academy of Engineering, 2004), retrieved 16 Aug 2007, http://www.nanotec.org.uk/finalReport.htm.

13. G. Oberdörster, E. Oberdörster, and J. Oberdörster, "Nanotoxicology: An Emerging Discipline Evolving from Studies of Ultrafine Particles," *Environmental Health Perspectives* **113**, 823-839 (2005).

14. C. Arden, R. T. Burnett, M. J. Thun, E. E. Calle, D. Krewski, K. Ito, and G. D. Thurston, "Lung Cancer, Cardiopulmonary Mortality, and Long-Term Exposure to Fine Particulate Air Pollution," *Journal of the American Medical Association* **287**, 1132-1141 (2002).

15. J. L. Mauderly, "Diesel Emissions: Is More Health Research Still Needed?," *Toxicological Sciences* **62**, 6-9 (2001).

16. J. Hansen, M. Sato, R. Reto, A. Lacis, and V. Oinas, "Global Warming in the Twenty-First Century: An Alternative Scenario," *Proceedings of the National Academy of Sciences* **97**, 9875-9880 (2000).

17. M. Z. Jacobson, "Strong Radiative Heating Due to the Mixing State of Black Carbon in Atmospheric Aerosols," *Nature* **409**, 695-697 (2001).

18. D. B. Kittelson, "Engines and Nanoparticles: A Review," *Journal of Aerosol Science* **29**, 575-588 (1998).

19. J. D. Herner, W. H. Robertson, and A. Ayala, "Investigation of Ultrafine Particle Number Measurements from a Clean Diesel Truck Using the European PMP Protocol," SAE Paper No. 2007-01-1114 (2007).

20. B. Giechaskiel, P. Dilara, E. Sandbach, and J. Andersson, "Particle Measurement Programme (PMP) Light-Duty Inter-Laboratory Exercise: Comparison of Different Particle Number Measurement Systems," *Measurement Science and Technology* **19**, (online at http://dx.doi.org/10.1088/0957-0233/1019/1089/095401) (2008).

21. G. J. Smallwood, "Nanoparticle Sensing: Detection and Monitoring of Nonvolatile Nanoparticulate Emissions in the Atmosphere," *The Rank Prize Funds Mini-Symposium on Photonics and Optics in Sustainable Energy*, Grasmere, UK, November 5-8 (2007).

22. R. Jullien and R. Botet, *Aggregation and Fractal Aggregates* (World Scientific, Singapore, 1987).

23. Ü. Ö. Köylü, Y. C. Xing, and D. E. Rosner, "Fractal Morphology Analysis of Combustion-Generated Aggregates Using Angular Light Scattering and Electron Microscope Images," *Langmuir* **11**, 4848-4854 (1995).

24. J. H. Seinfeld, *Atmospheric Chemistry and Physics of Air Pollution* (John Wiley & Sons, New York, 1986), p. 319.

25. P. O. Witze, "Diagnostics for the Measurement of Particulate Matter Emissions from Reciprocating Engines," *The Fifth International Symposium on Diagnostics and Modeling of Combustion in Internal Combustion Engines (COMODIA)*, Nagoya, (2001).

26. S. J. Harris and M. M. Maricq, "Signature Size Distributions for Diesel and Gasoline Engine Particulate Matter," *Journal of Aerosol Science* **32**, 749-764 (2001).

27. Ü. Ö. Köylü, "Quantitative Analysis of in Situ Optical Diagnostics for Inferring Particle/Aggregate Parameters in Flames: Implications for Soot Surface Growth and Total Emissivity," *Combustion and Flame* **109**, 488-500 (1997).

28. G. J. Smallwood, D. Clavel, D. Gareau, R. A. Sawchuk, D. R. Snelling, P. O. Witze, B. Axelsson, W. D. Bachalo, and Ö. L. Gülder, "Concurrent Quantitative Laser-Induced Incandescence and SMPS Measurements of EGR Effects on Particulate Emissions from a TDI Diesel Engine," SAE Paper No. 2002-01-2715 (2002).

29. M. Spencer and K. Prather, "Using ATOFMS to Determine OC/EC Mass Fractions in Particles," *Aerosol Science and Technology* **40**, 585-594 (2006).

30. H. Zhao and N. Ladommatos, "Optical Diagnostics for Soot and Temperature Measurement in Diesel Engines," *Progress in Energy and Combustion Science* **24**, 221-255 (1998).

31. M. Mohr, U. Lehmann, and J. Rutter, "Comparison of Mass-Based and Non-Mass-Based Particle Measurement Systems for Ultra-Low Emissions from Automotive Sources," *Environmental Science & Technology* **39**, 2229-2238 (2005).

32. A. C. Eckbreth, "Effects of Laser-Modulated Particulate Incandescence on Raman Scattering Diagnostics," *Journal of Applied Physics* **48**, 4473-4479 (1977).

33. K. Kohse-Höinghaus, R. Barlow, M. Aldén, and J. Wolfrum, "Combustion at the Focus: Laser Diagnostics and Control," *Proceedings of the Combustion Institute* **30**, 89-123 (2005).

34. C. Schulz, B. F. Kock, M. Hofmann, H. Michelsen, S. Will, B. Bougie, R. Suntz, and G. Smallwood, "Laser-Induced Incandescence: Recent Trends and Current Questions," *Applied Physics B: Lasers and Optics* **83**, 333-354 (2006).

35. "LIIscience.org", retrieved 1 Oct 2008, http://liiscience.org.

36. D. R. Snelling, G. J. Smallwood, R. A. Sawchuk, W. S. Neill, D. Gareau, W. L. Chippior, F. Liu, Ö. L. Gülder, and W. D. Bachalo, "Particulate Matter Measurements in a Diesel Engine Exhaust by Laser-Induced Incandescence and the Standard Gravimetric Procedure," SAE Paper No. 1999-01-3653 (1999).

37. D. R. Snelling, G. J. Smallwood, Ö. L. Gülder, W. D. Bachalo, and S. Sankar, "Soot Volume Fraction Characterization Using the Laser-Induced Incandescence Detection Method," *Proceedings of the 10th International Symposium on Applications of Laser Techniques to Fluid Mechanics*, Lisbon, July 10-13 (2000).

38. S. Dankers, A. Leipertz, S. Will, J. Arndt, K. Vogel, S. Schraml, and A. Hemm, "In-Situ Measurement of Primary Particle Sizes During Carbon Black Production," *Chemical Engineering & Technology* **26**, 966-969 (2003).

39. S. Schraml, S. Will, A. Leipertz, T. Zens, and N. D'Alfonso, "Performance Characteristics of TIRE-LII Soot Diagnostics in Exhaust Gases of Diesel Engines," SAE Paper No. 2000-01-2002 (2000).

40. B. Quay, T.-W. Lee, T. Ni, and R. J. Santoro, "Spatially Resolved Measurements of Soot Volume Fraction Using Laser-Induced Incandescence," *Combustion and Flame* **97**, 384-392 (1994).

41. R. Vander Wal and T. Ticich, "Cavity Ringdown and Laser-Induced Incandescence Measurements of Soot," *Appl. Opt* **38**, 1444–1451 (1999).

42. T. Ni, J. A. Pinson, S. Gupta, and R. J. Santoro, "Two-Dimensional Imaging of Soot Volume Fraction by the Use of Laser-Induced Incandescence," *Applied Optics* **34**, 7083-7091 (1995).

43. J. Hult, A. Omrane, J. Nygren, C. F. Kaminski, B. Axelsson, R. Collin, P.-E. Bengtsson, and M. Aldén, "Quantitative Three-Dimensional Imaging of Soot Volume Fraction in Turbulent Non-Premixed Flames," *Experiments in Fluids* **33**, 265-269 (2002).

44. L. A. Melton, "Soot Diagnostics Based on Laser Heating," *Applied Optics* **23**, 2201-2208 (1984).

45. C. J. Dasch, "New Soot Diagnostics in Flames Based on Laser Vaporization of Soot," *Proceedings of the Twentieth Symposium (International) on Combustion*, 1231-1237 (1984).

46. N. P. Tait and D. A. and Greenhalgh, "PLIF Imaging of Fuel Fraction in Practical Devices and LII Imaging of Soot," *Berichte der Bunsengesellschaft fuer Physikalische Chemie* **97**, 1619-1625 (1993).

47. D. L. Hofeldt, "Real-Time Soot Concentration Measurement Technique for Engine Exhaust Streams," SAE Paper No. 930079 (1993).

48. B. Mewes and J. M. Seitzman, "Soot Volume Fraction and Particle Size Measurements with Laser-Induced Incandescence," *Applied Optics* **36**, 709-717 (1997).

49. K. R. McManus, J. H. Frank, M. G. Allen, and W. T. Rawlins, "Characterization of Laser-Heated Soot Particles Using Optical Pyrometry," AIAA Paper No. 98-0159 (1998).

50. D. R. Snelling, G. J. Smallwood, I. G. Campbell, J. E. Medlock, and Ö. L. Gülder, "Development and Application of Laser-Induced Incandescence (LII) as a Diagnostic for Soot Particulate Measurements," *Advanced Non-Intrusive Instrumentation for Propulsion Engines AGARD Conference Proceedings* **598**, 23.21 – 23.29 (1997).

51. S. Will, S. Schraml, K. Bader, and A. Leipertz, "Performance Characteristics of Soot Primary Particle Size Measurements by Time-Resolved Laser-Induced Incandescence," *Applied Optics* **37**, 5647-5658 (1998).

52. D. R. Snelling, F. Liu, G. J. Smallwood, and Ö. L. Gülder, "Evaluation of the Nanoscale Heat and Mass Transfer Model of the Laser-Induced Incandescence: Prediction of the Excitation Intensity," Thirty Fourth National Heat Transfer Conference Paper No. NHTC2000-12132 (2000).

53. S. Schraml, S. Dankers, K. Bader, S. Will, and A. Leipertz, "Soot Temperature Measurements and Implications for Time-Resolved Laser-Induced Incandescence (TIRE-LII)," *Combustion and Flame* **120**, 439-450 (2000).

54. G. J. Smallwood, D. R. Snelling, F. Liu, and Ö. L. Gülder, "Clouds over Soot Evaporation: Errors in Modeling Laser-Induced Incandescence of Soot," *Journal of Heat Transfer* **123**, 814-818 (2001).

55. H. Michelsen, F. Liu, B. Kock, H. Bladh, A. Boiarciuc, M. Charwath, T. Dreier, R. Hadef, M. Hofmann, and J. Reimann, "Modeling Laser-Induced Incandescence of Soot: A Summary and Comparison of LII Models," *Applied Physics B: Lasers and Optics* **87**, 503-521 (2007).

56. F. Liu and D. Snelling, "The Unsteady-State Energy Conservation Equation for a Small Spherical Particle in LII Modeling," *Applied Physics B: Lasers and Optics* **89**, 115-121 (2007).

57. R. A. Dobbins, G. W. Mulholland, and N. P. Bryner, "Comparison of a Fractal Smoke Optics Model with Light Extinction Measurements," *Atmospheric Environment* **28**, 889-897 (1994).

58. M. Y. Choi, G. W. Mulholland, A. Hamins, and T. Kashiwagi, "Comparisons of the Soot Volume Fraction Using Gravimetric and Light Extinction Techniques," *Combustion and Flame* **102**, 161-169 (1995).

59. J. Wu, S. Krishnan, and G. Faeth, "Refractive Indices at Visible Wavelengths of Soot Emitted from Buoyant Turbulent Diffusion Flames," *Journal of Heat Transfer* **119**, 230 (1997).

60. W. H. Dalzell and A. F. Sarofim, "Optical Constants of Soot and Their Application to Heat Flux Calculations," *Journal of Heat Transfer* **91**, 100-104 (1969).

61. C. F. Bohren and D. R. Huffman, *Absorption and Scattering of Light by Small Particles* (John Wiley & Sons, New York, 1983).

62. O. Leroy, J. Perrin, J. Jolly, and M. Pealat, "Thermal Accommodation of a Gas on a Surface and Heat Transfer in CVD and PECVD Experiments," *Journal of Physics D* **30**, 499-509 (1997).

63. C. R. Shaddix and K. C. Smyth, "Laser-Induced Incandescence Measurements of Soot Production in Steady and Flickering Methane, Propane, and Ethylene Diffusion Flames," *Combustion and Flame* **107**, 418-452 (1996).

64. P. O. Witze, S. Hochgreb, D. Kayes, H. A. Michelsen, and C. R. Shaddix, "Time-Resolved Laser-Induced Incandescence and Laser Elastic Scattering Measurements in a Propane Diffusion Flame," *Applied Optics* **40**, 2443-2452 (2001).

65. R. L. Vander Wal and K. J. Weiland, "Laser-Induced Incandescence: Development and Characterization Towards a Measurement of Soot-Volume Fraction," *Applied Physics B* **59**, 445-452 (1994).

66. C. J. Dasch, "One-Dimensional Tomography: A Comparison of Abel, Onion-Peeling, and Filtered Backprojection Methods.," *Applied Optics* **31**, 1146-1152 (1992).

67. D. R. Snelling, K. A. Thomson, G. J. Smallwood, and Ö. L. Gülder, "Two-Dimensional Imaging of Soot Volume Fraction in Laminar Diffusion Flames," *Applied Optics* **38**, 2478-2485 (1999).

68. R. L. Vander Wal, Z. Zhou, and M. Y. Choi, "Laser-Induced Incandescence Calibration Via Gravimetric Sampling," *Combustion and Flame* **105**, 462-470 (1996).

69. D. R. Snelling, G. J. Smallwood, R. A. Sawchuk, W. S. Neil, D. Gareau, D. Clavel, W. L. Chippior, F. Liu, Ö. L. Gülder, and W. D. Bachalo, "In-Situ Real-Time Characterization of Particulate Emissions from a Diesel Engine Exhaust by Laser-Induced Incandescence," in *Diesel Particulate Emissions: Landmark Research 1994-2001*, J. H. Johnson, ed. (Society of Automotive Engineers, 2002).

70. B. J. McCoy and C. Y. Cha, "Transport Phenomena in the Rarefied Gas Transition Regime," *Chemical Engineering Science* **29**, 381-388 (1974).

71. C. B. Stipe, B. S. Higgins, D. Lucas, C. P. Koshland, and R. F. Sawyer, "Soot Detection Using Excimer Laser Fragmentation Fluorescence Spectroscopy," *Twenty-Ninth Symposium (International) on Combustion*, Sapporo, Japan, July 21-26 (2002).

72. P. Bengtsson and M. Aldén, "Soot-Visualization Strategies Using Laser Techniques," *Applied Physics B: Lasers and Optics* **60**, 51-59 (1995).

73. H. Michelsen, "Laser-Induced Incandescence of Flame-Generated Soot on a Picosecond Time Scale," *Applied Physics B: Lasers and Optics* **83**, 443-448 (2006).

74. M. Dansson, M. Boisselle, M. Linne, and H. Michelsen, "Complications to Optical Measurements Using a Laser with an Unstable Resonator: A Case Study on Laser-Induced Incandescence of Soot," *Applied Optics* **46**, 8095-8103 (2007).

75. S. Schraml, S. Will, and A. Leipertz, "Simultaneous Measurement of Soot Mass Concentration and Primary Particle Size in the Exhaust of a DI Diesel Engine by Time-Resolved Laser-Induced Incandescence (TIRE-LII)," SAE Paper No. 1999-01-0146 (1999).

76. J. Dec, A. zur Loye, and D. Siebers, "Soot Distribution in a Di Diesel Engine Using 2-D Laser-Induced Incandescence Imaging," SAE Paper No. 910224 (1991).

77. S. De Iuliis, F. Migliorini, F. Cignoli, and G. Zizak, "2D Soot Volume Fraction Imaging in an Ethylene Diffusion Flame by Two-Color Laser-Induced Incandescence (2c-LII) Technique and Comparison with Results from Other Optical Diagnostics," *Proceedings of the Combustion Institute* **31**, 869-876 (2007).

78. T. Meyer, S. Roy, V. Belovich, E. Corporan, and J. Gord, "Simultaneous Planar Laser-Induced Incandescence, Oh Planar Laser-Induced Fluorescence, and Droplet Mie Scattering in Swirl-Stabilized Spray Flames," *Applied Optics* **44**, 445-454 (2005).

79. V. Beyer and D. Greenhalgh, "Laser Induced Incandescence under High Vacuum Conditions," *Applied Physics B: Lasers and Optics* **83**, 455-467 (2006).

80. P. Desgroux, X. Mercier, B. Lefort, R. Lemaire, E. Therssen, and J. Pauwels, "Soot Volume Fraction Measurement in Low-Pressure Methane Flames by Combining Laser-Induced Incandescence and Cavity Ring-Down Spectroscopy: Effect of Pressure on Soot Formation," *Combustion and Flame* (2008).

81. M. Stephens, N. Turner, and J. Sandberg, "Particle Identification by Laser-Induced Incandescence in a Solid-State Laser Cavity," *Applied Optics* **42**, 3726-3736 (2003).

82. N. Moteki, "Effects of Mixing State on Black Carbon Measurements by Laser-Induced Incandescence," *Aerosol Science and Technology* **41**, 398-417 (2007).

83. T. Lehre, R. Suntz, and H. Bockhorn, "Time-Resolved Two-Color LII: Size Distributions of Nano-Particles from Gas-to-Particle Synthesis," *Proceedings of the Combustion Institute* **30**, 2585-2593 (2005).

84. J. Knipping, H. Wiggers, B. Kock, T. Huelser, B. Rellinghaus, and P. Roth, "Synthesis and Characterization of Nanowires Formed by Self-Assembled Iron Particles," *Nanotechnology* **15**, 1665-1670 (2004).

85. S. Maffi, F. Cignoli, C. Bellomunno, S. De Iuliis, and G. Zizak, "Spectral Effects in Laser Induced Incandescence Application to Flame-Made Titania Nanoparticles," *Spectrochimica Acta Part B: Atomic Spectroscopy* **63**, 202-209 (2008).

86. Y. Murakami, T. Sugatani, and Y. Nosaka, "Laser-Induced Incandescence Study on the Metal Aerosol Particles as the Effect of the Surrounding Gas Medium," *J. Phys. Chem. A* **109**, 8994-9000 (2005).

87. R. Vander Wal, G. Berger, T. Ticich, and P. Patel, "Application of Laser-Induced Incandescence to the Detection of Carbon Nanotubes and Carbon Nanofibers," *Appl. Opt* **41**, 5678-5690 (2002).

88. N. Dorval, A. Foutel-Richard, M. Cau, A. Loiseau, B. Attal-Trétout, J. Cochon, D. Pigache, P. Bouchardy, V. Krüger, and K. Geigle, "In-Situ Optical Analysis of the Gas Phase During the Formation of Carbon Nanotubes," *Journal of Nanoscience and Nanotechnology* **4**, 450-462 (2004).

89. D. B. Geohegan, A. Puretzky, I. Ivanov, G. Eres, Z. Liu, D. Styers-Barnett, H. Hu, B. Zhao, H. Cui, C. Rouleau, S. Jesse, P. F. Britt, H. Christen, K. Xiao, P. Fleming, and A. Meldrum, "Laser-Based Synthesis, Diagnostics, and Control of Single-Walled Carbon Nanotubes and Nanohorns for Composites and Biological Nanovectors," in *Photon-Based Nanoscience and Nanobiotechnology*, J. J. Dubowski and S. Tanev, eds. (Springer Netherlands, 2006).

90. V. Popov and L. Henrard, "Comparative Study of the Optical Properties of Single-Walled Carbon Nanotubes within Orthogonal and Nonorthogonal Tight-Binding Models," *Physical Review B* **70**, 115407 (2004).

91. M. E. Case and D. L. Hofeldt, "Soot Mass Concentration Measurements in Diesel Engine Exhaust Using Laser-Induced Incandescence," *Aerosol Science and Technology* **25**, 46-60 (1996).

92. S. Schraml, C. Heimgärtner, S. Will, A. Leipertz, and A. Hemm, "Application of a New Soot Sensor for Exhaust Emission Control Based on Time Resolved Laser Induced Incandescence (TIRE-LII)," SAE Paper No. 2000-01-2864 (2000).

93. G. J. Smallwood, D. R. Snelling, W. S. Neill, F. Liu, W. D. Bachalo, and Ö. L. Gülder, "Laser-Induced Incandescence Measurements of Particulate Matter Emissions in the Exhaust of a Diesel Engine," *Proceedings of the Fifth International Symposium on Diagnostics and Modeling of Combustion in Internal Combustion Engines (COMODIA)*, Nagoya, (2001).

94. G. J. Smallwood, D. R. Snelling, Ö. L. Gulder, D. Clavel, D. Gareau, R. A. Sawchuk, and L. Graham, "Transient Particulate Matter Measurements from the Exhaust of a Direct Injection Spark Ignition Automobile," SAE Paper No. 2001-01-3581 (2001).

95. K. Schäfer, J. Heland, D. H. Lister, C. W. Wilson, R. J. Howes, R. S. Falk, E. Lindermeir, M. Birk, G. Wagner, P. Haschberger, M. Bernard, O. Legras, P. Wiesen, R. Kurtenbach, K. J. Brockmann, V. Kriesche, M. Hilton, G. Bishop, R. Clarke, J. Workman, M. Caola, R. Geatches, R. Burrows, J. D. Black, P. Hervé, and J. Vally, "Nonintrusive Optical Measurements of Aircraft Engine Exhaust Emissions and Comparison with Standard Intrusive Techniques," *Applied Optics* **39**, 441-454 (2000).

96. M. G. Allen, B. L. Upschulte, D. M. Sonnenfroh, W. T. Rawlins, C. Gmachl, F. Capasso, A. Hutchinson, D. Sivco, and A. Cho, "Infrared Characterization of Particulate and Pollutant Emissions from Gas Turbine Combustors," AIAA Paper No. 2001-0789 (2001).

97. T. P. Jenkins, J. L. Bartholomew, P. A. DeBarber, P. Yang, J. M. Seitzman, and R. P. Howard, "Laser Induced Incandescence for Soot Concentration Measurements in Turbine Engine Exhausts," AIAA Paper No. 2002-0828 (2002).

98. P. O. Witze, "High-Energy, Pulsed Laser Diagnostics for Real-Time Measurements of Reciprocating Engine PM Emissions," *8th Diesel Engine Emissions Reduction Conference*, San Diego, August 25-29 (2002).

99. Ü. Ö. Köylü, "Quantitative Analysis of in Situ Optical Diagnostics for Inferring Particle/Aggregate Parameters in Flames: Implications for Soot Surface Growth and Total Emissivity," *Combustion and Flame* **109**, 488-500 (1996).

100. P. O. Witze, "Real-Time Measurement of the Volatile Fraction of Diesel Particulate Matter Using Laser-Induced Desorption with Elastic Light Scattering (LIDELS)," SAE Paper No. 2002-01-1685 (2002).

101. R. L. Vander Wal, T. M. Ticich, and J. R. West, "Trace Metal Detection by Laser-Induced Breakdown Spectroscopy," *Applied Spectroscopy* **53**, 1226-1236 (1999).

102. M.-D. Cheng, "Real-Time Measurement of Trace Metals on Fine Particles by Laser-Induced Plasma Techniques," *Fuel Processing Technology* **65/66**, 219-229 (2000).

103. J. P. Hessler, S. Seifert, and R. E. Winans, "Spatially-Resolved Small-Angle X-Ray Scattering Studies of Soot Inception and Growth," *Twenty-Ninth Symposium (International) on Combustion*, Sapporo, Japan, July 21-26 (2002).

104. H. Wang, B. Zhao, B. Wyslouzil, and K. Streletzky, "Small-Angle Neutron Scattering of Soot Formed in Laminar Premixed Ethylene Flames," *Twenty-Ninth Symposium (International) on Combustion*, Sapporo, Japan, July 21-26 (2002).

105. F. Liu, M. Yang, F. A. Hill, D. R. Snelling, and G. J. Smallwood, "Influence of Polydisperse Distributions of Both Primary Particle and Aggregate Size on Soot Temperature in Low-Fluence LII," *Applied Physics B Lasers and Optics* **83**, 383-395 (2006).

106. R. L. Vander Wal, T. M. Ticich, and A. B. Stephens, "Optical and Microscopy Investigations of Soot Structure Alterations by Laser-Induced Incandescence," *Applied Physics B* **67**, 115-123 (1998).

107. H. A. Michelsen, P. O. Witze, D. Kayes, and S. Hochgreb, "Time-Resolved Laser-Induced Incandescence of Soot: The Influence of Experimental Factors and Microphysical Mechanisms," *Applied Optics* **42**, 5577-5590 (2003).

108. S. De Iuliis, F. Migliorini, F. Cignoli, and G. Zizak, "Peak Soot Temperature in Laser-Induced Incandescence Measurements," *Applied Physics B: Lasers and Optics* **83**, 397-402 (2006).

109. D. R. Snelling, F. Liu, and G. J. Smallwood, "Determination of the Soot Absorption Function and Thermal Accommodation Coefficient Using Low-Fluence LII in a Laminar Coflow Ethylene Diffusion Flame," *Combustion and Flame* **136**, 180-190 (2004).

110. F. Liu, K. A. Thomson, and G. J. Smallwood, "Numerical Investigation of the Effect of Signal Trapping on Soot Measurements Using LII in Laminar Coflow Diffusion Flames," *9th Asia-Pacific International Symposium on Combustion and Energy Utilization*, Beijing, China, November 2-6 (2008).

111. G. J. Smallwood, "Advances in Diagnostics for the Study of Soot Formation," *Proceedings Canadian Section/Combustion Institute 2005 Spring Technical Meeting*, Halifax, Canada, May 15-18 (2005).

112. D. R. Snelling, G. J. Smallwood, F. Liu, Ö. L. Gülder, and W. D. Bachalo, "A Calibration-Independent Laser-Induced Incandescence Technique for Soot Measurement by Detecting Absolute Light Intensity," *Applied Optics* **44**, 6773-6785 (2005).

113. G. J. Smallwood, "Measurement of Combustion-Generated Nonvolatile Nanoparticles," *Proceedings Canadian Section/Combustion Institute 2008 Spring Technical Meeting*, Toronto, Canada, May 12-14 (2008).

114. H. A. Michelsen, "Understanding and Predicting the Temporal Response of Laser-Induced Incandescence from Carbonaceous Particles," *Journal of Chemical Physics* **118**, 7012-7045 (2003).

115. H. Bladh and P. Bengtsson, "Characteristics of Laser-Induced Incandescence from Soot in Studies of a Time-Dependent Heat-and Mass-Transfer Model," *Applied Physics B: Lasers and Optics* **78**, 241-248 (2004).

116. H. Bladh, P. Bengtsson, J. Delhay, Y. Bouvier, E. Therssen, and P. Desgroux, "Experimental and Theoretical Comparison of Spatially Resolved Laser-Induced Incandescence (LII) Signals of Soot in Backward and Right-Angle Configuration," *Applied Physics B: Lasers and Optics* **83**, 423-433 (2006).

117. H. Bladh, J. Johnsson, and P. Bengtsson, "On the Dependence of the Laser-Induced Incandescence (LII) Signal on Soot Volume Fraction for Variations in Particle Size," *Applied Physics B: Lasers and Optics* **90**, 109-125 (2008).

118. H. Michelsen, F. Liu, and H. Bladh, "Modeling Task," Third International Discussion Meeting and Workshop on Laser-induced incandescence: Quantitative interpretation, modelling, application, Ottawa, Canada, July 30 - August 1 (2008).

119. P. G. Wright, "On the Discontinuity Involved in Diffusion across an Interface (the Δ of Fuchs)," *Discussions of the Faraday Society* **30**, 100-112 (1960).

120. A. V. Filippov and D. E. Rosner, "Energy Transfer between an Aerosol Particle and Gas at High Temperature Ratios in the Knudsen Transition Regime," *International Journal of Heat and Mass Transfer* **43**, 127-138 (2000).

121. F. Liu, K. Daun, D. Snelling, and G. Smallwood, "Heat Conduction from a Spherical Nano-Particle: Status of Modeling Heat Conduction in Laser-Induced Incandescence," *Applied Physics B: Lasers and Optics* **83**, 355-382 (2006).

122. S. Kuhlmann, J. Reimann, and S. Will, "On Heat Conduction between Laser-Heated Nanoparticles and a Surrounding Gas," *Journal of Aerosol Science* **37**, 1696-1716 (2006).

123. G. M. Faeth and Ü. Ö. Köylü, "Soot Morphology and Optical Properties in Nonpremixed Turbulent Flame Environments," *Combustion Science and Technology* **108**, 207-229 (1995).

124. T. L. Farias, M. G. Carvalho, Ü. Ö. Köylü, and G. M. Faeth, "Computational Evaluation of Approximate Rayleigh–Debye–Gans/Fractal-Aggregate Theory for the Absorption and Scattering Properties of Soot," *Journal of Heat Transfer* **117**, 152-159 (1995).

125. T. Lehre, B. Jungfleisch, R. Suntz, and H. Bockhorn, "Size Distributions of Nanoscaled Particles and Gas Temperatures from Time-Resolved Laser-Induced-Incandescence Measurements," *Applied Optics* **42**, 2021-2030 (2003).

126. R. Starke, B. Kock, and P. Roth, "Nano-Particle Sizing by Laser-Induced-Incandescence (LII) in a Shock Wave Reactor," *Shock Waves* **12**, 351-360 (2003).

127. F. Liu, D. Snelling, and G. Smallwood, "A Critical Evaluation of the Thermal Accommodation Coefficient of Soot Determined by the Laser-Induced Incandescence Technique," *Proceedings of the 13th International Heat Transfer Conference*, Sydney, Australia, August 13-18 (2006).

128. D. R. Snelling, G. J. Smallwood, and Ö. L. Gülder, "Absolute Light Intensity Measurements in Laser-Induced Incandescence," US Patent No. 6,154,277 (2000).

129. D. R. Snelling, G. J. Smallwood, Ö. L. Gülder, F. Liu, and W. D. Bachalo, "A Calibration-Independent Technique of Measuring Soot by Laser-Induced in-Candescence Using Absolute Light Intensity," *The Second Joint Meeting of the US Sections of the Combustion Institute*, Oakland, California, March 25-28 (2001).

130. S. S. Krishnan, K.-C. Lin, and G. M. Faeth, "Extinction and Scattering Properties of Soot Emitted from Buoyant Turbulent Diffusion Flames," *Journal of Heat Transfer* **123**, 331-339 (2001).

131. D. R. Snelling, K. A. Thomson, G. J. Smallwood, Ö. L. Gülder, E. J. Weckman, and R. A. Fraser, "Spectrally Resolved Measurement of Flame Radiation to Determine Soot Temperature and Concentration," *AIAA Journal* **40**, 1789-1795 (2002).

132. Ö. L. Gülder, D. R. Snelling, and R. A. Sawchuk, "Influence of Hydrogen Addition to Fuel on Temperature Field and Soot Formation in Diffusion Flames," *Proceedings of the Combustion Institute* **26**, 2351-2358 (1996).

133. K. Tian, F. Liu, K. A. Thomson, D. R. Snelling, G. J. Smallwood, and D. Wang, "Distribution of the Number of Primary Particles of Soot Aggregates in a Nonpremixed Laminar Flame," *Combustion and Flame* **138**, 195-198 (2004).

134. S. De Iuliis, F. Cignoli, and G. Zizak, "Two-Color Laser-Induced Incandescence (2c-LII) Technique for Absolute Soot Volume Fraction Measurements in Flames," *Applied Optics* **44**, 7414-7423 (2005).

135. F. Migliorini, S. De Iuliis, F. Cignoli, and G. Zizak, "Absorption Correction of Two-Color Laser-Induced Incandescence Signals for Soot Volume Fraction Measurements," *Applied Optics* **45**, 7706-7711 (2006).

136. X. He, X. Ma, F. Wu, J. Wang, and S. Shuai, "Investigation of Soot Formation in Laminar Diesel Diffusion Flame by Two-Color Laser Induced Incandescence," SAE Paper No. 2008-01-1064 (2008).

137. C. Schoemaecker Moreau, E. Therssen, X. Mercier, J. Pauwels, and P. Desgroux, "Two-Color Laser-Induced Incandescence and Cavity Ring-Down Spectroscopy for Sensitive and Quantitative Imaging of Soot and Pahs in Flames," *Applied Physics B: Lasers and Optics* **78**, 485-492 (2004).

138. A. Boiarciuc, F. Foucher, and C. Mounaïm-Rousselle, "Soot Volume Fractions and Primary Particle Size Estimate by Means of the Simultaneous Two-Color-Time-Resolved and 2D Laser-Induced Incandescence," *Applied Physics B: Lasers and Optics* **83**, 413-421 (2006).

139. G. Yoder, P. Diwakar, and D. Hahn, "Assessment of Soot Particle Vaporization Effects During Laser-Induced Incandescence with Time-Resolved Light Scattering," *Applied Optics* **44**, 4211-4219 (2005).

140. K. Thomson, D. Snelling, G. Smallwood, and F. Liu, "Laser Induced Incandescence Measurements of Soot Volume Fraction and Effective Particle Size in a Laminar Co-Annular Non-Premixed Methane/Air Flame at Pressures between 0.5–4.0 Mpa," *Applied Physics B: Lasers and Optics* **83**, 469-475 (2006).

141. W. S. Neill, G. J. Smallwood, D. R. Snelling, R. A. Sawchuk, D. Clavel, D. Gareau, and W. L. Chippior, "Effect of EGR on Heavy-Duty Diesel Engine Emissions Characterized with Laser-Induced Incandescence," *ASME-ICED 2002 Fall Technical Conference*, New Orleans, Sept. 8-11 (2002).

142. Ü. Ö. Köylü and G. M. Faeth, "Optical Properties of Soot in Buoyant Laminar Diffusion Flames," *Journal of Heat Transfer* **116**, 971-979 (1994).

143. R. L. Vander Wal, T. M. Ticich, and A. B. Stephens, "Can Soot Primary Particle Size Be Determined Using Laser-Induced Incandescence?," *Combustion and Flame* **116**, 291-296 (1999).

144. F. Liu, G. J. Smallwood, and D. R. Snelling, "Effects of Primary Particle Diameter and Aggregate Size Distribution on the Temperature of Soot Particles Heated by Pulsed Lasers," *Journal of Quantitative Spectroscopy and Radiative Transfer* **93**, 301-312 (2005).

145. S. Dankers and A. Leipertz, "Determination of Primary Particle Size Distributions from Time-Resolved Laser-Induced Incandescence Measurements," *Applied Optics* **43**, 3726-3731 (2004).

146. F. S. Liu, B. J. Stagg, D. R. Snelling, and G. J. Smallwood, "Effects of Primary Soot Particle Size Distribution on the Temperature of Soot Particles Heated by a Nanosecond Pulsed Laser in an Atmospheric Laminar Diffusion Flame," *International Journal of Heat and Mass Transfer* **49**, 777-788 (2006).

147. B. Axelsson and P. E. Bengtsson, "Laser-Induced Incandescence for Soot Particle Size and Volume Fraction Measurements Using on-Line Extinction Calibration," *Applied Physics B* **72**, 361-372 (2001).

148. Ü. Ö. Köylü, C. S. McEnally, D. E. Rosner, and L. D. Pfefferle, "Simultaneous Measurements of Soot Volume Fraction and Particle Size/Microstructure in Flames Using a Thermophoretic Sampling Technique," *Combustion and Flame* **110**, 494-507 (1997).

149. K. Tian, K. A. Thomson, F. Liu, D. R. Snelling, G. J. Smallwood, and D. Wang, "Determination of the Morphology of Soot Aggregates Using the Relative Optical Density Method for the Analysis of TEM Images," *Combustion and Flame.* **144**, 782-791 (2006).

150. K. Tian, F. Liu, M. Yang, K. Thomson, D. Snelling, and G. Smallwood, "Numerical Simulation Aided Relative Optical Density Analysis of TEM Images for Soot Morphology Determination," *Proceedings of the Combustion Institute* **31**, 861-868 (2007).

151. K. Daun, B. Stagg, F. Liu, G. Smallwood, and D. Snelling, "Determining Aerosol Particle Size Distributions Using Time-Resolved Laser-Induced Incandescence," *Applied Physics B: Lasers and Optics* **87**, 363-372 (2007).

152. M. Hofmann, W. G. Bessler, C. Schulz, and H. Jander, "Laser-Induced Incandescence for Soot Diagnostics at High Pressures," *Applied Optics* **42**, 2052-2062 (2003).

153. M. Hofmann, B. Kock, T. Dreier, H. Jander, and C. Schulz, "Laser-Induced Incandescence for Soot-Particle Sizing at Elevated Pressure," *Applied Physics B: Lasers and Optics* **90**, 629-639 (2008).

154. K. Geigle, Y. Schneider-Kühnle, M. Tsurikov, R. Hadef, R. Lückerath, V. Krüger, W. Stricker, and M. Aigner, "Investigation of Laminar Pressurized Flames for Soot Model Validation Using SV-CARS and LII," *Proceedings of the Combustion Institute* **30**, 1645-1653 (2005).

155. M. Tsurikov, K. Geigle, V. Krüger, Y. Schneider-Kühnle, W. Stricker, R. Lückerath, R. Hadef, and M. Aigner, "Laser-Based Investigation of Soot Formation in Laminar Premixed Flames at Atmospheric and Elevated Pressures," *Combustion Science and Technology* **177**, 1835-1862 (2005).

156. J. Reimann, S. Kuhlmann, and S. Will, "Improvement in Soot Concentration Measurements by Laser-Induced Incandescence (LII) through a Particle Size Correction," *Combustion and Flame* (2008).

157. B. Kock, B. Tribalet, C. Schulz, and P. Roth, "Two-Color Time-Resolved LII Applied to Soot Particle Sizing in the Cylinder of a Diesel Engine," *Combustion and Flame* **147**, 79-92 (2006).

158. A. M. Brasil, T. L. Farias, and M. G. Carvalho, "A Recipe for Image Characterization of Fractal-Like Aggregates," *Journal of Aerosol Science* **30**, 1379-1389 (1999).

159. E. Therssen, Y. Bouvier, C. Schoemaecker-Moreau, X. Mercier, P. Desgroux, M. Ziskind, and C. Focsa, "Determination of the Ratio of Soot Refractive Index Function $E(m)$ at the Two Wavelengths 532 and 1064 nm by Laser-Induced Incandescence," *Applied Physics B: Lasers and Optics* **89**, 417-427 (2007).

160. Ü. Ö. Köylü and G. M. Faeth, "Optical Properties of Overfire Soot in Buoyant Turbulent Diffusion Flames at Long Residence Times," *Journal of Heat Transfer* **116**, 152-159 (1994).

161. C. W. Bruce, T. F. Stromberg, K. P. Gurton, and J. B. Mozer, "Trans-Spectral Absorption and Scattering of Electromagnetic Radiation by Diesel Soot," *Applied Optics* **30**, 1537-1546 (1991).

162. M. Schnaiter, H. Horvath, O. Mohler, K.-H. Naumann, H. Saathoff, and O. W. Schock, "UV-VIS-NIR Spectral Optical Properties of Soot and Soot-Containing Aerosols," *Journal of Aerosol Science* **34**, 1421-1444 (2003).

163. F. Liu, K. Daun, V. Beyer, G. Smallwood, and D. Greenhalgh, "Some Theoretical Considerations in Modeling Laser-Induced Incandescence at Low-Pressures," *Applied Physics B: Lasers and Optics* **87**, 179-191 (2007).

164. H. Guo, F. Liu, G. Smallwood, and Ö. Gülder, "The Flame Preheating Effect on Numerical Modelling of Soot Formation in a Two-Dimensional Laminar Ethylene–Air Diffusion Flame," *Combustion Theory and Modelling* **6**, 173-187 (2002).

165. R. Kelly, "On the Dual Role of the Knudsen Layer and Unsteady, Adiabatic Expansion in Pulse Sputtering Phenomena," *The Journal of Chemical Physics* **92**, 5047 (1990).

166. C. Stipe, B. Higgins, D. Lucas, C. Koshland, and R. Sawyer, "Inverted Co-Flow Diffusion Flame for Producing Soot," *Review of Scientific Instruments* **76**, 023908 (2005).

167. G. J. Smallwood, D. R. Snelling, R. A. Sawchuk, D. Clavel, and D. Gareau, "Design Optimization for High Sensitivity Two-Color LII," *2nd International Discussion Meeting and Workshop on Laser-Induced Incandescence: Quantitative Interpretation, Modelling, Application*, Bad Herrenalb, Germany, August 2-4 (2006).

168. G. J. Smallwood, D. R. Snelling, K. A. Thomson, and F. Liu, "Development of a High Sensitivity LII Instrument for Measuring Ultra-Low Concentrations of Soot," *32nd International Symposium on Combustion*, WiPP 4P087, Montreal, Canada, August 3-8 (2008).

169. D. R. Snelling, F. Liu, G. J. Smallwood, and Ö. L. Gülder, "Determination of the Soot Absorption Function and Accommodation Coefficient Using Low-Fluence LII," *Twenty-Ninth Symposium (International) on Combustion*, WIP 3-1354, Sapporo, Japan, July 21 - 26 (2002).

170. F. Goulay, P. Schrader, L. Nemes, M. Dansson, and H. Michelsen, "Photochemical Interferences for Laser-Induced Incandescence of Flame-Generated Soot," *Proceedings of the Combustion Institute* (2008).

171. J. Delhay, Y. Bouvier, E. Therssen, J. Black, and P. Desgroux, "2D Imaging of Laser Wing Effects and of Soot Sublimation in Laser-Induced Incandescence Measurements," *Applied Physics B: Lasers and Optics* **81**, 181-186 (2005).

172. M. Charwath, R. Suntz, and H. Bockhorn, "Influence of the Temporal Response of the Detection System on Time-Resolved Laser-Induced Incandescence Signal Evolutions," *Applied Physics B: Lasers and Optics* **83**, 435-442 (2006).

173. S. S. Krishnan, K. C. Lin, and G. M. Faeth, "Optical Properties in the Visible of Overfire Soot in Large Buoyant Turbulent Diffusion Flames," *Journal of Heat Transfer* **122**, 517-524 (2000).

174. Ü. Ö. Köylü and G. M. Faeth, "Spectral Extinction Coefficients of Soot Aggregates from Turbulent Diffusion Flames," *Journal of Heat Transfer* **118**, 415-421 (1996).

175. B. J. Stagg and T. T. Charalampopoulos, "Refractive Indices of Pyrolytic Graphite, Amorphous Carbon, and Flame Soot in the Temperature Range 25 Degree to 600 Degree C," *Combustion and Flame* **94**, 381-396 (1993).

176. B. M. Vaglieco, F. Beretta, and A. D'Alessio, "In Situ Evaluation of the Soot Refractive Index in the UV-Visible from the Measurement of the Scattering and Extinction Coefficients in Rich Flames," *Combustion and Flame* **79**, 3-4 (1990).

177. A. Borghesi and G. Guizzetti, in *Handbook of Optical Constants of Solids, Volume 2*, E. D. Palik, ed. (Academic, 1998), p. 449.

178. T. C. Bond and R. W. Bergstrom, "Light Absorption by Carbonaceous Particles: An Investigative Review," *Aerosol Science and Technology* **40**, 1-41 (2006).

179. T. D. Durbin, K. Johnson, D. R. Cocker, J. W. Miller, H. Maldonado, A. Shah, C. Ensfield, C. Weaver, M. Akard, N. Harvey, J. Symon, T. Lanni, W. D. Bachalo, G. Payne, G. Smallwood, and M. Linke, "Evaluation and Comparison of Portable Emissions Measurement Systems and Federal Reference Methods for Emissions from a Back-up Generator and a Diesel Truck Operated on a Chassis Dynamometer," *Environ. Sci. Technol.* **41**, 6199-6204 (2007).

180. G. J. Smallwood, G. Sherwood, V. Beyer, and D. A. Greenhalgh, "Real-Time Measurement of Diesel Nanoparticulates," *2004 Autumn Meeting of the Combustion Institute (British Section) on Particles in Flames*, Cambridge, UK, September 20 (2004).

181. G. J. Smallwood, B. J. Stagg, and W. D. Bachalo, "Investigation of LII for Online Measurement of Nanoparticle Surface Area in a Carbon Black Reactor," *Twenty-Ninth Symposium (International) on Combustion*, WIP 3-1411, Sapporo, Japan, July 21-26 (2002).

182. G. J. Smallwood, K. A. Thomson, F. Liu, and D. R. Snelling, "Measuring Soot at Atmospheric Concentration Levels with High Sensitivity LII," *32nd International Symposium on Combustion*, WiPP 4P088, Montreal, Canada, August 3-8 (2008).

183. P. O. Witze, W. D. Bachalo, B. Graskow, and G. J. Smallwood, "On-Board, Time-Resolved Diesel Particulate Measurements by Laser-Induced Incandescence," *14th CRC On-Road Vehicle Emissions Workshop*, San Diego, CA, March 29-31 (2004).

184. T. Huai, G. J. Smallwood, A. Ayala, W. D. Bachalo, G. Payne, P. O. Witze, K. Johnson, T. Durbin, D. J. Chernich, and H. Maldonado, "Comparison of Particulate Matter Emission Measurements by Laser-Induced Incandescence to the Gravimetric Procedure," *16th CRC On-Road Vehicle Emissions Workshop*, San Diego, USA, March 28-30 (2006).

185. K. Daun, G. Smallwood, and F. Liu, "Investigation of Thermal Accommodation Coefficients in Time-Resolved Laser-Induced Incandescence," *Journal of Heat Transfer* **130**, 121201 (2008).

186. R. Sommer and A. Leipertz, "Application of Laser-Induced Incandescence to Suspended Carbon Black Particles," *Optics Letters* **32**, 1947-1949 (2007).

187. R. C. Gujarathi, V. Kumar, S. A. Shimpi, W. D. Bachalo, and G. J. Smallwood, "Assessment of a Laser-Induced Incandescence Sensor for Real-Time Particulate Emissions Measurement," *18th CRC On-Road Vehicle Emissions Workshop*, San Diego, CA, March 31 – April 2 (2008).

188. S. C. Wang and R. C. Flagan, "Scanning Electrical Mobility Spectrometer," *Aerosol Science and Technology* **13**, 230-240 (1990).

189. B. Y. H. Liu and D. Y. H. Pui, "Electrical Neutralization of Aerosols," *Journal of Aerosol Science* **5**, 465-472 (1974).

190. V. Krüger, C. Wahl, R. Hadef, K. Geigle, W. Stricker, and M. Aigner, "Comparison of Laser-Induced Incandescence Method with Scanning Mobility Particle Sizer Technique: The Influence of Probe Sampling and Laser Heating on Soot Particle Size Distribution," *Measurement Science and Technology* **16**, 1477-1486 (2005).

191. N. Ladommatos, S. Abdelhalim, and H. Zhao, "The Effects of Exhaust Gas Recirculation on Diesel Combustion and Emissions," *International Journal of Engine Research* **1**, 107-126 (2000).

192. P. Ahlvik, L. Ntziachristos, J. Keskinen, and A. Virtanen, "Real Time Measurements of Diesel Particle Size Distribution with an Electrical Low Pressure Impactor," SAE Paper No. 980410 (1998).

193. M. M. Maricq, D. H. Podsiadlik, and R. E. Chase, "Size Distributions of Motor Vehicle Exhaust PM: A Comparison between ELPI and SMPS Measurements," *Aerosol Science and Technology* **33**, 239-260 (2000).

194. G. M. Wang and C. M. Sorensen, "Diffusive Mobility of Fractal Aggregates over the Entire Knudsen Number Range," *Phys Rev E Stat Phys Plasmas Fluids Relat Interdiscip Topics* **60**, 3036-3044 (1999).

195. P. A. Baron and K. Willeke, eds., *Aerosol Measurement: Principles, Techniques, and Applications,* Second ed., Wiley-InterScience, (2001), pp. 724-725.

196. P. H. McMurry, X. Wang, K. Park, and K. Ehara, "The Relationship between Mass and Mobility for Atmospheric Particles: A New Technique for Measuring Particle Density," *Aerosol Science and Technology* **36**, 227-238 (2002).

197. H.-J. Klingen and P. Roth, "Size Analysis and Fractal Dimension of Diesel Particles Based on Rem Measurements with an Automated Imaging System," *Journal of Aerosol Science* **20**, 861-864 (1989).

198. G. Skillas, S. Kunzel, H. Burtscher, U. Baltensperger, and K. Siegmann, "High Fractal-Like Dimension of Diesel Soot Agglomerates," *Journal of Aerosol Science* **29**, 411-419 (1998).

199. K.-O. Lee, R. Cole, R. Sekar, M. Y. Choi, J. Zhu, J. Kang, and C. Bae, "Detailed Characterization of Morphology and Dimensions of Diesel Particulates Via Thermophoretic Sampling," SAE Paper No. 2001-01-3572 (2001).

200. L. Kramer, O. Friedrichs, M. Traver, and K. Behnk, "Assessment of Various Particulate Measurement Methods During Different Combustion Modes," *16th CRC On-Road Vehicle Emissions Workshop*, San Diego, USA, March 28-30 (2006).

201. M. Cassinelli and P. O'Connor, "NIOSH Method 5040," NIOSH Manual of Analytical Methods (NMAM), Second Supplement to NMAM. 4th ed. DHHS (NIOSH) Publication (1998).

202. C. M. Sorensen, "Light Scattering by Fractal Aggregates: A Review," *Aerosol Science and Technology* **35**, 648–687 (2001).

203. G. J. Smallwood, D. R. Snelling, and P. O. Witze, "Advances in High Energy Laser Diagnostics (HELD) for the Measurement of Particulate Matter " *8th International ETH-Conference on Combustion Generated Particles*, Zürich, Switzerland, August 16-18 (2004).